

Geological and Geochemical Study of Martian Volcanic Provinces: Implications for Igneous Evolution of Mars

A thesis submitted in partial fulfilment of
the requirements for the degree of
Doctor of Philosophy

by

Alka Rani

(Roll No. 17330004)

Under the guidance of

Dr. Amit Basu Sarbadhikari

Associate Professor

Planetary Sciences Division

Physical Research Laboratory, Ahmedabad, India



DISCIPLINE OF EARTH SCIENCES

INDIAN INSTITUTE OF TECHNOLOGY GANDHINAGAR, INDIA

July, 2022

I dedicate this to ...

My mother, who taught me how to stay strong in life...

My father, who taught me how to live by my ideals...

My husband, who is my strength...

My entire family, without whom, this voyage wouldn't have been possible...

Having just one of you as a family is truly a blessing...

Declaration

I declare here that this thesis report represents my own ideas in my own words and I have included others ideas with appropriate citations from original sources. I also declare that I have followed all principles of academic honesty and integrity and have not misrepresented or fabricated or falsified any idea/fact/source/data in my submission. I understand that any violation of the above can cause disciplinary action by the Institute and can also evoke penal action from the sources which have thus not been properly cited or from whom proper permission has not been taken when needed.

Date:

Alka Rani
(Roll No.: 17330004)



Discipline of Earth Sciences

Indian Institute of Technology, Gandhinagar

Gandhinagar, Gujarat-382355

CERTIFICATE

It is certified that the work contained in the thesis titled “**Geological and Geochemical Study of Martian Volcanic Provinces: Implications for Igneous Evolution of Mars**” (Roll no: 17330004), has been carried out under my supervision and that this work has not been submitted elsewhere for a degree.

Dr. Amit Basu Sarbadhikari
(Thesis Supervisor)
Associate Professor
Planetary Sciences Division
Physical Research Laboratory,
Ahmedabad, India

Date:

Acknowledgments

My journey toward Ph.D. at Physical Research Laboratory (PRL), Ahmedabad, which started in 2017, has now come to an end; and finally, I am ready with my Ph.D. thesis. During this journey of my Ph.D. I learned that it is not just about getting a degree, but it is to learn to believe in oneself and never lose hope. Writing this particular section of my thesis gives me immense pleasure to express my gratitude to the people who gave their support, and have directly or indirectly motivated me throughout. I owe many people a substantial debt for helping me through the process that resulted in the document that follows and the achievement it represents. I hope that in lieu of the proper thanks to you all actually deserve, the next few lines will suffice in conveying my gratitude.

My start in planetary science and the experience that led me to come to Ahmedabad began at Physical Research Laboratory. First and foremost, I wish to express my deepest gratitude to my supervisor, Dr. Amit Basu Sarbadhikari, for providing continuous support during my Ph.D. I thank him for giving me the freedom to work on new ideas and encouraging me to learn new things. His positive attitude towards solving scientific problems encourages me to probe deeper into the subject. His valuable suggestions and critical comments have helped me to improve scientific outcomes. His constant guidance, inspiration, encouragement, and motivation during this entire period helped me at the time of research and writing of this thesis.

There are numerous other people without their support completion of my Ph.D. was not possible. I express my sincere gratitude to my Doctoral Scientific Committee (DSC) members, Prof. Jyotiranjana S. Ray, Dr. Neeraj Srivastava, and Dr. Megha Bhatt, who have always guided me during my thesis progress and provided constructive remarks on my research work. I am thankful to all of them for providing me with unending support and their friendly behavior, which always kept me motivated for my thesis work. I am also thankful to the Academic Committee members for their insightful comments and encouragement during my research period. I express my sincere thanks to all the faculty and staff members of the Planetary Sciences Division for their assistance in the form of academic and administrative guidance.

I am very grateful to the Director, Prof. Anil Bhardwaj; Dean, Prof. D. Pallamraju; PSDN Chairman, Prof. Varun Sheel; and Head of Academic Services, Dr. Bhushit Vaishnav for their constant support and assistance during my Ph.D. tenure to complete the thesis work. I thank the people from accounts, purchase, library, administration, canteen, CMD, dispensary, transport, and housekeeping sections for all the help they have provided me during my Ph.D. tenure. I am also thankful to the Computer Center staff, namely Jigar sir, Tejas sir, Mishra Ji, Vaibhav, and others for their extended help regarding computational problems. I deeply appreciate their support for providing me with a smooth computational facility at all times.

I would also like to extend my special regards to all my teachers who taught me at different stages of my professional career. Because of their teaching, I can reach a stage where I could write this thesis. Also, the inspiration, support, and cooperation that I have received from my group members are beyond the scope of any acknowledgment. I would still like to thank all my group members for helping me during my Ph.D. journey. Especially, Yash Srivastava, my junior, and Rishitosh K. Sinha their wonderful suggestions, discussions, and immense support kept me going through this journey. I learn a lot from them. Last but not least, I would like to express my heartfelt gratitude to Dr. Priyabrata Das, Dr. Siddhi Shah, Dr. Shefali Uttam, Varsha M. Nair, Sonam Jiterwal, Srirag Nambiar, and Rashmi for their moral support and for creating a fun-loving working atmosphere.

Doing a Ph.D. is extremely challenging work, which occasionally brings stress with it. It is this time when the help and support of friends relieve the stress and makes the journey memorable. Fortunately, I am lucky enough to have the support of a superb group of friends at PRL who are traveling the same road and understand the challenges. I have had the pleasure of working alongside many great people in my five years at PRL whom I will call friends for many years to come, but I want to specifically thank Abhay, Rajesh Yadav, Neeraj, and Sushant for their support and friendship that goes beyond words. It would be impossible for me to deny the unwavering support that I have received from Abhay in these five long years of my Ph.D. journey and for being the first person to approach, whenever I am in need. I hope that I have been, and in the future can be, just as important to you as you all are to me.

Words would fail in expressing the love, strength, and encouragement of my family and in-law's family members towards me. I want to thank those who brought me into this world and who, I've been told, could just as easily take me out. Words like 'lucky', 'blessed', and 'fortunate' do not adequately convey how I feel about having grandparents (Dhapa, Surja Ram Goswami, Sushma Devi, and Japan Giri), parents (Sunita Goswami and Prithvi Singh), in-laws (Puspa Devi and Dr. S.C. Goswami), brothers (Capt. Manjeet, Sushil, and Ravi), brother-in-law (Sandeep Goswami), Sister (Deepa Paliwal), Sister- in laws Poonam, and Vinita and my extended family I do. Never once was I told that there was something I could not do, nor that my curiosity about the world and the stars and the planets wasn't important or practical or worth exploring, nor that I should pursue a career that would make me more money instead of one that makes me happy. For everything you have given me, mummy, and Papa, thank you from the bottom of my heart. It is a debt that truly cannot be repaid, but one that I assure you I will pay forward. Apple of our eyes Rehanshi and Divisha, their smiles make me giggle even wider. Lastly but most importantly to Navdeep, my best friend, my husband, my love, my everything, I owe you more than I could ever possibly repay, most importantly for your support and patience.

My external collaborators, Drs. Olivier Gasnault, Goro Komatsu, and Donald R Hood are thanked kindly for their contributions and insight during the completion of each project. Specifically, I thank Dr. Suniti Karunatillake, Associate Professor at LSU Planetary Science Laboratory, Baton Rouge, LA 70803, United States, for numerous conversations, guidance, and patience. The reason I kept his name at the end was, that people usually tend to skip the paragraphs in between. To describe his contribution to this thesis, I just need to say this: he was the light at the end of the tunnel. I consider myself fortunate to have you as a collaborator. The continuous encouragement and guidance make me motivated throughout my Ph.D. Much of what I know about Martian geology today, I owe it to Dr. Suniti Karunatillake. Last but not least, I would like to thank all Planetary Science Laboratory (PSL) members, especially Augustus Bates, and Emmy Hughes, for all of their help throughout the years with great discussion.

Alka Rani

Abstract

Over the last four decades, planetary missions to Mars have highlighted that the red planet has been volcanically active throughout its history, starting from Noachian (>3.6 Ga) to Late Amazonian (<150 Ma). The temporal evolution of volcanism on Mars implies that volcanic activity has played a significant role in the geologic evolution of the Martian crust and mantle. Martian volcanic provinces are of great geologic interest as the composition of igneous rock formed from the eruption of magma tends to preserve the record of its thermochemical properties.

Overall, this thesis aims to develop a perspective view of spatiotemporal changes in thermochemical conditions and evolution of the Martian mantle. We have used the link between magma chemistry and mantle thermal state to rationalize the compositional variations in Martian magmatism. In this context, detailed geological and geochemical investigations of Arabia Terra, the newly discovered Noachian aged (>3.6 Ga) volcanic province, helps to estimate the mantle source composition and magmatic processes. This study further evaluates the role of Arabia Terra in the geologic evolution of early Mars. Detailed morphological and structural analysis of the Arabia Terra region indicates that various volcanic landforms developed in response to putative regional tectono-volcanism, which further provides pieces of evidence for volcanism in Arabia Terra. Our finding of igneous landforms within the Ramanathan crater represents a broader extent of the thinned Arabia Terra crust. We also observe a preferred orientation of the igneous features, which show parallel alignment to regional linear tectonic features. We suggest that the igneous intrusions within the crater were controlled preferably along the pre-existing weak planes (i.e., faults) in response to the regional tectonism, while the magmatism was primarily triggered by the crater-forming impact event. This study discusses the possible extent of volcanism in Arabia Terra and shows that the proposed super-volcanic activity is not only confined to the NW part of Arabia Terra, but is plausibly spread over the entire Arabia Terra.

Furthermore, the compositional analysis of Arabia Terra is carried out to demarcate the geochemical extent and deduce the bulk composition for geochemical and petrological investigations. In this study, we present a set of consolidated chemical

provinces of Mars, which delineate the geochemical extent of Arabia Terra. These consolidated geochemical provinces correlate with temporal changes in elemental abundances, suggesting evolving intrinsic primary processes and mantle sources. This relation of age versus compositional variability reveals significant information about Martian crustal and mantle evolution. Our geochemical investigation also shows that Arabia Terra has a coherent compositional signature and uniformity in mapped geology. Lastly, temporal changes in element abundances of the Noachian-aged Arabia Terra are analyzed to understand the magmatic processes and formation pressure-temperature (P-T) conditions.

To improve our understanding of magma genesis in Noachian-aged (>3.6 Ga) volcanic regions, a detailed geochemical and petrological analysis based on model melting/crystallization simulation has been carried out. Our investigation demonstrates that the magma of the Noachian age was produced by 8-12% partial melting of the primitive Martian mantle at a pressure ranging from 1.3 to 1.8 GPa. Furthermore, our study demonstrates that the formation pressure (1.3 ± 0.2 GPa) of Noachian-aged Arabia Terra is relatively lower than the younger Hesperian and Amazonian-aged volcanic provinces. This lower pressure corresponds to a shallow melting regime for Noachian-aged Arabia Terra, supporting our geological observations. Furthermore, a decreasing trend of the calculated mantle potential temperature of the Martian volcanic provinces from Noachian to Amazonian is quite discernible.

In this thesis, through the geological and geochemical investigations, the age-specific Martian volcanic provinces are undertaken to obtain insights into the spatiotemporal changes in the Martian mantle, most notably of the early Noachian Mars.

Keywords: Mars; Noachian period; Igneous provinces; Arabia Terra; Tectono-volcanism; Geochemical trends; Magma genesis; Magmatic processes

Table of Contents

Acknowledgments	ix
Abstract	xiii
Table of Contents	xv
List of Figures	xix
List of Tables	xxvii
Chapter 1 Introduction	1
1.1 Volcanism.....	1
1.2 Large volcanic structures on Mars	2
1.3 Volcanic evolutionary history of Mars.....	5
1.4 Possible signature of tectono-volcanism on Mars.....	6
1.5 Thermochemical evolution of Mars	8
1.6 Main research questions	11
1.7 Objective of the thesis	12
1.8 Study areas	13
1.9 Datasets and Software	14
1.9.1 Imagery data.....	14
1.9.2 Topography data	16
1.9.3 Geochemical data.....	17
1.9.4 Software	18
1.10 Thesis organization	19
Chapter 2 Tectono-volcanism in north-central Arabia Terra, Mars: Insights from morphology and structural analysis	21
2.1 Introduction	21
2.2 Data and methods	26
2.2.1 Morphology.....	26
2.2.2 Statistical and morphometric analysis	27
2.2.3 Thermophysical observations	29
2.3 Results	29
2.3.1 Geomorphic observations of tectonic features in Arabia Terra.....	29

.....	37
2.3.2 Morphological and morphometric observations of the studied crater (now named as Ramanathan crater).....	37
2.4 Discussion	51
2.4.1 Origin of wrinkle ridges in Arabia Terra and its regional significance .51	
2.4.2 Regional significance of distinct landforms in the studied Ramanathan crater.....	52
2.5 Conclusion.....	65
Chapter 3 Arabia Terra and other chemical provinces on Mars: Implications for geologic interpretations	67
3.1 Introduction	67
3.2 Data and methods	70
3.2.1 Mars Odyssey Gamma-Ray Spectroscopy (GRS).....	71
3.2.2 Trilogy of multivariate cluster analysis	73
3.2.3 Average Martian crust.....	77
3.2.4 Modified Box-Whisker plot.....	78
3.3 Results	79
3.3.1 Comparison of derived geochemical provinces present study versus previous studies.....	79
3.3.2 Consolidated map using a trilogy of multivariate analysis techniques..	87
3.3.3 Distinct geochemical provinces from the consolidated province map ..	88
3.4 Discussion	97
3.4.1 The geochemical extent of Arabia Terra	97
3.4.2 Extent of aqueous alteration.....	98
3.4.3 Chemical trends in Arabia Terra and Martian chemical provinces	101
3.5 Summary and conclusion	103
Chapter 4 Noachian volcanism and its implication for thermo-chemical evolution of early Mars.....	107
4.1 Introduction	107
4.2 Data and methods	111
4.2.1 Bulk composition	111
4.2.2 Model melting/crystallization simulation	111
4.3 Results	117
4.3.1 Compositional variability among Noachian-aged volcanic provinces	117
4.3.2 Calculation of Non-GRS elemental composition	117
4.3.3 Primary vs. secondary processes.....	123
4.3.4 Conditions of magma genesis	128
4.4 Discussion	132

4.4.1	Geochemical investigation of Noachian provinces.....	132
4.4.2	Implications of estimated formation P - T in volcanic provinces.....	135
4.4.3	Depth of melting and mantle potential temperature (T_p).....	137
4.4.4	Implication to cooling of Martian mantle.....	138
4.5	Summary and conclusion.....	140
Chapter 5 Summary and Future Work		143
5.1	Introduction.....	143
5.2	Tectono-volcanism in north-central Arabia Terra, Mars: Insights from morphology and structural analysis.....	144
5.3	Arabia Terra and other chemical provinces on Mars: Implications for geologic interpretations.....	145
5.4	Noachian volcanism and its implication for thermo-chemical evolution of early Mars.....	146
5.5	Potential for future work.....	148
Bibliography		149
List of Publications		171

List of Figures

<i>Figure 1.1: Location of volcanic provinces on Mars - Global shaded relief and superimposed transparent black-and-white MOLA map in Aitoff-projection with locations of the Tharsis, Elysium, Syrtis Major, circum-Hellas, and North-western Arabia Terra Volcanic Provinces and selected volcanoes. (Adapted after Hiesinger and Head III, 2004; Williams et al., 2010).</i>	4
<i>Figure 1.2: Martian evolution with time, representing a contribution of different processes that formed the surface. Volcanism is outlined by the red dashed line (adapted after Carr and Head, 2009).</i>	5
<i>Figure 1.3: Studied Noachian-aged volcanic provinces are outlined by black color boundaries, which are overlaid onto mapped geology (Tanaka et al., 2014; different colors indicate different geologic units). Yellow star represents the location of Ramanathan crater.</i>	14
<i>Figure 2.1: THEMIS day-time IR basemap of eastern Arabia Terra region overlain by color-coded MOLA-HRSC topographic map (location of Eastern Arabia Terra marked by the black box in the global map at upper left), showing distributions of craters with evidence of ridges, mounds, and mesas observed over the floor of depressions and wrinkle ridges. The white box in the global inset map indicates the study area of Michalski and Bleacher (2013). The Ramanathan crater of this study is marked by a red box and a red star on the globe of Mars.</i>	23
<i>Figure 2.2: Examples of other FFCs in Arabia Terra as marked in Figure 2.1, using CTX images (6 m/pixel). (CTX image credit: NASA/JPL-Caltech/MSSS).</i>	25
<i>Figure 2.3: a) Magnified view of the study crater using CTX images. The white box is the central part of the crater with distinct geomorphology shown in Figure 2.5a, and the yellow box represents the crater floor features outside the central part. b) THEMIS nighttime IR image illustrates the material property of different landforms within the crater. c) CTX image based geomorphic map of the study crater at 1:15,000 scale with the crater boundary marked by solid black line. The legend is shown at the right side with different relevant landforms present inside the crater. d) Mesas at the outside part of the crater floor are displaced from each other by fractures. Four blocks were plausibly parts of a single unit close to the crater rim wall, indicating a floor-fracture crater. Arrows mark the displacement direction of the adjacent blocks. (CTX image credit: NASA/JPL-Caltech/MSSS).</i>	36
<i>Figure 2.4: a) CTX images are used to determine the numeric model age by plotting the counted craters using Craterstats tool (version 2.0; Michael and Neukum, 2010), where we use craters with >1.2 km diameter. Black hollow circles, which represent the craters inside the study FFC, are counted for the crater age calculation; white circles outside the study FFC are used to determine the age of surrounding surface. b) Crater retention age of the study crater is deduced by Crater size-frequency distribution</i>	

(CSFD), using CraterTools, an ArcGIS extension (Kneissl et al., 2011; Michael et al., 2013). The CSFD statistic is inferred based on the production function provided by Ivanov (2001) and the impact-cratering chronology model of Hartmann and Neukum (2001). Age of the crater is Late Noachian or Early Hesperian (~ 3.6 Ga). (CTX image credit: NASA/JPL-Caltech/MSSS).37

Figure 2.5: a) 2D Digital Terrain Model (DTM) is overlain on CTX images of the central part of the crater, showing anomalous features of variable elevation at the central portion of the crater. (CTX image credit: NASA/JPL-Caltech/MSSS, DEM credit: USGS Astrogeology Science Center). b) CTX-DTM derived 3D view of central portion of the crater, showing different morphological features such as mounds, ridges, fault, mesas etc. CTX stereo images P21_009232_2084 and J10_04846_2083 (no vertical exaggeration) for both.39

Figure 2.6: Basement and Mesa units. a) An elliptical to irregular-shaped mesa with small craters on surface. b) Preserved layered strata at the crater floor. c) A basement block with ridged plain surface. d) A mesa as an erosional remnant of the pre-existing crater floor; inverted terrain on the mesa. (CTX image credit: NASA/JPL-Caltech/MSSS, HiRISE image credit: NASA/JPL-Caltech/University of Arizona).40

Figure 2.7: Mounds of the study crater. a) Mound overlies the flat basement unit, with rugged and serrated texture of layers exposed at top of mound, shown as an inset at bottom left; b) Mound flanks having flow-like features; c) Flow-like feature near mound, possibly originated from the mound that is associated with linear ridges. (CTX image credit: NASA/JPL-Caltech/MSSS, HiRISE image credit: NASA/JPL-Caltech/University of Arizona).41

Figure 2.8: Average cross-sectional elevation profiles (X1-X2 and Y1-Y2) of selected mound types using CTX DTM (CTX stereo image pair Id: P21_009232_2084 and J10_04846_2083; no vertical exaggeration). Mounds with conical shape (a1-a2) and a crater at its summit (b1-b2). c) Two-point azimuth technique indicates mounds are aligned in NW-SE direction relative to each other. See the text in Section 3.2 for details. (CTX image credit: NASA/JPL-Caltech/MSSS, DEM credit: USGS Astrogeology Science Center).42

Figure 2.9: Plot showing morphometric analysis of the mounds. Average mound height versus basal diameter for 25 mounds. The solid line represents the maximum likelihood fit. Standard error bars along the x-axis and y-axis are 11% and 12%, respectively. 43

Figure 2.10: Linear ridges of the study crater. a) Broad and long linear ridges; b) Arcuate or curvilinear type of linear ridges along with less-exposed small, abruptly terminated, substantially buried ridges; and c) Linear ridges with rectangular or polygonal box-like patterns. All types of ridges (a-c) having positive relief (~ -2520 m) nearly close to elevation of surrounding sedimentary deposits (~ -2530 m). d) and e) HiRISE images showing ridges with shedding boulders, similar to an exposed dike of Shiprock on Earth, as shown in Figure S6. The sun direction is shown with star marks and arrows. (CTX image credit: NASA/JPL-Caltech/MSSS, HiRISE image credit: NASA/JPL-Caltech/University of Arizona).45

Figure 2.11: a) Mapped distribution of boulders associated with ridges (ESP_018937_2085, ESP_036923_2085, PSP_009232_2085 and ESP_018726_2085); b) Slope map generated from HiRISE stereo Images (ESP_036633_2085_ESP_036923_2085 and PSP_008520_2085_PSP_009232_2085), depicting steep slope ($> 50^\circ$) of ridges and mounds with rough boulder-rich topmost part. The layered strata is almost horizontal. Dust is mostly accumulated at the crater floor, on the layered sediments, and lowest part of the ridges and mounds at a slope $<35^\circ$, i.e., the angle of repose for unconsolidated sediment on Mars. The index of slope values is mentioned in the different color scheme. (HiRISE image credit: NASA/JPL-Caltech/University of Arizona, DEM credit: USGS Astrogeology Science Center).46

Figure 2.12: Cross-cutting relationships among the observed geomorphic features. a) Exhumed linear ridges in a preserved section are associated with a mound. b1) Faulted blocks of a mesa, associated with a ridge; b2) 3D view from CTX-DTM image of b1 (No vertical exaggeration). c) Sharp contact between ridges and layered sedimentary rocks. Sedimentary layers are cross-cut by the ridges. Inset shows zoomed view of the white box part. (CTX image credit: NASA/JPL-Caltech/MSSS, HiRISE image credit: NASA/JPL-Caltech/University of Arizona, DEM credit: USGS Astrogeology Science Center).47

Figure 2.13: Morphometry of the ridges. a) A linear ridge along which elevation profile is drawn along A-A' line. CTX stereo images P21_009232_2084 and J10_04846_2083 (No exaggeration). b) A symmetric bell-shaped topographic profile of the ridge in cross-section view, showing the ridge is ~ 140 m high from the surroundings. The topmost 30-40 m is relatively less dust-covered and better exposed than the surroundings. The vertical dashed line is to show the dust-free topmost part of the ridge, which has a width of 100-150 m. c) Rose diagram of the orientation of ridges in our study crater. Orientation is weighted by the corresponding length of the ridges. d) and e) showing histogram plots of morphometric analysis of the ridges height and width. (CTX image credit: NASA/JPL-Caltech/MSSS, DEM credit: USGS Astrogeology Science Center).48

Figure 2.14: Nili Fossae and Nilosyrtris regional map by Saper and Mustard (2013), Ebinger and Mustard (2015, 2016), and Pascuzzo et al. (2019) based on CTX images. Here, the MOLA-colored topography is overlain on the CTX image mosaic and the delineated ridges inside the craters (marked as 'a', 'b', and 'c'). Corresponding rose diagrams are generated to depict the orientations of ridges in respective craters, as marked by the arrows. The orientation is weighted by the corresponding length of the ridges. (CTX image credit: NASA/JPL-Caltech/MSSS).54

Figure 2.15: a) and b) An exposed radial dike of Shiprock, Colorado Plateau, New Mexico viewed from the ground showing the erosion of the irregular crest and associated boulders, resulted as an erosional remnant of a volcano located in northwestern New Mexico. The photographs mainly feature a dike with boulders at its flanks. The dike is exposed as its host rock has eroded away revealing the positive relief

feature, we see today. Boulders are seen on the slopes and their number density decreases away from the dike. The exposed ridges in our study area on Mars are morphologically similar to the exposed Shiprock dike (Sources: a) <https://web.archive.org/web/20161018010808/http://www.panoramio.com/photo/44691497>, page title “Panoramio” and b) <http://written-in-stone-seen-through-my-lens.blogspot.com/2012/08/ship-rock-at-sunset-partially-exhumed.html>, posted by Dr. Jack Share (<https://www.blogger.com/profile/09068066012491070695>). The road and the standing human highlighted with the white circle in a) serve as references for the scale of the image, while b) is another side view of the same dike).55

Figure 2.16: (a) and (b) Layered mounds in our study crater, with serrated edges with visible boulders of several meters in diameter, similar to layered volcanic rocks on the flanks of Ascraeus Mons (c). Volcanic layering is compared with the layered sedimentary strata at Crommelin crater (d), and Becquerel crater (e) in western Arabia Terra at a similar spatial scale. (HiRISE image credit: NASA/JPL-Caltech/University of Arizona).57

Figure 2.17: Height vs basal diameter plots of Martian, lunar, and terrestrial mounds (after Hemmi and Miyamoto, 2017; Wan et al., 2021). Morphometric comparison among the measured mounds (in this study) and other terrestrial analogs, log-log plots showing mound height versus basal diameter. Dashed lines represent the best linear least square fits of parameters of each category.59

Figure 2.18: (a) Scoria cone with exposed dikes in Atakor volcanic field, Algeria (Google Earth; 23.37° N, 6.13° E). The inset at the bottom left is a 3D view of the cone, and at the upper right is a zoomed view of the top of cone, having rugged and serrated edges, exhumed due to erosion. (b) Scoria cone with associated lava flows at Sunset crater, San Francisco volcanic field north of Flagstaff, Arizona (Google Earth; 35.58° N, 111.63° W). A similar mound with flow feature is observed in our study crater. (c) Dozens of volcanic cones with lava flows at Uinkaret field, perched high atop the north rim of the western Grand Canyon (Google Earth; 3D view, 36.28° N, 113.16° W). Volcanic cones show a preferential alignment, similar to the mounds in our study crater.61

Figure 2.19: Left panel: Image of the interior part of the study crater with major landforms. Right panel: A schematic diagram and model for the origin of the volcanic landforms (not to scale). (HiRISE image credit: NASA/JPL-Caltech/ University of Arizona).62

Figure 2.20: Orientation of the landforms (dikes and cones) in our study crater and wrinkle ridges in Arabia Terra; all showing bimodal direction tending ~ NW-SE, indicating evidence of regionally distributed tectono-volcanism.64

Figure 3.1: Results obtained from multivariate analysis by NHC-PCA (a), HC-PCA (b), and t-GTC (c) methods, overlaid on the Mars Orbiter Laser Altimeter and High-Resolution Stereo Camera (MOLA-HRSC) data map to delineate the geochemical provinces. Provinces-2 and -4 do not appear in the t-GTC method (c) as they are compositionally similar to the average crustal composition (Tables 3.3-3.4). (d) The

consolidated contour map resulting from the synthesis of provinces derived from three different multivariate methods, overlaid on MOLA-HRSC to delineate the integrated geochemical provinces. The number of methods overlapping corresponding to each province is shown by the legends (0-III), and the intermediate province number is shown numerically (1 – 6).....84

Figure 3.2: (a) and (b) The consolidated geochemical provinces on Mars are derived by integrating provinces from three different multivariate techniques and overlaid onto mapped geology (Tanaka et al., 2014, different colors indicate different geologic units with major units in legend). Arabia Terra is shown in white dashed boundary line in (b).84

Figure 3.3: (a) The relative areal fractions of secular, transitional, and volcanic units within each chemical province corresponding to the consolidated geochemical map. The prefix “N” indicates Noachian, “H” indicates Hesperian, and “A” indicates Amazonian, and suffix “v” indicates the associated volcanic units (Tanaka et al., 2014). A detailed version of Figure 2a is given in Figure 2b as per Tanaka et al., 2014 geology map. (b) The four mapped geologic units (Tanaka et al., 2014) with the highest areal fractions are shown for each consolidated province and Arabia Terra, with the total areal fraction of remaining units indicated as others with orange color. The geologic unit notation of the I-1802 series is used.89

Figure 3.4: Modified box-and-whiskers diagram to compare the distribution of elements for all provinces to the global geochemistry of the average Martian crust. The top of the upper box represents 75th percentile/25th percentile ratio, the bottom of the lower box represents the 25th/75th percentile ratio, and the ratio of the medians by the boundary between them. The whiskers here represent the uncertainty on the ratio of medians using the Median Absolute Deviation (MAD) (Karunatillake et al., 2011). .90

Figure 3.5: Left panel shows a geological map of Lunae Planum overlain on MOLA-HRSC map. The corresponding modified box-and-whiskers diagram to compare the distribution of elements in Lunae Planum province to the global geochemistry of the average Martian crust is shown in the right panel.91

Figure 3.6: panel shows a geological map of Medusae Fossae Formation overlain on MOLA-HRSC map. The corresponding modified box-and-whiskers diagram to compare the distribution of elements in Medusae Fossae Formation province to the global geochemistry of the average Martian crust is shown in the right panel. The enrichment of volatiles within the Medusae Fossae Formation is clear, whereas other elements are relatively consistent with the average Martian crust.93

Figure 3.7: Figure 3.7: Cl vs K, Cl vs H₂O, and Cl vs S plots for Medusae Fossae Formation, Lunae Planum, and Southern Acidalia Planitia with the rest of the GRS data as a reference.93

Figure 3.8: Left panel shows a geological map of Southern Acidalia Planitia highlighted in white col overlain on MOLA-HRSC map. The corresponding modified box-and-whiskers diagram to compare the distribution of elements in Southern Acidalia

Planitia province to the global geochemistry of the average Martian crust is shown in right panel.94

Figure 3.9: Modified box-and-whiskers diagram to compare the distribution of elements for (a) Arabia Terra, and nearby regions viz. (b) Sinus Meridiani and Southern Acidalia Planitia (Figure 3.5) w.r.t the global geochemistry of the Average Martian Crust. Detailed discription of modified box-whiskers diagram is given in Figure 3.4.97

Figure 3.10: a) The Mg/Si vs. Al/Si diagram with Martian meteorites, Southern Acidalia Planitia, and Martian surface references plotted. Southern Acidalia Planitia data show the Al depletion follows a similar trend seen in Martian meteorites. The distinguishing characteristics might result from the depletion of Al during the early melting of mantle source regions of Mars. b) Ternary diagrams illustrating the scenarios to account for the chemical composition of Southern Acidalia Planitia region. The diagrams display the relative molar proportions of Si, Fe, Mg, Ca, Al, and S in the Southern Acidalia Planitia region, in a reference set of Martian basalts, including basalts analyzed in situ by rovers and basaltic meteorites.96

Figure 3.11: (a) The Chemical Index of Alteration ($CIA=100[Al_2O_3/(Al_2O_3+CaO+Na_2O+K_2O)]$) diagram is used to assess the extent of chemical weathering in the provinces A-D. For CIA, we are using standard molar abundances of oxides. Non-GRS Na_2O is calculated using Baratoux et al. (2014). (b) K (wt%) vs. Th (mg/kg) in several regions, consolidated provinces A-D including Arabia Terra and Average Martian Crust.99*

Figure 3.12: (a) Diagram of K/Th normalized to the bulk silicate Mars (~ 5300) versus GRS derived total volatile concentration. The modest variation in K/Th, which is consistent with the bulk Mars, implies low or no alteration at decimeter depths in the Noachian age Arabia Terra and consolidated provinces. The scatter values of Fe versus Si (b), Al versus Fe (c), and Ca versus Si (d) of the Arabia Terra and provinces A-D are represented by colored boxes (southern highland provinces A-C and Arabia Terra) and ellipse (northern lowland Province-D). The regional uncertainty is shown at the right corner of each plot, represented by the average of the standard error of mean (1σ) from all provinces and Arabia Terra (Table 3.5). From Noachian to Amazonian, all the three plots (b-d) exhibit a compositional tend, marked by a dashed arrow, except Province-D (Figure 3.12b-d). The prefix “N” indicates Noachian, “H” indicates Hesperian and “A” indicates Amazonian, and the suffix “v” indicates associated volcanic units, “h” indicates highland, “m” indicates middle and “lHl” indicates late Hesperian lowland. 104

Figure 4.1: Noachian to Amazonian age volcanic provinces are represented over MOLA-HRSC topographic map. Studied Noachain regions are outlined in black, whereas Hesperian volcanic provinces, located in the highlands south of the hemispheric dichotomy, are highlighted in blue and Amazonian provinces occurring as large shield volcanoes are highlighted in red adapted after Baratoux et al., 2011. . 110

Figure 4.2: Compositional variability among Noachian provinces w.r.t average Martian crust. Modified box-whiskers diagram to compare the distribution of elements for all provinces to the global geochemistry of the average Martian crust. The top of the upper box represents 75th percentile/25th percentile ratio, the bottom of the lower box represents the 25th/75th percentile ratio, and the ratio of the medians by the boundary between them. The whiskers here represent the uncertainty on the ratio of medians using the Median Absolute Deviation (MAD) (Karunatillake et al., 2011). 119

Figure 4.3: (a) K (wt. %) vs. Th (mg/kg) in several regions, Noachian age provinces N1, N2, Arabia Terra and average martian crust. (b) Ternary Diagram (CaO + Na₂O+K₂O)-(Al₂O₃)-(MgO + FeO) (CNK-A-MF) is used to investigate low pH aqueous alteration signature in Noachian age provinces (adapted from Hurowitz and McLennan [2007]), the dashed red line represents the olivine-feldspar join. Compositions that plot below the line are considered to be igneous rocks that are not weathered under moderate pH conditions. The black solid line represents subaqueous alteration trends at low pH, similar to those observed on Mars (Hurowitz and McLennan, 2007). Basalts weathered under these conditions trend toward the CNK-A join (A) and alteration fluids toward the MF apex (F). (c) Extent of chemical weathering for Noachian age volcanic provinces are calculated using the Chemical Index of Alteration (CIA=100*[Al₂O₃/(Al₂O₃+CaO+Na₂O+K₂O)). This diagram is used to assess the extent of chemical weathering in the provinces Arabia Terra, N1 and N2. For CIA, we are using standard molar abundances of oxides. Non-GRS Na₂O is calculated using Black Beauty. 124

Figure 4.4: Classification of primary composition. This diagram is used to illustrate the Total alkalis (Na₂O and K₂O) vs. silica (TAS) classification scheme for volcanic rocks based on their bulk chemical composition (La Bas et al., 1986). Noachian aged surface volcanics of Arabia Terra, N1 and N2 from GRS measurements with calculated Na₂O from Black Beauty. Shergottites, Clasts in NWA 7034/7533, chassignite and nakhlites, in situ rover data of basalts from Gusev and Gale Crater with Bounce Rock at Meridiani Planum are shown in this diagram. 125

Figure 4.5: Comparison of mantle melting model by p-MELTS with experimental data of Bertka and Holloway (1994) at 15 kbar. Each line represents a series of compositions produced by the results from pMELTS for each pressure and temperature combination. Data points are connected with a solid line. Solid points (orange color circles) represent experimental data at 15 kbar (Bertka and Holloway, 1994). The oxide trends are compared to the experimental results for iron-rich parent compositions at 10, 30, 32, 55, and 71 percent melt fractions to identify systematic differences of pMELTS from laboratory conditions. The resulting offsets allow the comparison between the liquid oxide compositions from pMELTS and the oxide concentrations derived from the GRS data for the surface within the Volcanic Province..... 126

Figure 4.6: a) Geochemical modeling for magmatic evolution in Noachian aged Volcanic Provinces including all volatiles. b) Geochemical Modeling for magmatic

evolution in Noachian aged Volcanic Provinces normalized with respect to all volatiles. Curves (SiO_2 vs FeO , SiO_2 vs MgO , SiO_2 vs K_2O , and SiO_2 vs Al_2O_3) in the oxide bivariate diagrams plots are based on the model calculations by pMELTS and represent isobaric lines with the pressure ranges between 1.2 kbar and 2.2 kbar at an increment of 0.2 kbar. The number (3, 5, 10, 20, 30, 40, 50) are degrees of partial melting for each isobaric curve. The color from dark blue to light blue in each plot represents increasing degree of partial melting. 128

Figure 4.7: Pressure and temperature (P-T) conditions are calculated for surface volcanics of the Noachian age derived from GRS. For comparison between similar age in situ basalts from Gusev, Gale, and Meridiani Planum is also shown in this P-T diagram. Dashed contours represent mantle potential temperature in degree Celsius, calculated by adding the latent heat of fusion to equilibrium temperature at which melt and solid mantle coexist and subtracting martian adiabatic gradient corresponding to the depth of melt. Also shown is the solidus of the nominally volatile-free Martian mantle (solid line, Kiefer et al., 2015). 134

Figure 4.8: Pressure and degree of partial melting of basalts from in situ investigation, surface volcanics (Noachian to Amazonian) from GRS measurements. Contours represent mantle potential temperature in degree Celsius. 138

Figure 4.9: Depth of melt formation vs mantle potential temperature for Noachian magmatism. The depth of melt and mantle potential temperature are derived from pressure and degree of partial melting. Heat flow contours (milliwatts per square metre) are calculated from the depth of melt and melting temperature assuming a conductivity of the lithosphere as $3.0 \text{ Wm}^{-1} \text{ K}^{-1}$ 136

Figure 4.10: The average mantle potential temperature (T_p °C) through time is estimated for basalts from Gusev, Gale, and Meridiani Planum, along with the studied Noachian volcanic provinces in this work. Hesperian and Amazonian surface volcanics are also plotted (from Baratoux et al., 2011). The best polynomial fit represents the cooling curve of the martian interior. 139

Figure 4.11: Schematic diagram for evolution of martian mantle over time. 140

List of Tables

<i>Table 2.1: Wrinkle ridges locations and their corresponding length and trend/orientation w.r.t geographic north.</i>	30
<i>Table 2.2: Morphometric parameters: basal diameter, height, and slope of the observed mounds.</i>	43
<i>Table 2.3: Descriptive statistics of ridge height.</i>	49
<i>Table 2.4: Descriptive statistics of ridge-width.</i>	50
<i>Table 2.5: Average slope of ridges calculated using height and width trigonometric ratio, height and width values are used from tables 2.3 and 2.4.</i>	50
<i>Table 2.6: Descriptive statistics of ridge-spacing between different sets of pairs.</i>	51
<i>Table 3.1: Comparison of GRS dataset archived at PDS vs. GRS data used in the present study (previously used by Hood et al., 2016, 2019; Plesa et al., 2018; Ojha et al., 2018, 2021). NA denotes the unavailability of data.</i>	74
<i>Table 3.2: Intermediate chemical provinces (1-6) from the three multivariate methods, their constituent geographic regions, and contribution to the consolidated provinces (last row). Abbreviations are K09: t-GTC method following Karunatillake et al. (2009); G10: HC-PCA method following Gasnault et al. (2010); T10: NHC-PCA method following Taylor et al. (2010).</i>	84
<i>Table 3.3: Summarized Results from modified box-whisker plots (cf. Karunatillake et al., 2011), compared to characterize compositional differences of the intermediate chemical provinces and their constituent regions. Empty boxes represent insignificant deviation from average crust. D and E denote the elemental median ratio, in modified box-whisker plots above (enrichment: E) or below (depletion: D) unity by at least 1 sigma. Abbreviations are E: Enrichment; D: Depletion; others are as per Table 4. Province-2 and -4 are not highlighted in t-GTC method.</i>	87
<i>Table 3.4: Ratio of stoichiometric oxides/elements for each intermediate province, '1', '3', '4', '5', and '6' relative to the average martian crust (AMC). The ratio compares with the corresponding propagated standard deviation. Uncertainty in each X/AMC ratio is calculated from $(X/AMC)[(\sigma_X/X)^2 + (\sigma_{AMC}/AMC)^2]^{1/2}$, where X (province) and AMC are mean concentrations of X and AMC. The values in bold show significant deviation from AMC. (Province-2 lacks minimum criteria of overlapping by at least two methods, therefore not highlighted in the consolidated province map).</i>	88
<i>Table 3.5: Arithmetic mean stoichiometric oxide mass fraction as a percentage (wt%, if not mentioned otherwise), elemental ratio, and its corresponding root means square uncertainty (σ) are calculated from mean measurement uncertainties for the grid points composing a geochemical province. Whereas, K/Th ratio uncertainty is calculated from</i>	

$[(K/Th)*((\sigma_K/K)^2+((\sigma_{Th}/Th)^2)]^{1/2}$ (GRS derived) of the consolidated chemical provinces. 88

Table 3.6: Summarized results from the modified box and whisker analyses (cf. Karunatillake et al., 2011), compared to characterize the relative distribution of chemical composition of the consolidated provinces. Empty boxes represent the insignificant deviation from the average crust. D and E denote the elemental median ratio, in modified box-whisker plots above (enrichment: E) or below (depletion: D) unity by at least 1 sigma. Abbreviations are as per Table 3.3. 97

Table 3.7: H₂O Abundance in Lunae Planum, Hesperia Planum, Syrtis Major, and Martian references. 103

Table 4.1: Bulk silicate Mars composition (BSM) after Taylor (2013). Updated after the DW85 composition (defined by Dreibus and Wanke, 1985). This composition is used as parental magma composition for p-MELTS thermodynamic simulations. 116

Table 4.2: Arithmetic mean of stoichiometric oxide mass fraction as a percentage (wt%, if not mentioned otherwise), and its corresponding standard error (GRS derived) of the Noachian Volcanic provinces with mid-latitudinal Average Martian Crust (AMC). 120

Table 4.3: Ratios of incompatible elements in Black Beauty. 122

Table 4.4: a) Arithmetic mean of stoichiometric oxide mass fraction as a percentage (wt%, if not mentioned otherwise), of the Noachian volcanic provinces without normalization with respect to volatiles. We consider all volatiles in the calculation of MgO values. Non-GRS oxides are estimated using ratios of incompatible elements in Black Beauty given in Table 4.3. 123

Table 4.4: b) Arithmetic mean of stoichiometric oxide mass fraction as a percentage (wt%, if not mentioned otherwise), of the Noachian volcanic provinces normalized with respect to volatiles. We consider all volatiles in the calculation of MgO values. Non-GRS oxides are estimated using ratios of incompatible elements in Black Beauty given in Table 4.3. 124

Table 4.5: a) Pressure (P), Temperature (T), degree of partial melt (F), depth of magma formation, and mantle potential temperature (T_p) is estimated for Arabia Terra, N1 and N2 Noachian provinces. The average composition derived from GRS corresponding to each study region includes the volatiles (H₂O, Cl, and S) in the calculation of Non-GRS MgO values. 133

Table 4.5: b) Pressure (P), Temperature (T), degree of partial melt (F), depth of magma formation, and mantle potential temperature (T_p) are estimated for Arabia Terra, N1 and N2 Noachian provinces. The average composition derived from GRS corresponding to each study region is Normalized with respect to volatiles (H₂O, Cl, and S) in the calculation of Non-GRS MgO values. 134

Abbreviations

AMC	Average Martian Crust
APXS	Alpha Particle X-Ray Spectrometer
BSM	Bulk Silicate Mars
CTX	Context Camera
GRS	Gamma Ray Spectrometer
HiRISE	High-Resolution Imaging Experiment
HRSC	High-Resolution Stereo Camera
MEX	Mars Express
MGS	Mars Global Surveyor
MOLA	Mars Orbiter Laser Altimeter
MER	Mars Exploration Rover
MEX	Mars Express
MRO	Mars Reconnaissance Orbiter
TES	Thermal Emission Spectrometer
THEMIS	Thermal Emission Imaging System

Chapter 1 Introduction

1.1 Volcanism

Planetary science research in the past several decades has established that, as on Earth, volcanism has been an extremely important process in the evolution of other terrestrial planetary bodies such as the Moon, Mars, Venus (Wilson, 2009; Platz *et al.*, 2015). Volcanism is a process that involves the transport of molten materials from a planet's interior to its surface. Perhaps the most important factor in shaping and comprehending planetary evolution is magmatism. It is a precise reflection of the chemical and physical constitution, as well as the planet's internal heat condition and budget. Volcanic activity represents a major way by which the terrestrial planets lose heat. On Earth, tectonic activity is intimately related to magmatism, which is in turn related to the larger-scale thermal convection process occurring in the mantle and core. Further, the physical properties of the planet and the nature of environmental conditions that exist at the surface have a significant impact on how the melts rise and erupt onto the surface, as well as the appearance of the landforms that result from these processes (Zimelman and Gregg, 2000). These factors include the planet's temperature and pressure, as well as the fundamental physical characteristics like magma density, composition, and volatile content, as well as planetary gravity and thermal gradient. The formation, ascent, eruption, and shape of volcanic deposits would have been significantly impacted by each of these (Head and Solomon, 1981; Wilson and Head, 1981; Wilson and Head, 1983). Finally, on Earth, the active geological processes associated with plate tectonism, like crustal subduction, mantle convection, active volcanism, and consequently venting of gases from the interior argue for the rationale of the maintenance of a dense atmosphere. Summarily, volcanic processes contribute to planetary heat loss, reveal interior compositions and physical crustal structure, and

form and replenish the atmosphere. Therefore, the study of volcanism is critical for understanding planetary structure and evolution in our Solar System and beyond.

In brief, Mars's crust-mantle system has evolved as a single-plate planet known as the Stagnant-lid regime (Golombek and Phillips, 2010a; Grott *et al.*, 2013). On Mars, regardless of the lack of plate tectonic activity, the majority of magma formed when a source or parent rock partially melted, possibly led by adiabatic decompression. The decompression melting could have resulted from thermal and density instabilities within the mantle and crust (Kiefer, 2013). The accumulated buoyant magma ascended and contributed to volcanism on Mars. The following sections provide the details of Martian volcanism through the ages.

1.2 Large volcanic structures on Mars

Since last four-decade from the Mariner 9 mission in 1972 till now, scientists have known that volcanic features cover a considerable portion of the Martian surface (Carr, 2007). Continuous Mars exploration added new facts to the intricate mosaic of the volcanic history of Mars (Carr, 2007). It was found that the extensive volcanic products are not distributed equally and contain a wide range of volcanic landforms (Werner, 2009) (Figure 1.1). Several types of volcanism have been observed on Mars, flat plains and infilled basins and local edifices classified as Montes (e.g., Olympus Mons or Elysium Mons, etc.), Tholii (e.g., Hecates Tholus), and Paterae (e.g., Alba or Nili Patera) based on their shape and size. Compared to Tholii, Montes edifices are larger and higher, whereas, Paterae are also larger with low-relief volcanoes. Strong morphological variation, similar to that found in various volcanic locations on Earth, is probably related to various eruption styles.

On Mars, the largest and most conspicuous volcanoes are in the Tharsis and Elysium regions. Tharsis volcanic province, which is characterized by a huge volcano-tectonic complex collectively known as Tharsis bulge, covers the western hemisphere of Mars. It is a massive, raised structure with a diameter of thousands of kilometres that covers up to 25% of Mars' surface (Greeley and Schneid, 1991). Tharsis bulge is

comprised of three enormous volcanoes (Arsia, Pavonis, and Ascraeus Mons) called Tharsis Montes, aligned in a northeast-southwest direction. Alba Mons, a part of the Tharsis bulge covers the northern part. The tallest shield volcano in our solar system, Olympus Mons, is also located on the western end of the Tharsis volcanic province (Figure 1.1).

The Elysium volcanic province, comprised of three volcanic centres, is located thousands of kilometres west of the Tharsis bulge (Figure 1.1). Elysium Mons, Hecates Tholus, and Albor Tholus are the three primary volcanoes that make up this enormous volcanic province, which spans about 2000 kilometres in diameter. Elysium Mons is the largest of these three volcanic edifices in this province. It is about 14 kilometres high and 375 kilometres across, however, the base or diameter varies depending on individual/specific definitions. By volume, Elysium Mons is only one-fifth the size of Arsia Mons. The northern half of Elysium province has Hecates Tholus, which is 4.8 km high and 180 km in diameter, while the southern part contains Albor Tholus, which is almost 150 km in diameter and 4.1 km high (Figure 1.1) (Hiesinger and Head III, 2004; Williams *et al.*, 2010).

Furthermore, prominent volcanic regions in the southern Highland include Syrtis Major and Hesperia Planum (Figure 1.1). Syrtis Major is a massive shield volcano with a diameter of 1200 km and a height of 2 km. Whereas, Hesperia Planum is a broad lava plain, consists of the ancient volcano Tyrrhenus Mons. Tyrrhenus Mons, also known as Patera, is a low-lying, eroded volcano that stands 1.5 km above the surrounding plains. Tyrrhenus Mons covers the western half of Hesperia Planum, with flat-floored valleys and ridges indicating friable and easily eroded material like volcanic ash.

Several flat-lying volcanic structures known as highland paterae can be found in the Southern Hemisphere, near Hellas Basin (Figure 1.1). One of Mars' earliest volcanic edifices can be found in this location. They have extremely low profiles, with cross-cut ridges and channels radiating outward from the center caldera complex, which is deteriorated. Tyrrhena Patera, Hadriaca Patera, Amphitrites Patera, Peneus Patera, Malea Patera, and Pityusa Patera are located to the northeast and southwest of Hellas,

respectively. Despite their small size, some paterae cover huge areas—Amphitrites Patera, for example, is larger than Olympus Mons, and Pityusa Patera, the largest, has a crater nearly large enough to fit Olympus Mons inside it.

Similarly, Arabia Paterae is a recently discovered volcanic province with enigmatic highland ridged plains (Figure 1.1). The low-relief paterae, including structural collapse termed as plain-style caldera complexes formed by massive effusive volcanism with explosive eruptions, give a resemblance to terrestrial supervolcanoes.

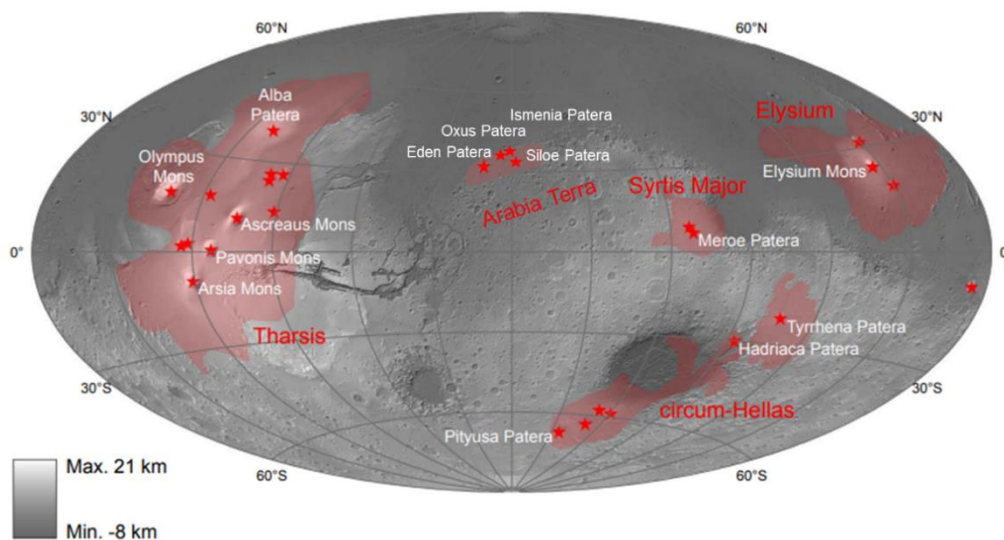


Figure 1.1: Location of volcanic provinces on Mars - Global shaded relief and superimposed transparent black-and-white MOLA map in Aitoff-projection with locations of the Tharsis, Elysium, Syrtis Major, circum-Hellas, and North-western Arabia Terra Volcanic Provinces and selected volcanoes. (Adapted after Hiesinger and Head III, 2004; Williams et al., 2010).

1.3 Volcanic evolutionary history of Mars

Volcanism on Mars has occurred throughout its geologic history from the earliest Noachian (4.5 to 3.6 Ga) to the latest Amazonian (3.1 Ga to the present) through the Hesperian period (3.6 to 3.1 Ga), with a clear trend of declination with age (Wilson and Head III, 2002) (Figure 1.2). The rate of volcanism was likely coupled with heat flow. The rate of volcanism might have started high and declined rapidly during the first few hundred million years, although geomorphic evidence of the volcanism during these early times has been mostly destroyed.

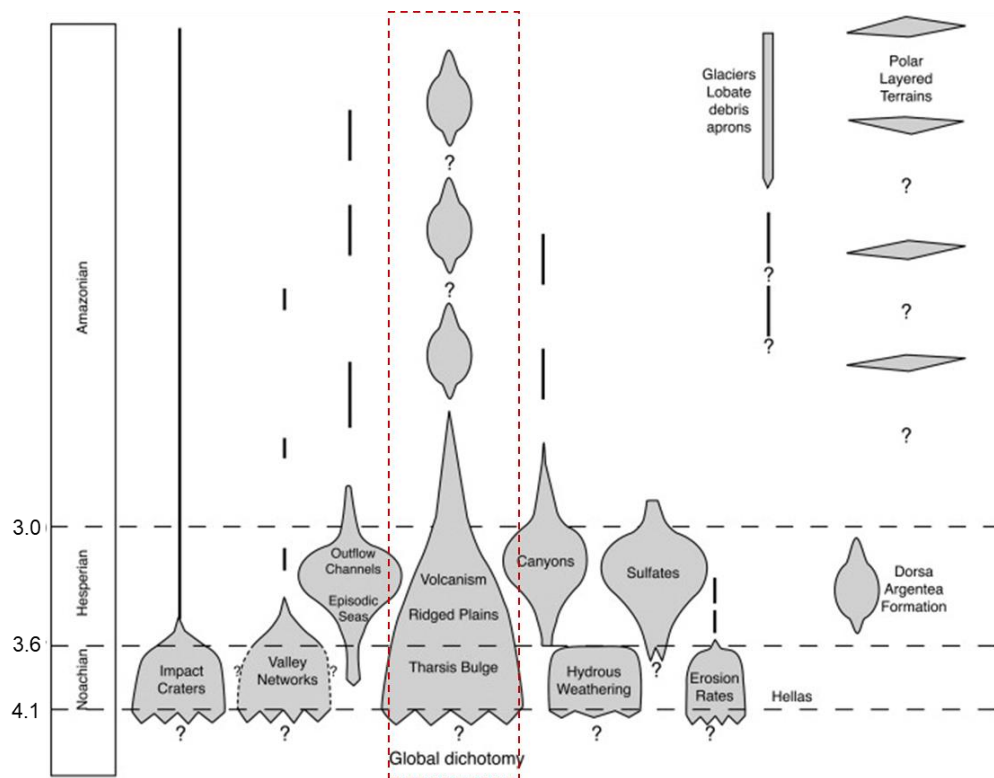


Figure 1.2: Martian evolution with time, representing a contribution of different processes that formed the surface. Volcanism is outlined by the red dashed line (adapted after Carr and Head, 2009).

Noachian volcanism is most notable in the Tharsis region, while the evidence is limited to late-Noachian (~3.7 Ga) (Phillips *et al.*, 2001). The preserved geomorphic pieces of evidence of Hesperian volcanism depict ridged plains and low shield-like central edifices. Based on the preserved shreds of evidence on the Martian surface, it is clear

that volcanic activity was at its peak in the Hesperian period. Volcanic activity in the Amazonian was largely in, and peripheral to the Tharsis and Elysium regions, where the large shields continued to grow and lava plains continued to accumulate (Carr and Head, 2010). Thus, the timescale for large-scale, regional volcanic activity, such as that observed in Tharsis, Syria, Hesperia, and Elysium, coincides not only with the early- to mid-Noachian period when the Martian surface and atmospheric environments have been interpreted to be "warm and wet," but also with the later period when atmospheric conditions evolved to become more like those that exist today (Figure 1.2).

1.4 Possible signature of tectono-volcanism on Mars

Unlike Earth, Mars' crust-mantle system has evolved as a single-plate planet called the Stagnant-lid regime throughout its history (Golombek and Phillips, 2010a; Grott *et al.*, 2013), believed to be tectonically inactive. However, the signature, observational evidence, and its interpretation, on the other hand, suggest that this was not the case in Mars' early geological history. The style of deformation observed over Mars is different from Earth's deformation due to plate tectonics, resulting in large shield volcanoes over the Martian surface (Carr, 1973). Although several features are observed over the Martian surface, some characteristics of the Tharsis bulge formation have been proposed to be tectonically driven (Williams *et al.*, 2008). The alignment of Ascraeus, Pavonis, and Arsia Mons suggests that they were generated by a crustal plate sliding over a hot spot, similar to the Earth's Hawaiian volcanic islands (cf. Ahmad and Nair, 2021; Pozzobon *et al.*, 2021). The local scale signature of thrust and normal faults deformation depicts the presence of stresses induced by some kind of tectonic activity. The radial and bulge-centered normal faults are observed on the Tharsis bulge. Based on the structural cross-cutting relationship, it has been observed that intense tectonic activity occurred during Noachian, while there are occurrences of these faults in a few localized regions during Amazonian (Tanaka *et al.*, 1991; Banerdt *et al.*, 1992; Golombek *et al.*, 1996; Anderson *et al.*, 2001). At the global scale, Mars shows one of the most intriguing physiographic features (Watters, 2003) at the highland-lowland transition, the global dichotomy boundary. MOLA topographic information depicts that

the planet's northern hemisphere is significantly lower than the southern and has been resurfaced more recently, meaning that the crustal thickness beneath the surface is notably bimodal. Mantle convection is one of the postulated possible origins of the dichotomy (Zhong and Zuber, 2001; Elkins-Tanton and Hager, 2005; Roberts and Zhong, 2006; Debaille *et al.*, 2009), however, its origin is highly debatable (Wilhelms and Squyres, 1984; Frey and Schultz, 1988; Andrews-Hanna, Zuber and Banerdt, 2008).

Another example of possible tectonics triggered due to the formation of the Tharsis bulge is Valles Marineris (VM) (~3000 km long, 8 km deep) formation. This immense feature was likely initiated by normal faulting in Early Hesperian. On the other hand, the structural analysis of VM fault zones provides possible evidence for large-scale strike-slip faulting on Mars (Yin, 2012). Nevertheless, the present depth and width of VM may be explained by mass wasting and collapse activity rather than pure fault displacement (Lucchitta *et al.*, 1992; Schultz, 1998; Andrews-Hanna, Zuber, and Banerdt, 2008).

Another feature resulting from compressive stresses is called wrinkle ridges (Golombek *et al.*, 2001; Golombek and Phillips, 2010a). These features are elongated, several tens of km in length, with sinuous structures. Various mechanical models have been proposed to explain the formation of wrinkle ridges like subsurface or fold propagation of thrust fault, shallow detachments, and buckling of crust (Watters, 1993, 2003; Mangold *et al.*, 1998; Schultz, 2000; Golombek *et al.*, 2001). Wrinkle ridges are present across the planet, viz. around Tharsis bulge, most of Hesperian plains, and Arabia Terra, a Noachian highland terrain (Rani *et al.*, 2021). The ubiquity of wrinkle ridges all over Martian earlier landforms, especially Noachian and Hesperian, suggests a relationship with global stress due to the cooling of Mars, but not because of the presence of Tharsis bulge (Chicarro, Schultz and Masson, 1985; Mangold *et al.*, 2000; Beuthe, 2010; Nahm and Schultz, 2010).

1.5 Thermochemical evolution of Mars

Volcanic eruptions create diverse landforms, rock types, and terrains that provide a window into the chemical composition, thermal state, and evolutionary history of a planet's interior. The composition of magma mainly depends on the initial composition of the mantle source, and pressure-temperature at which the melt forms. The processes like partial melting, fractional crystallization, assimilation, etc., may change the composition of magma as it ascends and cools, forming evolved magma. The composition of evolved magma is distinct from the primitive magma that resembles the composition of the mantle source. The type of volcanic eruption (explosive or effusive) depends on the compositions of melt (felsic or basaltic) and the presence of volatiles in the melt.

Crystallization of the basaltic melts at or near the surface of Mars, driven adiabatically from deep interior, have displaced a large amount of high heat-producing elements to the crust from the mantle. Detailed information about the surface chemical composition has been derived from various remote sensing, lander, and in-situ rover analysis, along with the lab-based studies of the Martian meteorites (cf. Christensen et al., 2005; Basu Sarbadhikari et al., 2009, 2011; Baratoux et al., 2011, 2013, Agee et al., 2013; Wray et al., 2013; Filiberto 2017). The systematic acquisition of the surface concentration of Fe, K, and Th has been observed over time, using Gamma-Ray Spectrometer (GRS) elemental data from NASA's Mars Odyssey. With the ever-expanding dataset, our understanding of the chemical composition and the interpretative thermal structure of Mars is rapidly growing. Previous reviews on theoretical study (cf. Toksöz and Hsui, 1978; Ruiz, 2014; Parro *et al.*, 2017), and data analysis (cf. Baratoux *et al.*, 2011; 2013) summarized chemical constraints on the thermal history of Mars. However, the study of thermal condition of the Martian interior remains the most uncertain and speculative subject. Quantitative estimation of temperature distribution through geologic time remains the key challenge in understanding the geochemical and petrological evolution of Mars.

Theoretical calculations based on several geological and geophysical observational data postulated Mars inefficiently cooled over time after the cessation of endogenic magnetic field during Noachian-Hesperian transition (Breuer and Moore, 2007; Ruiz *et al.*, 2011; Ruiz, 2014). This might have caused limited cooling or even a heating-up of Noachian-Hesperian lithosphere than before that period (Ruiz, 2014). Another theoretical calculation based on chemical data suggested that more than 50% of the high heat-producing elements are concentrated in the crust of Mars (Plesa *et al.*, 2018). However, all these numerical calculations were heavily dependent upon the exact estimation of the high heat-producing elements concentration at the Martian crust, resulting in various results and following interpretations.

The GRS-derived Si, Fe, and Th concentrations on the volcanic provinces have been applied to calculate the mantle melting processes, which yielded systematic variations over time, showing cooling of mantle and thickening of the lithosphere from the period of Hesperian to Amazonian (Baratoux *et al.*, 2011). However, using GRS-data limited the application to the spatially extensive volcanic regions, which were earlier well-defined, e.g., those Hesperian and Amazonian ones. A solution applied to the problem faced with the spatially large footprints of GRS data in evaluating Noachian volcanic regions by using orbital spectroscopy that provides the mineral information of all ages because of its high resolution (Baratoux *et al.*, 2013). The mineralogical evolution derived from Thermal Emission Spectrometer (TES), is consistent with olivine-low-Ca pyroxene-rich volcanic rocks in Noachian to the Ca-rich pyroxene of Hesperian and Amazonian (Filiberto, 2017; Baratoux *et al.*, 2013; Ody *et al.*, 2013). These later studies suggested that the Noachian rapid crust-building phenomena is volcanic not the global magma ocean crystallization scenario (Baratoux *et al.*, 2013). However, these mineralogical studies could not directly take into account the abundance of the heat-producing elements, and therefore, these studies could only predict a wide range of pressure-temperature conditions of formation and simultaneous uncertain crustal thickness and heat flow of the Noachian time of Mars.

The in-situ rover studies at Meridiani, Gusev, and Gale are also consistent with the convective cooling of the Martian interior (Filiberto 2017). The in-situ observations,

however, have drawbacks. In absence of plate-tectonism, Martian surface consists of huge volcanic regions owing to plume magmatism. Chemical data from a very localized region is prone to internal fractionation and any interpretation based on that may have issues to register the primary melt composition.

Lab-based studies of the Martian meteorites have the intrinsic issues of their limited temporal distribution, e.g., the crystallization age of the SNC (Shergotty-Nakhla-Chassigny) meteorites is 1.3-0.5 Ga (Filiberto 2017). Further, their origin from unknown localities makes them difficult to correlate spatially in terms of their crystallization regions.

Perhaps all the above-mentioned various observations have considered homogenous and dry Martian mantle. The study of Martian meteorites indicates that the Martian mantle is heterogenous (Basu Sarbadhikari *et al.*, 2009, 2011), with volatiles present (Halliday *et al.*, 2001; Mezger, Debaille, and Kleine, 2013), which affects the melting of mantle and solidus temperature (Médard and Grove, 2006; Balta and McSween, 2013; Tuff, Wade, and Wood, 2013; Filiberto, Gross and McCubbin, 2016). The morphologic characteristics of Amazonian shield volcanoes are consistent with effusive volcanism (Plescia, 2004; Schumacher and Breuer, 2007), whereas ancient volcanism with the presence of volcanoclastic rocks is consistent with explosive activity, linked to high volatiles present in magma (Bandfield, Amador and Thomas, 2013).

Moreover, the recent in-situ analysis at Gale (Sautter *et al.*, 2014, 2015a) and newly found Martian meteorite breccia NWA 7034/7533/7475 (collectively known as Black Beauty; Agee *et al.*, 2013; Humayun *et al.*, 2013) indicate alkaline Noachian rocks and felsic clasts, respectively, suggests a complex scenario instead of simple extraction of basaltic crust as a result of convective cooling of the mantle over time, which cannot be extrapolated back to Noachian period. In-situ and remote sensing analysis, therefore, deciphers more magmatic diversity in the Noachian period than in younger periods (Christensen *et al.*, 2005; Rogers and Fergason, 2011; Flahaut *et al.*, 2012; Carter and Poulet, 2013; Wray *et al.*, 2013; Pan, Rogers and Michalski, 2015; Sautter *et al.*, 2015a). Therefore, the origin of the early crust is still debatable, whether

they are the product of Noachian volcanic activity or attributed to preserved remnants of magma ocean crystallization or mantle overturn-driven melting

1.6 Main research questions

A fundamental question of the early forming Martian crust is the magmatic condition, processes, and composition of the mantle source. Martian volcanism has been active throughout its history, initiated in the Noachian (>3.6 Ga) and continued to the Late Amazonian (<150 Ma) (Robbins *et al.*, 2011). Compared to Earth, Mars is a less geologically active planet, which helped it preserve all geological features that occurred at its early stage of formation. Therefore, Martian volcanism has been studied extensively, morphologically, morphometrically, and compositionally (Baratoux *et al.*, 2011, 2013; Michalski and Bleacher, 2013). Most of the geomorphological studies of the volcanic regions are of Hesperian to Amazonian time (Robbins *et al.*, 2011). This is because there were no known Noachian volcanic regions on Mars until the geomorphological study by Michalski and Bleacher (2013), which recognized and established Arabia Terra as the oldest volcanic province of Mars. Long-term degradation and resurfacing might lead to significant geological modifications to the Noachian volcanic terrains, responsible for showing no clear morphological evidence of volcanism. This complicates the detailed investigation of Noachian volcanism (Scott and Tanaka, 1981). The earlier studies suggest that magmatism has evolved from Hesperian to Amazonian (Baratoux *et al.*, 2011). Extensive magmatism and volcanism are expected in the early stage of Martian crust formation (Greeley and Schneid, 1991; Nimmo and Tanaka, 2005; Breuer and Spohn, 2006; Grott *et al.*, 2007; Kronberg *et al.*, 2007; Morschhauser *et al.*, 2011). Therefore, in absence of the chemical observations of Noachian-aged volcanism, the understanding of the thermochemical evolution of Mars, especially at its earliest period remains the major gap area for early Martian geology.

Volcanic features of Noachian volcanism include low-shield highland paterae and ridged planes (Werner, 2009; Neukum *et al.*, 2010). Morphological, and

stratigraphic studies of these isolated volcanic constructs (>3.8 Ga) were classified into three groups based on their stage of degradation and morphological similarities to shield volcanos (Xiao *et al.*, 2012). However, the type and style of Noachian-aged volcanism remains to be understood, which could also infer the thermal evolution and formation of the Martian crust at its early stage.

1.7 Objective of the thesis

This thesis aims to

- Understand the type and style of Noachian volcanism
- Understand the internal thermal condition and processes viz., magmatic differentiation, mantle melting during Noachian through geochemical study
- Link between magma chemistry and mantle thermal state to rationalize certain variations, viz., pressure (P), temperature (T), melting depth, and heat flow to infer the thermal evolution and formation of the Martian mantle and crust at its early stage.
- Develop a perspective view of spatiotemporal changes in thermochemical conditions to infer the geological evolution of Mars.

The Noachian volcanic regions, Arabia Terra, and the ones in Solis (named as N1), and Argyre (named as N2) (Figure 1.3) are the study regions. The more specific scientific objectives are as follows:

- To infer the extent of regionally distributed tectono-volcanism in the Arabia Terra region, and explain the origin of Arabia Terra's enigmatic ridged plains. Later, use the demarcated regional occurrence to extract the chemical composition.
- Delineate the chemical provinces of Mars to understand the geochemical distribution of volcanic provinces of varied ages, which helps us to provide an overview of the spatiotemporal compositional variability of volcanic provinces and their geologic interpretations.

- Estimate the bulk chemical composition of Arabia Terra and other Noachian-aged volcanic provinces.
- Finally, infer the mantle source composition and magmatic processes that prevailed during Noachian and evaluate the role of Arabia Terra in the geologic evolution of Mars.

1.8 Study areas

In this thesis, mainly three regions, viz., Arabia Terra, and two other Noachian-aged volcanic provinces (N1 and N2) (Figure 1.3) are considered for detailed investigation. The Arabia Terra region is one of the oldest provinces of Mars with highly cratered plains. Arabia Terra is situated at an important geologic division between the Martian highlands and lowlands. Geologically, Arabia Terra extends across the prime meridian of Mars from 30° E to 300° E and the equator to ~50° N, covering an area of ~ 12x10⁶ km². Based on morphological evidences and geophysical characteristics, Arabia Terra has been proposed as a giant basin of ~3000 km diameter. Past studies suggest that Arabia Terra experienced extensive surface modification (McGill, 2000; Hynes and Phillips, 2001) by glacial (Carr, 2007; Zeilhofer et al., 2018), fluvial (Dohm *et al.*, 2007; Davis *et al.*, 2016), massive impact (Dohm *et al.*, 2007), aeolian (Rodriguez *et al.*, 2010; Silvestro *et al.*, 2011), tectonic (Anguita *et al.*, 1997) and hydrothermal processes (Noe Dobrea *et al.*, 2010; Oehler and Allen, 2010). In recent studies, Arabia Terra has been recognized as an ancient **explosive volcanic province** of Mars during the Noachian period (Michalski and Bleacher, 2013). The broad range of process interpretations at times contradict each other, warranting further study of Arabia Terra to gain insight into its evolution. Noachian-aged (> 3.6 Ga) volcanic regions Solis (named N1), and Argyre (named N2) lie in the southern part of Tharsis province. These regions (N1 and N2) consist of Noachian-aged lava flow, with well-preserved caldera with shield-like edifices volcanic construct (Dohm and Tanaka, 1999; Xiao *et al.*, 2012), whereas Arabia Terra lacks lava flow and shield calderas (Michalski and Bleacher, 2013).

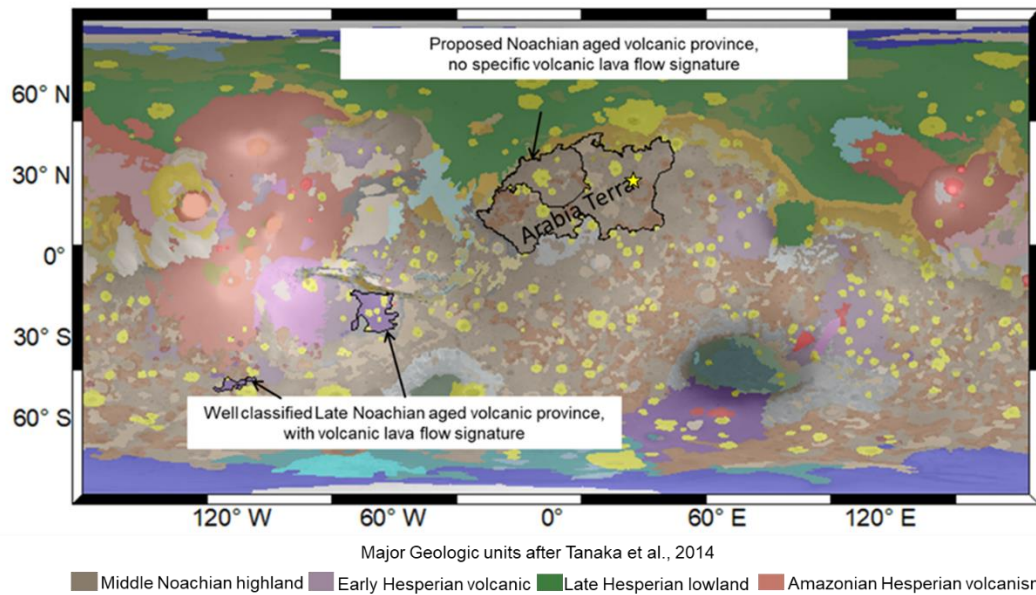


Figure 1.3: Studied Noachian-aged volcanic provinces are outlined by black color boundaries, which are overlaid onto mapped geology (Tanaka et al., 2014; different colors indicate different geologic units). Yellow star represents the location of Ramanathan crater.

1.9 Datasets and Software

1.9.1 Imagery data

1.9.1.1 High-Resolution Imaging Science Experiment (HiRISE)

HiRISE onboard the Mars Reconnaissance Orbiter (MRO) is currently orbiting Mars. It is imaging the Martian surface since 2006, at a resolution of 0.25 m/pixel from an altitude of ~300 kilometres. The swath width of the HiRISE image is ~ 6 km in size. It is designed to provide shreds of evidence of active surface processes and landscape evolution at higher resolution. The high-resolution images provide unprecedented views of layered materials, gullies, channels, and other science targets, in addition to characterizing possible future landing sites. HiRISE covers two types of imagery viz.

grayscale and false-colored photos. Approximately one-fifth of the field of view of grayscale photographs is covered by color images, which are obtained in grayscale images (McEwen *et al.*, 2007). Mars Orbital Data Explorer (ODE) of the Planetary Data System (PDS) Geosciences Node is used to download the HiRISE images in Pyramidized JPEG 2000 (JP2) format.

1.9.1.2 ConTeXt Camera (CTX)

CTX onboard the MRO is now orbiting Mars and collecting grayscale (black and white) images at a resolution of 6 m/ pixel over a 30 km broad swath, captured from ~ 300 km altitude. CTX started imaging the Martian surface in 2006 and has since covered more than 90% of the planet. It is designed to provide the context images for the MRO HiRISE and other instruments. It also collects stereo pairs of certain, crucial science targets, and monitors changes occurring on Mars (Malin *et al.*, 2007). Mars ODE of the PDS Geosciences Node is used to download the CTX images in Pyramidized GeoTIFF format.

1.9.1.3 Thermal Emission Imaging System (THEMIS) day/night time infrared images

The Thermal Emission Imaging System (THEMIS) is a camera onboard Mars Odyssey. It images Mars in the visible and infrared parts of the electromagnetic spectrum at a spatial resolution of 18 m/pixel and 100 m/pixel respectively. THEMIS has also mapped global Mars in both day and night infrared, to determine the thermal properties of the surface. THEMIS detects the visible and infrared reflections from the Martian surface to make a map showing the location of different mineral concentrations and their relationship to various landforms. However, in this work, we mainly used infrared (day and night) THEMIS camera data, for thermal properties (Christensen *et al.*, 2002).

1.9.2 Topography data

1.9.2.1 Mars Orbiter Laser Altimeter (MOLA)

MOLA was one of the five instruments onboard the Mars Global Surveyor (MGS) spacecraft. The major objective of MOLA was to map the Martian topography. MOLA uses the Laser Altimeter instrument, which fires infrared laser pulses toward the Martian surface at a rate of 10 times/second and measured the time of flight to determine the distance of MGS spacecraft to the Martian surface. The range measurements resulted in precise topographic maps of Mars at an average accuracy of each point is original ~100 m in horizontal position and the total elevation uncertainty is at least ± 3 m (Smith *et al.*, 2001).

1.9.2.2 MOLA-HRSC blended Global DEM

MOLA-HRSC represents a combination of two datasets viz. Mars Orbiter Laser Altimeter and High-Resolution Stereo Camera. This dataset is not directly derived from any instrument onboard the spacecraft. However, this data product combines two different instrument datasets, viz. digital elevation model (DEM) data from the HRSC on board the Mars Express (MEX) spacecraft of the European Space Agency and the MOLA onboard NASA's Mars Global Surveyor spacecraft. HRSC is a stereo camera orbiting Mars and has nine charge-coupled devices (CCD) line sensors arranged in parallel allowing simultaneous stereo imaging of Mars. The spatial resolution and vertical accuracy of digital elevation models created from HRSC stereo images are ~ 50 m and ~10 m, respectively. However, DEM derived from HRSC stereo lacks a global coverage of Mars. To obtain a global coverage DEM of Mars that has a higher spatial resolution, HRSC is blended with MOLA, which has global coverage. Therefore, HRSC stereo-generated DEM is blended with MOLA DEM to derive global DEM which has a spatial resolution of 200 m/pixel, which is represented as Mars MGS MOLA - MEX HRSC Blended DEM Global 200m v2 and is downloaded from USGS (Ferguson *et al.*, 2017; Laura & Ferguson, 2016).

1.9.2.3 CTX & HiRISE Digital Elevation Model (DEM)

MOLA followed by MOLA-HRSC blended global DEM datasets that provide a global topographic variability of the Martian surface. Due to the coarser resolution of these datasets, it is difficult to investigate the local or smaller features. Therefore, for local studies, high-resolution stereo pairs of CTX and HiRISE images are used to derive the DEM. These datasets lack global coverage like MOLA and MOLA-HRSC. Martian Surface Data Processing Service (MarsSI) pipeline is used to generate the CTX and HiRISE DEM. To generate DEMs, MarsSI aims to process the products using AMES automated stereo pipelines on its computing hardware

1.9.3 Geochemical data

1.9.3.1 Gamma-Ray Spectrometer (GRS)

Gamma rays can be produced by two means of source, 1) natural sources of gamma rays include radioactive isotopes such as potassium-40, Thorium-232, Uranium-235, and -238, and 2) chemical elements in soils and rocks emit uniquely identifiable signatures of energy in the form of gamma rays when exposed to cosmic rays (charged particles in space that come from the stars, including our sun). The GRS looks at these signatures, or energies, coming from the elements present in the Martian soil. Gamma rays are highest-energy electromagnetic (EM) radiation typically greater than 100 keV, have frequencies greater than 10¹⁹ Hz, and wavelengths of less than 10⁻¹¹ m (Boynton *et al.*, 2007).

The Gamma-Ray Spectrometer (GRS) is a gamma-ray spectrometer onboard the Mars Odyssey spacecraft. GRS is a suite of three different instruments working together to collect data that will permit the mapping of elemental concentrations on the surface of Mars. The instruments are a gamma-ray spectrometer (GS), a neutron spectrometer (NS), and a high-energy neutron detector (HEND). The instruments are complementary in that the neutron instruments have much better counting statistics and can sample to greater depths than the GS, but the GS determines the abundance of many more elements. Working together the instruments are most powerful at mapping the

distribution of hydrogen, both over the surface and as a function of depth in the upper few tens of centimetres (Boynton *et al.*, 2007).

1.9.4 Software

1.9.4.1 ArcGIS

ArcGIS is a software used for mapping and data analysis. All the maps and geomorphic analyses in this thesis work are accomplished using ESRI software package ArcGIS 10.5. Furthermore, ArcMap, a 3D analyst toolkit is used to analyze the digital elevation models. Inbuilt, the ArcScene program derives the 3D representation of digital elevation models.

1.9.4.2 R language and Matlab

For statistical computing and data analysis, R and Matlab programming languages and environments are used. We have used the “Statistics and Machine Learning Toolbox” for statistical analysis and the “Mapping Toolbox” for the derivation of plots. R language (R Development Core Team, 2007) is an open-source environment. We have used NbClust Package (Charrad *et al.*, 2014) and Diana Package for cluster analysis.

1.9.4.3 pMELTS

We used pMELTS model calculations to estimate the pressure and temperature conditions of the studied regions. The pMELTS algorithm (Smith and Asimow, 2005) of program alphaMELTS is based on equilibrium phase calculations and uses an internally consistent thermodynamic dataset (Ghiorso *et al.*, 2002).

1.10 Thesis organization

The entire thesis is divided into five chapters. **Chapter 1** presents the basic introduction and research background, as well as the major research objectives with a brief introduction to the regions of interest. **Chapter 2** focuses on the extent of regionally distributed tectono-volcanism in the North-Central Arabia Terra region, which is our primary emphasis in terms of applying Noachian volcanism to determine the magmatic evolution of Mars. In this chapter, we use geomorphological, morphometric, and cross-cutting relationships among cones and exhumed dikes to constrain the regional extent of volcanic provinces and decode the evidence of tectono-volcanism in Arabia Terra. **Chapter 3** delineates the geochemical provinces of Mars using nine elements (Si, Fe, Al, Ca, K, Th, and volatiles H₂O, Cl, and S). This study determines the geochemical extent and bulk composition of Arabia Terra. **Chapter 4** constrains magma genesis in Noachian-aged volcanic regions utilizing petrological analysis of similar locations to deduce the magmatic processes and pressure-temperature (P-T) condition of formation of the mantle source from which our observed Noachian regions have evolved. We have also limited the depth of melt using the thermal vigour of melting in the Martian mantle. **Chapter 5** summarizes the primary outcomes and conclusions based on the studies reported in this thesis. This chapter also offers a discussion of future projects that can be undertaken.

Chapter 2 Tectono-volcanism in north-central Arabia Terra, Mars: Insights from morphology and structural analysis

2.1 Introduction

Arabia Terra extends across the prime meridian of Mars from 30° E to 300° E in longitude and latitude from the equator to ~50° N, spanning an area of ~ 12 x10⁶ km². Arabia Terra, as characterized by surface dating from crater-size frequency distributions (Michalski and Bleacher, 2013) and geological mapping (Tanaka *et al.*, 2014), is one of the oldest (Late to Mid-Noachian) landscapes on Mars. Results of many past studies converge on the possibility that Arabia Terra was subjected to extensive surface modification (McGill, 2000; Hynek and Phillips, 2001) by glacial (Carr, 2007; Zeilhofer, Chandler, and Barlow, 2018), fluvial (Davis *et al.*, 2016), aeolian (Rodriguez *et al.*, 2010; Silvestro *et al.*, 2011), hydrothermal processes (Noe Dobrea *et al.*, 2010; Oehler and Allen, 2010). The tectonic activity signature derived from wrinkle ridges is also evident in Arabia Terra (Anguita *et al.*, 1997; Anderson *et al.*, 2008).

The orbiter missions Mars Global Surveyor (2000) and Mars Odyssey (2001) along with Viking-era information suggest that Arabia Terra is a unique region, unlike other highland regions on Mars. There are different hypotheses concerning Arabia Terra formation and alteration of terrain. A circular high albedo and low thermal inertia feature (Christensen *et al.*, 2001) at the center of Arabia Terra province is hypothesized

as an ancient giant basin, formed early in Martian history when the lithosphere was thin and magnetic dynamo was active (Dohm *et al.*, 2007). Subsequent events like sediment deposition with water enrichment (Barlow and Perez, 2003) took place during the Noachian period with high erosion rates. Additionally, after the formation of the giant basin, the thin lithosphere led to the rapid adjustment of isostatic equilibrium (Dohm *et al.*, 2007). Over time, impact cratering, fluvial erosion, and other geologic processes modified the basin material. Many impact craters in this region have ejecta morphologies and central pits, indicating that parts of the basin are still water-enriched today.

Moore (1990), on the other hand, proposes pyroclastic tuffs in Arabia terra, which supports pyroclastic mantling deposits. This idea may appear troublesome since pyroclastic tuffs are associated with explosive volcanic eruptions on Earth. The explosive eruptions on Earth are caused by viscous, high-silica magma, whereas Mars is almost completely basaltic (low-silica). However, the low atmospheric pressure of Mars compared to Earth may cause magma to be disrupted into much smaller particles during an eruption. The increased effusion rate and deeper fragmentation depth on Mars also encourage explosive eruptions (Carr, 2007). However, the lack of a nearby source vent is the biggest drawback of this hypothesis. Finally, a decade later, the possible source of these pyroclastic deposits has been discovered by Michalski & Bleacher (2013). Based on crater population, morphologic investigations, and structure analysis, such as the presence of volcanic features and significant faulting consistent with collapse suggest that the linked depressions in craters represent a large caldera complex formed in the Late Noachian to Early Hesperian. Unlike adjacent craters of similar age and size which show a signature of extensive alteration with moderate depth-to-diameter (d/D) ratios and intact impact-induced features, these studied calderas exhibit a lack of morphological signatures of ejecta, crater rims, and central peaks. Contextually, supervolcanism in the northwestern Arabia Terra region has been suggested based on possible plains-style caldera complexes (Michalski and Bleacher, 2013; Figure 2.1). In addition, numerous faults and fractures with multiple volcanic

vents have been observed over the floor of depressions that forms the calderas (Oxus, Ismenia, Eden, Siloe & Euphrates Patera) of the supervolcano complex. Notably, in this case, the fractures formed in the depressions are not suggested to have an impact origin.

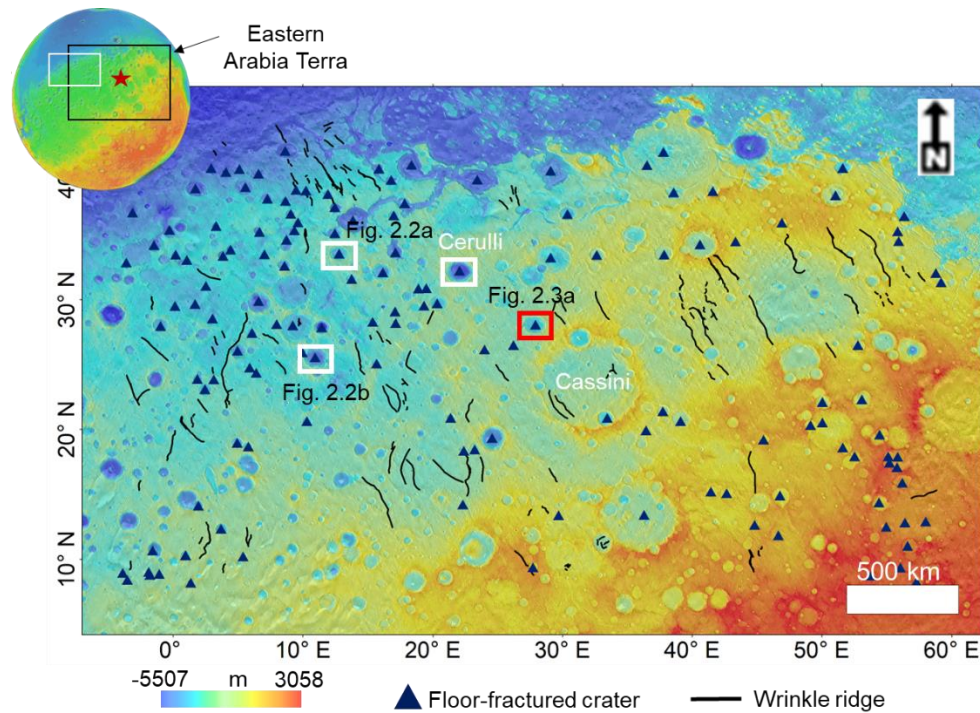


Figure 2.1: THEMIS day-time IR basemap of eastern Arabia Terra region overlain by color-coded MOLA-HRSC topographic map (location of Eastern Arabia Terra marked by the black box in the global map at upper left), showing distributions of craters with evidence of ridges, mounds, and mesas observed over the floor of depressions and wrinkle ridges. The white box in the global inset map indicates the study area of Michalski and Bleacher (2013). The Ramanathan crater of this study is marked by a red box and a red star on the globe of Mars.

The densely cratered landscape of Arabia Terra (Greeley and Guest, 1987) is broadly characterized as having a relatively thin crust (Neumann et al., 2004). This thin crust features numerous wrinkle ridges and fault scarps, indicating regional-scale tectonism (Golombek et al., 2001; Anderson *et al.*, 2008; Bamberg *et al.*, 2014). Furthermore, proposed ‘plain-style caldera complexes’ in northern Arabia Terra may have entailed super-eruptions in this region (Michalski and Bleacher, 2013). The rapid

ascent of magma aided by a high abundance of dissolved gases coupled to either regional extension or thermal erosion of the crust beneath Arabia Terra has been suggested for such ancient volcanism (Michalski and Bleacher, 2013), with emerging supportive evidence from geochemical studies (Rani et al., 2021). If validated, plain-style caldera complexes would transform previous understanding of igneous activity on early Mars. Meanwhile, similarities in wrinkle ridge orientations span from south-western Arabia Terra on Noachian ridged plateau unit (Greeley and Guest, 1987) to the north-western Arabia Terra at the plain-style caldera complexes (Michalski and Bleacher, 2013). However, the extent of spatially distributed volcanic centers across Arabia Terra and the possibility of regional magmatic processes intruding tectonically driven faults (i.e., tectono-magmatism) remain unknown.

To infer the extent of regionally distributed volcanism in the Arabia Terra region, and explain the origin of Arabia Terra's enigmatic ridged plains, we conducted a detailed morphological and structural investigation within the Arabia Terra region (geographic extent: -4°E to 60°E and 44°N to 8°N) (Figure 2.1). We have observed macrostructures represent a possible sub-surface tectonic deformation called wrinkle ridges that is exceptionally enormous viz. tens to thousands of kilometres in length. Further to constrain the origin of wrinkle ridges in the context of the geological history of Arabia Terra, we have investigated the craters. In that context, we have delineated the craters (Total: 146) with faults and fractures along with evidence of ridges, mounds, and mesas observed over the floor of depressions (Figure 2.1). We find that 11 craters have preserved ridges, mounds, and mesas inside the crater (Figure 2.2). Likely, the combination of all these three features is not evident inside all of the crater's depression. However, the unnamed crater (now named **Ramanathan crater**; ~ 85 km diameter; centered at 27.95° N, 28.12° E), unlike other craters within Arabia Terra preserves distinct features at the centre of the crater are oriented in the direction of linear tectonic features (wrinkle ridges) in Arabia Terra (Figure 2.3a). Therefore, to constrain the origin of wrinkle ridges in the context of the geological history of Arabia Terra, we have carried out a detailed investigation of the Ramanathan crater which provides

possible evidence related to tectono-volcanism in Arabia Terra. Therefore, a detailed morphological, morphometric and structural study with high-resolution imagery of the distinct landforms in Ramanathan crater has been used to constrain the regional extent of volcanic provinces and unveil the evidence of possible tectono-volcanism in the North-Central Arabia Terra. The main objective of this study is to infer whether the exposed features were impact-induced or derived from igneous intrusion, from a morphological and structural geology perspective. Additionally, we also aim to interpret a probable stratigraphic sequence of formation and exhumation of the geologic units observed on the floor of the studied Ramanathan crater. Furthermore, two recent studies by Chu *et al.*, 2021; Whelley *et al.*, 2021 along with this study by Rani *et al.*, 2020 and Rani *et al.*, 2021, support the caldera collapse hypothesis and reveal a broader extent of volcanic resurfacing in Arabia Terra than proposed by Michalski & Bleacher (2013), implying widespread unrecognized early volcanism on Mars.

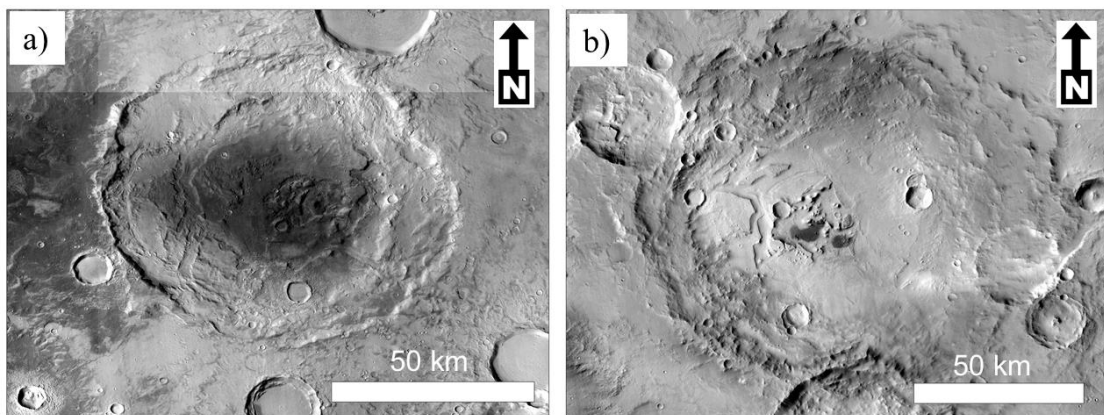


Figure 2.2: Examples of other FFCs in Arabia Terra as marked in Figure 2.1, using CTX images (6 m/pixel). (CTX image credit: NASA/JPL-Caltech/MSSS).

The chapter is structured as follows: First, we describe the datasets and methods. To delineate the volcanic extent in Arabia Terra, we delineate the tectonic features, followed by possible craters with depression which consist of possible volcanic landforms in Arabia Terra. We describe the age estimated for the study. Thereafter, we describe the morphometric characteristics of the features observed in the interior of the studied crater. Finally, we summarize the observations and results, compare the

observations with previously reported sites having ridges, mounds, and mesas, and finally provide a discussion on the origin of the features observed in the interior of the studied crater to address the main aim of this study, i.e., the observed features are impact-induced or from regional igneous intrusion processes. Furthermore, this study describes the putative regional tectono-volcanic relationships and provides pieces of evidence of volcanic resurfacing in Arabia Terra.

2.2 Data and methods

2.2.1 Morphology

Thermal Emission Imaging System (THEMIS)-daytime infrared (IR) basemap (~100 m/pixel) (Christensen *et al.*, 2003) is used to delineate the wrinkle ridges in Arabia Terra. Morphological observations are carried out to identify the geomorphic features (i.e., linear and wrinkle ridges, mounds, etc.) inside and outside the study crater using the images from the High-Resolution Imaging Science Experiment (HiRISE; ~0.25m/pixel) and Context Camera (CTX; ~6 m/pixel) onboard the Mars Reconnaissance Orbiter (MRO) (Malin *et al.*, 2007; McEwen *et al.*, 2007). MRO High-Resolution Imaging Science Experiment (HiRISE; ~ 0.25 cm/pixel; McEwen *et al.*, 2007) images are used to identify the boulders at flanks of ridges because the boulders are generally larger than the resolution of HiRISE, but smaller than the resolution of CTX. The georeferenced HiRISE, CTX images, and THEMIS day-time IR basemap downloaded from the PDS Geosciences Node Mars Orbital Data Explorer (ODE) are analyzed using the ESRI's (Environmental Systems Research Institute, Inc. Redlands, CA, USA) ArcMap10.0 Geographical Information System.

To characterize and correlate the linear geologic features (i.e., ridges) of the study crater with any regional tectonism that may have been active in the past, we plot the orientations of the linear features in the rose diagram. Topographic variability of the North-central Arabia Terra is analyzed using Mars Orbiter Laser Altimeter and

High-Resolution Stereo Camera (MOLA-HRSC) blended Digital Elevation Model (DEM) data (spatial resolution ~ 200 m/pixel) (Ferguson et al., 2018).

For the detailed topographic investigation of morphological units identified inside the studied crater, CTX stereo imagery is used for generating Digital Terrain Models (DTMs) (Malin *et al.*, 2007; Shean *et al.*, 2011). The built-in pipelines of the Mars Information System (MarsSI: emars.univ-lyon1.fr) are used to process the CTX stereo imagery and to create the DTMs (Quantin-Nataf *et al.*, 2018). One CTX stereo image pair, covering mainly the central portion of the crater, is available for the study crater. CTX DTMs are used for height, width and slope estimates of morphologic units present inside the crater. We have also generated slope maps by HiRISE DTM using ArcGIS.

2.2.2 Statistical and morphometric analysis

The numeric model age of the crater has been calculated by plotting the counted craters using Craterstats 2.0 (Michael and Neukum, 2010). We consider >1 km diameter craters for calculating the numerical model age of the study crater. Crater size-frequency distribution (CSFD) is obtained inside and outside the crater using the CraterTools, an ArcGIS extension (Kneissl, van Gasselt, and Neukum, 2011; Michael, 2013). The CSFD statistic is inferred based on the production function provided by Ivanov, (2001) and the impact-cratering chronology model of Hartmann and Neukum, 2001.

Using CTX DTM, we estimate mound morphometry with average height (H), average basal diameter (W), and average flank slope (α). Highly degraded and very small-sized mounds of a few tens of meters in height (< 50 m) are excluded from the morphometric calculations. Topographic profiles are drawn along the cross-sections of the mounds. The height of the mounds is calculated by subtracting the values of the surrounding areas adjacent to the mound from the maximum elevation point. The average basal diameter and the average height of the mounds are calculated by taking the average of two profiles along N-S and E-W directions to avoid the influence of

irregularity in shape. The uncertainty in measuring the average basal diameter and average mound height is estimated by dividing the mean by deviation from the least square best fit. The slope of each of the mounds is calculated manually by numerical differentiation of the cone's shape using the following formula

$$\alpha_z(h) = 0.1 \int_{h-0.05}^{h+0.05} \alpha(h') dh' \text{ --- (2.1)}$$

where $h = \frac{z-z_0}{z_1-z_0}$, $h \in (0.05, 0.95)$; z_0 corresponds to the zero height i.e. base level; z_1 corresponds to the maximum height (after Brož *et al.*, 2015).

HiRISE DTMs, are used to calculate we calculate the height, width, length, and spacing of the ridges and generate a slope map. We also calculate the slope angle of the ridges by dividing the height by width to depict the steepness of the ridges. The linear ridges' orientation is obtained by weighting the direction with the length, which represents the vector quantity that can be computed as the azimuth ranging from 0^0 to 360^0 in a rose diagram.

To characterize the correlations in the spatial distributions or orientation of mounds, we use a two-point azimuth technique, within ArcGIS, which measures the alignment of the mounds relative to each other (Lutz, 1986; Bleacher *et al.*, 2009; Roberts *et al.*, 2011). The most accurate method for representing the spatial correlations of mounds is to express them as points in space using probabilistic lattice point distributions (Wadge and Cross, 1988). We utilize the acute angle between each connecting line segment of the mounds and an imaginary geographic N-S line as the azimuth to identify the paleo-propagation direction of the mounds. Using rose diagram, we depict the preferred structural orientation of the mounds. In this study, the 'dominant' trend refers to the azimuthal trend with the highest frequency of the line alignments, whereas the less azimuth frequency is less significant than the 'dominant' alignment. This technique has been widely utilized in investigations of the structural geology of igneous mounds/vents at various scales, e.g., tens of meters to thousands of

kilometers, to identify trends among the mounds (Wadge and Cross, 1988; Bleacher *et al.*, 2009; Roberts *et al.*, 2011).

2.2.3 Thermophysical observations

We also characterize thermophysical properties such as thermal inertia (TI) of different surface materials, on the studied features using the Thermal Emission Imaging System (THEMIS) onboard Mars Odyssey. It is a multispectral imager that works in both Visible (VIS, ~ 30 m/pixel) and Infrared (IR, ~ 100 m/pixel) wavelengths. The IR imager acquired images in both Martian daytime as well as nighttime, whereas the VIS imager acquired images only in the Martian daytime (Christensen *et al.*, 2003). We use qualitative THEMIS Infrared (IR; ~ 100 m/pixel) nighttime imagery (THEMIS_TI_Mosaic_Quant_00N000E, band 9, transparent to the atmosphere, absolute accuracy ~ 1 K) to calculate thermal inertia (Christensen *et al.*, 2003; Fergason, Christensen and Kieffer, 2006)). Because nighttime, especially pre-dawn IR images intrinsically depend on material properties, are free or show a little effect from albedo, and are minimally affected by topographic variation (Cushing *et al.*, 2009), observed in high-resolution images by CTX and HiRISE. The nature of the surface materials viz. hard rock vs. soft unconsolidated sand or dust can be distinguished using the range of values of the THEMIS_TI, e.g., high values indicate rocky basement surface while low values indicate dust cover surface. We use this relationship to distinguish the different geomorphic units as well as dust-covered surfaces.

2.3 Results

2.3.1 Geomorphic observations of tectonic features in Arabia Terra

Mapping of linear tectonic features (e.g., wrinkle ridges) and their analysis can provide a better understanding of the geologic and tectonic history of a region on Mars. To provide a constraint on the tectonic evolution of Arabia Terra, re-investigation and construction of wrinkle ridges map and their orientation have been analyzed.

Based on the comprehensive regional investigation of Arabia Terra, we have delineated the wrinkle ridges (Figure 2.1), which represent the most common tectonic features in Arabia Terra. The detailed structural mapping using THEMIS day-time IR basemap of the Arabia Terra region reveals fewer macrostructures especially in eastern and southern parts as compared to other parts. We mapped ~177 wrinkle ridges. The wrinkle ridges in Arabia Terra ranges from 5 to 475 km in length (Table 2.1). We analyzed their orientations based on the measured geographic orientation. Results from the mapped ridges indicate NW-SE preferred orientations (Figure 2.1). The wrinkle ridges run for several 10s to a few 100s of km long, classified as tectonic macrostructures. These macrostructural wrinkle ridges run in NW-SE direction with a parallel to sub-parallel orientation across several kilometres, indicating a broadly bimodal orientation pattern with linear strikes.

Table 2.1: Wrinkle ridges locations and their corresponding length and trend/orientation w.r.t geographic north.

Latitude	Longitude	Length (km)	Orientation (°)
28.79	5.63	476	284.1
31.12	55.26	314	270.0
12.74	16.80	280	288.9
26.63	46.16	250	306.8
32.20	48.59	243	38.9
35.38	50.49	222	294.1
29.32	39.84	218	20.7
38.42	12.93	207	297.9
17.96	22.59	206	307.4
25.97	40.78	199	315.0
15.58	44.86	195	271.9

33.12	41.32	182	295.2
16.06	22.03	171	337.4
16.02	17.83	170	288.8
31.67	43.50	164	289.8
19.08	2.23	162	351.8
22.89	28.99	159	254.1
27.00	-2.31	159	328.9
17.47	18.17	158	315.8
24.31	14.70	154	315.4
39.90	14.28	147	282.9
21.64	17.39	146	251.4
22.05	-2.73	146	297.0
17.71	-0.47	143	65.4
30.52	32.56	142	273.8
23.14	16.21	134	291.3
21.17	30.69	129	318.7
18.43	16.93	126	242.8
25.91	18.22	122	245.5
14.76	57.05	122	26.2
31.57	42.32	121	300.1
11.64	2.80	121	113.5
32.31	1.90	115	315.8
22.23	23.04	113	71.9
16.10	23.81	112	274.3
29.15	52.75	112	294.1
10.60	44.44	106	295.9
12.82	2.54	102	291.0
32.76	47.97	97	245.3
9.50	27.32	94	333.4
24.87	24.94	92	304.3
42.17	8.64	89	290.2
12.25	5.66	86	280.6
26.69	8.02	82	299.4
22.22	-2.78	80	61.9
30.10	52.31	79	289.5
30.29	41.06	77	295.0

26.54	50.41	76	306.5
30.12	29.71	75	321.7
25.19	8.03	72	324.7
22.16	1.98	71	301.6
16.01	29.54	68	328.4
28.90	29.49	67	304.6
17.18	22.77	67	296.0
24.96	42.06	65	321.3
28.45	19.72	62	65.9
32.29	42.92	61	306.9
31.01	39.13	60	242.1
29.36	-1.69	58	280.3
26.82	16.11	57	301.8
37.02	25.77	56	303.7
38.99	9.54	55	297.3
29.20	40.50	55	302.4
41.51	10.36	55	282.5
39.27	10.98	54	292.3
31.20	9.87	51	325.4
29.19	41.48	51	287.1
22.64	4.22	49	259.4
38.00	26.45	49	287.7
31.48	57.93	48	296.6
11.15	5.77	47	258.3
24.95	33.90	46	283.6
35.25	50.58	44	300.3
43.67	12.26	44	33.7
20.05	0.98	44	306.5
15.39	-2.66	43	272.3
20.86	1.38	43	275.2
23.93	41.62	43	335.9
38.81	13.96	42	327.5
40.02	13.65	42	328.7
9.60	3.94	41	227.5
41.51	10.12	40	290.6

33.03	42.21	40	301.0
29.77	29.45	40	69.7
38.34	11.22	39	297.6
26.58	3.36	39	304.8
30.47	39.05	38	272.4
40.16	12.97	37	337.1
37.84	10.58	37	313.5
9.75	-3.30	37	269.1
38.73	26.08	37	275.4
33.40	51.88	37	321.3
23.48	18.00	37	312.2
26.32	2.97	36	308.2
39.80	14.36	36	324.6
38.46	13.01	34	270.0
18.54	16.84	34	230.1
10.66	44.48	33	290.3
29.68	55.44	32	309.3
43.04	11.75	30	47.4
11.26	2.01	30	250.2
27.18	3.92	30	293.2
13.79	27.57	30	46.1
39.04	9.25	29	284.0
28.60	40.13	29	296.6
37.84	12.20	28	297.8
38.83	15.61	27	317.2
11.24	33.00	26	269.0
38.25	26.40	26	272.3
38.66	12.49	25	270.0
33.06	52.36	25	275.7
26.85	16.52	25	325.1
29.66	39.21	25	283.2
24.74	3.00	24	272.3
29.08	40.95	24	323.1
28.49	9.67	24	268.3
37.73	14.04	24	335.7
41.45	3.12	23	304.2

10.62	45.12	23	280.6
32.23	56.33	22	288.4
30.51	41.01	22	243.4
23.23	-3.24	22	284.6
28.72	41.51	22	214.2
37.95	10.33	22	280.0
31.91	56.56	21	318.7
23.57	34.10	21	236.3
11.15	32.71	21	272.6
23.75	-3.45	21	292.9
23.05	4.49	21	25.3
39.32	10.35	20	296.6
13.81	28.73	20	309.6
28.05	9.66	20	259.4
24.51	33.70	19	24.1
34.93	10.24	19	292.2
40.30	12.40	18	280.8
9.63	44.53	18	299.2
41.93	4.01	18	296.6
29.76	54.71	18	296.6
38.27	12.91	17	308.7
37.62	26.09	17	296.6
30.58	54.15	17	310.2
31.31	41.15	17	272.9
27.19	15.16	16	288.8
40.58	8.87	15	292.2
31.69	42.15	15	67.9
24.19	33.52	15	55.7
20.89	0.60	15	90.0
9.32	44.66	14	301.7
27.90	41.11	14	303.2
23.52	17.70	14	22.6
10.86	33.21	14	29.3
22.17	17.73	14	278.4
8.80	27.76	13	309.3

11.19	33.25	13	48.2
21.56	18.00	12	234.9
10.91	45.38	11	76.9
21.16	1.60	11	18.4
11.70	33.08	11	18.1
30.44	55.00	11	302.5
30.84	39.07	10	271.5
30.16	54.54	10	296.6
40.41	9.04	10	310.4
35.45	10.16	9	266.3
9.62	30.42	9	258.1
9.55	30.30	8	33.7
13.96	28.63	8	322.2
9.24	30.25	8	320.8
39.57	10.25	7	45.7
11.59	32.92	7	43.5
9.46	30.38	6	300.5
14.04	28.45	6	299.4
9.56	30.59	5	43.2

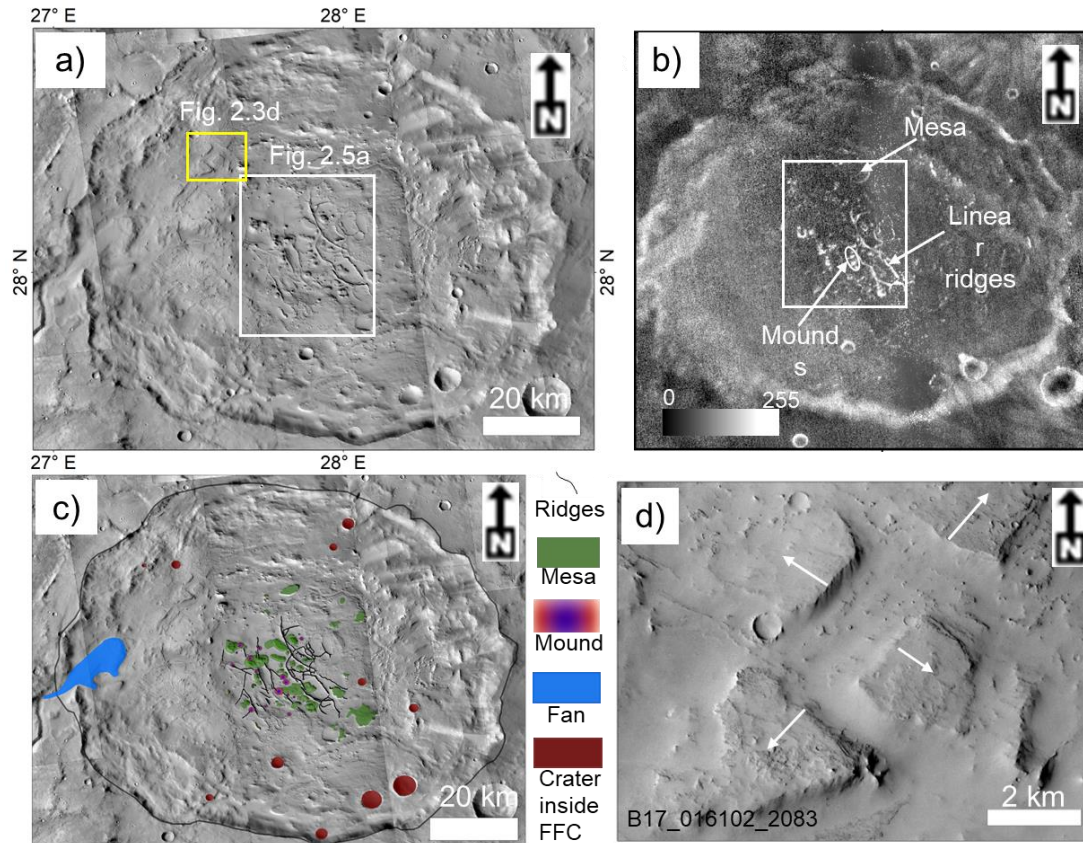


Figure 2.3: a) Magnified view of the study crater using CTX images. The white box is the central part of the crater with distinct geomorphology shown in Figure 2.5a, and the yellow box represents the crater floor features outside the central part. b) THEMIS nighttime IR image illustrates the material property of different landforms within the crater. The quantitative estimation (ID: THEMIS_TI_Mosaic_Quant_00N000E_100mpp) shows $TI \sim 140 \text{ Jm}^{-2}\text{K}^{-1}\text{s}^{-1/2}$ for mounds and ridges. c) CTX image based geomorphic map of the study crater at 1:15,000 scale with the crater boundary marked by solid black line. The legend is shown at the right side with different relevant landforms present inside the crater. d) Mesas at the outside part of the crater floor are displaced from each other by fractures. Four blocks were plausibly parts of a single unit close to the crater rim wall, indicating a floor-fracture crater. Arrows mark the displacement direction of the adjacent blocks. (CTX image credit: NASA/JPL-Caltech/MSSS).

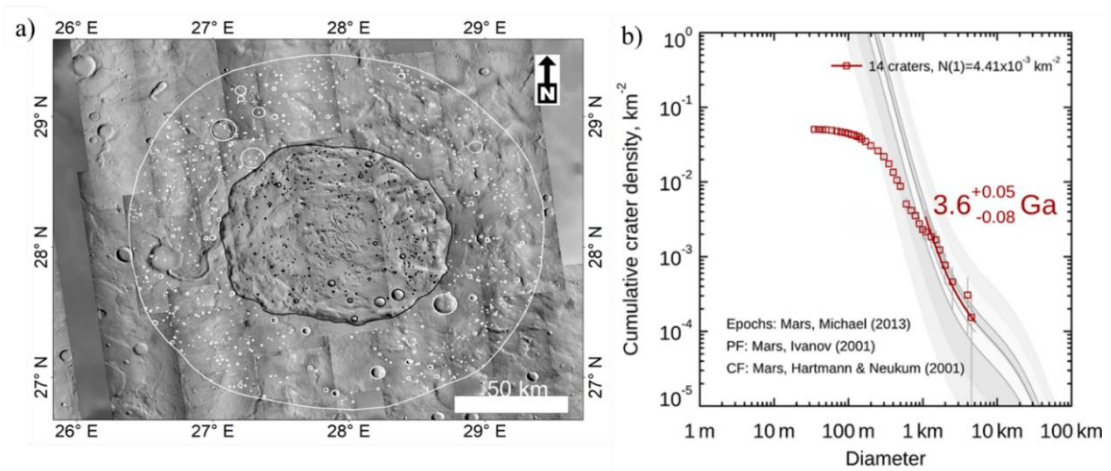


Figure 2.4: a) CTX images are used to determine the numeric model age by plotting the counted craters using Craterstats tool (version 2.0; Michael and Neukum, 2010), where we use craters with >1.2 km diameter. Black hollow circles, which represent the craters inside the study FFC, are counted for the crater age calculation; white circles outside the study FFC are used to determine the age of surrounding surface. b) Crater retention age of the study crater is deduced by Crater size-frequency distribution (CSFD), using CraterTools, an ArcGIS extension (Kneissl et al., 2011; Michael et al., 2013). The CSFD statistic is inferred based on the production function provided by Ivanov (2001) and the impact-cratering chronology model of Hartmann and Neukum (2001). Age of the crater is Late Noachian or Early Hesperian (~ 3.6 Ga). (CTX image credit: NASA/JPL-Caltech/MSSS).

2.3.2 Morphological and morphometric observations of the studied crater (now named as Ramanathan crater)

The thermal nighttime image (THEMIS TI) provides information for the thermo-physical study of the numerous landforms seen in CTX and HiRISE high-resolution visible wavelength. The central geomorphic features (linear ridges and mounds; Figure 2.3a) of the crater exhibit higher thermal inertia values ($140 \text{ Jm}^{-2}\text{K}^{-1}\text{s}^{-1/2}$) than the surroundings ($40 \text{ Jm}^{-2}\text{K}^{-1}\text{s}^{-1/2}$) (Figure 2.3b). The linear ridges and mounds have much

higher TI values ($40\text{--}45 \text{ Jm}^{-2}\text{K}^{-1}\text{s}^{-1/2}$) than the equal elevation landform mesas. The linear ridges and mounds of our study crater stand out strongly from the surrounding landscape, especially mesa and sedimentary layers, in this nighttime THEMIS IR view (Figure 2.3b). These values are much higher than those in the immediate vicinity of the study crater, although this area is generally dust-obscured (Farrand, Gaddis and Keszthelyi, 2005; Williams, Moersch and Fergason, 2018).

The 85-kilometer-diameter study crater (Figure 2.3a) has been eroded significantly. Based on 14 mapped craters in the study crater with a diameter of more than 1 km, the numerical model age of the crater as calculated using the least-square fit age using Crater size-frequency distribution (CSFD) is $3.6^{+0.05}_{-0.08}$ Ga (Figure 2.4a-b). This numerical age corresponds to the Late Noachian - Early Hesperian epoch. Given that the study crater lacks a distinguishable ejecta blanket, doming of the crater floor and shows abundant evidence for erosion, crater rim degradation, redistribution of material within the mantling units, terrain inversion, and aeolian activity, the crater size-frequency distributions may be more accurately represent the surface age of the landscape rather than the formation age of the landscape. A few hundred kilometers of fluvial channel entered the study crater, most likely connecting with Cerulli crater (130 km in diameter, 300 km to the southeast), breached the western rim, and deposited a fan near the rim (Figures 2.1, 2.3a-c). Layered sedimentary strata have been found on the crater floor, which was most likely deposited by the incised channel(s). The crater floor annulus along the rim wall is characteristic of a typical floor-fractured crater (FFC), with fractures and dividing the floor into mesas ranging in size from a few hundred meters to two kilometers (Figure 2.3d). Diverse geomorphic features with positive relief, such as mounds, linear ridges, mesas, and faults at the central part of the crater over the layered sedimentary rocks, are identifiable from shape and appearance (Figures 2.3c, 2.5a,b). The isolated mesas are nearly elliptical, elongated, and irregularly shaped; mounds are semi-circular to circular cone-shaped elevated features; and ridges are long and linear with very high length-to-width ratios (Figures 2.3c, 2.5a,b).

2.3.2.1 Mesas

The distribution of geomorphic features observed inside the crater is shown on a simplified morphologic map in Figure 2.3c. The interior of the crater's floor is stratified and has mesa-like features (Figure 2.6a,b). The isolated mesas are of near elliptical, elongated, and irregular shapes with steep flanks. Also, the plain surface on the basement unit at the central part of the crater consists of ridged plain features (Figure 2.6c). The terraced sedimentary layers are occasionally characterized by elliptical or irregular-shaped positive relief features, which resemble mesas, up to ~ 150 m high (Figure 2.6a-b,d). The crater floor in the low-lying regions, where eroded, exposes nearly horizontal layers and terraces on the scarps (Figure 2.6a-b). Isolated mesa tops have a high crater areal density, which is consistent with the crater floor's original

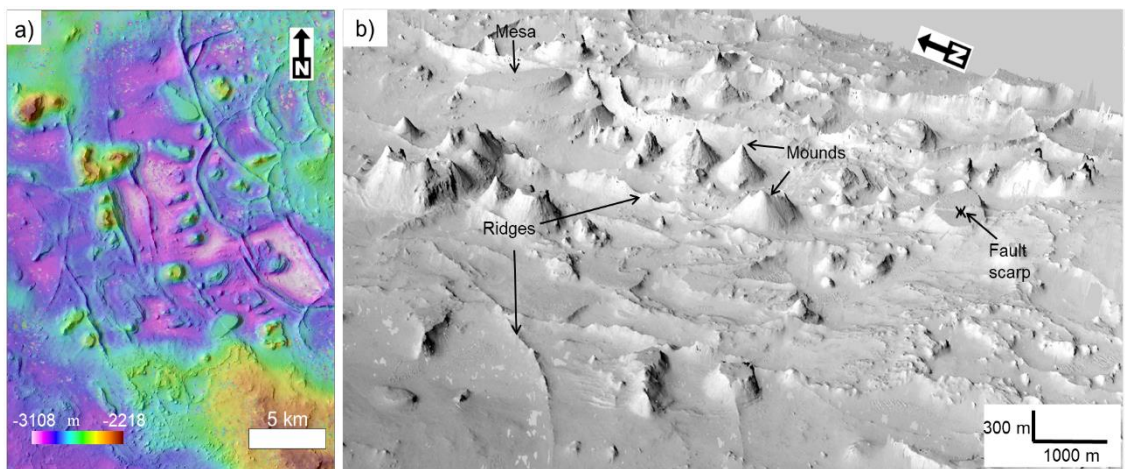


Figure 2.5: a) 2D Digital Terrain Model (DTM) is overlain on CTX images of the central part of the crater, showing anomalous features of variable elevation at the central portion of the crater. (CTX image credit: NASA/JPL-Caltech/MSSS, DEM credit: USGS Astrogeology Science Center). b) CTX-DTM derived 3D view of central portion of the crater, showing different morphological features such as mounds, ridges, fault, mesas etc. CTX stereo images P21_009232_2084 and J10_04846_2083 (no vertical exaggeration) for both.

surface, with a few inverted terrain features at the top (Figure 2.6d). Mesas, unlike mounds, are mostly distributed randomly, without preferential orientation or association with ridges (Figures 2.3c, 2.5a).

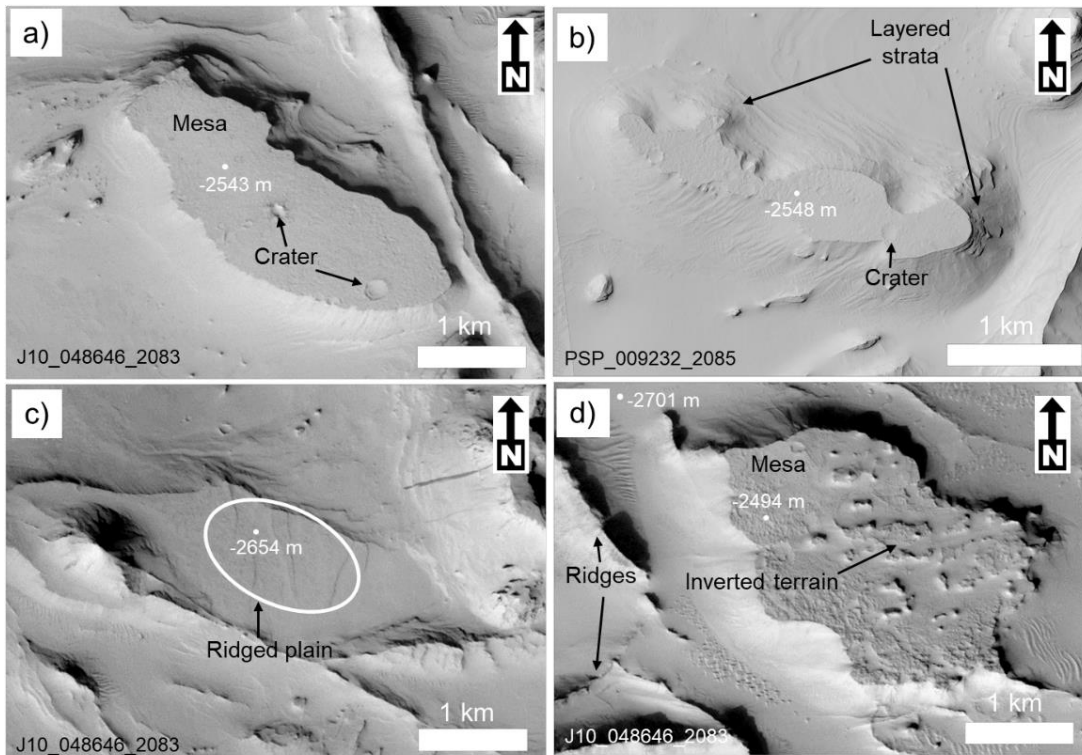


Figure 2.6: Basement and Mesa units. a) An elliptical to irregular-shaped mesa with small craters on surface. b) Preserved layered strata at the crater floor. c) A basement block with ridged plain surface. d) A mesa as an erosional remnant of the pre-existing crater floor; inverted terrain on the mesa. (CTX image credit: NASA/JPL-Caltech/MSSS, HiRISE image credit: NASA/JPL-Caltech/University of Arizona).

2.3.2.2 Mounds

In the interior of the crater floor, we observe 25 conical mounds. Their bases are circular (up to ~1.8 km diameter) with a few exhibiting depressions at the peak, which resemble summit craters of terrestrial scoria cones (Figures 2.5a, 2.7). In this study area, mounds of significant size ($H > 200$ m) are layered and superposed on the

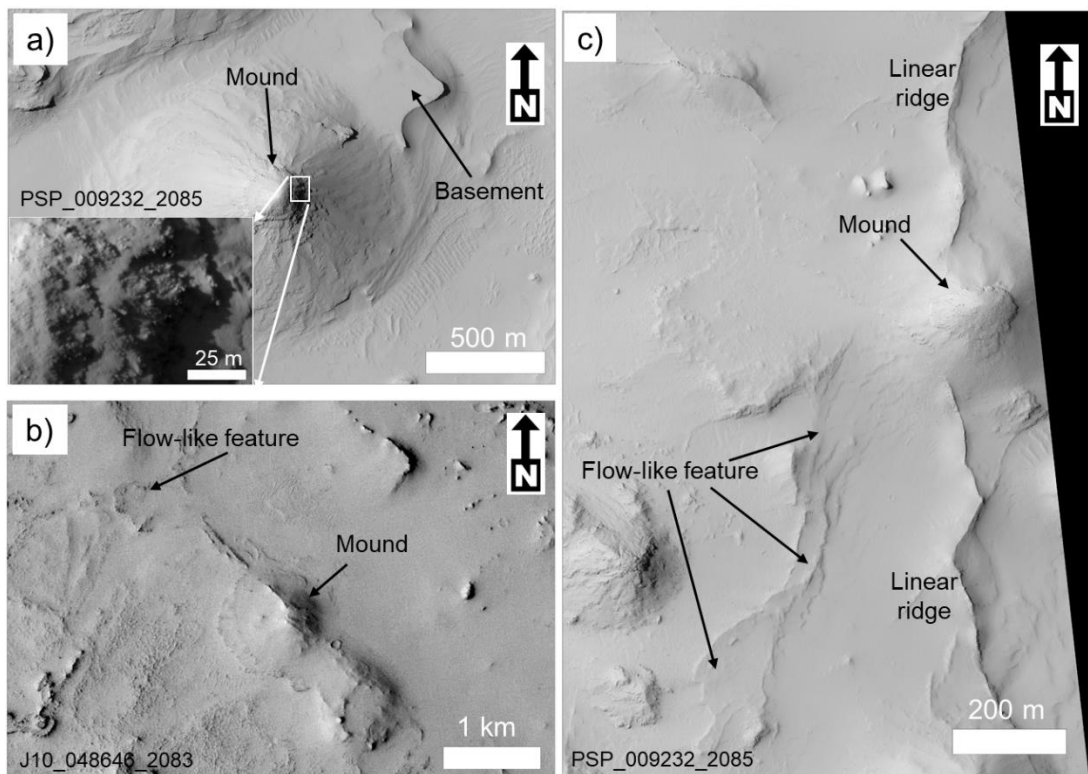


Figure 2.7: Mounds of the study crater. a) Mound overlies the flat basement unit, with rugged and serrated texture of layers exposed at top of mound, shown as an inset at bottom left; b) Mound flanks having flow-like features; c) Flow-like feature near mound, possibly originated from the mound that is associated with linear ridges. (CTX image credit: NASA/JPL-Caltech/MSSS, HiRISE image credit: NASA/JPL-Caltech/University of Arizona).

pre-existing crater floor basement (Figure 2.7a). The flanks of some of the mounds are well-exposed and are less mantled by dust compared to other mounds. The remaining mounds have a smooth texture and show minor terraces on the flanks wherever the dust cover is thin. A few cone-shaped mounds have a flow-like feature with a down-slope flow direction (Figure 2.7b-c). Qualitatively, the flow-like layers dip such that they intersect elevation contours. Meanwhile, linear ridges are associated with the mounds, which are generally underlain by the basement unit (Figure 2.7a). At the scale of a few tens of meters, the layers of the mounds are characterized by serrated edges with triangular-shaped protrusions dipping down the flank (Figure 2.7a).

We have estimated the morphometry of 25 symmetric and asymmetric mounds (Table 2.2). Given the constraints of CTX DTM resolution, which corresponds to a ~ 54 m point spread function, and only one pair HiRISE DTM coverage at the central part of the crater, this rule excludes mounds less than 50 m in height. The mound's transect profiles reveal a variety of features, ranging from conical shapes to summit craters (Figure 2.8a-b). The average basal diameter is from 290 to 1780 m (mean = 686, median = 562, SD = 393) and the average mound heights range from 58 to 348 m (mean = 146, median = 127, SD = 82.5) with height to diameter ratio of 0.144 to 0.309 with 4 % uncertainty of the mean. The estimated standard errors of the mean in average basal diameters and the average height of mounds are 12 % and 11%, respectively (Figure 2.9 and Table 2.2). The average slope of the mounds is less than 35° , with 3% error,

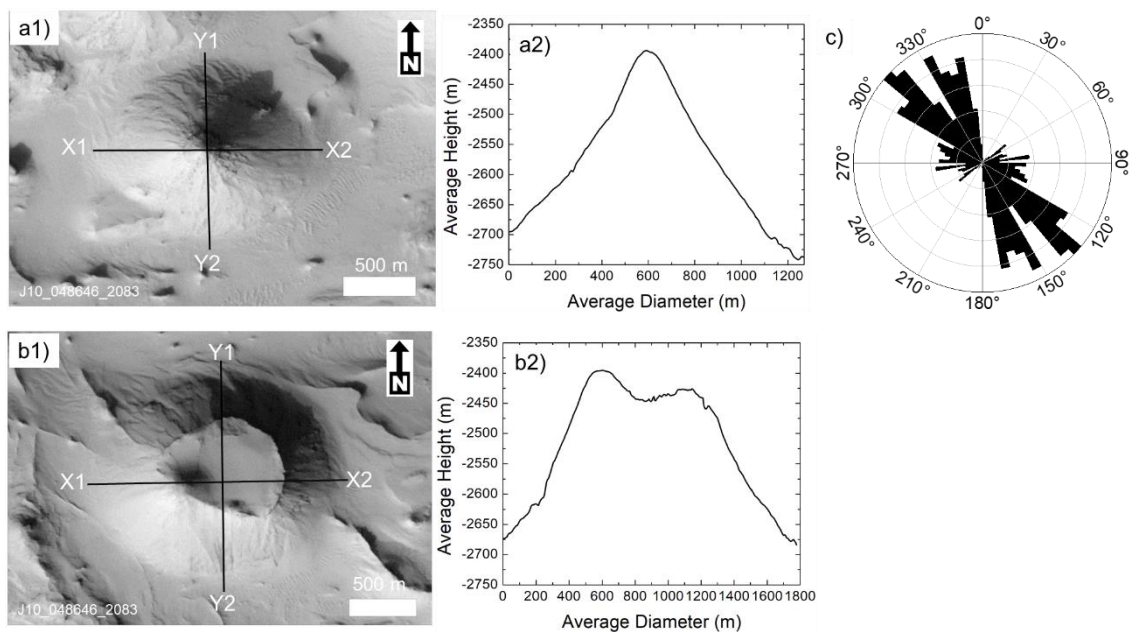


Figure 2.8: Average cross-sectional elevation profiles ($X1-X2$ and $Y1-Y2$) of selected mound types using CTX DTM (CTX stereo image pair Id: P21_009232_2084 and J10_04846_2083; no vertical exaggeration). Mounds with conical shape (a1-a2) and a crater at its summit (b1-b2). c) Two-point azimuth technique indicates mounds are aligned in NW-SE direction relative to each other. See the text in Section 3.2 for details. (CTX image credit: NASA/JPL-Caltech/MSSS, DEM credit: USGS Astrogeology Science Center).

which could be subject to further uncertainties associated with the CTX-DTM generation. The mean azimuth of the mounds is NW-SE on $\sim 127^\circ$ (Figure 2.8c).

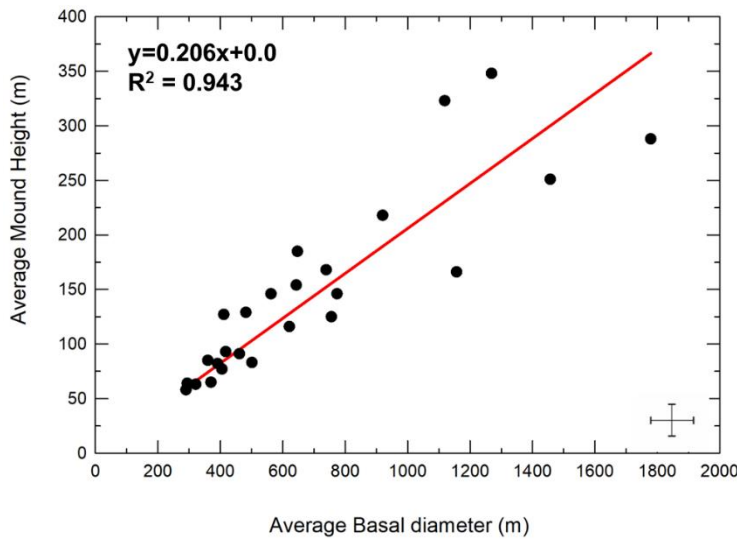


Figure 2.9: Plot showing morphometric analysis of the mounds. Average mound height versus basal diameter for 25 mounds. The solid line represents the maximum likelihood fit. Standard error bars along the x-axis and y-axis are 11% and 12%, respectively.

Table 2.2: Morphometric parameters: basal diameter, height, and slope of the observed mounds.

Mound ID	Average Basal diameter (W_{co} , m)	Average Height (H_{co} , m)	Average slope (deg)	Maximum slope (deg)	H_{co}/W_{co}
M1	920	218	28.0	45.9	0.236
M2	1457	251	21.3	33.2	0.172
M3	411	127	32.9	54.1	0.309
M4	774	146	20.7	36.4	0.189
M5	461	91	25.2	40.6	0.197
M6	647	185	33.3	51.2	0.286
M7	1779	288	32.3	68.1	0.162

M8	1269	348	33.4	53.0	0.274
M9	1119	323	35.0	78.7	0.289
M10	756	125	18.7	32.4	0.165
M11	391	82	23.9	39.9	0.209
M12	360	85	29.4	58.1	0.237
M13	370	65	23.3	37.4	0.176
M14	1157	166	27.1	62.3	0.144
M15	739	168	25.7	52.5	0.228
M16	562	146	31.8	58.9	0.260
M17	482	129	32.4	73.2	0.268
M18	643	154	26.9	51.9	0.239
M19	290	58	26.1	39.3	0.201
M20	321	63	24.9	65.4	0.196
M21	294	64	25.4	50.2	0.217
M22	621	116	24.7	51.2	0.186
M23	417	93	23.6	32.0	0.223
M24	405	77	20.6	36.5	0.190
M25	501	83	20.5	29.8	0.167

2.3.2.3 Ridges

In addition to the mounds, the central crater's floor also comprises a network of long, narrow linear ridges (Figures 2.5a, 2.10). The majority of ridges are well-exposed and exhumed, up to 20 km long and 150 m high, showing varying geometry from straight to curvilinear and orthogonal types (Figure 2.10a-c). The tops of the ridges are less dusty and more exposed than the surroundings. The ridges are darker-toned and appear rougher in texture than the surroundings. Furthermore, the lowermost units consist of another set of ridges, that are less pronounced, narrower, and discontinuous, with straight to slightly curvilinear geometries (up to 50 m high) where they are exposed (Figure 2.10a). In certain portions, the overall network of the broad and long linear ridges is nearly parallel for a few kilometers, branching into smaller linear ridges,

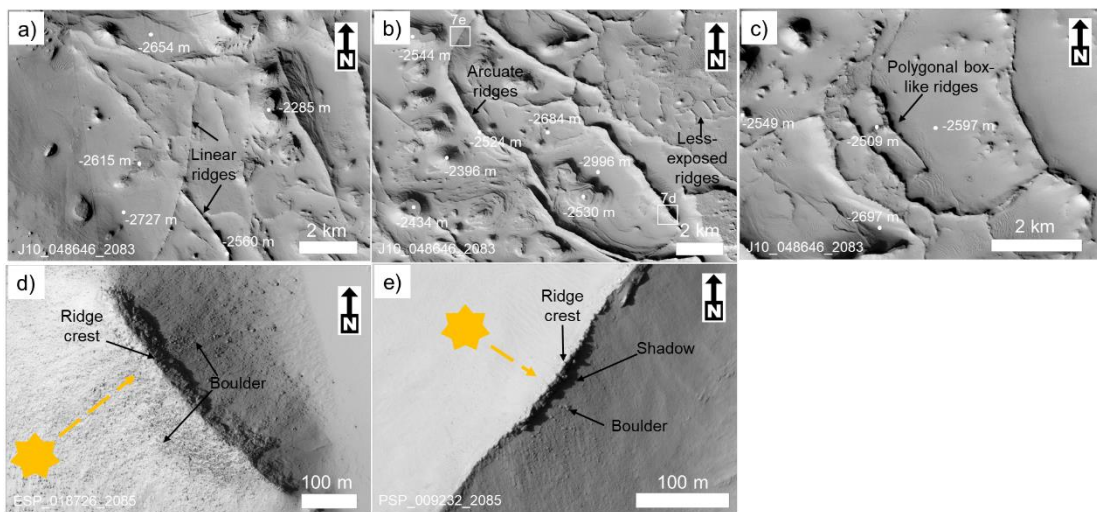


Figure 2.10: Linear ridges of the study crater. a) Broad and long linear ridges; b) Arcuate or curvilinear type of linear ridges along with less-exposed small, abruptly terminated, substantially buried ridges; and c) Linear ridges with rectangular or polygonal box-like patterns. All types of ridges (a-c) having positive relief (~ -2520 m) nearly close to elevation of surrounding sedimentary deposits (~ -2530 m). d) and e) HiRISE images showing ridges with shedding boulders, similar to an exposed dike of Shiprock on Earth, as shown in Figure S6. The sun direction is shown with star marks and arrows. (CTX image credit: NASA/JPL-Caltech/MSSS, HiRISE image credit: NASA/JPL-Caltech/University of Arizona).

bifurcating or converging (Figure 2.10b), and on a few occasions forming rectangular or polygonal box-like patterns (Figure 2.10c). The long parallel ridge group is more visually prevalent than the subordinate smaller-size ridge group, which is typically coupled with the parallel ridges that are either branched out, merged, and connected at a high angle or sub-orthogonally to the dominant parallel ridges (Figures 2.5a, 2.10a-c).

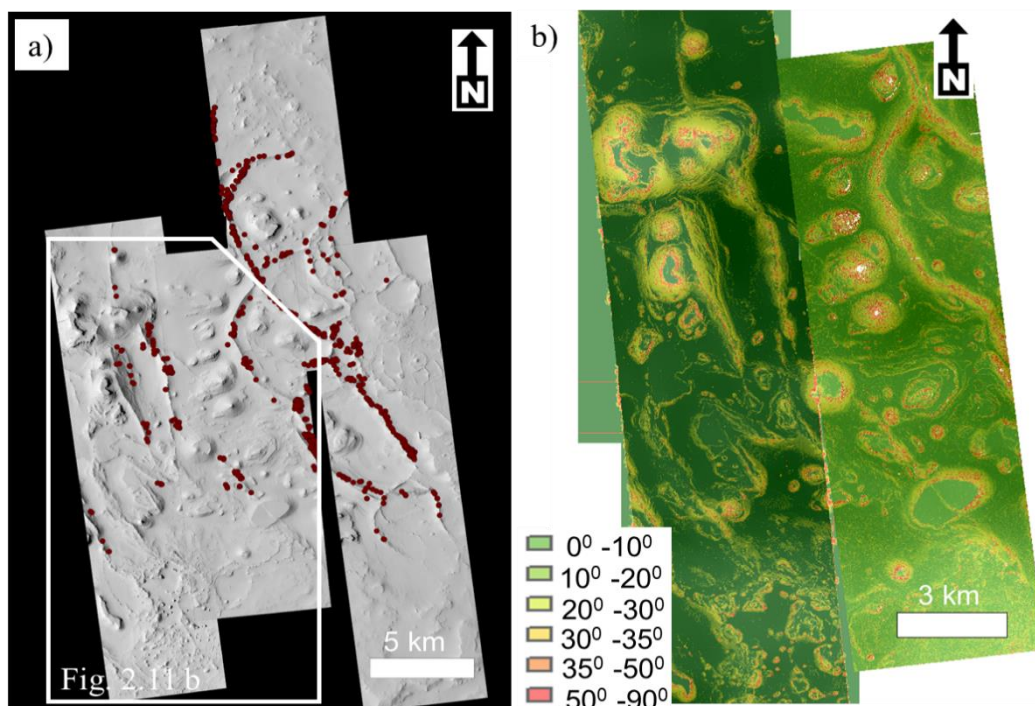


Figure 2.11: a) Mapped distribution of boulders associated with ridges (ESP_018937_2085, ESP_036923_2085, PSP_009232_2085 and ESP_018726_2085); b) Slope map generated from HiRISE stereo Images (ESP_036633_2085_ESP_036923_2085 and PSP_008520_2085_PSP_009232_2085), depicting steep slope ($> 50^\circ$) of ridges and mounds with rough boulder-rich topmost part. The layered strata is almost horizontal. Dust is mostly accumulated at the crater floor, on the layered sediments, and lowest part of the ridges and mounds at a slope $< 35^\circ$, i.e., the angle of repose for unconsolidated sediment on Mars. The index of slope values is mentioned in the different color scheme. (HiRISE image credit: NASA/JPL-Caltech/University of Arizona, DEM credit: USGS Astrogeology Science Center).

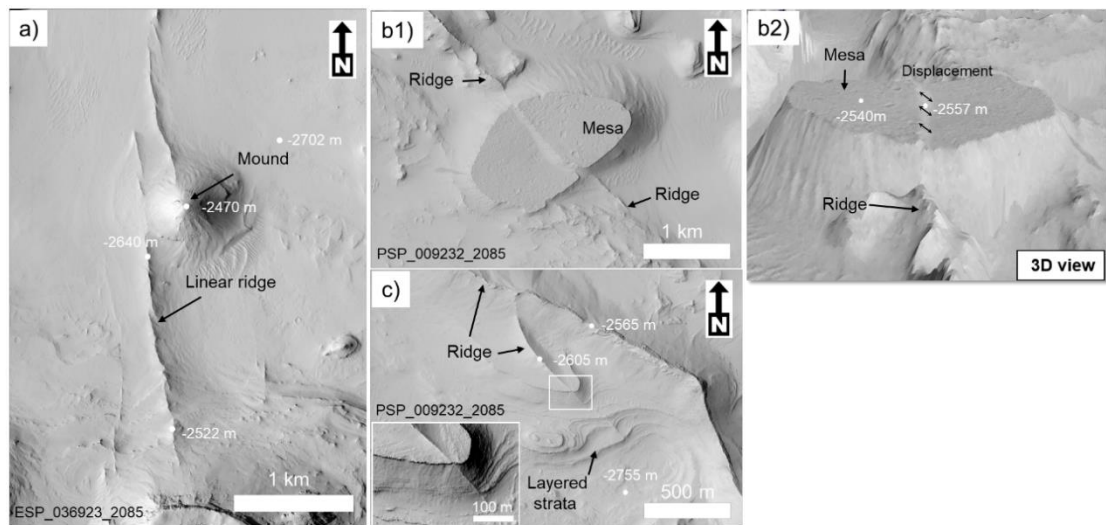


Figure 2.12: Cross-cutting relationships among the observed geomorphic features. a) Exhumed linear ridges in a preserved section are associated with a mound. b1) Faulted blocks of a mesa, associated with a ridge; b2) 3D view from CTX-DTM image of b1 (No vertical exaggeration). c) Sharp contact between ridges and layered sedimentary rocks. Sedimentary layers are cross-cut by the ridges. Inset shows zoomed view of the white box part. (CTX image credit: NASA/JPL-Caltech/MSSS, HiRISE image credit: NASA/JPL-Caltech/University of Arizona, DEM credit: USGS Astrogeology Science Center).

At the flanks of ridges shed boulders are also present and we could trace them at a scale of 1:1000 to 1:2000 on HiRISE images (Figures 2.10d,e, 2.11a). Boulder density is high along steep ridge flanks with slopes ranging from 63° - 78° , with an average of $\sim 67^{\circ}$. The shed boulder density decreases away from the ridges (Figure 2.10d,e). The dense pattern of the linear ridges can be visually characterized as either those that begin or end at the mounds (Figures 2.7c, 2.12a) or those that are connected with the mounds (Figures 2.7c, 2.8b1). At the inner-most central part of the study crater, where the mounds are observed, the ridge tops are at or below the elevation of the base of the mounds (Figure 2.5a). The observed ridges are not associated with the mounds at the outer part of the center of the crater. On the other hand, the orientation of the innermost ridge-mound system and the outer ridges is uniform. There is a significant linear ridge that crosscuts at least one mesa along a steep fault plane (Figure 2.12b1,b2). The

preserved section of layered sedimentary strata and inverted terrain shows a sharp contact between the linear ridge and the sedimentary rocks (Figure 2.12c).

Morphometric study of linear ridges shows symmetric bell-shaped profiles for transects perpendicular to the ridge length (Figure 2.13a,b). The profiles show steep

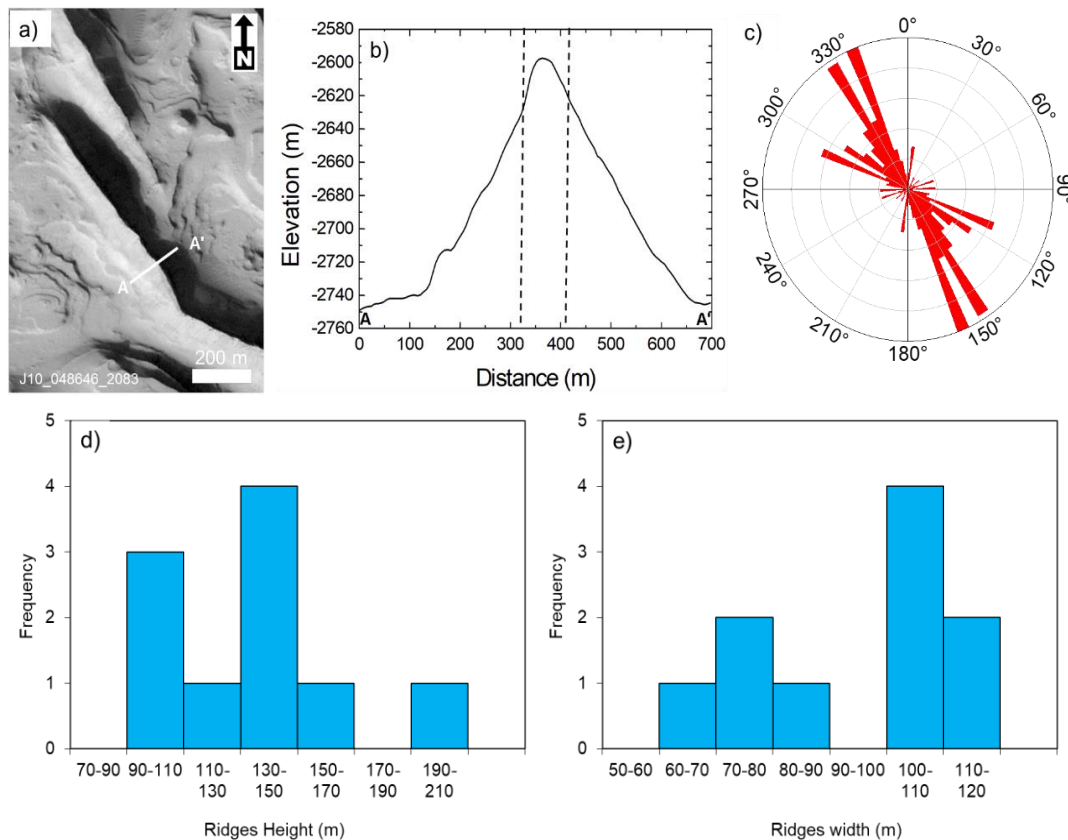


Figure 2.13: Morphometry of the ridges. a) A linear ridge along which elevation profile is drawn along A-A' line. CTX stereo images P21_009232_2084 and J10_04846_2083 (No exaggeration). b) A symmetric bell-shaped topographic profile of the ridge in cross-section view, showing the ridge is ~140 m high from the surroundings. The topmost 30-40 m is relatively less dust-covered and better exposed than the surroundings. The vertical dashed line is to show the dust-free topmost part of the ridge, which has a width of 100-150 m. c) Rose diagram of the orientation of ridges in our study crater. Orientation is weighted by the corresponding length of the ridges. (CTX image credit: NASA/JPL-Caltech/MSSS, DEM credit: USGS Astrogeology Science Center). d) and e) showing histogram plots of morphometric analysis of the ridges height and width.

flanks and narrow crests. The ridges are less dusty, and the more exposed part is ~30-40 m high and roughly 100-150 m wide (Figure 2.13b). The height, width, and slope of the ridges range between 73-185 m, 61-118 m, and 63°-78°, respectively (Figures 2.11b and 2.13d,e; Tables 2.3-2.5). The average spacing among the ridges is $\sim 4.3 \pm 1.6$ km (Table 2.6). The mapped ridges exhibit a pronounced NW-SE orientation with $\sim 80\%$ of the total length of all the ridges, while the subordinate group accounts for $\sim 20\%$ of the total length of the ridges and exists at a high angle to the dominant group (Figure 2.13c). The NW-SE-oriented linear ridges have a parallel to sub-parallel distribution over several kilometers, suggesting a roughly bimodal orientation pattern with linear strikes.

Table 2.3: Descriptive statistics of ridge height.

Ridge		R1	R2	R3	R4	R5	R6		R7	R8	R9	R10
Mean		185	128	143	125	77	102		88	73	125	117
Std. Deviation		23	10	25	18	10	26		21	8	15	51
Std. Error		13	6	14	10	6	14		11	4	8	29
95% Confidence Interval for Mean	Lower Bound	128	102	82	80	51	38		37	54	88	11
	Upper Bound	242	154	204	170	103	166		139	92	162	244
Median		190	125	140	130	80	90		94	75	125	130
Minimum		160	120	120	105	65	85		65	65	110	60
Maximum		205	140	169	140	85	132		105	80	140	160

Table 2.4: Descriptive statistics of ridge-width.

Ridge	R1	R2	R3	R4	R5	R6	R7	R8	R9	R10
Mean	104	102	61	118	87	104	80	74	113	102

Std. Deviation		5	10	4	8	6	5	5	4	13	3
Std. Error		3	6	2	4	4	3	3	2	7	2
95% Confidence Interval for Mean	Lower Bound	91	76	51	99	71	91	68	65	82	94
	Upper Bound	117	128	71	137	103	117	92	83	145	109
Median		102	105	60	120	90	102	80	75	115	100
Minimum		100	90	57	110	80	100	75	70	100	100
Maximum		110	110	65	125	92	110	85	77	125	105

Table 2.5: Average slope of ridges calculated using height and width trigonometric ratio, height and width values are used from tables 2.3 and 2.4.

Ridge	R1	R2	R3	R4	R5	R6	R7	R8	R9	R10	Average
Width (m)	104	102	61	118	87	104	80	74	113	102	95
Height (m)	185	128	143	125	77	102	88	73	125	117	116
Slope (degree)	74	68	78	65	60	63	66	63	66	66	67

Table 2.6: Descriptive statistics of ridge-spacing between different sets of pairs.

Ridge pairs	R1-R6	R2-R6	R2-R9	R3-R4	R3-R7	R5-R8	R6-R9	Average	Std. Dev.
Spacing (km)	7.3	4.3	5.0	4.2	3.9	3.0	2.5	4.3	1.6

2.4 Discussion

2.4.1 Origin of wrinkle ridges in Arabia Terra and its regional significance

Unlike Earth, Mars's crust-mantle system has evolved as a single-plate plate-tectonically inactive planet throughout its history (Golombek and Phillips, 2010b; Grott *et al.*, 2013). However, the geomorphic signature, observational evidence, and interpretation suggest that Mars was not tectonically inactive throughout its geological history. The study area Arabia Terra preserves the signature of tectonic activity in the form of wrinkle ridges (Anguita *et al.*, 1997; Anderson *et al.*, 2008).

To provide a constraint on the tectonic evolution of Arabia Terra and its origin, we have re-investigated and constructed a map of tectonic features and analyzed their orientation. Previous studies have shown several hypotheses, e.g., the observed center of tectonic activity may include regional uplift related to the growth of Tharsis (Phillips *et al.*, 2001), planetary cooling-related contraction (Barosio and Galicia, 2002), and plate tectonism (Connerney *et al.*, 2005), all of which may not be mutually exclusive. Our study delineates wrinkle ridges over Arabia Terra (Figure 2.1). These features show a bi-directional orientation, predominantly NW-SE trending. The bi-directional orientation in the Arabia Terra shows that the tectonism is not originally resulted from the effect of a proposed giant ancient impact, like large Isidis and Utopia basins. The ridges within the Isidis and Utopia basins are numerous, showing a complex radial and concentric pattern (Thomson and Head III, 2001; Tanaka *et al.*, 2003), suggesting that stresses are related to basin subsidence. Fewer ridges are present in Hellas, although they tend to be radial, interpreted as wrinkle ridges formed from compressional deformation (Nimmo and Tanaka, 2005), unlike wrinkle ridges observed in our study region. A distinct center of tectonic activity based on the orientation of wrinkle ridges of Arabia Terra is compared with that of the western hemisphere (e.g., the highest standing portion of Tharsis, excluding the volcanoes near Syria Planum), which shows concentric compressional features resulting in multi-directionally oriented ridges

(Anderson *et al.*, 2001), unlike the bi-directionally oriented wrinkle ridges of Arabia Terra.

According to the volcanic model, the wrinkle ridges form as linear conduits by magmatic intrusion or extrusion or a combination of both, associated with the mantle plumes. The observed wrinkle ridges in Arabia Terra were most plausibly the result of the supervolcanic activity of the Noachian Mars, as proposed by Michalski and Bleacher (2013). The Arabia Terra region perhaps underwent flexural loading and internal shrinking of the lithosphere during the development of this immense supervolcanic province. Therefore, these macrostructures (wrinkle ridges) represent a possible tectonically-induced deformation in the Martian crust that is exceptionally enormous viz. tens to thousands of kilometres in length. Further to constrain the origin of wrinkle ridges in the context of the geological history of Arabia Terra, we have investigated the Ramanathan crater which provides possible evidence related to tectono-volcanism in Arabia Terra on a local scale in detail.

2.4.2 Regional significance of distinct landforms in the studied Ramanathan crater

2.4.2.1 On the occurrence of linear ridges

The kilometer-long, hundreds of meters high, and wide linear ridges, consistent with sharp crest and bidirectional NW-SE trends, are of different origin than those of the other parts of Arabia Terra. In different places, the ridges are sinuous and usually exhibit sub-horizontal meter- to decimeter-scale internal layering, implying they are inverted channels (cf. Pain, Clarke, and Thomas, 2007; Davis *et al.*, 2016). In our study area the lack of tributaries, obvious sinuosity, braided pattern, quasi-circular pattern, paleo-meander type relics, etc., of the linear ridges argue against the fluvial origin of the ridges (e.g., inverted channels or eskers). Unlike ridges in our study crater which crosscut obstacles (Figures 2.7c, 2.12a), the common sedimentary ridges are sinuous in nature and circumvent large obstacles (Ghatan and Head III, 2004; Banks *et al.*, 2009).

In addition, the ridges do not morphologically resemble aeolian remnant features on Mars-like transverse aeolian ridges (TARs). TARs typically occur as up to thousands of individual bedforms in a small field having narrow ridge-to-ridge spacing (mean wavelength of ~40 m; Balme and Gallagher, 2009; Nagle-McNaughton and Scuderi, 2021) and elongate in shape (Bourke *et al.*, 2006). However, the ridges in our study crater are often up to ~20 km long, with a steep slope and narrow crests, and the average ridge-to-ridge spacing is more than a kilometer.

Mineralization along pre-existing fractures or faults is also unlikely to cause the observed ridges within our target study crater. For example, a small network of linear ridges formed through mineralized deposits (Mg-rich clay or calcium sulfate veins) in Gale and Eberswalde are only centimeter in scale and light-toned (cf. Nachon *et al.*, 2014; Crumpler *et al.*, 2015), unlike those in our study crater. Furthermore, no evidence of ridge-mound associations has been found in Gale or Eberswalde. Even large vein formation structures (namely, boxwork) are distinct from the observed ridges of the crater. For example, unlike the ridges in our crater (Figure 2.13c), the Nili Fossae ridges lack a dominant directionality (Figure 2.14). The Nili Fossae ridges (~ 20 m high) are similarly dwarfed by our study crater's hundreds of meter-high linear ridges, which tower above the surroundings. The ridges found in the studied FFC are also more linear compared to ridges of the Nili Fossae region (Head and Mustard, 2006; Fassett and Head, 2008; Saper and Mustard, 2013; Pascuzzo *et al.*, 2019).

Swarms of dikes and associated volcanic cones (Friese *et al.*, 2013), much like the linear ridge and mound association in our study crater can imply volcanic origin. Similar features exist in Amazonian dikes, the Huygens–Hellas region (Head *et al.*, 2006), and the Elysium Rise - Utopia Basin region (Pedersen, Head, and Wilson, 2010), which have been interpreted as magmatic dikes. Therefore, a plausible explanation for the parallel alignment of the linear ridges could be magma ascent from the underlying magmatic source forming magmatic dikes parallel to trough-bounding linear structures. In addition, the boulders shedding near the flanks of ridges (Figures 2.10d,e, 2.11a) resemble the Shiprock formation on the Colorado Plateau, New Mexico (Figure 2.15) and exhumed radial magmatic dikes within the Medusae Fossae Formation (MFF) on

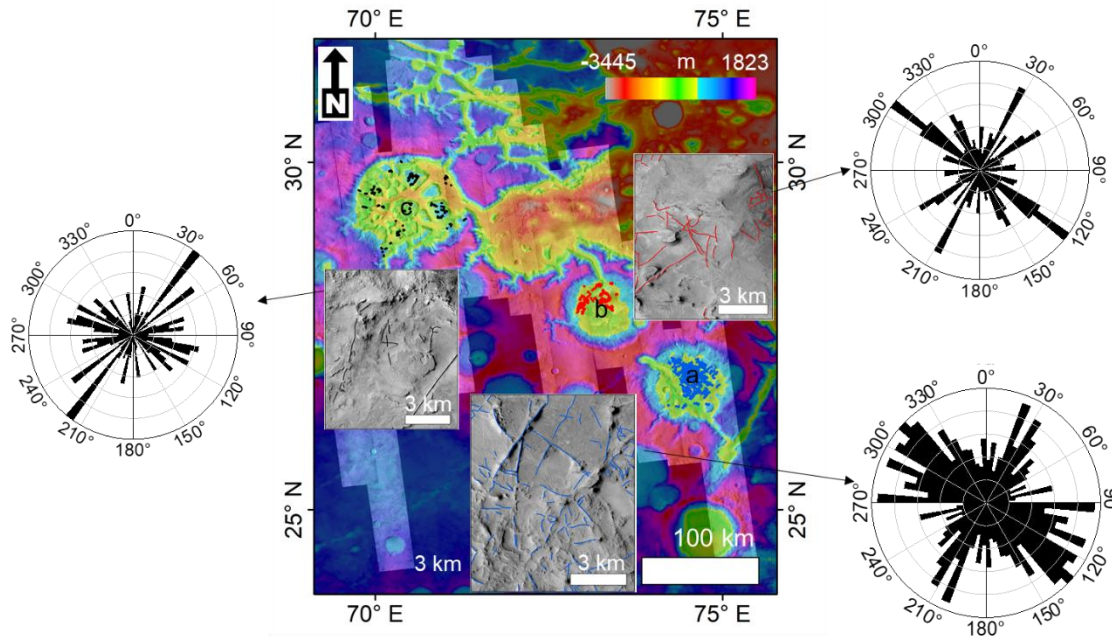


Figure 2.14: Nili Fossae and Nilosyrtris regional map by Saper and Mustard (2013), Ebinger and Mustard (2015, 2016), and Pascuzzo *et al.* (2019) based on CTX images. Here, the MOLA-colored topography is overlain on the CTX image mosaic and the delineated ridges inside the craters (marked as 'a', 'b', and 'c'). Corresponding rose diagrams are generated to depict the orientations of ridges in respective craters, as marked by the arrows. The orientation is weighted by the corresponding length of the ridges. (CTX image credit: NASA/JPL-Caltech/MSSS).

Mars (Kerber *et al.*, 2017). Erosion has resulted in a large population of boulders sourced from the ridges. Because of their similar morphology, the exhumed dikes of Shiprock (Figure 2.15) can be considered a terrestrial counterpart to the ridges in our study crater.

Morphologically, the few box-like polygonal ridges of our study crater differ from those reported by Kerber *et al.* (2017) and Pascuzzo *et al.* (2019), including those in Nili Fossae, Nilosyrtris, Gale crater, Sinus Meridiani, and Hellas basin. They lack the dominant orientation of polygonal sedimentary ridges and constitute an irregular ridge network (Kerber *et al.*, 2017; Pascuzzo *et al.*, 2019). However, the dominant orientation of the long parallel ridge group in our study crater (Figure 2.13c) is most plausibly

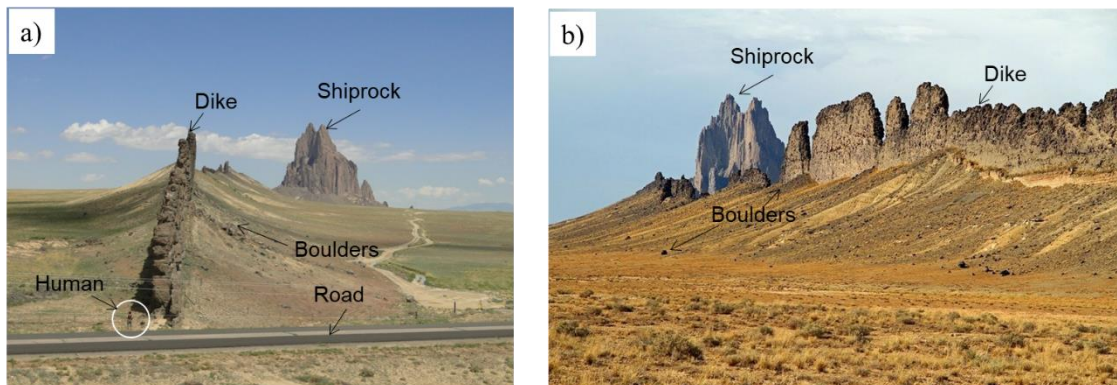


Figure 2.15: a) and b) An exposed radial dike of Shiprock, Colorado Plateau, New Mexico viewed from the ground showing the erosion of the irregular crest and associated boulders, resulted as an erosional remnant of a volcano located in northwestern New Mexico. The photographs mainly feature a dike with boulders at its flanks. The dike is exposed as its host rock has eroded away revealing the positive relief feature, we see today. Boulders are seen on the slopes and their number density decreases away from the dike. The exposed ridges in our study area on Mars are morphologically similar to the exposed Shiprock dike (Sources: a) <https://web.archive.org/web/20161018010808/http://www.panoramio.com/photo/44691497>, page title “Panoramio” and b) <http://written-in-stone-seen-through-my-lens.blogspot.com/2012/08/ship-rock-at-sunset-partially-exhumed.html>, posted by Dr. Jack Share (<https://www.blogger.com/profile/09068066012491070695>). The road and the standing human highlighted with the white circle in a) serve as references for the scale of the image, while b) is another side view of the same dike).

controlled by a pre-existing fracture system induced by regional stress, comparable to the terrestrial igneous dike system (cf. Stephens *et al.*, 2017, 2018). The shorter subordinate ridges, most of which are mostly oriented at a high angle to the longer parallel ridges, are typical of terrestrial volcanic fields and do not reflect the regional stress field (cf. Baer, 1991; Virgo, Abe and Urai, 2014). The ridge groups in our study crater and those of terrestrial analogs are arguably distinct from those seen within the volcanic domains of Utopia Planitia, where different ridge groups are not spatially related (Lanz *et al.*, 2010). In this context, the MFF is the region that most closely

resembles our FFC (Kerber *et al.*, 2017). The similarities are: (1) broad ridges branching into smaller ridges, (2) ridges being parallel in some locations, (3) ridges forming rectangular to near-circular to polygonal box-like patterns, (4) ridges shedding dark boulders, (5) ridges often having strikingly similar height and width, and (6) ridges are being exhumed from the surrounding terrain. These similarities are crucial to inferring the origin of ridges inside our study crater. The MFF similarity, and its presumably pyroclastic provenance (Mandt *et al.*, 2008), indicate that the ridges are made of more competent rocks, such as crystalline igneous materials, as contrasted to the underlying layered sedimentary rocks.

2.4.2.2 Provenance of mounds

On Mars, mounds are primarily formed by a combination of several key processes: preferential erosion of sedimentary units, volcanism, a diapir-like outflow of sediment-laden fluid, or a combination of the two, a process known as mud volcanism. Mud volcanism versus small-scale igneous volcanism is exemplified by the various widely distributed mounds in the northern lowlands at Chryse and Acidalia Planitia (Hodges and Moore, 1979; Frey *et al.*, 1979; Lucchitta, 1981; Wilson and Head, 1994; Tanaka, 1997; Fagents *et al.*, 2002; Farrand *et al.*, 2005; McGowan, 2009; Keszthelyi *et al.*, 2010; Oehler and Allen, 2010; Komatsu *et al.*, 2011, 2016; Hemmi and Miyamoto, 2018; Brož *et al.*, 2019; McNeil *et al.*, 2021). Mud volcanoes typically have smooth mound materials (Hemmi and Miyamoto, 2017). They also commonly date to the late Hesperian to middle Amazonian and range in height from 1-70 m and diameter from 40-1400 m (Hemmi and Miyamoto, 2017; 2018). The sedimentary layered deposits in the Firsoff, Becquerel, Kotido, and Crommelin craters in southwestern Arabia Terra, which have been formed by glacial, fluvial, or eolian processes, show similar size (cf. Zabusky *et al.*, 2012; Pondrelli *et al.*, 2015; McNeil *et al.*, 2021). In addition, the mounds in our study crater lie at the central portion of the crater, which contrasts with mounds lying typically near the crater rim in the western and southwestern Arabia Terra. Unlike the mounds in this work, the sedimentary mounds

in south Chryse Planitia (western Arabia Terra) are associated with buried impact structures and formed through differential erosion after the pre-mound layer was indurated by mineralization from groundwater (McNeil *et al.*, 2021). This would indicate that the mounds within the study crater have a different provenance (not mineralized or sedimentary) than those elsewhere in Arabia Terra. Furthermore, the observed mounds in the study crater differ in both scale and morphology from typical layered sedimentary deposits and mud volcanoes.

The mounds within the study crater exhibit layering (Figure 2.16a,b), which resemble volcanic layers similar to those along the flanks of Ascræus Mons (Figure

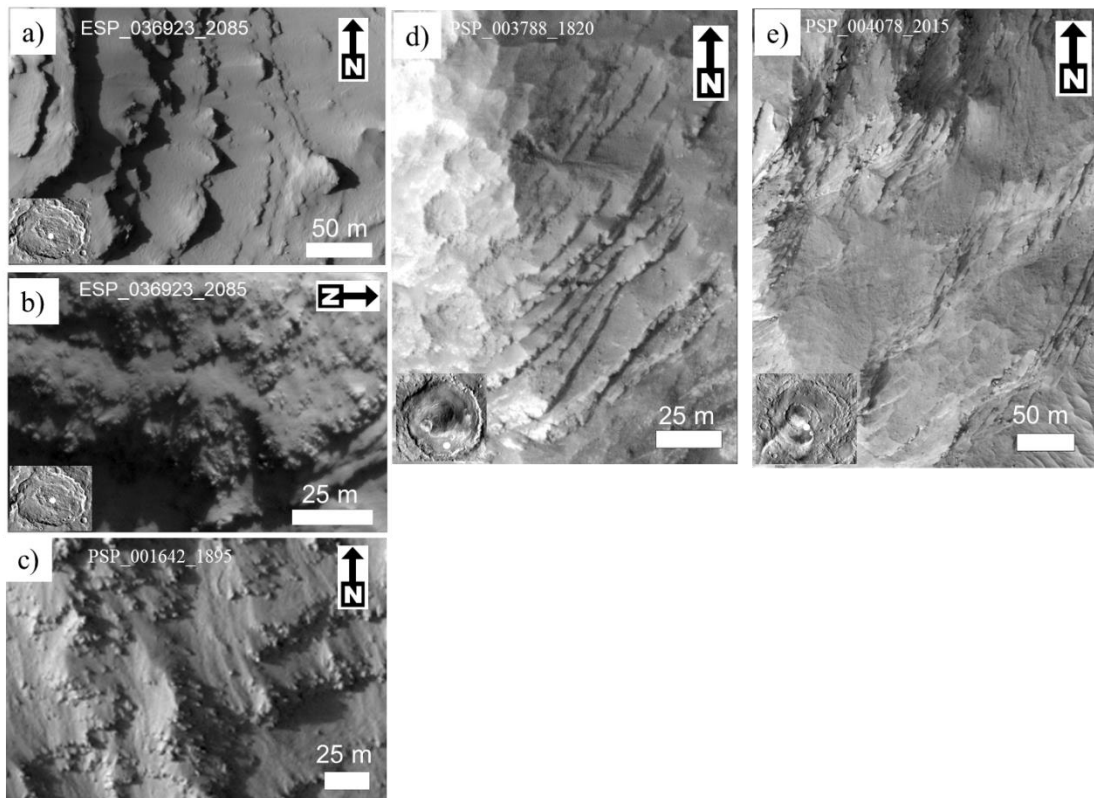


Figure 2.16: (a) and (b) Layered mounds in our study crater, with serrated edges with visible boulders of several meters in diameter, similar to layered volcanic rocks on the flanks of Ascræus Mons (c). Volcanic layering is compared with the layered sedimentary strata at Crommelin crater (d), and Becquerel crater (e) in western Arabia Terra at a similar spatial scale. (HiRISE image credit: NASA/JPL-Caltech/University of Arizona).

2.16c), but not those of other hypothesized sedimentary layered deposits on Mars (Ivanov *et al.*, 2014; Pondrelli *et al.*, 2015). In comparison to the normal uniform and rhythmic sedimentary layers observed in depositional settings such as the Crommelin and Becquerel craters, the sectional view of the mounds of our study crater reveals some significant differences in the structures and textures of the layering (Figure 2.16d,e). The volcanic layers, in contrast to the sedimentary layers, are less eroded as a consequence of the welding and jointing of the more rigid crystalline materials that occurred during the lava flow emplacement (Ivanov *et al.*, 2014). As a result, the drop-off of lava blocks and formation of joints, and fragmentation are prevalent resulting in extremely rough edges of the volcanic layers (Ivanov *et al.*, 2014). The layers of the mounds of our study crater are characterized by rugged, serrated edges with triangular-shaped protrusions plunging down the flank, which resemble eroded volcanic materials (Figures 2.7a, 2.16a,b) and are uncharacteristic of typical Martian mud volcanoes. Furthermore, the height-to-diameter ratio of the mounds ranges from 0.144 to 0.309 (Table 2.2) with an average of 0.216, a range similar to terrestrial lava domes but two orders of magnitude larger than conventional mud volcanoes (after Table 4 of Hemmi and Miyamoto, 2018).

The mounds in the study crater range in height from tens of meters to hundreds of meters in basal diameter, making them too high (up to ~ 350 m, Table 2.2) to be the spring mounds, which are, low-profile landforms in general (Allen and Oehler, 2008; Oehler and Allen, 2010). Further, the lack of preserved morphological evidence for fluid expulsion processes (Pondrelli *et al.*, 2011, 2015) cast doubt on the mounds' genesis as a spring deposit. The FFC's cone-shaped mounds also include flow-like features (Figure 2.7b,c), which are comparable to volcanic cones found on Mars (Meresse *et al.*, 2008; Lanz *et al.*, 2010; Brož and Hauber, 2012; Brož *et al.*, 2017) and on Earth (Ulrich, 1987). In addition, the characteristics of flow features resemble ridged plain lavas at the basement block in our study crater (Figure 2.6c) and mirror the geology in Eden Patera in northern Arabia Terra (Michalski and Bleacher, 2013). As a result, the conical mounds are most likely volcanic cones (Figure 2.8a,b), and the flow-like characteristics associated with the mounds are the lava flows associated with the

cones (Figure 2.7b,c). The study crater's mounds lack fracture patterns, unlikely that the mounds originated as pingos formed in periglacial environments (Balme and Gallagher, 2009; Burr, Tanaka, and Yoshikawa, 2009).

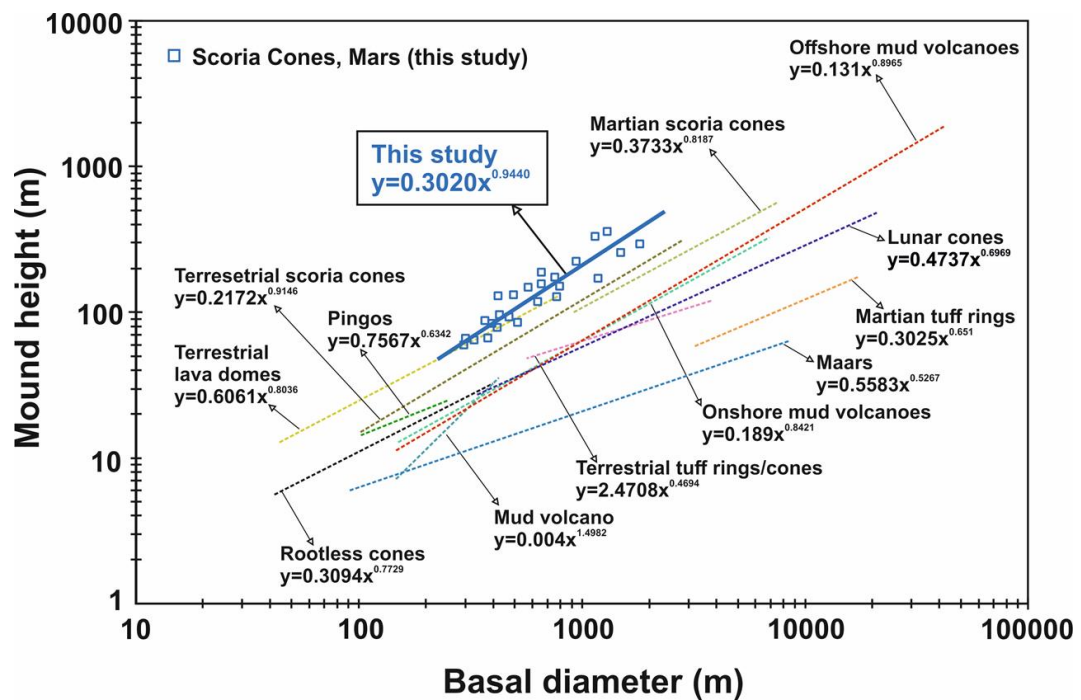


Figure 2.17: Height vs basal diameter plots of Martian, lunar, and terrestrial mounds (after Hemmi and Miyamoto, 2017; Wan et al., 2021). Morphometric comparison among the measured mounds (in this study) and other terrestrial analogs, log-log plots showing mound height versus basal diameter. Dashed lines represent the best linear least square fits of parameters of each category.

We also morphometrically compare the slope, height, and basal diameter of the mounds to previously known volcanic cones on Mars and Earth (Hemmi and Miyamoto, 2017, 2018). A close resemblance between the study crater and Martian scoria cones, terrestrial scoria cones, and lava domes has been observed (Figure 2.17). On the other hand, the slope-scaling factor of the mounds in our study crater (height/width ~ 0.94) resembles the terrestrial (~ 0.91) scoria cones more than the Martian (~ 0.82) counterparts (Figure 2.17). Although earlier studies have shown that Martian and terrestrial scoria cones are similar in shape and size (Wood, 1979), the

lower gravity and atmospheric pressure on Mars than on Earth suggests that Martian scoria cones would be lower in height and larger in basal diameter than those on Earth (Wilson and Head, 1994; Fagents and Wilson, 1996; Parfitt and Wilson, 2009; Brož *et al.*, 2015). Furthermore, a previous study (Brož and Hauber, 2012; Brož *et al.*, 2015) focused on Amazonian-aged scoria cones, which are considerably younger than the mounds in our study crater (late Noachian to early Hesperian). The Martian atmosphere possibly rarefied from Noachian to the Amazonian (Wordsworth, 2016).

As a result, any volcanic cones formed on ancient Mars have to be different in shape than the Amazonian scoria cones. Furthermore, the older mounds in our study crater were subjected to differential erosion for a much longer period than the younger scoria cones on Mars, which could explain the difference in the calculated slope-scaling factor. Mounds and ridges with significant thermal inertia may suggest high density and thermal conductivity, implying more resistant material than the softer surrounding layered units. In contrast, the lower values of the thermal inertia of the surrounding surface materials most likely represent unconsolidated sediment or dust cover (Figure 2.3b). As a result, the thermal inertia observations support the igneous origin of the mounds and ridges.

Many terrestrial analogues exist, with volcanic fields forming over a stratified substrate. One example is in Atakor volcanic field, Algeria; a scoria cone with rugged and serrated edges and exposed dikes, which crosscut the underlying layered sediments, lies exhumed due to erosion (Figure 2.18a). Sunset (SP) crater in the San Francisco volcanic field north of Flagstaff, Arizona, is a terrestrial analogue (Figure 2.18b) for monogenetic volcanic cone-associated lava flow (Ulrich, 1987). The Uinkaret volcanic field in northwestern Arizona is another terrestrial analogue. Uinkaret, situated between fault-controlled sedimentary basement, is an NS-trending volcanic field of cinder cones and basalt flows near the western Grand Canyon (Figure 2.18c). These volcanic cones rise far above the sedimentary rocks of the Grand Canyon (Crow *et al.*, 2008). The terrestrial analogs, along with the combined geomorphology, morphometric analysis,

stratigraphic relation, and thermal properties of the topographic features favor our volcanic cone and magmatic dike interpretation.

2.4.2.3 Stratigraphic relationship among the observed landforms

We reconstruct the sequence of events for the stratigraphy of this study crater using the age, superposition, and crosscutting relationships described in sections 2.3.1-2.3.3 (Figure 2.19). The dense crater population and inverted relief on the basement and the mesa tops imply that the mesas are derived from the remnant part of the original crater floor (Figure 2.6a,b,d). Isolated mesas with layers and sedimentary terraces likely

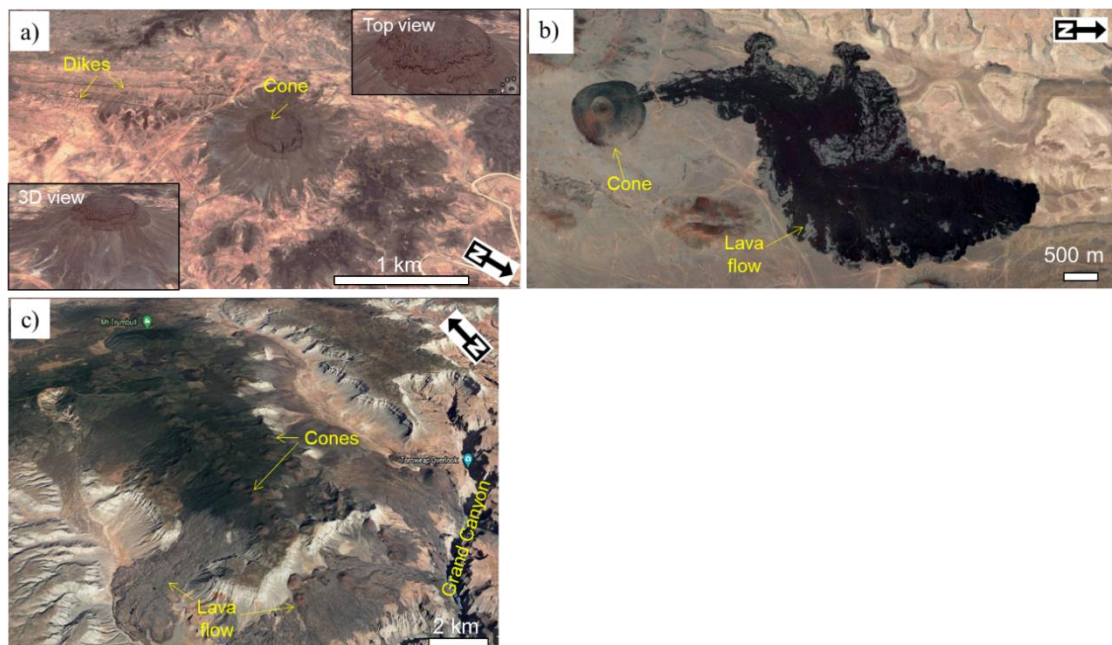


Figure 2.18: (a) Scoria cone with exposed dikes in Atakor volcanic field, Algeria (Google Earth; 23.37° N, 6.13° E). The inset at the bottom left is a 3D view of the cone, and at the upper right is a zoomed view of the top of cone, having rugged and serrated edges, exhumed due to erosion. (b) Scoria cone with associated lava flows at Sunset crater, San Francisco volcanic field north of Flagstaff, Arizona (Google Earth; 35.58° N, 111.63° W). A similar mound with flow feature is observed in our study crater. (c) Dozens of volcanic cones with lava flows at Uinkaret field, perched high atop the north rim of the western Grand Canyon (Google Earth; 3D view, 36.28° N, 113.16° W). Volcanic cones show a preferential alignment, similar to the mounds in our study crater.

formed from preferential erosion of the basement unit (Figure 2.6b). Additionally, dikes crosscut the mesas along steep fault planes (Figure 2.12b) and the underlying sedimentary rocks along sharp boundaries (Figure 2.12c), indicating that the dikes are younger than the mesas and sedimentary unit (Figure 2.19). The cones are underlain by the older sedimentary unit (Figure 2.7a), indicating that they are older than the crater's sedimentary deposits (Figure 2.16).

Although the exact superposition relationship between the magmatic dikes and volcanic cones cannot be determined due to extensively degraded landscapes, however, the parallel orientation of the dikes to the azimuth of the cones and similar thermal inertia between the two, are consistent with a syngenetic relation. The dikes and cones in the innermost part of the study crater interior are always spatially and structurally associated with each other (Figures 2.3a,b, 2.5a), implying that the innermost dike-cone

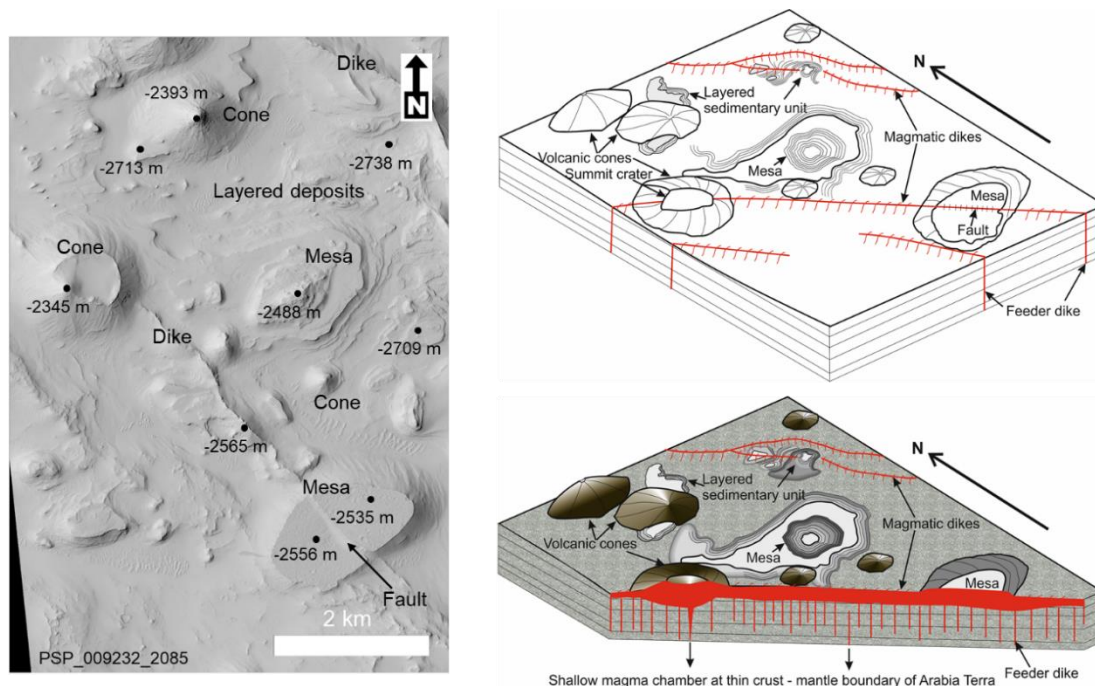


Figure 2.19: Left panel: Image of the interior part of the study crater with major landforms. Right panel: A schematic diagram and model for the origin of the volcanic landforms (not to scale). (HiRISE image credit: NASA/JPL-Caltech/ University of Arizona).

system and outer dikes formed at different times during multiphase igneous activity, but likely formed from a shared source. The outer well-exposed curvilinear dikes may have been emplaced in the subsurface prior to the innermost dike-cone system. The outer dikes' summits are higher than the base of the inner cones, indicating that the cones post-date the dikes. However, the exposed inner dikes' summits are topographically below the bases of cones implying the cogenesis of the inner cone-dike system. Furthermore, interior volcanism may have volumetrically exceeded the outer annulus as the landscape would have been the deepest at the crater interior. The inner dikes were most likely formed close to the surface by a shallow magma chamber with additional material that was likely contributed by the occasional volcanic outpouring from the volcanic cones. In either case, the cone-dike geologic unit is younger in comparison to the layered sedimentary rocks and mesa units (Figure 2.19).

2.4.2.4 Possible provenance of igneous features

The presence of cones and dikes at the center of a crater raises another question about their origin: were the igneous features formed as a result of impact-induced magmatism or by regionally expressed volcanism? Impact-induced intrusive igneous landforms, like dikes, rarely occur within impact craters of Mars, except proximal to pre-existing volcanism (Ivanov and Melosh, 2003). An impact creating a > 300 km diameter is needed for the typical Martian crust, to induce local magmatism (Ivanov and Melosh, 2003; Elkins-Tanton and Hager, 2005). This makes impact-induced magmatism within our study crater unlikely, as its diameter is ~85 km. The impact may have exhumed ancient igneous landforms, but any positive relief features (e.g., the cones) would have been damaged, which we don't observe. Therefore, Arabia Terra, on the other hand, could be an area of thinned crust (Neumann *et al.*, 2004), over which impact-triggered magmatism may be possible.

The co-alignment of the cones and dikes suggests a putative subsurface structural control on the formation of the landforms inside the crater. Also, the non-radial orientation of the cones and dikes may also indicate a maximum horizontal compressive stress in the NW-SE direction (Figures 2.8c, 9c). The NW-SE preferred

orientation of Arabia Terra's large tectonic features (e.g., wrinkle ridges) (Figure 3 of Dohm *et al.*, 2007; Figure 5 of Anderson *et al.*, 2008) resembles the orientations of the dikes and azimuths of the cones within Ramanathan crater (Figure 2.20). Through propagating subsurface compressional faults and folds to the surface, the wrinkle ridges throughout Arabia Terra (Figures 2.1, 2.20) may impose a typically homogeneous, regional crustal stress along with the NW-SE orientation at the time of formation (Golombek *et al.*, 2001; Saper and Mustard, 2013). The preferred alignment of the vents and fissures along the steeply-dipping faults or fractures is prevalent in terrestrial volcanic fields (Le Corvec *et al.*, 2013; Martí *et al.*, 2016). The bidirectional nature of volcanic landforms within Ramanathan crater as well as the enormous tectonic features of Arabia Terra implies regional endogenic tectono-magmatism rather than exogenic impact-induced processes.

Furthermore, the Ramanathan crater is an FFC. The FFCs on Mars are characterized by extensive faults, fractures, and joints along with knobs, ridges, and

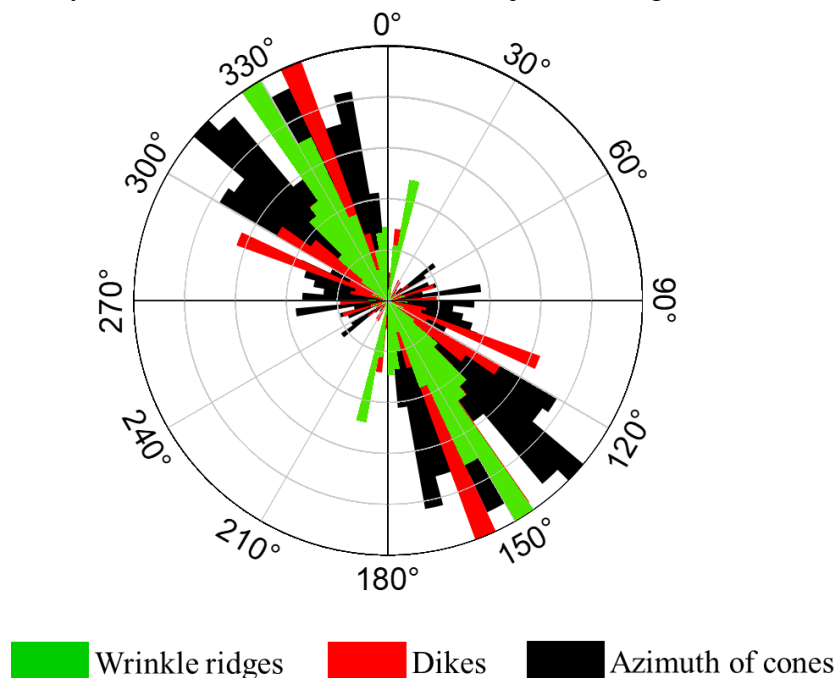


Figure 2.20: Orientation of the landforms (dikes and cones) in our study crater and wrinkle ridges in Arabia Terra; all showing bimodal direction tending ~ NW-SE, indicating evidence of regionally distributed tectono-volcanism.

mesas on the crater floor, mostly related to impact-cratering events ((Head and Mustard, 2006; Fassett and Head, 2007). Only a few FFCs, especially those occurring in volcanic provinces, appear to be altered by igneous activity (Schultz and Glicken, 1979; Bamberg *et al.*, 2014). Typically, FFCs on Mars lack such a distinct combination of ridges and mounds at the center of the crater. The ridges inside FFCs are usually randomly oriented (Figure 2.14), showing that the ridges are impact-induced fracture fills. The majority of the outside portion of the floor of the Ramanathan crater close to the crater rim wall exhibits typical characteristics of an FFC on Mars. However, the consistent orientation of dikes and cones at the crater center with regional linear tectonic features across Arabia Terra cannot be explained by the simple impact event that formed the host crater. Our finding of the preferential dike and cone orientation reinforces the likelihood of crustal modification in response to regional tectono-magmatism.

Arabia Terra's crust is thinner than that of the southern highlands, more closely resembling the crustal thickness of the northern lowlands (Neumann *et al.*, 2004). In addition to emerging in a thin crust, our study crater's hypothesized preferred orientation of magmatic cone-dike systems converges with pre-existing tectonic structures, such as the wrinkle ridges of Arabia Terra. As a result, we propose that the FFC-forming impact (re)activated steeply dipping linear regional tectonic features, causing intrusion by pre-existing magma bodies, particularly in the central crater floor where the excavation was deepest. The preferential orientation reinforces the likelihood of crustal modification in response to regional tectono-magmatism, perhaps associated with magmatism in Noachian Arabia Terra (cf. Michalski and Bleacher, 2013; Whelley *et al.*, 2021).

2.5 Conclusion

The crust of Arabia Terra is thinner than that of the southern highlands, resembling that of the northern lowlands. Our regional investigation of pre-existing tectonic structures such as Arabia Terra's wrinkle ridge anticipated that orientation converges with magmatic cone-dike systems' of Ramanathan crater. Therefore, our

finding of igneous dikes and cones within the Ramanathan crater may represent a broader extent of the thinned crust and could be a function of regional tectono-magmatism, an inference based on the similar orientations of linear features in the Ramanathan crater and Arabia Terra. As a result, the late Noachian - early Hesperian Ramanathan crater in the North-Central Arabia Terra region, describes a new class of diminutive volcanic centres and provides pieces of evidence of volcanic resurfacing in Arabia Terra. Furthermore, the presence of dikes and cones predominantly at Ramanathan crater's center, suggests that the igneous structures formed during the syn-deformational stage of the impact, or that volcanism was later rejuvenated along linear weak zones (i.e., faults and fractures). This was likely facilitated by a thinner crust proximal to the dichotomy boundary (cf. Michalski and Bleacher, 2013). While the formation of the volcanic structures in the Ramanathan crater cannot be explained by impact-induced magmatism, magmatism triggered by the impact that was further facilitated by a thin crust is plausible. Therefore, this study illustrates that the possible extent of volcanism is not only constrained in the NW part of Arabia Terra, as shown by previous studies, but it has a regional significance most plausibly throughout the entire Arabia Terra. Furthermore, the preferential orientation and areal distribution of the volcanic features motivate future work on the flexural loading and internal shrinking of the crust of Arabia Terra during the period of late Noachian - early Hesperian.

Chapter 3 Arabia Terra and other chemical provinces on Mars: Implications for geologic interpretations

3.1 Introduction

Similar to terrestrial Hawaiian volcanoes, the most prominent volcanoes on Mars correspond to enormous topographic shields. Unlike other shield volcanos on Mars, a recent discovery of new plains-style caldera complexes in North-western (NW) Arabia Terra (Michalski and Bleacher, 2013) are the collapsed calderas without immediately recognized shield topography. This type of caldera is characterized as a summit with constructional features built by layer upon layer of lava. Therefore, it could be possible that there were unrecognized volcanoes on Mars as they simply have heavily eroded or no topography at all. These calderas could indicate significantly high explosive volcanism, and collapse owing to subsurface magma migration, or both, in Arabia Terra (Michalski and Bleacher, 2013). The second chapter (North Central Arabia Terra: Rani *et al.*, 2021) and a few recent studies (Siloe Patera and Hiddekel Cavus of North Eastern Arabia Terra: Chu *et al.*, 2021; whole Arabia Terra: Whelley *et al.*, 2021), discuss the possible extent of volcanism in Arabia Terra, which shows that the proposed supervolcanic activity is not only confined to the NW part of Arabia Terra. Furthermore, these recent studies describe the geology of these calderas in the Arabia Terra region, and their putative regional tectono-volcanic relationships, and provide pieces of evidence for volcanic resurfacing in Arabia Terra. In addition, Whelley *et al.* (2021) have provided stratigraphic evidence for early Martian explosive volcanism which took place all over Arabia Terra. Collectively, Noachian-aged Arabia Terra

represents many fundamental aspects of Martian geology (Irwin et al., 2013), such as (i) a thinner crust than the other parts of the southern highland (Zuber *et al.*, 2000), (ii) large-scale structural and tectonic deformation, (iii) preserved large, thick, and complex sedimentary records (Malin and Edgett, 2000), and (iv) volcanic resurfacing (Chu *et al.*, 2021; Rani *et al.*, 2021; Whelley *et al.*, 2021) with volatile-rich surface. In the backdrop of the most eroded Noachian landscapes, it is therefore imperative to demarcate the volcanic area of Arabia Terra chemically.

In addition, various studies theorize the volatiles enrichment in Arabia Terra differentially. However, the source of these volatile is still unknown. Along with unconstrained bulk composition, the nature of volatile distribution with the relative importance of volatile origin (sedimentary or volcanic) processes remains unknown in Arabia Terra. Hence, we intend to address here whether volatile enrichment relates broadly to the sedimentary processes of Arabia Terra, or is the unique result of the volcanic resurfacing themselves. First, we demarcate the geochemical extent of Arabia Terra and deduce the bulk composition of the study region, which is further used for geological and geochemical analysis. However, confirming the localization of distinct chemical regions, e.g., the Noachian study area Arabia Terra, can be erroneous based on geomorphological evidences only. This is because chemical species are prone to weathering, alteration, and transportation processes, especially mixing can be pronounced along the regional boundaries of adjacent provinces. To robustly constrain the chemical boundary of Arabia Terra, it is imperative to draw the global distribution of the chemical provinces with the latest available chemical dataset and confirm with the previous studies. Michalski and Bleacher (2013) and three other contemporaneous studies (Chu *et al.*, 2021; Rani *et al.*, 2021; Whelley *et al.*, 2021) have shown the widespread nature of Arabia Terra volcanism, however, the distinct chemical boundary of Arabia Terra has not been defined. Therefore, bulk chemical composition of a Noachian province could never be studied in detail to decode its magmatic and source composition history.

A decade ago, the distribution of chemical provinces, defined on Mars using global nuclear spectroscopy of K, Th, Fe, Si, Ca, Cl, and H₂O (stoichiometrically equivalent H₂O of H) abundance has been examined (Karunatillake *et al.*, 2009; Gasnault *et al.*, 2010; Taylor *et al.*, 2010). Those studies have transformed the interpretation of geological processes as diverse as regolith hydration and mantle evolution. However, past individual multivariate analyses yielded different sets of provinces such as each multivariate analysis showing slight differences in the areal extent, suggesting methodological and data-dependent variability. For example, Taylor *et al.* (2010) used primary composition, which was normalized with respect to H₂O, Cl, and S. There was no direct detection of S and Cl from GRS but those were estimated using mean SO₃/Cl ratio (viz., 8.9) of soils at the Mars Exploration Rover landing sites (Brückner *et al.*, 2008; Taylor *et al.*, 2010). The resulting geochemical provinces by Taylor *et al.* (2010) demonstrate that Arabia Terra lacks a consistent compositional signature but does have uniformity in mapped geological units, indicating that Arabia Terra is not compositionally unique. Since the global chemical mass fraction map shows a significant enrichment of H₂O, it's possible that the volatiles played an important role in the geologic history of Arabia Terra. The lacking compositional signature and uniformity in mapped geology may arose in the earlier studies because of not considering the volatiles, leaving Arabia Terra as not compositionally unique region in Taylor *et al.* (2010). Further, the lack of an inter-methodological synthesis to characterize geological processes have hindered subsequent works and stymied advances with other datasets (cf. Rogers and Hamilton, 2015). In addition, key chemical data were unavailable or available only in a preliminary state for the original trilogy papers (Karunatillake *et al.*, 2009; Gasnault *et al.*, 2010; Taylor *et al.*, 2010): Aluminium (Al), sensitive to both igneous evolution and secondary mineralogy (cf. Nimmo and Tanaka, 2005; Ehlmann *et al.*, 2011; McLennan, 2012); and Sulfur (S), sensitive to cycling processes within the Martian critical zone across the atmosphere and crust (Halevy *et al.*, 2007; King and McLennan, 2010). Hence, province stability to the inclusion of Al and S, is also unknown, presenting additional uncertainties for geologic insight. Noteworthy to mention here that subsequent works (Baratoux *et al.*,

2014; Ojha *et al.*, 2018; Plesa *et al.*, 2018) incorporated those key elemental data in their respective studies.

To derive the average geochemistry of Arabia Terra, first, a methodological variability-independent consolidated geochemical province map is required to constrain the geochemical extent of Arabia Terra using multivariate analysis techniques. Therefore, a *trilogy* of multivariate cluster analysis methods (Karunatillake *et al.*, 2009; Gasnault *et al.*, 2010; Taylor *et al.*, 2010) applied to the chemical maps derived from Mars Odyssey gamma-ray (GRS) and neutron spectroscopy to identify chemical provinces and support interpretations of the regional-scale geology of Arabia Terra and other provinces. The use of GRS's decimeter scale depth sensitivity circumvents the dust obscuration difficulties encountered by other remote sensing methods such as VNTIR in the Arabia Terra region. Here refined nine elemental mass fraction maps are used from the GRS dataset: key rock-forming elements (Fe, Si, Ca, and Al) with large ion lithophiles (K and Th) and volatiles (Cl, S and stoichiometrically equivalent H₂O of H) to resolve the aforementioned challenges. Furthermore, we synthesize and advance prior multivariate methods (Karunatillake *et al.*, 2009; Gasnault *et al.*, 2010; Taylor *et al.*, 2010) to derive the first consolidated chemical provinces of Mars (Rani *et al.*, 2022) and compute the average geochemistry of Arabia Terra, by evaluating the extent of coherent compositional signature and uniformity in mapped geology of Arabia Terra.

3.2 Data and methods

We summarize the analysis of Gamma-Ray spectroscopic data using a trilogy of multivariate analyses. Details of GRS data production, detection, and gamma-fluxes conversion to elemental concentrations are given by Boynton *et al.* (2007) and Taylor *et al.* (2010). A detailed description of statistical methods is given below, which adapts and advances the methods developed by Karunatillake *et al.* (2009); Gasnault *et al.* (2010); Taylor *et al.* (2010).

3.2.1 Mars Odyssey Gamma-Ray Spectroscopy (GRS)

We use chemical maps derived from GRS spectra to delineate the chemically distinct provinces. The average decimetre sampling depth and coarse resolution of GRS overcome the effects of fine dust mantles making GRS elemental analysis ideal for primary and secondary geological process studies on broad scales. GRS measures the energy spectrum of gamma photons emitted from the Martian surface. Characteristic spectral peaks in this spectrum allow us to measure the abundance and distribution of most major rock-forming elements, along with some minor elements present on the Martian surface. There are two main processes on the Martian surface that give rise to gamma-photon emission. Gamma photons can be emitted from the decay of natural radioactive elements (K and Th) or emissions induced by cosmic particle interactions with the Martian atmosphere and non-radioactive elements of the Martian surface. However, due to increasing H (reported as stoichiometric H₂O mass fractions) towards the poles causing mass dilution for radioactive elements and compositional modelling issues for others due to neutron moderation, derived chemical maps are restricted to the mid-to-low latitudes, roughly within $\pm 50^\circ$ at a resolution of $5^\circ \times 5^\circ$ pixels (Boynton *et al.*, 2007). We use the latest refined datasets of GRS, including Al and S used in the literature (cf., Hood *et al.*, 2016, 2019; Ojha *et al.*, 2018, 2021), and compare them with GRS data used a decade ago (Boynton *et al.*, 2007, Karunatillake *et al.*, 2009, Gasnault *et al.*, 2010 & Taylor *et al.*, 2010), including the archived data at the NASA Planetary Database System (https://pds-geosciences.wustl.edu/ody/ody-m-grs-5-elements/v1/odgm_xxxx/data/smoothed/). The delineation of provinces also mitigates the substantial spatial autocorrelation inherent in the GRS data.

3.2.1.1 Comparison of GRS datasets: old vs refined

We compare more refined datasets of GRS in this study with the archived data at PDS used a decade ago (Boynton *et al.*, 2007; Karunatillake *et al.*, 2009; Gasnault *et al.*, 2010; Taylor *et al.*, 2010). We compare the ratio of these two datasets and calculate the corresponding propagated standard deviation (Table 3.1) for each element Cl, Fe,

H₂O, K, Si, and Th. However, to delineate our consolidated province map, we also include Al, S, and Ca elements. The ratio shows a close relation to unity, which indicates general agreement of the current chemical maps with their corresponding prior versions. Our subsequent analyses use the refined chemical maps exclusively as used by prior workers (Hood et al., 2016, 2019; Plesa et al., 2018; Ojha et al., 2021).

Table 3.1: Comparison of GRS dataset archived at PDS vs. GRS data used in the present study (previously used by Hood et al., 2016, 2019; Plesa et al., 2018; Ojha et al., 2018, 2021). NA denotes the unavailability of data.

	Cl	Fe	H ₂ O	K	Si	Th	Al	S	Ca
Archived GRS data at PDS									
Average	0.48	15.2	3.97	0.34	21.3	0.65	NA	NA	NA
Std Deviation	0.1	1.51	1.03	0.05	0.73	0.12	NA	NA	NA
GRS data used in the present study									
Average	0.47	13.7	3.9	0.38	21.6	0.61	4.49	2.18	5.00
Std Deviation	0.08	1.36	1.02	0.06	0.88	0.12	1.15	0.26	0.8
Datasets compared									
Average of ratio at each pixel (Present data/Archived data)	0.98	0.9	0.98	1.12	1.01	1.03	NA	NA	NA
Propagated standard deviation	0.26	0.13	0.36	0.24	0.05	0.27	NA	NA	NA

3.2.2 Trilogy of multivariate cluster analysis

We apply three multivariate cluster analyses to discern a set of internally uniform chemical provinces that reflect the compositional variability of the Martian crust with additional chemical data (Al, S, and Ca). The three methods consist of non-hierarchical clustering with principal component analysis (NHC-PCA: Taylor et al., 2010), hierarchical clustering with principal component analysis (HC-PCA: Gasnault et al., 2010), and modified student's t-test to distinguish spatially overlapping Gaussian tail clusters (t-GTC: Karunatillake et al., 2009). All three methods are discussed in more detail below. In the first step, for both the non-hierarchical cluster with principal component analysis (NHC-PCA) and hierarchical cluster with principal component analysis (HC-PCA), normalization is applied to the elemental compositional range to determine weight by relative variability. The normalization helps to provide information about the statistical significance of the mean composition of each calculated cluster. The normalization (z-score) is calculated by subtracting the global mean from each pixel point and dividing it by the standard deviation, formula is given as follows:

$$Z - score = \frac{(c_i - m)}{SD} \text{ -----(3.1)}$$

Where c_i is the mass fraction of the element at the i th pixel, m is the global arithmetic mean mass fraction, and SD is the global standard deviation of that element across the entire Martian surface mapped by GRS. The normalization makes the range for all pixels ranging from ~ -3 to $+3$.

3.2.2.1 Non-hierarchical (k-means) cluster analysis with principal component analysis (NHC-PCA)

The first technique starts with a PCA followed by a non-hierarchical clustering, which augments the previously used k -mean cluster analysis by Taylor et al. (2010). In addition to 4-elements (Fe, Si, Ca, and K), as used by Taylor et al. (2010), we include all GRS-derived volatiles (H₂O, S, and Cl), along with Al and Th in the present study,

to assess both primary and secondary processes on the Martian landscape. Although Th was not used for the delineation of provinces by Taylor et al. (2010), Th was discussed in their statistical calculations, citing the highly correlated Th to K. The data is first normalized using z-score steps as mentioned in the introduction.

PCA is a complementary method to cluster analysis and is used first for cluster (province) extraction. PCA seeks the best linear transformation of the original data by deriving a new set of uncorrelated principal components equal to the number of variables ordered in decreasing order of variance. PCA is suitable to explore relationships among multi-dimensional data, and when effective, it reduces the number of statistically meaningful dimensions. We use the first four PCs out of nine, which sums to more than ~ 80% of the total variance. We applied PCA to the GRS data prior to the non-hierarchical and hierarchical cluster analysis.

The next step after applying PCA is *k*-means clustering: a non-hierarchical method that assigns each pixel of the map to one of a number of clusters (fixed *a priori*) to maximize the inter-cluster distance while minimizing the intra-cluster dispersion. In addition to the volatiles, we include the previously unavailable elemental maps (Ca, Al) along with the remaining elements (K, Th, Fe, Si) used in the original work (Taylor et al., 2010) and published by Boynton et al. (2007). We use the R language (R Development Core Team, 2007) to establish a *k*-mean clustering algorithm to determine clusters. NbClust Package (Charrad et al., 2014) of the R language is used for *k*-mean clustering and optimizing the best number of clusters. To evaluate the quality of a clustering solution, the average silhouette width for each cluster is calculated (Rousseeuw, 1987). The silhouette width determines how well each element lies within its cluster and the high average silhouette width indicates a functional clustering (described in Gasnault et al., 2010). The average silhouette method computes the average silhouette of observations for different values of *k*, and determines the maximum average silhouette over the range of *k* values. The optimal number of clusters is 4, 5, and 6, from which we chose 6 clusters for our study, as the silhouette width

parameters change significantly after 4 to 6, relative to too many clusters resulting which is insignificant considering the GRS footprint.

3.2.2.2 Hierarchical cluster analysis with PCA (HC-PCA)

The second technique starts with a PCA followed by hierarchical clustering. Here, the same dataset is used as above in the NHC-PCA method. Additionally, the consolidated province map includes S, Th, and Al compared to Gasnault et al. (2010), which didn't consider Th in their definition of the province since it is highly correlated to K. Gasnault et al. (2010) also did not include Al in the definition of provinces but discussed its abundances in the final results because the Al data were at a preliminary stage at that time. The data are normalized using the same steps as mentioned in section 3.2.2.

Hierarchical cluster analysis (HCA) is a method with two possible approaches, an agglomerative bottom-up system (individual observations are progressively merged within growing clusters as one moves up the hierarchy) and a divisive top-down system (beginning with all the observations as a single group, and splits are performed recursively as one descends the hierarchy) (Cormack, 1971). The advantage of HCA over non-HCA (such as *k*-means) is that its output follows a well-structured hierarchy that is more informative than an unstructured set of clusters. Therefore, it can be easier to decide the optimal number of clusters that are otherwise unknown *a priori*. The hierarchy is usually presented in a tree-like structure called a dendrogram. A divisive (HCA) algorithm (Diana Package of R language is used for clustering) of Kaufman and Rousseeuw (2009) is applied to the first four principal components to obtain progressively more homogenous (and spatially small) clusters, similar to what was done originally (Gasnault et al., 2010). We have investigated the divisive algorithm based on a dendrogram for a number of clusters (e.g., 4, 5, & 6) for more than a single solution. The dendrogram shows that the increasing number of clusters above six does not reveal strong cluster combinations. Therefore, we have chosen six as an optimal number of clusters. Here again, the silhouette parameter is used as a cluster validity criterion (Rousseeuw, 1987), and the average overall silhouette width is calculated. It is

challenging to interpret silhouette width values systematically. However, to obtain each cluster's most representative map pixels without pixels overlapping different clusters, we consider the ideal average silhouette width cluster above 0.25, as lower than that indicates robust clustering is absent (Kaufman and Rousseeuw, 2009).

3.2.2.3 Modified student's t-test overlapping area with a threshold

The third method used to delineate chemically distinct provinces is a modified student's t-test to calculate each element's deviation from bulk Mars. The 't' test parameter is determined at i^{th} pixel with

$$t_i = \frac{(c_i - m)}{\sqrt{s_{m,i}^2 + s^2}} \quad \text{-----}(3.2)$$

where c_i is the mass fraction of the element at the i^{th} pixel, m is the global arithmetic mean mass fraction, $s_{m,i}$ is the statistical uncertainty of c_i , and s is the standard deviation of that element across the entire Martian surface mapped by GRS. This method is applied element by element to generate a new map of t-scores. We include S along with (Ca, Al) in this work (not available during the publication of Karunatillake et al., 2009) and the remaining GRS-detected elements (K, Th, Fe, Si, H₂O, and Cl) used by Karunatillake et al. (2009). This t-parameter normalizes the data according to the standard deviation of the dataset and includes each point's uncertainty, compensating for individual points with high uncertainty. We defined the Gaussian Tail Clusters (GTC) based on significant deviations ($t_i = \pm 1, \pm 1.5 \ \& \ \pm 2$) from the average Martian crust for each element, with higher deviations imparting a higher confidence level. The sign of threshold represents the corresponding depletion (negative) or enrichment (positive) of the element at a particular pixel (Karunatillake et al., 2009). The GTCs delineate the spatial overlap of multiple elements with deviations over $|t_i|=1$. The overlap of GTCs area must significantly overcome the effect of uncertainties in spatial autocorrelation and larger than the $\sim 7.4^\circ$ footprint of the GRS. To overcome this impact, we consider the overlap of at least 2 GTCs to form a chemically distinct

province when the overlapping region is equal to or exceeds an aerial threshold of nine contiguous pixels. We represent the elemental combination at different Lat-Long, corresponding to each combination different for enrichment (E), depletion (D), and the threshold value (1s, 1.5s, 2s) (e.g., [Al, S] 1s DE). To visualize the output corresponding to each Lat-Long, a generated map depicting the chemically distinct regions was overlaid over MOLA-HRSC.

In summary, the three methods optimize clustering differently but still present spatially overlapping trends suggestive of distinct provinces. NHC-PCA optimizes Euclidian distances between cluster centres, where the number of clusters is specified a priori. In comparison, HC-PCA builds a hierarchy of clusters using a top-down clustering approach based on a divisive algorithm (Kaufman & Rousseeuw, 2009), where the complete Martian landscape mapped by GRS belongs to one cluster and is split iteratively, moving down the hierarchy to highlight the differences between the sub-clusters. The modified t-GTC method identifies spatially contiguous areas where two or more elements deviate from their respective average mid-to-low latitude crustal abundances by one standard deviation or greater. The t-GTCs and HC-PCA-derived provinces reduce spatial autocorrelation biases by using unclassified (boundary) pixels to separate provinces from each other. Complementarily, the NHC-PCA method delineates border-sharing provinces. We further combine the intermediate provinces from the NHC-PCA, HC-PCA, and t-GTC methods into a consolidated map using a spatial contouring approach.

3.2.3 Average Martian crust

The mid-latitude chemical map pixels from the GRS excluding the study region are used to represent the Martian crustal composition as average chemistry. We consider the mid-latitude extent of GRS to represent an average of different geological units, possibly homogenized to substantial depth due to impact gardening, making the GRS-based geochemistry a suitable proxy for the crustal average (Taylor, Boynton, *et al.*, 2006; Taylor, 2013). Therefore, we use an average of mid-latitude GRS pixels to proxy for the average Martian crust composition. This measure of

average is similar to the previous estimations (Taylor et al., 2010). However, unavailable elements (e.g., Al, Ca, and S) during previous studies (Taylor et al., 2010) are considered in this work.

3.2.4 Modified Box-Whisker plot

Modified Box-Whisker plots are an effective way to display a comparison between two distributions and are therefore well suited for comparing our provinces to the global geochemistry of the average Martian crust distribution (Karunatillake et al., 2011; Ojha et al., 2021). The modified box-whisker plots use three key ratios: 75th percentile of one province over the 25th percentile of average Martian crust, a ratio of 50th percentiles (median ratio) of province vs. average Martian crust, and the ratio of the 25th percentile of the province over the province 75th percentile of average Martian crust. The chemical province is considered enriched or depleted in a specified element relative to the average Martian crust if the median ratio of the two provinces is greater than or less than 1, respectively. To measure the dispersion of each median, Median Absolute Deviation (MAD) (Bevington and Robinson, 2003) is calculated. As we calculate dispersion, the presented error bars are conservative and used to assess the significance of any observed enrichment or depletion. If a median ratio exceeds unity, and the MAD does not intersect unity, this suggests a significant enrichment even if it is small in magnitude. The graphical distribution analyses of the modified box-whisker plot captures the high and low extents of the distribution and compare the centres.

3.3 Results

3.3.1 Comparison of derived geochemical provinces present study versus previous studies

3.3.1.1 Comparison based on NHC-PCA (K-mean) analysis

To characterize the igneous provinces, Taylor et al. (2010) re-normalized the non-volatile elements with the volatiles (H₂O, Cl, and S). However, our interest is to assign the surface composition with the primary or secondary processes, especially in our study region Arabia Terra, which promoted this study to consider the volatiles along with the other available elements by GRS. This study further includes previously idle Al and Th by Taylor et al. (2010). Therefore, a difference in the apparent abundances of the elements between the two calculations is discernible, as we find our calculated elemental values to be consistently lower than that of Taylor et al. (2010). The provinces are not identical in some cases (Figure 3.1a). For example, a decade ago the geographically single region Arabia Terra, is sub-divided into three different geochemical compositions (Taylor et al., 2010). However, recent geochemical provinces derived from the inclusion of the volatiles and Al, and Th effectively depicts that geochemically Arabia Terra represents a single unit (Figure 3.2b).

Furthermore, Meridiani Planum is reclassified in association with the Medusae Fossae Formation region, whereas the previous maps classify Meridiani Planum as a part of Chryse Planitia near the dichotomy boundary. Notably, Taylor et al. (2010) grouped all volcanic landscapes into a single volcanic unit irrespective of age. However, our findings reveal that the different age volcanic regions form separate provinces, resulting from incorporating Al and volatiles like S in the consolidated geochemical mapping. Compared to Taylor et al. (2010), we identify a broader extent of Province-D that includes the province's western (Acidalia Planitia) and eastern part (Utopia Planitia) of the Martian lowlands, which spatially overlaps with Mars Global Surveyor (MGS) Thermal Emission Spectrometer (TES)-derived Surface Type 2

mineralogy primarily. The region was interpreted as of andesitic or basaltic andesitic composition based on spectral comparisons and derived mineral abundance (Bandfield et al., 2000; Rogers et al., 2007). Also, unlike the Taylor et al. (2010) province map, derived from the NHC-PCA method in this study lacks small clusters (a few pixels; Figure 3.1a).

3.3.1.2 Comparison based on HC-PCA analysis

The HC-PCA method is more or less similar to previous work by Gasnault et al. (2010). However, the number of provinces we identified is six (Figure 3.1b). In contrast, the previous work sub-divided the Martian surface into five chemical provinces, which might result from variance contribution in principal component space and incorporation of new elements Al, S, and Th in province delineation. Redistribution of sub-regions within the cluster took place, especially in equatorial regions. For example, Amazonis–Tharsis, and Sabaea–Arabia are both classified in the parent cluster P211 and their sub-clusters (P211A and P211B; Figure 16C of Gasnault et al., 2010). Whereas, P211B is characterized by Noachian Sabaea–Arabia terrains, whereas P211A is dominated by Amazonian terrains named as Amazonis–Tharsis (Gasnault et al., 2010). The incorporation of S, Al in the total dataset in this work would further divide P211 into two-parent clusters, such as Province-3 (western Tharsis) and Province-5 (Sinus Meridiani and Medusae Fossae Formation), which were classified as sub-clusters from a single parent cluster in Gasnault et al. (2010). However, Medusae Fossae Formation and Sinus Meridiani are geographically located in the opposite hemisphere with different evolving histories. Province P110A, P110B, and P110C of Gasnault et al. (2010) are partly comparable to Province-1, whereas Syrtis Major, an early Hesperian province, was absent in the map of Gasnault et al. (2010). The largest sub-province, P110A extends into the Noachian terrains from the central meridian to longitude 150° W, whereas P110B sub-province surrounding Hellas basin and including the northern part of Promethei Terra, Hesperia Planum, part of Tyrrhena Terra, and the southern part of Terra Sabaea, and P110C sub-province Gasnault et al.

(2010). Province-4 in the new geochemical map partly corresponds to P110B and P211B of Gasnault et al. (2010), which now corresponds to a single province.

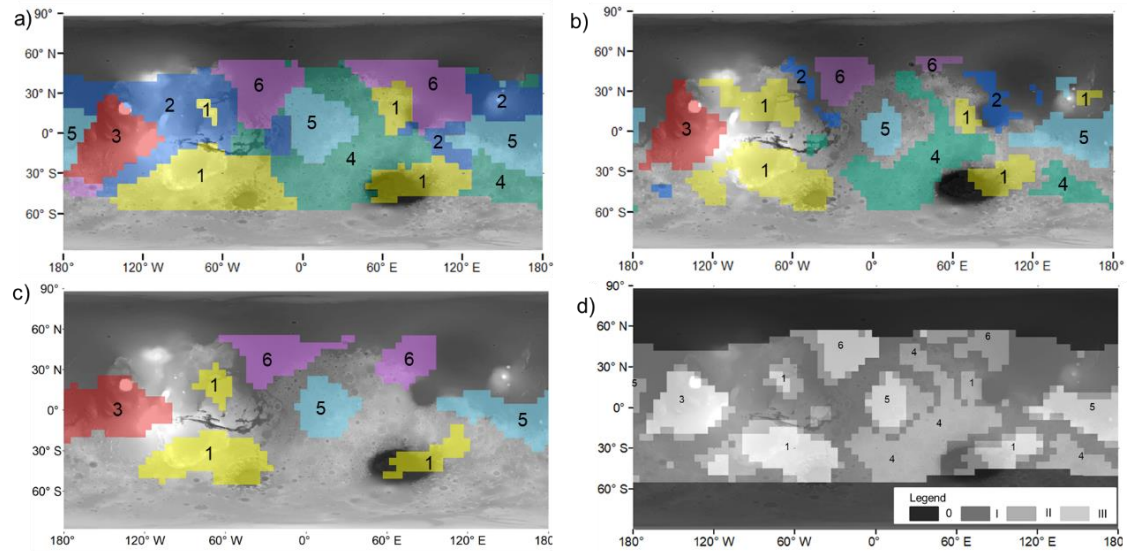


Figure 3.1: Results obtained from multivariate analysis by NHC-PCA (a), HC-PCA (b), and t-GTC (c) methods, overlaid on the Mars Orbiter Laser Altimeter and High-Resolution Stereo Camera (MOLA-HRSC) data map to delineate the geochemical provinces. Provinces-2 and -4 do not appear in the t-GTC method (c) as they are compositionally similar to the average crustal composition (Tables 3.3-3.4). (d) The consolidated contour map resulting from the synthesis of provinces derived from three different multivariate methods, overlaid on MOLA-HRSC to delineate the integrated geochemical provinces. The number of methods overlapping corresponding to each province is shown by the legends (0-III), and the intermediate province number is shown numerically (1 – 6).

3.3.1.3 Comparison based on t-GTC analysis

The t-GTC method delineates only the compositional provinces, which shows a significant deviation at one sigma or higher from the average Martian crust. Moreover, the t-GTC method (Figure 3.1c) further classified those provinces with a progressive increase in the complexity of analysis to identify less extreme differences. Therefore, the results of t-GTC analysis are opposite in comparison to the other two methods

(NHC-PCA and HC-PCA) that maintain spatial coherence among the delineated chemical provinces. The incorporation of S along with (Ca, Al) in this work has delineated new provinces while the chemical boundary of some provinces correlates well in our new map (Figure 3.1c) with geological and geomorphological boundaries. For example, Meridiani Planum appears in the new t-GTC method due to the incorporation of S which is highly abundant in this region; this result is lacking in Karunatillake et al. (2009). Similarly, the delineation of the Medusae Fossae Formation geochemical region overlays more appropriately over the geomorphic extent of the Medusae Fossae Formation region. A few geochemical provinces, like regions that lie in the northwestern and southern part of the Hellas basin in Karunatillake et al. (2009), disappeared in our consolidated map (Figure 3.2a), perhaps due to the incorporation of Al. Small clusters consist of a few pixels absent in the consolidated map, resulting from a larger number of elements and due to the incorporation of a more spatial threshold than the previous studies.

Table 3.2: Intermediate chemical provinces (1-6) from the three multivariate methods, their constituent geographic regions, and contribution to the consolidated provinces (last row). Abbreviations are K09: t-GTC method following Karunatillake et al. (2009); G10: HC-PCA method following Gasnault et al. (2010); T10: NHC-PCA method following Taylor et al. (2010).

Multivariate method	Province-1	Province-2	Province-3	Province-4	Province-5	Province-6
K09 (t-GTC)	Southern highland + Lunae Planum + Hesperia Planum	N/A	Western part of Tharsis	N/A	MFF + Sinus Meridiani	Acidalia Planitia + Utopia Planitia

G10 (HC-PCA)	Southern highland + Lunae Planum + Hesperia Planum + Syrtis Major + Small eastern extent of Elysium	Chryse Planitia + part of Utopia Planitia and Isidis basin	Western part of Tharsis	Arabia Terra + Noachis + Cimmeria + western Terra Sirenum	MFF + Sinus Meridiani + Small North-western extent of Elysium	Acidalia Planitia
T10 (NHC-PCA)	Southern highland + Small extent of Lunae Planum + Hesperia Planum+ Syrtis Major	Tempe Terra+ Elysium volcanic province	Western part of Tharsis	Arabia Terra + Noachis + Cimmeria + western Terra Sirenum	MFF + Sinus Meridiani	Acidalia Planitia + Utopia Planitia + Eastern part of Nili Fossae
Consolidated Provinces	Southern highland + Lunae Planum + Hesperia Planum + Syrtis Major: Province-A		Western part of Tharsis: Province-B		MFF + Sinus Meridiani: Province-C	Acidalia Planitia + Utopia Planitia: Province-D

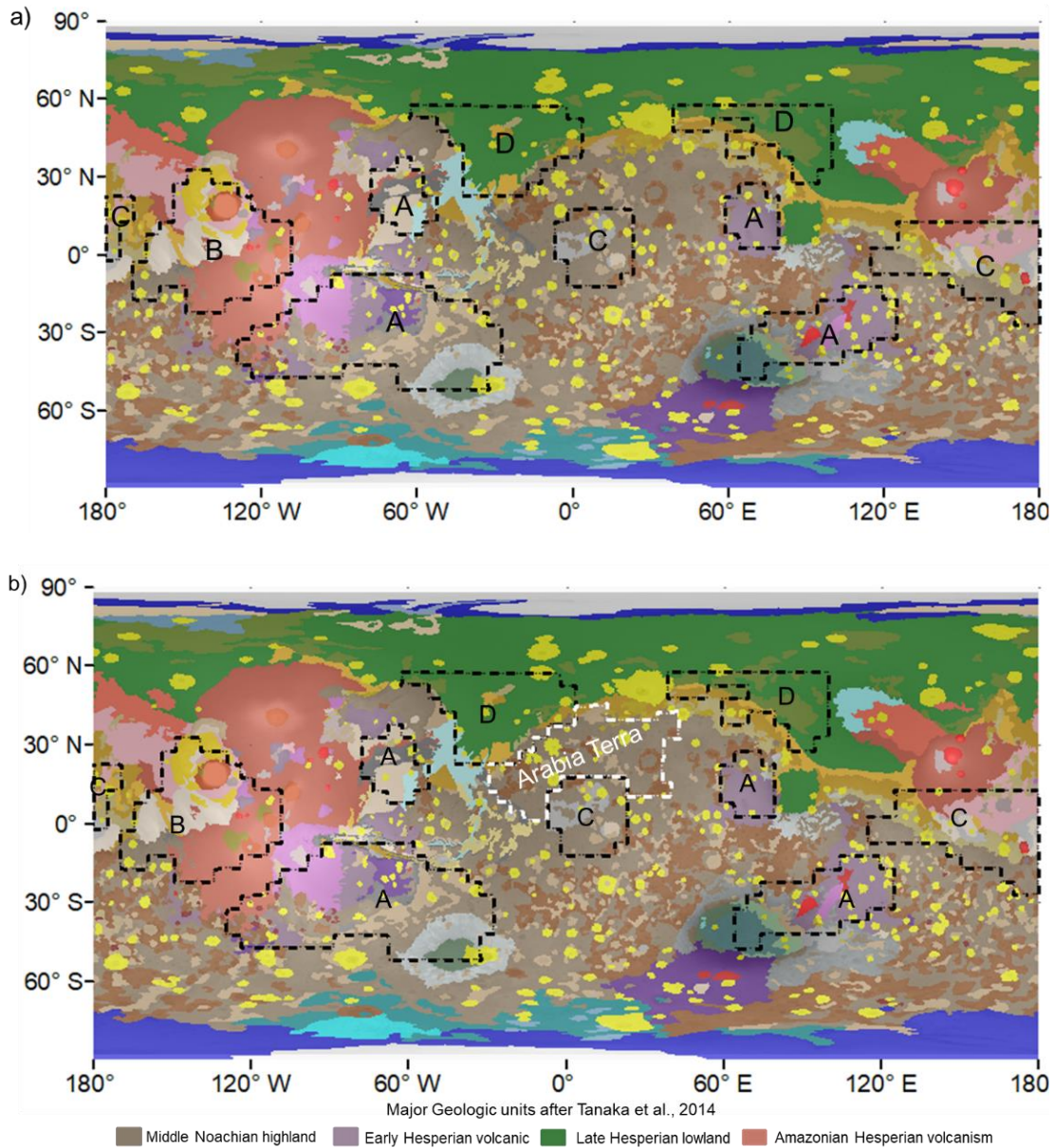


Figure 3.2: (a) and (b) The consolidated geochemical provinces on Mars are derived by integrating provinces from three different multivariate techniques and overlaid onto mapped geology (Tanaka et al., 2014, different colors indicate different geologic units with major units in legend). Arabia Terra is shown in white dashed boundary line in (b).

Table 3.3: Summarized Results from modified box-whisker plots (cf. Karunatillake et al., 2011), compared to characterize compositional differences of the intermediate chemical provinces and their constituent regions. Empty boxes represent an insignificant deviation from the average crust. D and E denote the elemental median ratio, in modified box-whisker plots above (enrichment: E) or below (depletion: D) unity by at least 1 sigma. Abbreviations are E: Enrichment; D: Depletion; others are as per Table 4. Province-2 and -4 are not highlighted in t-GTC method.

	Province-1			Province-2		Province-3			Province-4		Province-5			Province-6		
	K09	G10	T10	G10	T10	K09	G10	T10	G10	T10	K09	G10	T10	K09	G10	T10
K	D	D	D	E										E	E	E
Fe				E		D	D	D	D	D				E	E	E
Si				E		D	D							E	E	E
Ca				D			D	D	E	E	E					
Th	D	D	D											E	E	E
Al	E	E	E	D		D	D	D						D	D	D
H ₂ O	D	D	D	D							E	E	E			
Cl	D	D	D			E	E	E				E	E			
S	D	D	D								E	E	E			

Table 3.4: Ratio of stoichiometric oxides/elements for each intermediate province, '1', '3', '4', '5', and '6' relative to the average martian crust (AMC). The ratio compares with the corresponding propagated standard deviation. Uncertainty in each X/AMC ratio is calculated from $(X/AMC)[(\sigma_X/X)^2 + (\sigma_{AMC}/AMC)^2]^{1/2}$, where X (province) and AMC are mean concentrations of X and AMC. The values in bold show significant deviation from AMC. (Province-2 lacks minimum criteria of overlapping by at least two methods, therefore not highlighted in the consolidated province map).

	Province-1	Province-3	Province-4	Province-5	Province-6
K ₂ O	0.81±0.03	0.98±0.03	1.03±0.07	0.93±0.03	1.30±0.04
FeO	0.99±0.08	0.86±0.07	0.90±0.08	1.12±0.09	1.13±0.10
SiO ₂	1.00±0.08	0.92±0.07	1.01±0.06	1.00±0.08	1.06±0.09
CaO	0.9±0.2	0.8±0.2	1.1±0.2	1.1±0.3	1.0±0.3
Th	0.79±0.1	1.02±0.1	0.86±0.12	0.97±0.1	1.3±0.1
Al ₂ O ₃	1.3±0.4	0.65±0.3	1.09±0.4	1.01±0.4	0.73±0.4
H ₂ O	0.7±0.1	1.08±0.2	1.02±0.2	1.38±0.2	0.87±0.2
Cl	0.87±0.08	1.30±0.10	0.94±0.10	1.21±0.10	0.98±0.11
SO ₃	0.9±0.1	1.11±0.1	0.99±0.1	1.20±0.2	0.95±0.2
K/Th	1.1±0.1	0.97±0.1	1.03±0.1	0.98±0.1	1.00±0.1

Table 3.5: Arithmetic mean stoichiometric oxide mass fraction as a percentage (wt%, if not mentioned otherwise), elemental ratio, and its corresponding root means square uncertainty (σ) are calculated from mean measurement uncertainties for the grid points composing a geochemical province. Whereas, K/Th ratio uncertainty is calculated from $[(K/Th)*((\sigma_K/K)^2 + ((\sigma_{Th}/Th)^2)]^{1/2}$ (GRS derived) of the consolidated chemical provinces.

Oxides	Province-A	Province-B	Province-C	Province-D	Mid-latitude Average Martian Crust (AMC)
K ₂ O	0.35±0.01	0.42±0.01	0.40±0.01	0.56±0.02	0.43±0.01
FeO	16.1±0.9	14.0±0.8	18.2±1.1	18.4±1.2	16.3±1.0
SiO ₂	42.7±2.3	39.1±2.1	42.4±2.6	44.9±3.0	42.5±2.5
CaO	6.6±1.2	5.9±1.1	7.9±1.4	6.9±1.7	7.0±1.3
Th mg/kg	0.48±0.04	0.62±0.05	0.59±0.05	0.80±0.06	0.61±0.05
Al ₂ O ₃	10.6±2.1	5.5±1.8	8.6±2.2	6.2±2.6	8.5±2.2
H ₂ O	2.9±0.4	4.2±0.4	5.5±0.5	3.5±0.6	3.9±0.5
Cl	0.41±0.03	0.61±0.03	0.57±0.04	0.46±0.04	0.47±0.03
SO ₃	4.9±0.5	6.0±0.5	6.5±0.6	5.2±0.7	5.4±0.6
K/Th	6060±580	5600±430	5680±520	5800±440	5760±470

3.3.2 Consolidated map using a trilogy of multivariate analysis techniques

All the above three methods lead to large chemically uniform provinces; the provinces for any given method do not show dramatic compositional variability, reinforcing the subdued variability in chemical maps of Mars. Moreover, provinces that overlap spatially across the methods (Table 3.2) even if driven by different multivariate trends are compositionally similar (Tables 3.3-3.4). This further justifies our contour-consolidation method yielding the merged chemical province map (Figure 3.1d; Tables 3.4-3.5). Therefore, we combine the intermediate provinces from the NHC-PCA, HC-

PCA, and t-GTC methods into a consolidated map using a spatial contouring approach. A contour map of provinces is made by categorizing the regions into three levels: provinces derived from all three-methods overlapping, provinces with any two-methods overlapping, and provinces with no overlap (Figure 3.1d). We demarcate the boundaries of final provinces resulting from at least two-methods overlapping, reducing the spatial uncertainty in any method. Provinces that deviate minimally from the average Martian crust composition are omitted so that the consolidated chemical province map highlights crustally distinct regions. Applying these steps, we retain four of the intermediate provinces. To avoid any confusion between the prior individual geochemical province maps (Figure 3.1a-c) and the consolidated ones (Figure 3.2a), we label ‘Province-1’ as ‘Province-A’, ‘Province-3’ as ‘Province-B’, ‘Province-5’ as ‘Province-C’, and ‘Province-6’ as ‘Province-D’. In addition, we use mapped geology (Tanaka et al., 2014) for context on chemical trends.

3.3.3 Distinct geochemical provinces from the consolidated province map

All three methods lead to a set of large chemically uniform provinces, with minimal intra-province compositional variance, reinforcing the subdued variability in the chemical maps of Mars. The intermediate sets of chemical provinces resulting from the three underlying methods discussed above are labeled numerically (Province-1 to Province-6; Figures 3.1a-c; Tables 3.2-3.3). Province-2 from NHC-PCA and HC-PCA methods lacks the minimum criterion of at least two methods overlapping (Figure 3.1d). Therefore, Province-2 and 4 are de-prioritized in the consolidated chemical province map (Figure 3.1d). However, Province-4 which is one of the largest geochemical provinces is compositionally identical to the average Martian crust within statistical uncertainty. This province is dominated by Noachian age regions, including Arabia Terra. The geochemical boundary of Arabia Terra is demarcated by excluding the nearby provinces C and D. Moreover, provinces that overlap spatially across the methods are compositionally similar even if driven by different multivariate methods

(Tables 3.4). This further justifies our contour-consolidated method yielding the merged chemical province map (Figure 3.1 and Tables 3.4-3.5). Overall, overlapping areas labeled as ‘Province-1’ in Figures 3.1a-c have been combined into ‘Province-A’, ‘Province-3’ into ‘Province-B’, ‘Province-5’ into ‘Province-C’, and ‘Province-6’ into ‘Province-D’, resulting in four consolidated provinces (Figures 3.2a-b and Tables 3.2 and 3.5). Compositional consistency across the numeric intermediate provinces enables this synthesis. While geographically widely-separated areas may constitute a single province, such regions show some compositional heterogeneity. Therefore, we consider one sub-region from each province viz. Lunae Planum region from Province-A, Medusae Fossae Formation from Province-C, and Southern Acidalia Planitia from

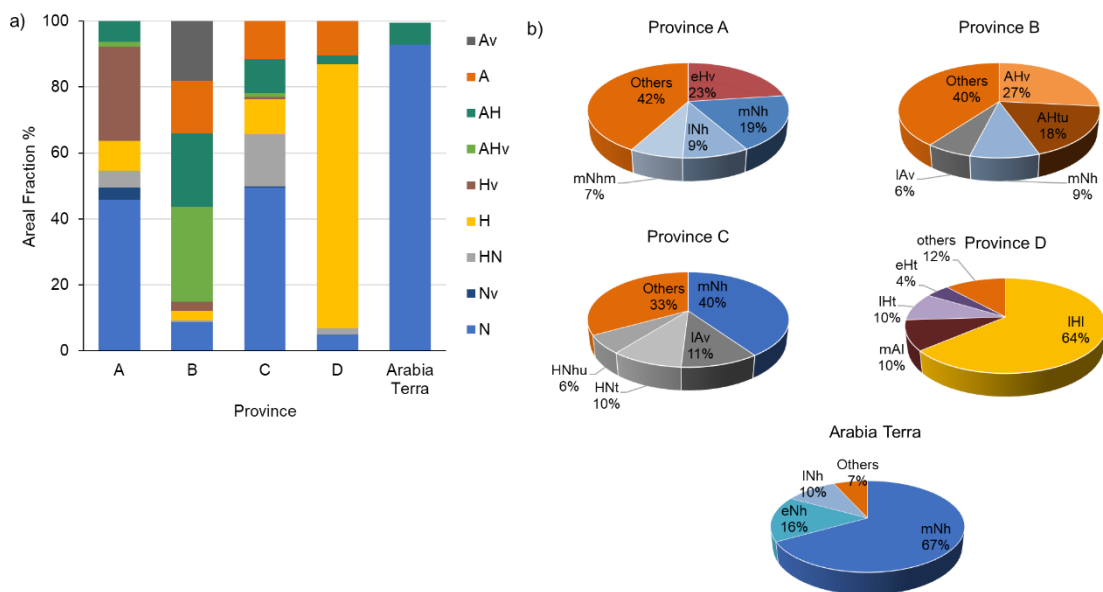


Figure 3.3: (a) The relative areal fractions of secular, transitional, and volcanic units within each chemical province corresponding to the consolidated geochemical map. The prefix “N” indicates Noachian, “H” indicates Hesperian, and “A” indicates Amazonian, and suffix “v” indicates the associated volcanic units (Tanaka et al., 2014). A detailed version of Figure 2a is given in Figure 2b as per Tanaka et al., 2014 geology map. (b) The four mapped geologic units (Tanaka et al., 2014) with the highest areal fractions are shown for each consolidated province and Arabia Terra, with the total areal fraction of remaining units indicated as others with orange color. The geologic unit notation of the I-1802 series is used.

Province-D, as case studies on geologic insight, revealing diverse mantle sources and magmatic processes in volcanic areas. Province-B doesn't have any sub-region it only consists of Tharsis, which is not considered as a case study. This study enabled to characterize the role of possible global ashfall units, and evaluate the relative roles of igneous versus aqueous environments.

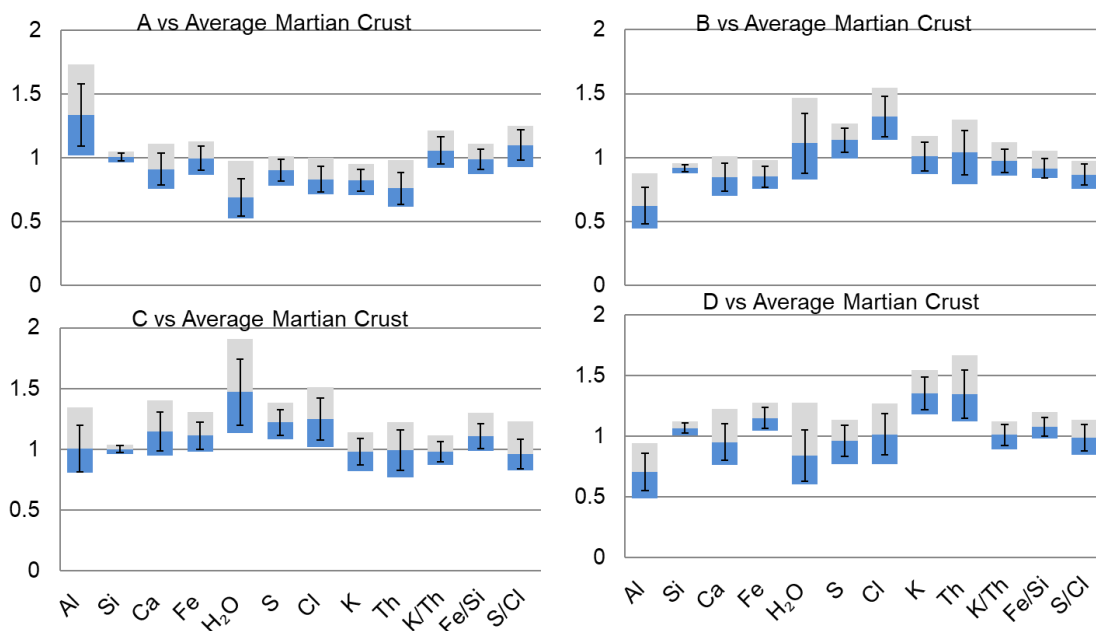


Figure 3.4: Modified box-and-whiskers diagram to compare the distribution of elements for all provinces to the global geochemistry of the average Martian crust. The top of the upper box represents 75th percentile/25th percentile ratio, the bottom of the lower box represents the 25th/75th percentile ratio, and the ratio of the medians by the boundary between them. The whiskers here represent the uncertainty on the ratio of medians using the Median Absolute Deviation (MAD) (Karunatillake et al., 2011).

3.3.3.1 Province-A

Four geographically distributed regions in the southern highlands (viz. southern part of Valles Marineris consists of Syria, Solis and Thaumasia planum, Lunae Planum,

Hesperia Planum, and Syrtis Major) constitute Province-A (Figure 3.2a). This province broadly represents mid and late Noachian highlands (> 30%) to early Hesperian-aged volcanic units (> 20%) (Figures 3.3a-b), containing most of the large Hesperian volcanic provinces. This province is enriched in Al and depleted in K, Th, and volatiles (H₂O, S, Cl) relative to the average Martian crust (Figure 3.4 and Tables 3.4-3.6). The K/Th and S/Cl ratios are above average, while the Fe/Si ratio is consistent with the average Martian crust.

Lunae Planum region, which lies between Chryse Planitia and Olympus Mons, in Province-A is a geologically distinct plateau of early Hesperian-aged highland material (Tanaka et al., 2014) (Figures 3.2a-b). Geochemically, Lunae Planum is depleted in K, Th, and H₂O relative to the average Martian crust. A detailed study indicates this region follows the general K and Th crustal correlation on Mars and substantially overlaps with the K and Th distribution in Hesperia and Thaumasia Planum (Figure 3.5). H₂O depletion in the Lunae Planum is also comparable in magnitude to that in the vicinity of Greater Thaumasia (Hood et al., 2016).

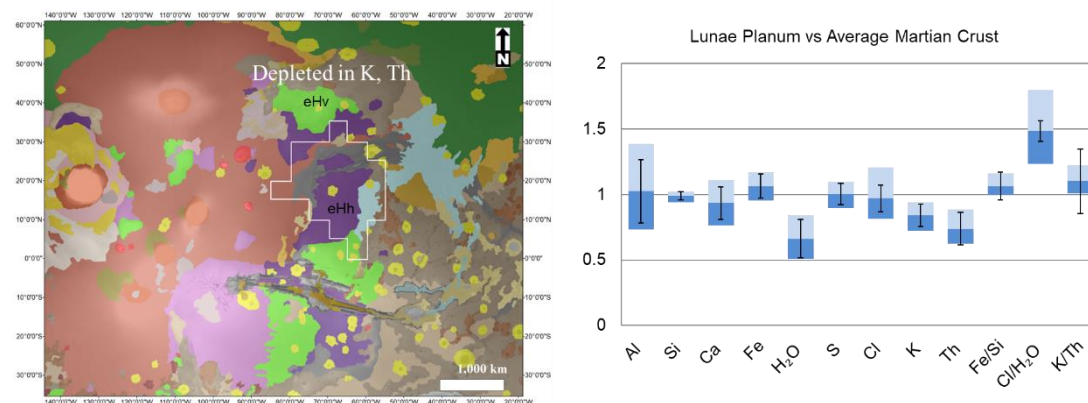


Figure 3.5: Left panel shows a geological map of Lunae Planum overlain on MOLA-HRSC map. The corresponding modified box-and-whiskers diagram to compare the distribution of elements in Lunae Planum province to the global geochemistry of the average Martian crust is shown in the right panel.

3.3.3.2 Province-B

Province-B comprises the south-western part of Tharsis bulge which consists of Amazonian and Amazonian-Hesperian aged volcanic units (> 30%) with Amazonian to Hesperian transitional geological units (~ 18%) (Figures 3.3a-b). The distribution of K and Th is consistent with the average Martian crust (Taylor, *et al.*, 2006b); however, the K/Th ratio is slightly low compared to the average Martian crust (Figure 3.4 and Tables 3.4-3.6). This province is moderately depleted in Si, Ca, and Fe and highly depleted in Al, while the volatiles (especially Cl and S) are highly enriched relative to the average Martian crust. The S/Cl ratio is depleted from preferential Cl enrichment. Compared to the average Martian crust, the Fe/Si ratio is below average.

3.3.3.3 Province-C

Province-C consists of two geographic regions: Sinus Meridiani and Medusae Fossae Formation, dominated by mid-Noachian highlands (~ 40 %) (Figures 3.2a, 3.3a-b; Table 3.2). These regions are enriched in volatiles (H₂O, Cl, and S) (cf. Diez *et al.*, 2008; Feldman *et al.*, 2011; Maurice *et al.*, 2011), while Fe, Ca are slightly enriched relative to the average Martian crust (Figure 3.4 and Tables 3.4-3.6). The ratio of S/Cl and K/Th is consistent with the average Martian crust. However, Fe enrichments make the Fe/Si ratio higher relative to the average Martian crust.

To characterize the possible global ashfall units, we consider a case study of the discrete wind-sculpted outcrops of Province-C's mid-Noachian Medusae Fossae Formation regions, which extend along the equator (Figures 3.2a-b), while their origin remains uncertain (cf. Kerber and Head, 2010; Zimbelman and Scheidt, 2012; Wilson *et al.*, 2018). Geochemically, the Medusae Fossae Formation region is highly enriched in Fe, Ca, and volatiles (S, Cl, and H₂O) relative to the average Martian crust (Figure 3.6) (Keller *et al.*, 2006). However, the abundance of K, Th, Al, Si, and the value of K/Th is consistent with the Martian crust. As highly incompatible elements in igneous processes, the ratio of Cl/K would inherit the initial mantle abundance (Taylor *et al.*,

2010). Although the ratio is globally maintained, the Medusae Fossae Formation region shows significantly different Cl/K than the rest of Mars. Chlorine is highly abundant, and K is generally lower than that in the average Martian crust (Figure 3.7)

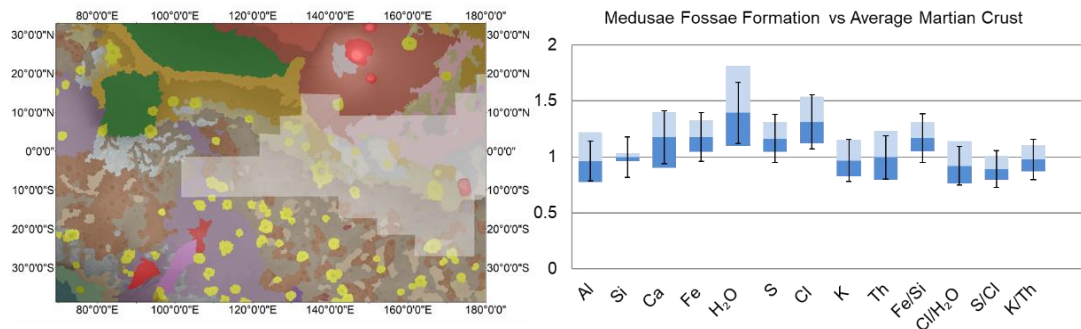


Figure 3.6: Left panel shows a geological map of Medusae Fossae Formation overlain on MOLA-HRSC map. The corresponding modified box-and-whiskers diagram to compare the distribution of elements in Medusae Fossae Formation province to the global geochemistry of the average Martian crust is shown in the right panel. The enrichment of volatiles within the Medusae Fossae Formation is clear, whereas other elements are relatively consistent with the average Martian crust.

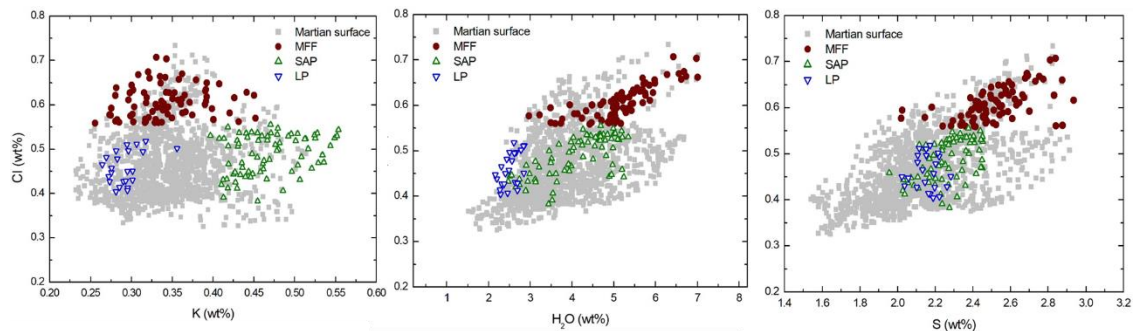


Figure 3.7: Cl vs K, Cl vs H₂O, and Cl vs S plots for Medusae Fossae Formation, Lunae Planum, and Southern Acidalia Planitia with the rest of the GRS data as a reference.

3.3.3.4 Province-D

Two regions of broadly late Hesperian lowlands form Province-D (> 60%) (Figures 3.3a-b). It is confined to Southern Acidalia Planitia and Utopia Planitia of the Northern lowland near the dichotomy boundary (Figure 3.2a and Table 3.2). Since both these regions are found within the northern lowlands and the northern extent of each is

obscured by the chemical mapping boundary, they may constitute a larger, contiguous region. The broader extent of Province-D, which includes the western and eastern part of this province, spatially overlaps with the TES-derived Surface Type 2 mineralogy in the Martian northern lowlands (Bandfield, Hamilton, and Christensen, 2000; Rogers, Bandfield and Christensen, 2007; Rogers and Hamilton, 2015). This province is highly depleted in Al, enriched in Si, Fe, K, and Th relative to the average Martian crust (Figure 3.4 and Tables 3.4-3.6), contrasting with other provinces. The K/Th and S/Cl ratio is consistent with the average Martian crust, whereas Fe/Si is higher.

To evaluate the relative roles of igneous versus aqueous environments, we study Province-D's Southern Acidalia Planitia, which is a late Hesperian plain area (Tanaka et al., 2014) in the northern lowlands. Southern Acidalia Planitia geographically lies between Tharsis and Arabia Terra (Figures 3.2a-b). Geochemically, Southern Acidalia Planitia is enriched in K, Th, Fe, and Si and depleted in Al relative to the rest of the average Martian crust (Figure 3.8). Despite K and Th enrichment, the K/Th ratio of Southern Acidalia Planitia is consistent with the Martian crust (Figure 3.8). Al/Si versus Mg/Si plots of Southern Acidalia Planitia show a slope different from the Martian crust

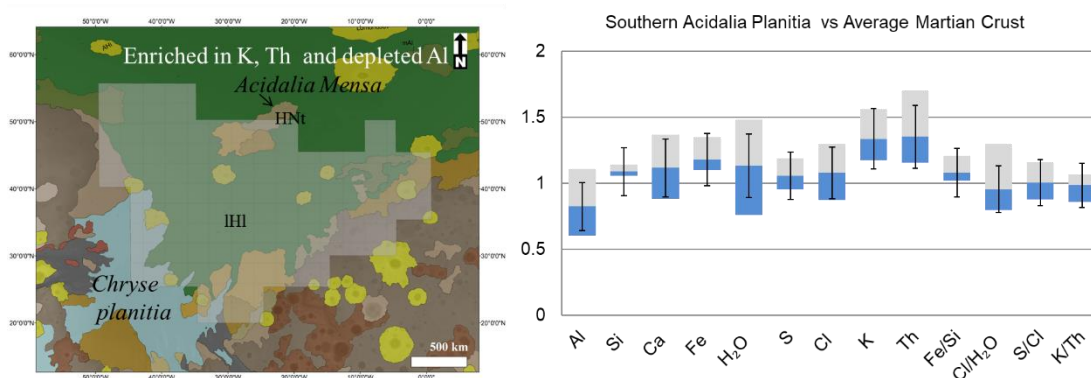


Figure 3.8: Left panel shows a geological map of Southern Acidalia Planitia highlighted in white overlain on MOLA-HRSC map. The corresponding modified box-and-whiskers diagram to compare the distribution of elements in Southern Acidalia Planitia province to the global geochemistry of the average Martian crust is shown in right panel.

(Figure 3.9a). Also, the ternary analysis of the non-detection of Al-bearing sulfates (Figures 3.9b).

Table 3.6: Summarized results from the modified box and whisker analyses (cf. Karunatillake et al., 2011), compared to characterize the relative distribution of chemical composition of the consolidated provinces. Empty boxes represent the insignificant deviation from the average crust. D and E denote the elemental median ratio, in modified box-whisker plots above (enrichment: E) or below (depletion: D) unity by at least 1 sigma. Abbreviations are as per Table 3.3.

	Province-A	Province-B	Province-C	Province-D
K	D			E
Fe		D		E
Si		D		E
Ca		D		
Th	D			E
Al	E	D		D
H ₂ O	D		E	
Cl	D	E	E	
S	D	E	E	

3.3.3.4 Arabia Terra

Geographically, the study area Arabia Terra region lies in the southern highland near the dichotomy boundary (Figure 3.2b). Arabia Terra region's geochemical boundary is demarcated by excluding the nearby sub-regions of provinces C and D. Arabia Terra region is a sub-region of Province-4 (Figure 3.1) which is one of the largest geochemical provinces and is compositionally identical to the average Martian crust within statistical uncertainty. However, Arabia Terra is enriched in H₂O and Th with respect to the average Martian crust (Figure 3.10a and Tables 3.4-3.6). The K/Th ratio is slightly below the average, while the Fe/Si and S/Cl ratios are consistent with

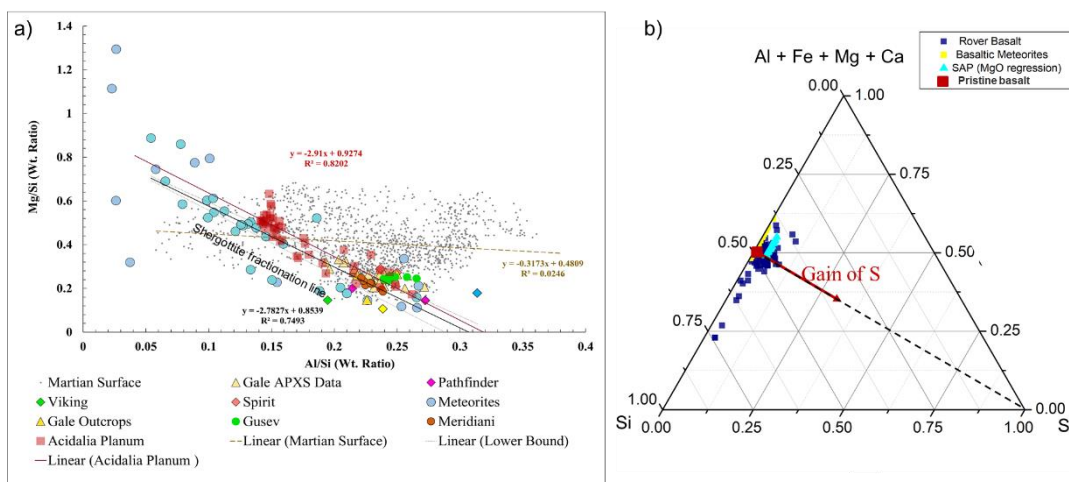


Figure 3.9: a) The Mg/Si vs. Al/Si diagram with Martian meteorites, Southern Acidalia Planitia, and Martian surface references plotted. Southern Acidalia Planitia data show the Al depletion follows a similar trend seen in Martian meteorites. The distinguishing characteristics might result from the depletion of Al during the early melting of mantle source regions of Mars. b) Ternary diagrams illustrating the scenarios to account for the chemical composition of Southern Acidalia Planitia region. The diagrams display the relative molar proportions of Si, Fe, Mg, Ca, Al, and S in the Southern Acidalia Planitia region, in a reference set of Martian basalts, including basalts analyzed in situ by rovers and basaltic meteorites.

the average Martian crust. This region broadly represents early to late Noachian highlands (> 93%) (Figures 3.3a-b).

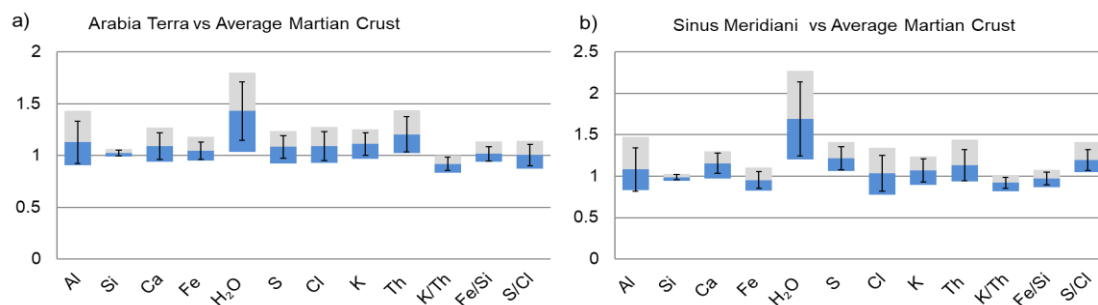


Figure 3.10: Modified box-and-whiskers diagram to compare the distribution of elements for (a) Arabia Terra, and nearby regions viz. (b) Sinus Meridiani and Southern Acidalia Planitia (Figure 3.5) w.r.t the global geochemistry of the Average Martian Crust. Detailed description of modified box-whiskers diagram is given in Figure 3.4.

3.4 Discussion

3.4.1 The geochemical extent of Arabia Terra

The consolidated map depicts Arabia Terra as a coherent compositional signature and uniformity in mapped geology, unlike the chemical provinces in previous studies (cf. Taylor et al., 2010). Regional proximity and adjacent chemical boundary have made the region of Arabia Terra necessary to compare with the two sub-regions Southern Acidalia Planitia of Province-D and Sinus Meridiani of Province-C (Figure 3.2b). This would help in checking the compositional variability among these regions and any compositional overlapping that may have taken place, especially at their common boundaries. In the north-western part of Arabia Terra, a small chemical overlapping with Southern Acidalia Planitia can't be ruled out, which was not detected in earlier studies (cf. Taylor et al., 2010). This small chemical overlapping might represent evidence of resurfacing in the nearby marginal area such as the boundary between Southern Acidalia Planitia and N-W Arabia Terra (Figure 3.2b). The southern

part of Arabia Terra shares proximity with Sinus Meridiani. Previous rover and orbital investigation of Sinus Meridiani shows the signature of aqueous alteration, with enrichment of H₂O, S, and depletion of S/Cl with K/Th ratio (Figure 3.10b). On the other hand, the Arabia Terra region is enriched in H₂O, not S, unlike the regional proximity shared in its southern part. Furthermore, the S/Cl ratio is not deviating from the average Martian crust. Southern Acidalia Planitia is also compositionally different from Arabia Terra; Southern Acidalia Planitia is enriched in Si, Fe, K, and Th w.r.t. average Martian crust, while Arabia Terra is enriched in H₂O and Th w.r.t. average Martian crust (Figure 3.10a). Therefore, this compositional variability helps us to demarcate the geochemical extent of Arabia Terra (Figure 3.2), excluding the geomorphic part from the southern and NW of Arabia Terra shared by sub-regions of provinces C and D.

3.4.2 Extent of aqueous alteration

We first evaluate the extent of aqueous alteration evident at a regional scale in decimeter depths. The Chemical Index of Alteration ($CIA = Al_2O_3 / (Al_2O_3 + CaO + Na_2O + K_2O) \times 100$) in standard molar abundances of oxides corresponding to the provinces A-D and Arabia Terra is < 50 , which indicates no signature of weathering (Figure 3.11a) at the broad scales of GRS. The K/Th ratio is similar across all the provinces with the average Martian crust within statistical uncertainty (Figures 3.4 and 3.11b). Specifically, K/Th ratio is effectively invariant with the abundance of the volatiles (H₂O, S, and Cl) even across the maximum in Province-C and Noachian-aged Arabia Terra to a minimum in Province-A (Figure 3.12a). The most incompatible mapped elements, K and Th (partition coefficient $\ll 1$; Borg and Draper, 2003) do not fractionate in the solid phases during magmatic processes.

Therefore, our study shows that even the volatile-rich regions are compositionally consistent with water-limited isochemical weathering throughout Mars's geologic history (Hurowitz and McLennan, 2007; Tosca *et al.*, 2008).

Consequently, the provinces are broadly representative of well-preserved igneous materials at least to decimeter depth scales and averaged over a few hundred kilometres along the surface.

To evaluate the relative roles of igneous versus aqueous environments, we considered Lunae Planum and Southern Acidalia Planitia in detail as the case studies. Although Lunae Planum is depleted in K and Th, this region follows the general K and Th crustal correlation on Mars. Consequently, Lunae Planum's K and Th depletion likely reflects volcanic resurfacing, not aqueous weathering (Taylor et al., 2006b). Given minimal chemical weathering across the provinces, the H₂O depletion is likely volcanic and could suggest a dry mantle source as predicted for Hesperian volcanism (cf. Balta and McSween, 2013). However, the mantle evolution model also predicts high Th abundances, which is not seen in our study. Overall, Lunae Planum likely follows the same volcanic evolution trends as identified in the Greater Thaumasia area, i.e., low H₂O abundance and temporally decreasing K and Th, which may be a part of the same evolving volcanic province (Hood et al., 2016). Furthermore, higher K and Th

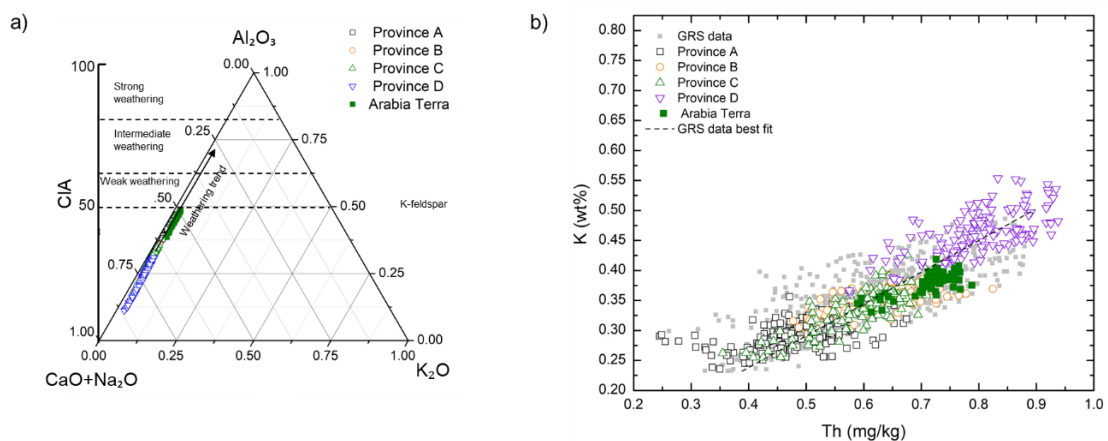


Figure 3.11: (a) The Chemical Index of Alteration ($CIA=100*[Al_2O_3/(Al_2O_3+CaO+Na_2O+K_2O)]$) diagram is used to assess the extent of chemical weathering in the provinces A-D. For CIA, we are using standard molar abundances of oxides. Non-GRS Na₂O is calculated using Baratoux et al. (2014). (b) K (wt%) vs. Th (mg/kg) in several regions, consolidated provinces A-D including Arabia Terra and Average Martian Crust.

abundance within Lunae Planum relative to Greater Thaumasia could place it as the oldest member of an underlying volcanic series.

Despite K and Th enrichment, the K/Th ratio of Southern Acidalia Planitia is consistent with the Martian crust, which suggests primary rock composition (Karunatillake *et al.*, 2006; Taylor *et al.*, 2006b), diverging from the extensive alteration posited by Bouley *et al.* (2020). The Al depletion in Southern Acidalia Planitia best correlates with that of the mean basaltic shergottite composition (Nimmo and Tanaka 2005) and given the similar K, Th, and K/Th ratio signatures, it is more likely to be related to mantle composition than chemical weathering (Taylor *et al.*, 2006b) at least at the scales of our observations. Al/Si versus Mg/Si plots of Southern Acidalia Planitia show a slope different from the Martian crust but resembling that of younger Martian meteorites (Figure 3.9a). Also, the non-detection of Al-bearing sulfates (Figure 3.9b) that would result from low-pH aqueous alteration (McLennan, 2012) supports an igneous origin for the apparent depletion of Al. Further, mineralogical observations by Compact Reconnaissance Imaging Spectrometer for Mars (CRISM) reveal mafic mineral signatures in outcrops, crater ejecta, and central peaks of the craters in Southern Acidalia Planitia (Pan *et al.*, 2017) resembling Hesperian-aged volcanism (Salvatore *et al.*, 2010). The collective K and Th enrichment and Al-depletion can best be explained by a low degree of partial melting at high pressure derived from a garnet-rich mantle source for Southern Acidalia Planitia.

In the Medusae Fossae Formation region, Cl is highly abundant, and K is generally lower than the average Martian crust, consistent with Cl enrichment in airborne dust and volcanic aerosol (Newsom and Hagerty, 1997; Goetz *et al.*, 2005). Meanwhile, high S and Cl content, moderately high H₂O (Figure 3.7), fine-grained nature, preserved primary mineralogy, and extensive erosional features suggest that Medusae Fossae Formation is the source of the global dust reservoirs of Mars (Ojha *et al.*, 2018). Thus, our work supports the provenance of Martian dust from mostly mechanical weathering and transport of a pyroclastic ashfall unit, which possibly arose from SW-oriented paleo-winds during Tharsis volcanic eruptions (Keller *et al.*, 2006;

Diez *et al.*, 2009). Our results don't support the hypothesis of water-ice existence in polar layer-like deposits to explain the volatile enrichment in the equatorial Medusae Fossae Formation (Wilson *et al.*, 2018). Summarily, the voluminous pyroclasts of Medusae Fossae Formation are most likely the product of low-moderate degree partial melting of a distinct volatile-rich mantle source during the mid-Noachian age in comparison to the late Noachian - Amazonian volcanic provinces of the Martian highlands.

Table 3.7: H₂O Abundance in Lunae Planum, Hesperia Planum, Syrtis Major, and Martian references.

	H ₂ O (wt %)	Standard Deviation (1 σ)
Lunae Planum	2.52	0.03
Hesperia Planum	3.47	0.30
Syrtis Major	3.57	0.13
Thaumasia Planum	2.91	0.27
Southern Highlands	3.83	1.02
Martian Surface	3.90	1.01

3.4.3 Chemical trends in Arabia Terra and Martian chemical provinces

Earlier work by Taylor *et al.* (2010) grouped all volcanic landscapes into a single province irrespective of age. However, our study supports the findings (Karunatillake *et al.*, 2009; Gasnault *et al.*, 2010) that volcanic regions form separate provinces by age (Figure 3.3a). Moreover, the minimally weathered volcanic composition of provinces

A-C and Arabia Terra region in the southern highlands of Mars shows distinct geochemical trends. Unlike southern highlands, Province-D, the late Hesperian lowland unit, deviates from the chemical trend (Figures 3.12b-d), indicating distinct lithology. The provinces A-C and Arabia Terra of mid-Noachian age have higher average Fe- and Si-concentration, however, it decreases with age like in Amazonian (Figures 3.12b). Similarly, Al-Fe and Ca-Si plots also depict similar depletion chemical trends from provinces A-C and Arabia Terra of mid-Noachian age to Amazonian (Figures 3.12c-d). As hypothesized by Balta and McSween (2013), higher SiO₂ in older regions of Mars may indicate dehydration melting of the mantle with hundreds of mg/kg water, similar to that of Province-A and -C including Arabia Terra region of our study, in contrast to the relatively silica-depleted younger Province-B. Unlike Earth, considering the stagnant-lid regime of Mars (Golombek and Phillips, 2009; Grott et al., 2013), the decrease of SiO₂ and concomitant increase in olivine component in the parent magma from the oldest to youngest volcanic terrains of southern highlands could be explained by the growth of lithospheric thickness, which would increase the formation pressure, supporting the results of Baratoux et al. (2013). This contrasts with the topmost micron-layer observation by TES, suggestive of weathering reflected by the non-detection of olivine in the Hesperian highland terrains, at the spatial resolution of 1 pixel per degree (Rogers and Hamilton, 2015). GRS-scale footprints in this study consistently reveal the igneous crustal composition albeit weathering processes were prevalent during Martian surface evolution. In addition, high Ca/Al for Province-B and -D could indicate a path for sampling a high-pressure, garnet-rich source (Treiman, 2005; Dasgupta and Hirschmann, 2007; Balta and McSween, 2013). The abundances of K and Th are relatively low in late Noachian – early Hesperian Province-A as compared to Hesperian-Amazonian Province-B, mid-Noachian Province-C, and Arabia Terra in the highland volcanic terrains (Figure 3.11b). Earlier studies advocated the early Noachian crust-building phenomenon for the enrichment of these large ion lithophile elements (LILEs: K and Th) in Noachian than Hesperian terrains (Rogers and Hamilton, 2015). However, our study shows that the youngest volcanic province also contains a high relative abundance of those LILEs, which contradicts the hypothesis of LILE

fractionation during the early Noachian crust formation. Moreover, the non-systematic trend of the abundances of LILEs and other secular chemical trends may necessitate complex melting processes in a highly differentiated mantle source on a regional to global scale (cf. Basu Sarbadhikari et al., 2016, 2017; Udry et al., 2020) that existed from the early-stage evolution of Mars. Morphologic, structural (Chapter 2), and chemical analyses are used to delineate the volcanic extent of Arabia Terra. Unlike the chemical provinces in previous studies (cf. Taylor et al., 2010), the geochemical investigation shows that Arabia Terra has a coherent compositional signature and uniformity in mapped geology. Regardless of how heavily dust is mantled over Arabia Terra, the compositional variations follow a chemical trend identical to other dust-free or mildly dust-covered provinces-A and -C of similar age. Furthermore, various geologic investigation of the Arabia Terra region depicts that the GRS-derived composition represents a primary igneous composition.

3.5 Summary and conclusion

The first consolidated chemical provinces of Mars reveal several geochemical signatures of broad geologic importance. Compared to prior works, the emergence of distinct regions as well as the exclusion of previously suggested provinces reflects our methodological advances along with the use of Al and S. Our findings demonstrate chemical trends among the southern highland provinces A-C and Arabia Terra that may indicate complex processes of an evolving degree of partial melting within a highly differentiated mantle source. The distinct lithology of the late Hesperian lowland unit, Province-D, does not follow the secular chemical trends like highland provinces. This could provide a mechanism for sampling a high-pressure, garnet-rich source for Province-D. We also find that even older volatile-rich regions preserve igneous geochemistry, indicating how throughout Mars's geologic history, water-limited isochemical weathering dominated regionally to decimeter depths scales. Specifically, as a distinct plateau of early Hesperian-aged highlands, the Lunae Planum region shows

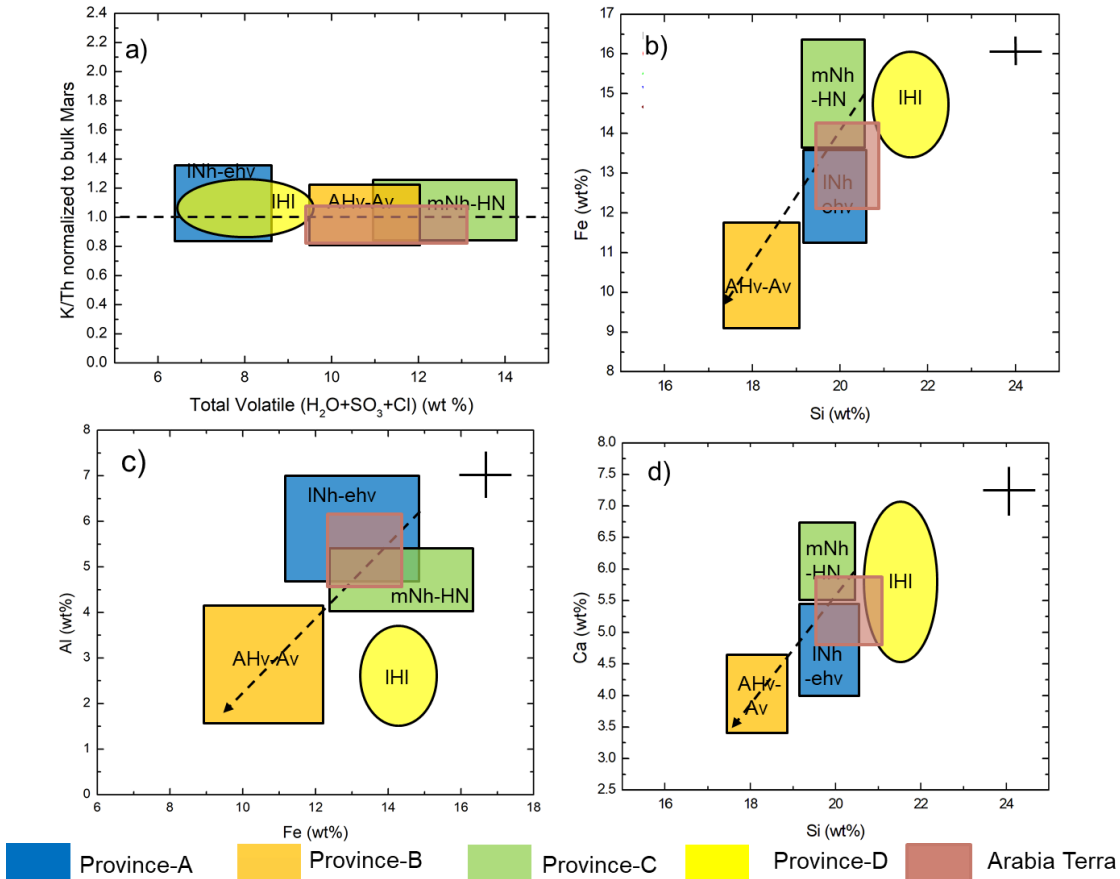


Figure 3.9: (a) Diagram of K/Th normalized to the bulk silicate Mars (~ 5300) versus GRS derived total volatile concentration. The modest variation in K/Th , which is consistent with the bulk Mars, implies low or no alteration at decimeter depths in the Noachian age Arabia Terra and consolidated provinces. The scatter values of Fe versus Si (b), Al versus Fe (c), and Ca versus Si (d) of the Arabia Terra and provinces A-D are represented by colored boxes (southern highland provinces A-C and Arabia Terra) and ellipse (northern lowland Province-D). The regional uncertainty is shown at the right corner of each plot, represented by the average of the standard error of mean (1σ) from all provinces and Arabia Terra (Table 3.5). From Noachian to Amazonian, all the three plots (b-d) exhibit a compositional trend, marked by a dashed arrow, except Province-D (Figure 3.12b-d). The prefix “N” indicates Noachian, “H” indicates Hesperian and “A” indicates Amazonian, and the suffix “v” indicates associated volcanic units, “h” indicates highland, “m” indicates middle and “IHI” indicates late Hesperian lowland.

compositional links – and possibly shared provenance - with Province-A, much like Hesperia Planum, Syrtis Major, and part of Greater Thaumasia. The similarity of Province-C's K/Th trend with the average crust and enrichment of volatiles (especially S and Cl) supports mostly regional volcanic materials (e.g., ashfall pyroclastic deposits), especially for the Medusae Fossae Formation, despite volatiles' enrichment. In contrast to provinces A-C, Southern Acidalia Planitia of Province-D in the northern lowlands is lithologically distinct with the highest abundance of K and Th of the provinces. However, the similarity of K/Th and depletion of Al relative to the average crust argues against sedimentary signatures of putative paleo-ocean(s). The northern lowlands may mostly represent the mafic crust of Mars, which might have originated from a low degree of partial melting at high pressure as suggested by high abundances of incompatible elements (K, Th) and Al- depletion rather than the conventional thought that the northern lowlands are highly fractionated. Our geochemical investigation shows that Arabia Terra has a coherent compositional signature and uniformity in mapped geology. Regardless of how heavily dust is mantled over Arabia Terra, the compositional variations follow a chemical trend identical to other dust-free or mildly dust-covered regions like Province-A and Province-C of similar age. Therefore, Arabia Terra represents a primary igneous composition. These findings demonstrate the overall utility of the integrative multivariate methodology that we have developed for Martian geochemical data, motivating possible applications to other planetary bodies (e.g., Mercury, Moon, and Vesta) with comparable datasets.

Chapter 4 Noachian volcanism and its implication for thermo-chemical evolution of early Mars

4.1 Introduction

Since last four-decades planetary space missions to Mars starting from the Mariner 9 mission in 1972 till the present show that Mars (the red planet) has been volcanically active throughout its history, starting from Noachian (>3.6 Ga) to Late Amazonian (<150 Ma) (Robbins et al., 2011). The temporal evolution of Martian volcanism or volcanic activity has played a significant role in the crustal and mantle evolution of Mars. Partial melting of the planetary interiors led to the formation of melts whose composition is related to the source mantle composition and the ambient pressure-temperature conditions of melting. When such melts reach the surface, in the form of lava, the solidified melts provide us the possibility of using the surface composition to infer degrees and depths of melting at the mantle source as functions of time. Mars is geologically active. However, unlike Earth, the absence of plate tectonism and the weathering and erosional activities are less prominent, which results in good preservation of its early geological surficial features. Preservation of the earlier records further enables us to explore the early thermal evolution of the Martian mantle. Furthermore, the link between magma chemistry and mantle thermal state has been used to rationalize certain compositional variations in Martian magmatism. Martian volcanism has been studied extensively, morphologically, morphometrically (Xiao et al., 2012), and compositionally (El Maarry *et al.*, 2009; Baratoux et al., 2011; Baratoux et al., 2013; Grott et al., 2013). Earlier studies probed the magmatic evolution of Mars in Hesperian (3.6 Ga-3.0 Ga) and Amazonian (<3.0 Ga) timescales (Baratoux et al.,

2011). Based on gamma-ray observations, the surface volcanic units reveal that there has been a composition transition from Hesperian SiO₂ (44–47 wt %) to Amazonian SiO₂ (41–44 wt %). The variation was also seen in FeO content from the Hesperian to the Amazonian (Baratoux et al., 2011). Based on the chemical variation of surface volcanic provinces, an independent line of evidence has been proposed to constrain the thermal evolution of the Martian mantle during the Hesperian to Amazonian (Baratoux et al., 2011). This geochemical investigation infers an ~ 80 K drop in mantle temperature with a ~ 50-kilometer increase in the thickness of the lithosphere over this period.

Although extensive magmatism and volcanism are expected in the early stage of Martian crust formation (Greeley and Schneid, 1991; Nimmo and Tanaka, 2005; Breuer and Spohn, 2006; Grott *et al.*, 2007; Kronberg *et al.*, 2007; Morschhauser, Grott, and Breuer, 2011), the Noachian-aged volcanic chemistry is not yet well understood despite being a significant source of data for early Martian geologic studies (Greeley and Spudis, 1981; Tanaka et al., 1991). Low shield highland paterae and ridged planes are characteristics of Noachian volcanic features (Neukum et al., 2010; Werner, 2009). However, persistent erosion and resurfacing could have caused substantial geological changes that make a thorough examination of Noachian volcanism difficult (Scott and Tanaka, 1981). Previous studies demarcated prominent, isolated positive relief volcanic constructs in the southern highland regions, spatially adjacent to Tharsis and circum-Hellas volcanic provinces (Xiao et al., 2012). Morphological, and stratigraphic studies of these isolated volcanic constructs (>3.8 Ga) were classified into three groups based on their stages of degradation and morphological similarities to terrestrial shield volcanos (Xiao et al., 2012). However, earlier thermochemical investigation at the early stage of Mars is limited by the less constrained composition of the Noachian period.

The newly discovered Noachian-age large volcanic province of Arabia Terra (Chu et al., 2021; Michalski and Bleacher, 2013; Rani et al., 2021; Whelley et al., 2021) help us to quantify the chemical composition of the Noachian-aged volcanic

province. We use orbital datasets, which provide a significant elemental composition at the scale of the gamma-ray data resolution (Chapter 3 for more details). In addition, we also consider two other late Noachian-aged volcanic regions, Solis (N1) and Argyre (N2) that lie in the southern part of Tharsis province and show volcanic lava flow signatures (Tanaka et al., 2014). Noachian-aged volcanic provinces (N1 & N2) lie south of Valles Marineris called Thaumasia Planum and the Eastern part of Terra Sirenum, respectively. The N1 region overlaps with the chemical province 70 of Karunatillake et al. (2009) and Hood et al. (2016), whereas N2, a small exposure of the Noachian volcanic province, lies a little far southwest of the N1 region (Figure 4.1). In this study, we use the mapped geologic units by Tanaka et al. (2014) to delineate the N1 and N2 spatial extent and quantify their regional geological distribution. The volcanic regions N1 and N2, comprise mainly (~ 80-90%) late Noachian volcanic (INv) units with a little amalgamation of Amazonian-Hesperian transition units. These regions (N1 and N2) are composed of lava flows from the Noachian period that has well-preserved calderas and shield volcanic constructs (Dohm and Tanaka, 1999; Xiao et al., 2012). In contrast, Arabia Terra lacks lava flow and shield calderas (Michalski and Bleacher, 2013).

The geochemical and petrologic analysis of Noachian-aged volcanic provinces in Solis (N1), Argyre (N2), and the newly discovered volcanic province Arabia Terra (Tanaka et al., 2014) (Figure 4.1) help us to understand the internal thermal condition and *vis-à-vis* early dynamics of Martian magmatic processes such as magmatic differentiation, degree, and depth of melting in the Noachian age. We compare our results from Noachian rocks at the in-situ landing sites (Gale, Gusev, Meridiani Planum, etc.; adapted from Filiberto *et al.*, 2012; Treiman and Filiberto, 2015) to investigate the variations of magmatic processes in the early Mars. At those landing sites, Martian rovers, Spirit, Opportunity, and Curiosity analyzed the surface basalts at different geographical locations on Mars.

This study aims to develop a perspective of spatiotemporal changes in thermochemical conditions in the interior of Mars. For that, we study here the internal thermal conditions and magmatic processes viz., magmatic differentiation, mantle melting, and crystallization during Noachian through the geochemical investigation of Arabia Terra and other Noachian-aged volcanic provinces. The study of various types and styles of Noachian-aged volcanism intends to infer the thermal evolution and formation of the Martian crust at its early stage. Furthermore, this study attempts to subsequently establish a link to infer the geochemical evolution of Mars from Noachian time.

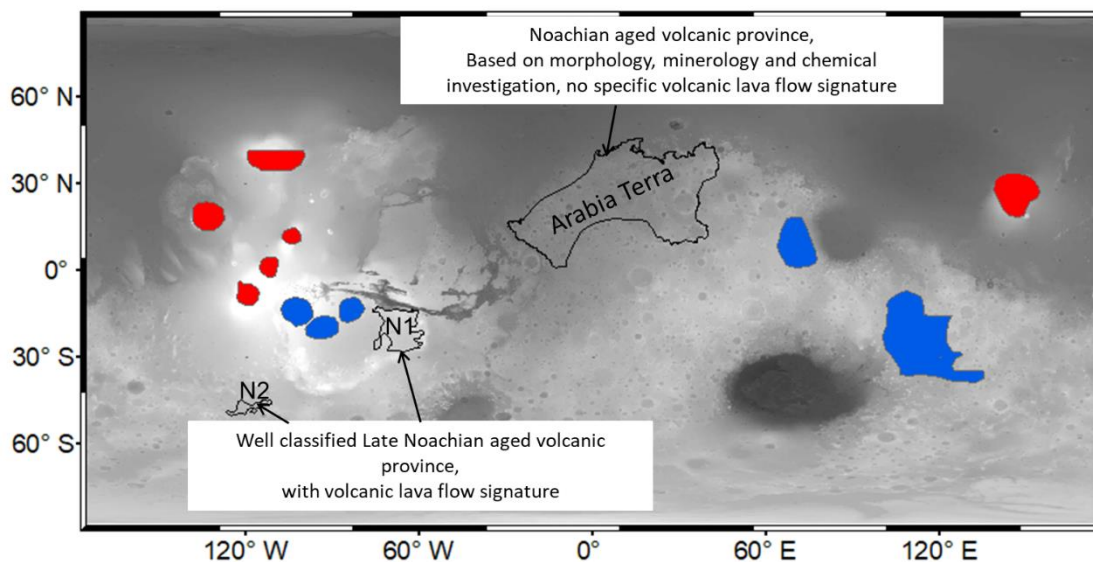


Figure 4.1: Noachian to Amazonian age volcanic provinces are represented over MOLA-HRSC topographic map. Studied Noachian regions are outlined in black, whereas Hesperian volcanic provinces, located in the highlands south of the hemispheric dichotomy, are highlighted in blue and Amazonian provinces occurring as large shield volcanoes are highlighted in red adapted after Baratoux et al., 2011.

4.2 Data and methods

4.2.1 Bulk composition

The bulk composition of the study regions is derived from the latest elemental mass fraction maps using Nuclear Spectroscopy data onboard Mars Odyssey 2001 (Boynton et al., 2007). Five-degree resolution maps were released for the elements, Al, Ca, Fe, Si, K, Th, H₂O, Cl, and S with the first tens of centimetres penetration ability of GRS below the surface (Boynton et al., 2007). This work includes all major rock-forming elements as we are interested in assessing the geochemical nature of primary rocks derived from their respective mantle-forming Noachian age volcanic surface. Please refer to **section 3.2** for a detailed description of GRS data and their working.

This work also includes previously published chemical analyses of shergottite meteorites (Lodders, 1998; Filiberto *et al.*, 2012; Treiman and Filiberto, 2015) and in situ analyses of the landing sites basalts. Alpha Proton X-ray Spectrometer (APXS) based in-situ rock analyses at Gusev Crater, Meridiani Planum (Filiberto et al., 2011), and Gale Crater are chosen including MSL Curiosity ChemCam analysis (Wiens *et al.*, 2012; Filiberto and Dasgupta, 2015). In order to eliminate uncertainty in any given analysis and to provide a comprehensive thermal evolution of the Noachian period, in situ analyses of basalts and surface volcanics of comparable ages are compared.

4.2.2 Model melting/crystallization simulation

For magma formation and crystallization simulation, MELTS algorithm is one of the most widely used programs in the Martian, lunar and terrestrial settings (Ghiorso et al., 2002). MELTS algorithm is capable of simulating compositions and mineral phases of basaltic melt crystallization (Balta and McSween, 2013a). pMELTS is an advanced version of MELTS. pMELTS allows higher pressure (1-3 GPa) regimes based on the thermodynamic properties of the system. We choose pMELTS over the standard MELTS, because of our focus on peridotite compositions at pressures above 1 GPa.

The previous works (cf. El Maarry et al., 2009; Baratoux et al., 2011, 2013; Filiberto, 2017) also ensure consistency of pMELTS uses for investigating the petrology of the Fe-rich Martian mantle. Furthermore, pMELTS simulations show higher accuracy compared to MELTS at high pressure (Balta and McSween, 2013a; Basu Sarbadhikari et al., 2016, 2017).

4.2.2.1 Estimation of pressure (P) and temperature (T)

We applied the following method to estimate the pressure (P) and Temperature (T) conditions of Noachian-aged regions. First, we used pMELTS algorithm (Ghiorso et al., 2002) to estimate the formation depth, degree of melting, mantle potential temperature, and associated mantle heat flow. In the present study, the composition of the primary melt along with its probable crystallization sequence is calculated for varying degrees of partial melting. The thermal evolution of the mantle and associated changes in the degree of partial melting of magma formation are deduced by using isobaric curves in P-T space.

Since Mars lacks plate tectonic activity, a simple model magma evolution, e.g., batch melting-based calculation is considered. Batch melting simulates a closed system and considers a melting condition in which the melt is in equilibrium with the solid residue throughout the melting process. As the pMELTS simulation (Ghiorso et al., 2002) is not optimized for Fe-rich mantle, the simulations result in an overestimation of orthopyroxene stability (Hirschmann *et al.*, 1998). However, the model melting/crystallization calculations are performed with pMELTS and all the pMELTS calculations are further corrected for the iron-rich composition of the primitive mantle of Mars (Dreibus and Wänke, 1985). To account for the iron-rich source in the Martian mantle, this offset correction is applied to the liquid compositions derived from pMELTS. We also did technical advancement from the earlier work (El Maarry et al., 2009) by including a greater number of elemental oxides to constrain the P-T condition.

The predicted mantle composition of Bulk Silicate Mars (primitive/undifferentiated Martian mantle composition) is adopted from Taylor (2013) (modified after Dreibus and Wänke, 1985) (Table 4.1) in this work to encompass the potential thermal condition of the Noachian period. The compositions of liquid in equilibrium with the mantle at the base of the lithosphere are computed under various P-T conditions to account for potential differences in the thermal condition among the Noachian-aged volcanic provinces. We perform simulations with isobaric pressures ranging from 1.0 to 3.0 GPa at intervals of 0.2 GPa and temperatures varying from 1000 to 2000 °C with 1 °C intervals. We take into account liquid compositions in the oxide form of elements (such as SiO₂, FeO, MgO, Al₂O₃, and K₂O) to obtain an estimation of the magma source conditions. Afterward, we compare the pMELTS-derived and published experimental values at 15 kbar (Bertka and Holloway, 1994) to determine the offsets corresponding to each oxide. This offset correction is applied to each pMELTS-derived liquid (Bertka and Holloway, 1994) composition. The small temperature increments provide enough resolution to select liquid compositions as a function of partial melting at melt fractions of 3%, 5%, 10%, 20%, 30%, 40%, and 50%. These intervals of partial melting allow the plotting of oxide compositions for each pressure interval.

In pMELTS simulation, we consider the magma sources at various nominally hydrous conditions (0-185 ppm) (Dreibus and Wanke, 1987; Taylor, 2013) to check how the H₂O concentration can affect the solidus and viscosity of melt resulting from flux melting (Grott *et al.*, 2013), and affecting the melt compositions. In each of the fixed P-T regimes, we run the model calculations at various nominally hydrous conditions (e.g., 39 ppm: Dreibus and Wanke, 1987; 185 ppm, an average from range 150-220 ppm: Taylor, 2013). This range can be correlated with the hydrous conditions reported by previous works for the Martian mantle using the Martian meteorites studies (cf. Le Bas *et al.*, 1986; McSween *et al.*, 2006; McSween, Taylor and Wyatt, 2009; Sautter *et al.*, 2015b).

Table 4.1: Bulk silicate Mars composition (BSM) after Taylor (2013). Updated after the DW85 composition (defined by Dreibus and Wanke, 1985). This composition is used as parental magma composition for p-MELTS thermodynamic simulations.

Oxides (wt%)	BSM
SiO ₂	43.7±1.0
TiO ₂	0.14±0.01
Al ₂ O ₃	3.0±0.1
FeO	18.1±1.0
CaO	2.43±0.01
MgO	30.50±0.05
MnO	0.44±0.06
Na ₂ O	0.5±0.1
K ₂ O	0.040±0.002
P ₂ O ₅	0.15±0.05
Cr ₂ O ₃	0.73±0.04

Another critical input for the pMELTS program is the reaction pathway for the oxygen buffer. Generally, we can constrain the oxygen fugacity of a system as a function of temperature from the specific assemblage of minerals. Different pathways are used for rocks with different assemblages of minerals containing elements of various oxidation states. Based on the study of basaltic shergottite meteorites, Ghosal et al., (1998) suggested oxygen fugacity as -3 log units below the Fayalite–Magnetite–Quartz (FMQ) buffer and assume compositions contain this buffer assemblage. FMQ-3 was found to be optimal for Martian basalts (Ghosal et al., 1998), which we used in this study.

4.2.2.2 Estimation of mantle potential temperature

The estimated pressure, temperature, and degree of partial melt are used to further constrain the mantle potential temperature (T_p) of melts and its possible evolution. The following formula is used to calculate the mantle potential temperature (T_p):

$$T_p = T_{avg_eq} + T_f - T_g \quad (4.1)$$

where, T_{avg_eq} is average temperature derived from pMELTS corresponding to estimated pressure and degree of partial melt for melt composition; T_f is the latent heat of fusion; and T_g is the Martian temperature gradient correction for adiabatic cooling.

In addition, we also corrected the effect of latent heat of fusion on the temperature using the expression as follows:

$$T_f = F \left(\frac{H_f}{C_p} \right) \quad (4.2)$$

where F is the degree of partial melt; H_{fus} ($6.4 \times 10^5 \text{ J K}^{-1}\text{kg}^{-1}$) is the heat of fusion (Kiefer, 2003), and C_p ($1200 \text{ J K}^{-1}\text{kg}^{-1}$) (Kiefer, 2003; Filiberto and Dasgupta, 2015) is the heat capacity at a constant pressure.

4.2.2.3 Estimation of surface heat flow

The thermal boundary layer structure of a terrestrial body mainly comprises two parts; in the upper part (crust and upper mantle), heat is transported by conduction while convection dominates in the lower part (lower mantle), also called the convective boundary layer. The surface heat flow upper limits are calculated by including heat-producing elements (HPE) in the crust and the mantle lithosphere, whereas lower limits are obtained by using zero lithospheric heat sources (steady state). The significant homogeneity of elemental abundances measured by Mars Odyssey GRS suggests that

the martian crust is much less geochemically varied than the Earth's crust (Taylor et al., 2006), which is consistent with a strong mixing by cratering (e.g. Taylor et al., 2006), and with the absence of large-scale crustal recycling, at least since the early part of the history of Mars (e.g., Frey, 2006). Therefore the equation for heat flow from HPE in the crust is given:

$$T_z = T_s + \frac{Qz}{k_c} - \frac{\rho_c H_c z^2}{2k_c} \text{ --- --- (4.3)}$$

where T_s is the surface temperature, Q is the surface heat flow, k_c is the thermal conductivity of the crust, ρ_c is the density of the crust, and H_c is the crustal heat production rate per unit mass. We use a surface temperature of 220 K, the present-day mean surface temperature on Mars (Kieffer et al., 1977), which is consistent with the inference of low near-surface temperatures deduced for most of the past 4 Ga from ALH84001 thermochronology (Shuster and Weiss, 2005). Considering the persisting uncertainty in the Martian thermal boundary layer structure and its rheological properties, we have taken a simplistic case where we calculate the heat flow assuming a constant thermal conductivity of crust, $k_{crust} \sim 3.0 \text{ W m}^{-1} \text{ K}^{-1}$ (Ruiz, 2014; Parro et al., 2017). We calculate the amount of radioactive heat generated by prime radioactive ^{40}K , ^{232}Th , ^{235}U , and ^{238}U elements. We use the following formula:

$$Q_r = \sum_{i=1}^4 C_i Q_i \exp\left[\frac{\ln(2)t}{\tau_{1/2}^i}\right] \text{ --- --- (4.4)}$$

where i refers to each of four long-lived isotopes, C_i is element concentration multiplied by isotope fractional abundance at the present day, Q_i heating rate, the half-life, and t time. U is calculated using Agee et al., 2013 Black beauty ratios on the Martian surface. We have used Black beauty NWA 7034 for reference because it is remarkably similar to the geochemistry of the rocks and soils at Gusev Crater and the average Martian crust composition from the Odyssey Orbiter GRS (Cartwright et al., 2014).

4.3 Results

4.3.1 Compositional variability among Noachian-aged volcanic provinces

The compositional variability among Noachian provinces: Arabia Terra, N1, and N2 with respect to average Martian crust are shown by modified box-whisker plots (Figure 4.2). Both Noachian provinces N1 & N2 are compositionally similar with a few variations, they are enriched in Al and depleted in Ca, volatiles (H₂O, Cl), K & Th. Thorium is more depleted as compared to K; therefore K/Th ratio is high. However, it is not significantly depleted up to 1 sigma deviation from the average Martian crust. Arabia Terra is little enriched in Th relative to K, resulting in depletion of the K/Th ratio. Moreover, Fe/Si ratio is consistent in all three Noachian provinces. The mean oxide mass fraction and its corresponding standard error of Noachian volcanic provinces with the Average Martian crust (AMC) are derived from nuclear spectroscopy (Table 4.2).

4.3.2 Calculation of Non-GRS elemental composition

It is noteworthy to mention that the non-GRS elements like Mg, Na, Ti, P, and Mn are needed to be calculated to provide inputs to the model melting and crystallization simulations. The oxides of these non-GRS elements account for more or less ~ 15 wt% of basaltic rock. Magnesium is one major rock-forming element, on which the model melting and crystallization calculations, which are based on thermodynamic data of melt and various solid phases, are heavily dependent. The other four elements more-or-less behave like incompatible elements during the magmatic processes (e.g., partial melting and fractional crystallization). In an earlier study, Baratoux et al (2014) have shown that the ratios P₂O₅/K₂O, Na₂O/TiO₂, MnO/FeO, and TiO₂/P₂O₅ are approximately constant in the basaltic shergottites. In that study, the surface abundances of Na₂O, TiO₂, P₂O₅, and MnO were estimated using the average values of these ratios in the basaltic shergottites. The ratios were measured sequentially

starting from the one P_2O_5/K_2O , in which one GRS-derived element K is there (Baratoux et al., 2014). We follow the same protocol to calculate the non-GRS elements Na, Ti, P, and Mn. However, it has been shown that the alkali content in shergottites is reasonably lower than that in the average Martian surface, and therefore, shergottites may not be the true representative of the surface composition (McSween, Taylor and Wyatt, 2009). Also, in Baratoux et al (2014), the derived elemental ratios from shergottites are distinct from Gusev surface basalts, which implies the Martian shergottite meteorites represent a biased sampling of the Martian surface with unknown ejection locations.

Table 4.2: Arithmetic mean of stoichiometric oxide mass fraction as a percentage (wt%, if not mentioned otherwise), and its corresponding standard error (GRS derived) of the Noachian Volcanic provinces with mid-latitudinal Average Martian Crust (AMC).

Oxide	Noachian N1	Noachian N2	Arabia Terra	Average Martian Crust (AMC)
SiO ₂	43.4±2.0	43.1±2.0	43.5±1.0	43.0±2.0
FeO	16.7±0.8	15.8±0.8	17.0±0.9	16.3±0.9
CaO	6.2±1.0	5.5±1.0	7.9±0.3	7.0±1.0
Al ₂ O ₃	11.4±2.0	11.7±2.0	9.4±0.7	8.5±2.0
K ₂ O	0.35±0.01	0.41±0.01	0.49±0.02	0.43±0.07
Th mg/kg	0.47±0.04	0.55±0.03	0.75±0.02	0.61±0.02
H ₂ O	2.8±0.4	2.4±0.3	5.0±0.5	3.90±0.7
SO ₃	5.2±0.4	4.6±0.5	6.1±0.3	5.4±0.7
Cl	0.40±0.02	0.39±0.02	0.52±0.02	0.47±0.08

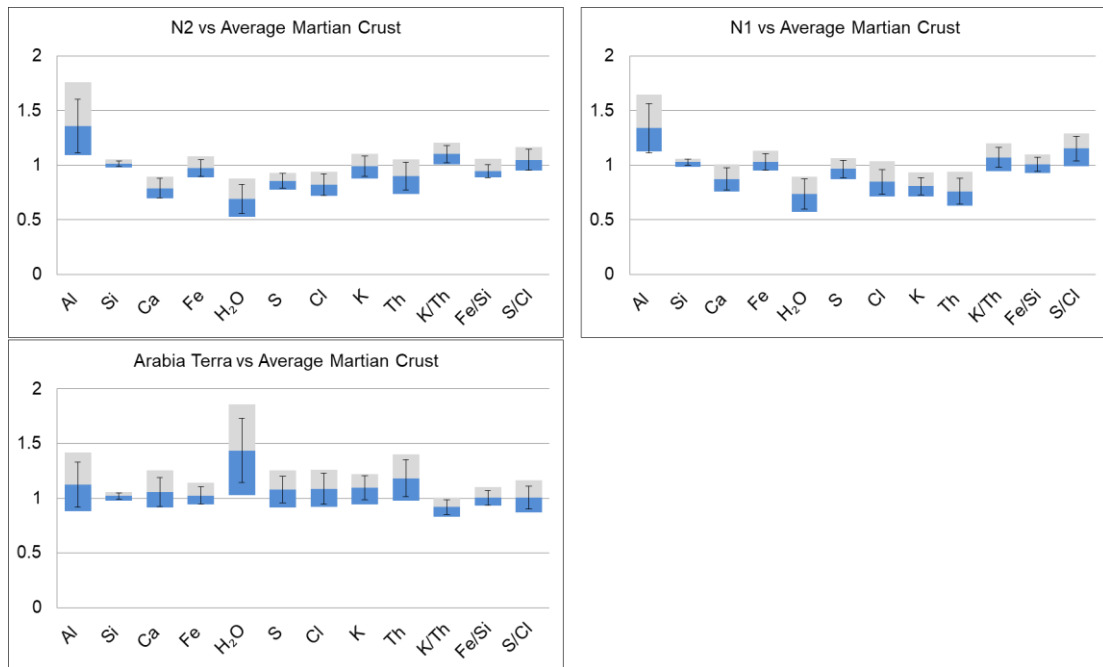


Figure 4.2: Compositional variability among Noachian provinces w.r.t average Martian crust. Modified box-whiskers diagram to compare the distribution of elements for all provinces to the global geochemistry of the average Martian crust. The top of the upper box represents 75th percentile/25th percentile ratio, the bottom of the lower box represents the 25th/75th percentile ratio, and the ratio of the medians by the boundary between them. The whiskers here represent the uncertainty on the ratio of medians using the Median Absolute Deviation (MAD) (Karunatillake et al., 2011).

Therefore, rather than using the group of basaltic shergottites, we consider the newly found Martian meteorite breccia NWA 7034/7533/7475 (Black Beauty; Agee et al., 2013; Humayun et al. 2013) for calculating the ratios P_2O_5/K_2O , Na_2O/TiO_2 , MnO/FeO , and TiO_2/P_2O_5 as they are remarkably similar to the geochemistry of the rocks and soils at Gusev crater and the average Martian crust composition from the Odyssey Orbiter GRS. Unlike other SNC meteorites, Black Beauty has higher concentrations of alkali elements (Na and K) similar to Gusev rocks and GRS average Martian crust. In addition, other major and minor elemental ratios, such as Mg/Si, Al/Si, and Ni/Mg, complement Black Beauty with Gusev crater rocks. Moreover, the bulk chemistry of Black Beauty is strikingly similar to the data collected from the Martian

surface by orbiter and lander data, which allows for a direct link between this Martian meteorite and data from spacecraft from Mars, unlike other SNC meteorites. Therefore, Black Beauty best represents the Martian crust (Agee et al., 2013) in the Noachian age (Humayun et al., 2013) and can be used to calculate other non-nuclear spectroscopy elements, using P_2O_5/K_2O , Na_2O/TiO_2 , MnO/FeO , and TiO_2/P_2O_5 ratios, where K_2O and FeO are derived from GRS. The average values of these ratios and their standard deviations for Black Beauty meteorites are given in Table 4.3. Finally, we calculate the concentration of MgO at the surface of Mars by the difference between GRS-derived chemical composition and the elemental ratio-derived compositions for the oxides: Na_2O , TiO_2 , P_2O_5 , and MnO , assuming a 100% sum for all major element oxides. Our Mg calculation for the study regions satisfies the $Mg\#$ ($Mg\# = 100 * (MgO / (MgO + FeO))$) values proposed by Baratoux et al. (2014).

Table 4.3: Ratios of incompatible elements in Black Beauty

Ratio	Na_2O/TiO_2	TiO_2/P_2O_5	MnO/FeO	P_2O_5/K_2O
Our study using Black Beauty	3.021 ± 1.02	0.909 ± 0.4	0.021 ± 0.001	3.05 ± 1.00
Baratoux et al., 2014^a	1.374 ± 0.337	1.151 ± 0.265	0.025 ± 0.001	4.297 ± 0.939
Other studies	1.55^b	1.17^c	0.0256^d	

^a Baratoux et al. [2014], ^bTreiman *et al.*, [1986], ^cTreiman, [2003] and ^dDreibus and Wanke [1985].

Table 4.4: a) Arithmetic mean of stoichiometric oxide mass fraction as a percentage (wt%, if not mentioned otherwise), of the Noachian volcanic provinces without normalization with respect to volatiles. We consider all volatiles in the calculation of MgO values. Non-GRS oxides are estimated using ratios of incompatible elements in Black Beauty given in Table 4.3.

Oxides/ Study Provinces	N1	N2	Arabia Terra
SiO ₂	43.4	43.1	43.5
TiO ₂	0.97	1.13	1.26
Al ₂ O ₃	11.4	11.7	9.4
FeO	16.7	15.8	17.0
MnO	0.33	0.32	0.34
MgO	11.4	12.5	7.4
CaO	6.2	5.5	7.5
Na ₂ O	2.9	3.4	3.8
K ₂ O	0.35	0.41	0.46
P ₂ O ₅	1.1	1.2	1.4
H ₂ O	2.8	2.6	5.1
S	2.1	1.8	2.3
Cl	0.4	0.4	0.5
Th ppm	0.47	0.54	0.71
Total	100	100	100
Mg#	54	59	44

Table 4.4: b) Arithmetic mean of stoichiometric oxide mass fraction as a percentage (wt%, if not mentioned otherwise), of the Noachian volcanic provinces normalized with respect to volatiles. We consider all volatiles in the calculation of MgO values. Non-GRS oxides are estimated using ratios of incompatible elements in Black Beauty given in Table 4.3.

Oxides/ Study Provinces	N1	N2	Arabia Terra
SiO ₂	45.5	45.0	47.3
TiO ₂	1.01	1.18	1.36
Al ₂ O ₃	11.9	12.2	10.2
FeO	17.5	16.5	18.5
MnO	0.35	0.33	0.37
MgO	12.6	13.7	9.0
CaO	6.5	5.8	8.1
Na ₂ O	3.1	3.6	4.1
K ₂ O	0.37	0.43	0.49
P ₂ O ₅	1.1	1.29	1.5
Th ppm	0.47	0.54	0.71
Total	100	100	100
Mg#	56	60	46

4.3.3 Primary vs. secondary processes

To gain further insight into the chemical composition and regional chemical processes that prevailed in studied Noachian-aged provinces, we use K/Th fractionation, and two molar fraction-based ternary diagrams including the Chemical Index of Alteration ($CIA=100*[Al_2O_3/(Al_2O_3+CaO+Na_2O+K_2O)]$). Using ternary diagrams and CIA values we assess the evidence for aqueous-alteration activity of igneous rocks on the Martian surface.

Being the most incompatible elements, observed by GRS, K and Th (partition coefficient $\ll 1$; Borg and Draper, 2003) do not fractionate in the solid phases; consequently, the K/Th ratio represents the mantle source value. Thus K/Th ratio correlates strongly in igneous rocks. While the rocks undergo surficial alteration, K behaves like a mobile element and Th is less resistant to weathering, which leads to the change in K/Th ratio from the primary fractionation line. Figure 4.3a shows no significant deviation of K/Th ratio of Arabia Terra and N1 & N2 from the average Martian crust.

To understand the contribution of low pH aqueous alteration in observed geochemical anomalies in the study regions, we use a molar ternary diagram with apices (Al_2O_3) – ($CaO + Na_2O+K_2O$) – ($MgO + FeO$) denoted (A-CNK-MF) (Nesbitt and Wilson, 1992; Hurowitz and McLennan, 2007; Ming *et al.*, 2008) (Figure 4.3b). This ternary is traditionally used to provide qualitative insight into weathering trend of olivine-bearing basalts under aqueous alteration in both terrestrial and Martian conditions (Hurowitz and McLennan, 2007). According to Nesbitt and Wilson (1992) and Hurowitz and McLennan (2007), igneous rocks that have been altered in low-pH aqueous conditions tend to plot below the feldspar-olivine join and move away from the MF apex to a rock composition with more Al_2O_3 than in their original, unaltered conditions. Figure 4.3b depicts that our study areas are plotted beneath the olivine-

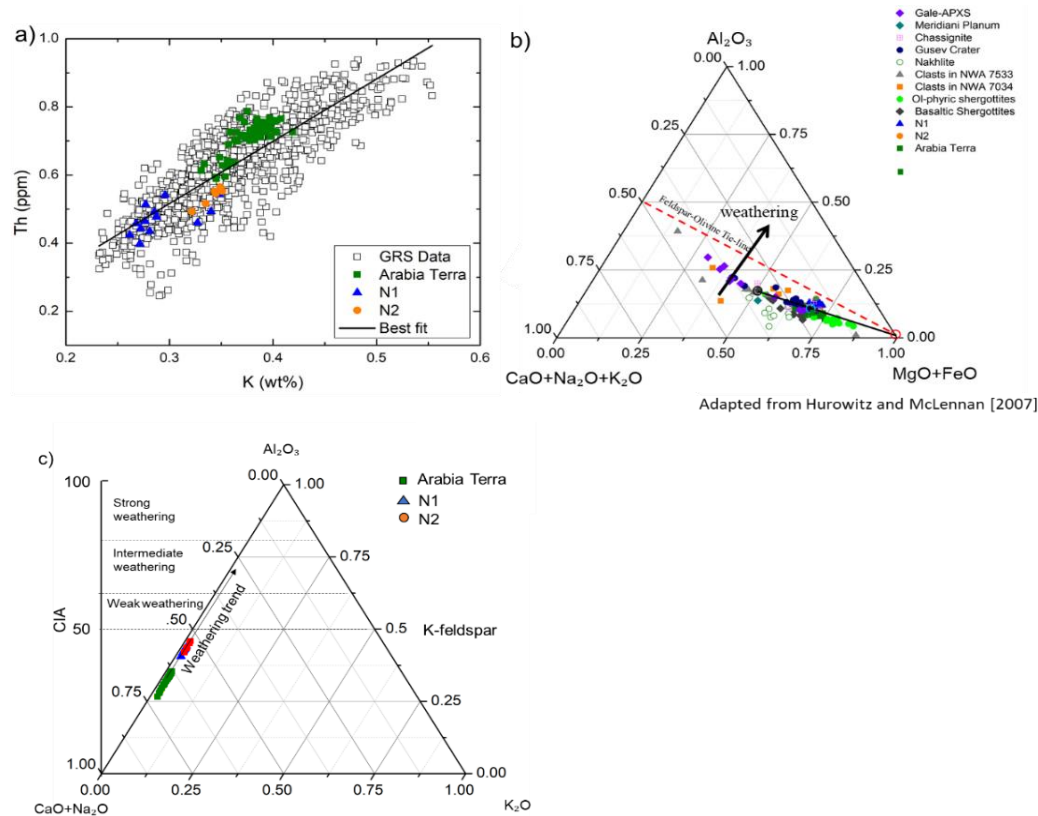


Figure 4.3: (a) K (wt. %) vs. Th (mg/kg) in several regions, Noachian age provinces N1, N2, Arabia Terra and average martian crust. (b) Ternary Diagram ($CaO + Na_2O + K_2O$)-(Al_2O_3)-($MgO + FeO$) (CNK-A-MF) is used to investigate low pH aqueous alteration signature in Noachian age provinces (adapted from Hurowitz and McLennan [2007]), the dashed red line represents the olivine-feldspar join. Compositions that plot below the line are considered to be igneous rocks that are not weathered under moderate pH conditions. The black solid line represents subaqueous alteration trends at low pH, similar to those observed on Mars (Hurowitz and McLennan, 2007). Basalts weathered under these conditions trend toward the CNK-A join (A) and alteration fluids toward the MF apex (F). (c) Extent of chemical weathering for Noachian age volcanic provinces are calculated using the Chemical Index of Alteration ($CIA = 100 * [Al_2O_3 / (Al_2O_3 + CaO + Na_2O + K_2O)]$). This diagram is used to assess the extent of chemical weathering in the provinces Arabia Terra, N1 and N2. For CIA, we are using standard molar abundances of oxides. Non-GRS Na_2O is calculated using Black Beauty.

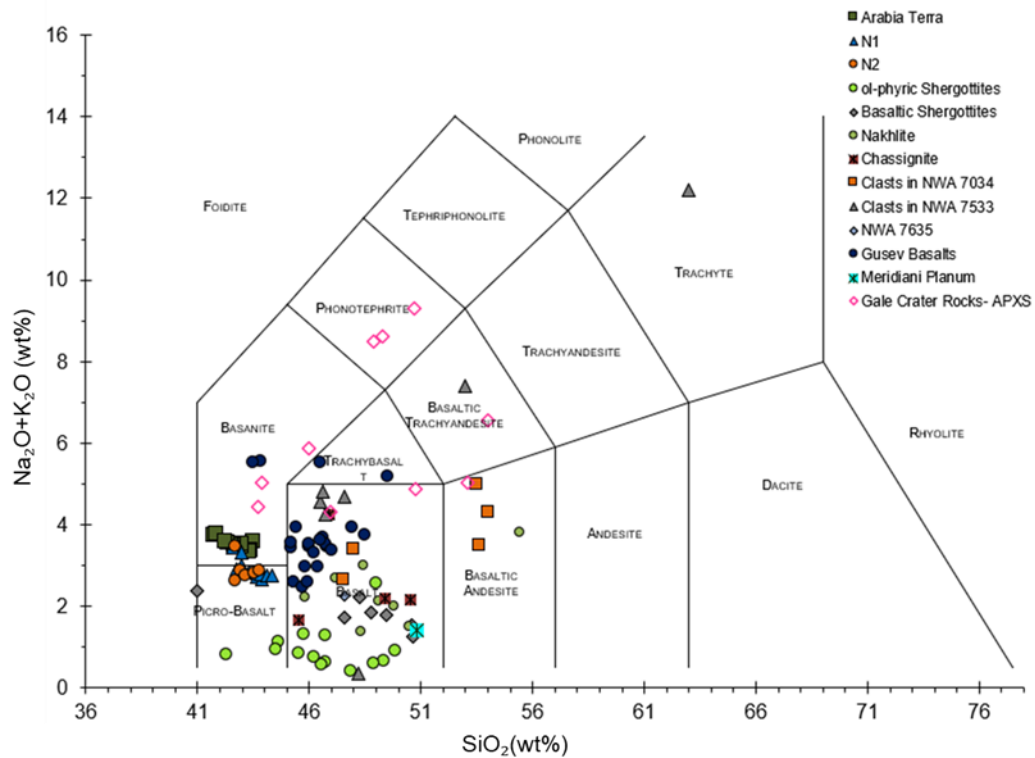


Figure 4.4: Classification of primary composition. This diagram is used to illustrate the Total alkalis (Na_2O and K_2O) vs. silica (TAS) classification scheme for volcanic rocks based on their bulk chemical composition (La Bas et al., 1986). Noachian aged surface volcanics of Arabia Terra, N1 and N2 from GRS measurements with calculated Na_2O from Black Beauty. Shergottites, Clasts in NWA 7034/7533, chassignite and nakhilites, in situ rover data of basalts from Gusev and Gale Crater with Bounce Rock at Meridiani Planum are shown in this diagram.

feldspar trend line and follow a similar trend of typical Martian basalts as the average Martian crust and Martian meteorites.

Furthermore, the extent of chemical weathering is assessed using the Chemical Index of Alteration (CIA). CIA is a method for calculating the chemical weathering of a sample based on the sensitivity of silicate minerals to chemical remobilization (Nesbitt and Young, 1982). Figure 4.3c demonstrates that the CIA value for the Arabia Terra region ranges between 30 and 35, while the CIA values for N1 and N2 are somewhat high, between 42 and 47.

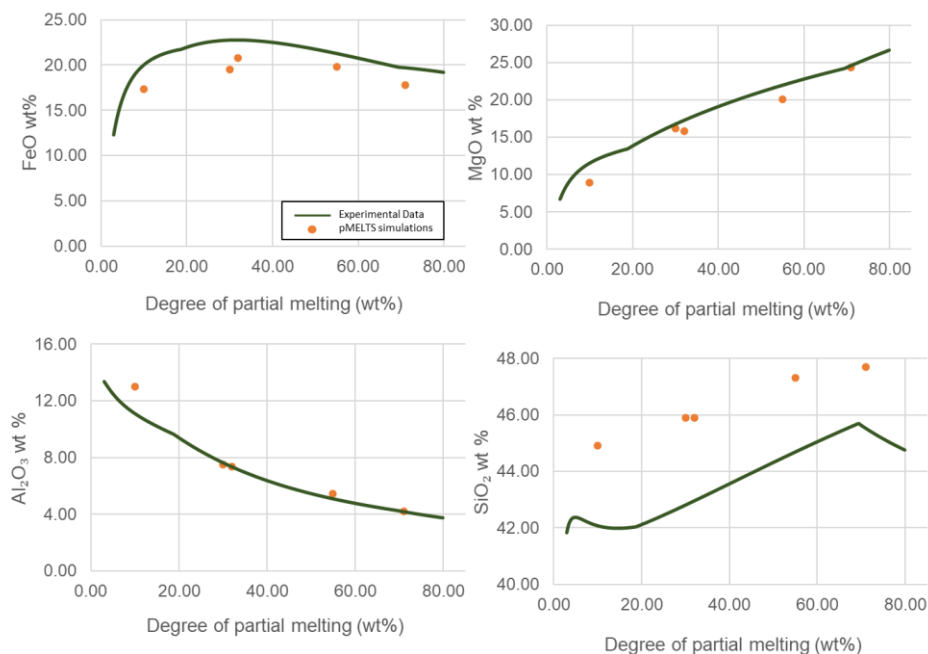
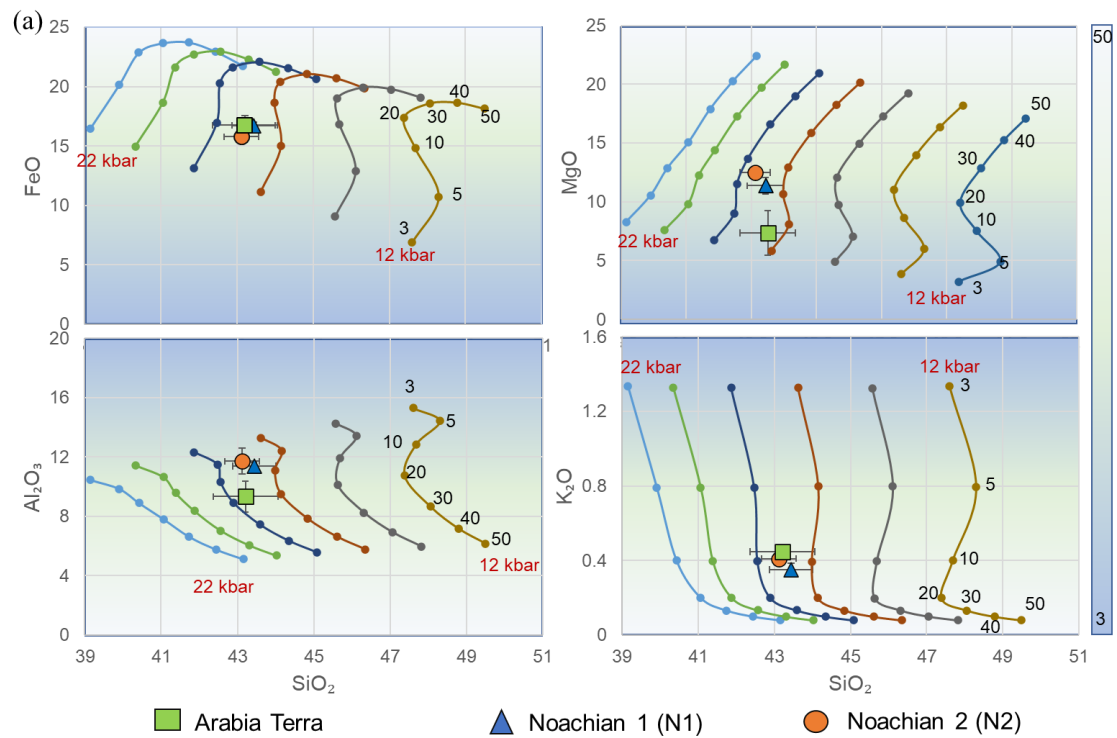


Figure 4.5: Comparison of mantle melting model by *p*-MELTS with experimental data of Bertka and Holloway (1994) at 15 kbar. Each line represents a series of compositions produced by the results from *p*MELTS for each pressure and temperature combination. Data points are connected with a solid line. Solid points (orange color circles) represent experimental data at 15 kbar (Bertka and Holloway, 1994). The oxide trends are compared to the experimental results for iron-rich parent compositions at 10, 30, 32, 55, and 71 percent melt fractions to identify systematic differences of *p*MELTS from laboratory conditions. The resulting offsets allow the comparison between the liquid oxide compositions from *p*MELTS and the oxide concentrations derived from the GRS data for the surface within the Volcanic Province.

As an essential part of compositional analysis, we used the total alkali-silica (TAS) diagram to classify the primary composition of study regions (Arabia Terra, N1 & N2). TAS was typically designed to classify terrestrial magma but it has been used frequently to classify Martian volcanic rocks and meteorites (cf. Le Bas et al., 1986; McSween *et al.*, 2006; McSween et al., 2009; Sautter *et al.*, 2015b). Previous work has shown that compositional comparisons can be made between remotely sensed and in situ data using a TAS diagram (McSween et al., 2009; Agee et al., 2013; Hood et al.,

2016). The GRS-derived bulk composition of Arabia Terra, N1 & N2 Noachian provinces are plotted in the TAS diagram showing the values in the ranges of 2.5-4 wt% (alkalis) and 43±3 wt% (SiO_2) (Figure 4.4). To compare the compositional variability of the Noachian age, similar age Martian basalt chemistry derived from rover study and meteorite data is also used in TAS diagram (Filiberto, 2017). The bulk composition in basaltic meteorites (olivine-phyric and basaltic shergottites) are quite limited: 45±5 wt% SiO_2 and <2.0 wt% total alkalis (McSween et al., 2009; Filiberto, 2017). The newly discovered regolith breccia NWA 7034 further expands the compositional range of Martian meteorites, 46.6 wt% SiO_2 and 3.6 wt% total alkalis (Agee et al., 2013; Humayun et al., 2013; Udry *et al.*, 2014; Santos *et al.*, 2015). Surface basaltic rocks at Gusev crater analyzed by MER Spirit, have a bulk silica content of 45±5 wt% and total alkali content (2–6 wt%). The rocks analyzed by Curiosity at Gale crater have a much wider range in both total alkalis and silica than the shergottites or the rocks at Gusev crater and Meridiani Planum.



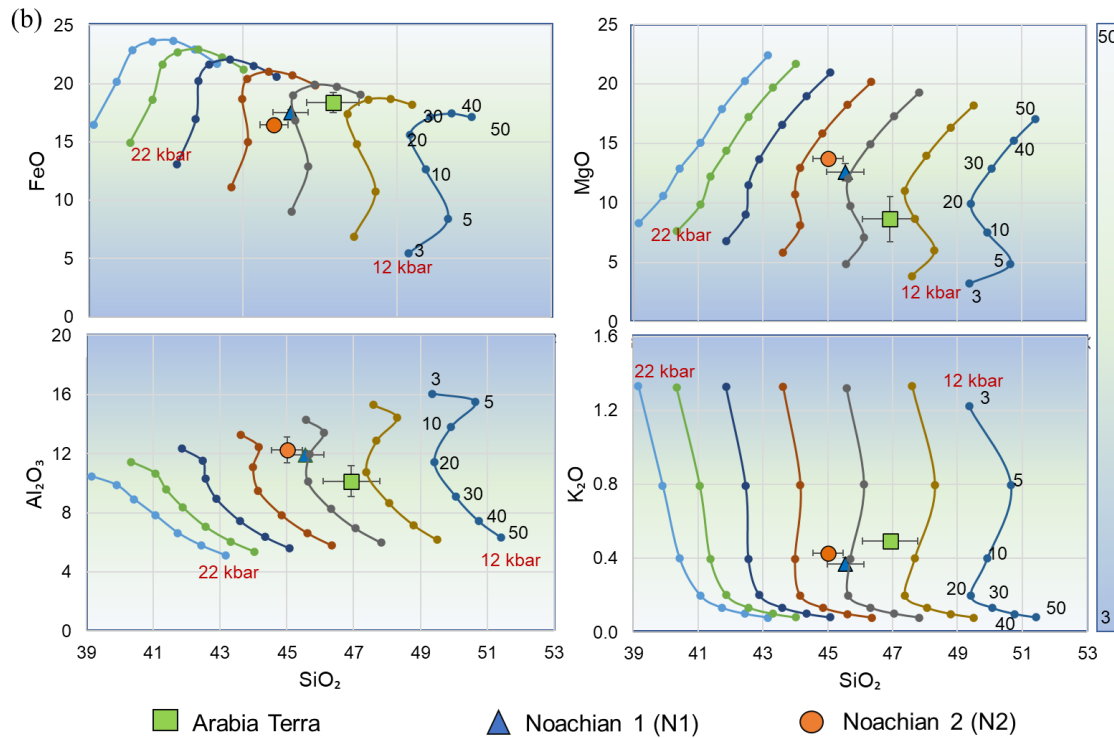


Figure 4.6: a) Geochemical modeling for magmatic evolution in Noachian aged Volcanic Provinces including all volatiles. b) Geochemical Modeling for magmatic evolution in Noachian aged Volcanic Provinces normalized with respect to all volatiles. Curves (SiO_2 vs FeO , SiO_2 vs MgO , SiO_2 vs K_2O , and SiO_2 vs Al_2O_3) in the oxide bivariate diagrams plots are based on the model calculations by pMELTS and represent isobaric lines with the pressure ranges between 1.2 GPa and 2.2 GPa at an increment of 0.2 GPa. The number (3, 5, 10, 20, 30, 40, 50) are degrees of partial melting for each isobaric curve. The color from dark blue to light blue in each plot represents increasing degree of partial melting.

4.3.4 Conditions of magma genesis

The model calculations of magmatic processes have been performed using pMELTS (Smith and Asimow, 2005). These simulations have been performed at 3-50 % of partial melts, with fixed oxygen fugacity QFM-3. This approach has been extensively used to model the partial melting of Fe-rich parent compositions of Mars

(El Maarry et al., 2009; Baratoux et al., 2011; Balta and McSween, 2013). The pMELTS model calculations follow a similar trend in oxide concentration as a function of melt fraction with a systematic offset relative to elemental oxide values from Bertka and Holloway (1994). This offset was attributed by Hirschmann et al. (1998) to excessive stability in the processing of the mineral orthopyroxene in the solid phase assemblage of the mantle. The offset correction approach is first employed by El Maarry et al. (2009) to adjust for the observed offset in the pMELTS calculations. El Maarry et al. (2009) first estimated the average offset from four oxides SiO_2 , FeO , CaO , and Al_2O_3 at 30 %, 32 %, and 55 % partial melting corresponding to 15 kbar pressure. In this present study, we advance this technique with the calculated offsets corresponding to the other four oxides viz. SiO_2 , FeO , MgO , and Al_2O_3 at 3 %, 10%, 30%, 32%, and 55% of partial melt (Figure 4.5, Table 4.4). The offsets have been calculated under various nominally hydrous conditions (0-185 ppm) of the mantle (Dreibus and Wanke, 1987; Taylor, 2013). These offset corrections corresponding to all oxides are further used in different isobaric conditions to make the Fe-rich Martian mantle composition compatible with this study.

4.3.4.1 Average formation *P-T*

The pMELTS algorithm is based on phase diagram calculation and uses an internally consistent thermodynamic data set (cf. Ghiorso et al. 2002; Asimow et al. 2005). The different liquid compositions derived from pMELTS simulations are represented in a series of elemental oxide variations using bivariate plots (Figures 4.6a-b) at different isobaric conditions as a function of the degree of partial melt. Various plots are SiO_2 vs FeO , SiO_2 vs MgO , SiO_2 vs K_2O , and SiO_2 vs Al_2O_3 . The variation in the liquid composition on these plots indicates the formation pressure condition and the degree of partial melting. The isobaric melt curves represent the function of the degree of partial melt in the range of 3-50%. These curves are corrected for the calculated offsets for each oxide, except K_2O because it lacks in the experimental works (cf. Bertka and Holloway, 1994). However, since K is a directly GRS-derived element, it has a very high signal-to-noise ratio. Therefore, we used it without offset correction,

which was done in previous studies too (Susko et al., 2017). These bivariate curves indicate that the silica content of liquids generally increases with an increasing degree of partial melting (from right to left). All these melt curves are used to determine the formation pressure of the study regions (Figures 4.6a-b).

To estimate the formation pressure and degree of partial melt for the composition corresponding to Noachian-aged volcanic provinces, Arabia Terra, N1, and N2, GRS-derived chemical data have been used corresponding to each bivariate plot of oxide pairs. The mantle melt pressure and degree of partial melting for the magma source beneath are represented by the overlapping average composition (Figures 4.6a-b). The average composition of Arabia Terra and pMELTS simulations suggests a pressure range from 1.3 GPa to 1.7 GPa with and without normalization of volatiles (Figures 4.6a-b, Tables 4.5a-c), whereas, N1 and N2 pressure range from 1.4 GPa to 1.7 GPa (Figure 4.6a-b, Tables 4.5a-c). However, the degree of partial melt (F) is not consistent for the various oxide pairs. Considering the homogenous mantle at the source region, incompatible Th in rock is inversely proportional to the degree of partial melt (Baratoux et al., 2011). Therefore, we have used Th inverse relationship to find the more appropriate degree of partial melting of the magma source. The ratio of average surficial Th concentration (GRS data) and Th concentration of BSM (Taylor, 2013, Table 4.3) is used to estimate the degree of partial melt. The degree of partial melt is ~8.1% in Arabia Terra, 12.3% in N1, and 10.8% in N2.

Similar formation P-T conditions have been estimated for surface basalts, NWA7034 clasts, and other Martian meteorites. The formation P-T conditions for the Gusev crater basalts are 1.2 ± 0.3 GPa pressure and 1415 ± 45 °C temperature (Filiberto and Dasgupta, 2011). The only basaltic rock at Meridiani Planum has a formation pressure of ~0.5 GPa and a temperature of ~1401 °C, which is lower compared to Gusev (Filiberto and Dasgupta, 2011). The magma genesis conditions for basalts at Gale crater are more complex compared to Gusev and Meridiani Planum. The average P-T conditions at which Gale basalts are produced are 1.6 ± 1 GPa and 1408 ± 140 °C (Filiberto and Dasgupta, 2015; Filiberto, 2017).

Table 4.5: a) Pressure (P), Temperature (T), degree of partial melt (F), depth of magma formation, and mantle potential temperature (T_p) are estimated for Arabia Terra, N1, and N2 Noachian provinces. The average composition derived from GRS corresponding to each study region includes the volatiles (H_2O , Cl, and S) in the calculation of Non-GRS MgO values.

Study Provinces	P (GPa)	F (%)	Density (Kg/m ³)	Depth (km) = $P/(g*\rho)$	Martian gradient	Average equilibrium temperature ($T^{\circ}C$)	Latent heat of fusion	T_p (mantle potential temperature) ($^{\circ}C$)
Arabia Terra	1.7	8.1	3083	149	26.8	1364	43.2	1380
N1	1.7	12.3	3065	149	26.8	1386	65.5	1425
N2	1.7	10.8	3045	150	27.0	1379	57.6	1410

Table 4.5: b) Pressure (P), Temperature (T), degree of partial melt (F), depth of magma formation, and mantle potential temperature (T_p) are estimated for Arabia Terra, N1, and N2 Noachian provinces. The average composition derived from GRS corresponding to each study region is Normalized with respect to volatiles (H_2O , Cl, and S) in the calculation of Non-GRS MgO values.

Study Provinces	P (GPa)	F (%)	Density (Kg/m ³)	Depth (km) = $P/(g*\rho)$	Martian gradient	Average equilibrium temperature ($T^{\circ}C$)	Latent heat of fusion	T_p (mantle potential temperature) ($^{\circ}C$)
Arabia Terra	1.3	8.1	3083	114	20.5	1317	43.2	1340
N1	1.4	12.3	3065	123	22.1	1353	65.5	1396
N2	1.5	10.8	3045	133	23.9	1356	57.6	1390

The Martian meteorite regolith breccia clasts in NWA7034 and 7533 yield formation P-T conditions at 1.2 ± 0.6 GPa and 1380 ± 119 °C, which is comparable with the basalts of Gusev and Gale craters (Udry et al., 2014; Filiberto and Dasgupta, 2015). However, the yielded formation condition range is large in the regolith breccia (Agee et al., 2013; Humayun et al., 2013; Santos et al., 2015; Wittmann *et al.*, 2015). The formation conditions of olivine phyric shergottites are very much different from that of the in-situ basalts, orbiter-derived chemistry, and NWA7034 / NWA7533 breccia. Based on experimental and modelling results the average formation conditions for the shergottites are 3.8 ± 1.4 GPa and 1681 ± 40 °C (Kiefer *et al.*, 2016).

4.4 Discussion

The geochemical analysis and petrologic simulations of Noachian-aged volcanic provinces provide insight into the magmatic evolution of early Mars. We focus on major element analyses of the basaltic compositions of our study regions Arabia Terra, N1 & N2 to constrain the Noachian age igneous rock type, degree of weathering, pressures, and temperatures of magmatic formation with depth and degree of magma genesis.

4.4.1 Geochemical investigation of Noachian provinces

In this section, we investigate the origin of variation in the absolute abundances of these elements to know whether they represent variations in melt generation or secondary modification processes over the Noachian surface. We use K/Th fractionation and molar fraction-based ternary analysis with CIA. K/Th ratio depicts modest to low variation in K/Th with respect to the average Martian crust (Figure 4.3a) which may be explained by inherent variations in igneous rocks (Taylor et al., 2006). To understand the contribution of low pH aqueous alteration, A-CNK-MF ternary diagram is used (Hurowitz and McLennan, 2007). The A-CNK-MF ternary diagram shows that our study areas are plotted beneath the olivine-feldspar trend line and follow

a similar trend of typical Martian basalts as the average Martian crust and Martian meteorites suggesting no aqueous alteration (Figure 4.3b). Moreover, A-CNK-MF ternary analysis depicts a lack of signature of the substantial alteration as they compositionally overlap with Martian meteorites and follow a low-pH aqueous trend that was experimentally examined by Hurowitz and McLennan (2007). Furthermore, we investigate the extent or degree of weathering in study regions using CIA. The CIA, which uses standard molar abundances of oxides, corresponds to < 50 for the Noachian volcanic provinces (Figure 4.3c), indicating no to minimal signature of weathering at this broad scale of GRS. Consequently, the observed composition suggests provinces dominantly record primary igneous composition at the GRS scale observation.

Furthermore, the enrichment of Al in N1 and N2 provinces could have resulted from early Al differentiation in the Martian mantle (McSween et al., 2009). The observed depletion of Ca in N1 and N2 in Noachian provinces compared to relatively younger Hesperian and Amazonian provinces studied by Baratoux et al. (2011) indicate the presence of low-calcium pyroxene (LCP) compatible with TES observation (Baratoux et al. 2013). Arabia Terra region is mantled by dust, therefore we further investigate the possible origin of dust using the S/Cl ratio. Our calculated mean molar S/Cl ratio for Arabia Terra (~ 4.6) does not fall within the global dust molar ratio range (3.0 – 4.4). The observed little enrichment of S in Arabia Terra, coupled with an S/Cl molar ratio diverging from that of Martian dust (Ojha et al., 2018), supports sulfur adsorbed or chemically bound in the soil and regolith from volcanic degassing.

In addition, the classification of the primary composition using GRS-derived chemistry for Noachian age provinces Arabia Terra, N1 & N2 depicts a little enrichment of alkalis with low SiO₂ values ($\sim 43 \pm 3$ wt%) compared to the SNC meteorites (45 ± 5 wt%) (Figure 4.4). Nevertheless, surface chemistry of studied Noachian age provinces and Gusev basalts show a similarly restricted range in total alkali content; however, Gusev basalt has a slightly higher bulk silica content (45 ± 5 wt%) (McSween et al., 2006a; McSween et al., 2006b). Compared to the igneous Bounce rock at Meridiani Planum, analyzed by the MER Opportunity rover, Noachian age provinces have higher total alkalis and lower bulk silica composition (Zipfel *et al.*,

2011). The rocks analyzed by the Curiosity rover at Gale crater have a much wider range of both total alkalis and silica than compared to those of the Noachian age provinces of this study, the rocks at Gusev crater and Meridiani Planum and shergottite composition (Sautter et al., 2015; Treiman *et al.*, 2016). All the above analyses with extended datasets suggest that the Martian crust is substantially more heterogeneous than was previously believed. Each new landing site and new orbiter dataset offers additional evidence of the variety of Martian igneous rocks. The diverse compositional

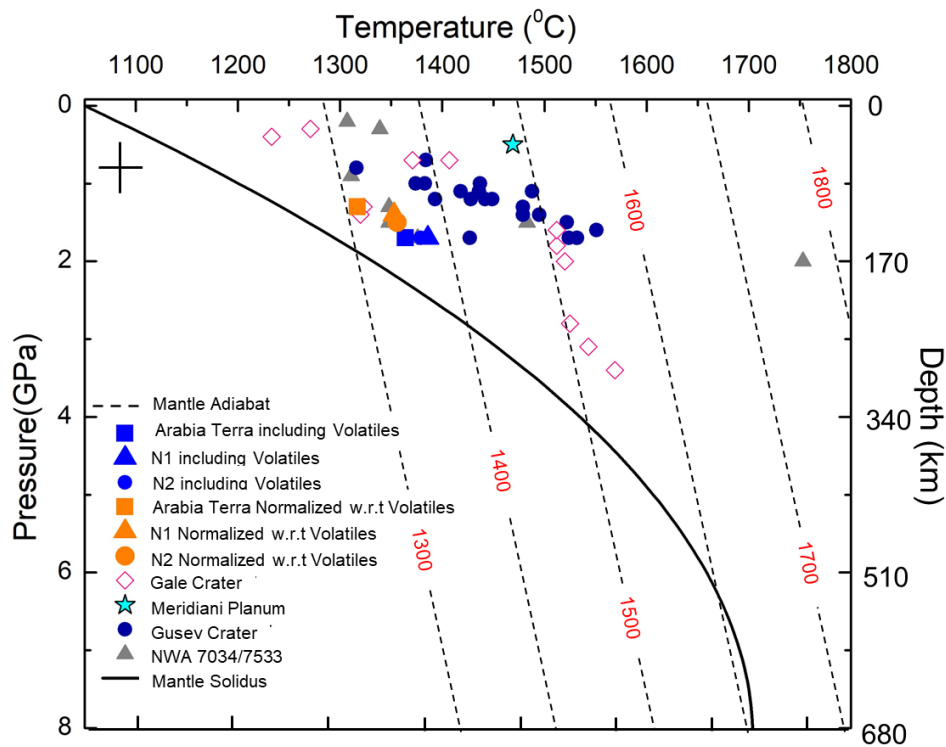


Figure 4.7: Pressure and temperature (P - T) conditions are calculated for surface volcanics of the Noachian age derived from GRS. For comparison between similar age *in situ* basalts from Gusev, Gale, and Meridiani Planum is also shown in this P - T diagram. Dashed contours represent mantle potential temperature in degree Celsius, calculated by adding the latent heat of fusion to equilibrium temperature at which melt and solid mantle coexist and subtracting martian adiabatic gradient corresponding to the depth of melt. Also shown is the solidus of the nominally volatile-free Martian mantle (solid line, Kiefer *et al.*, 2015).

variation throws the challenges to decode the diverse mantle conditions and the magmatic processes.

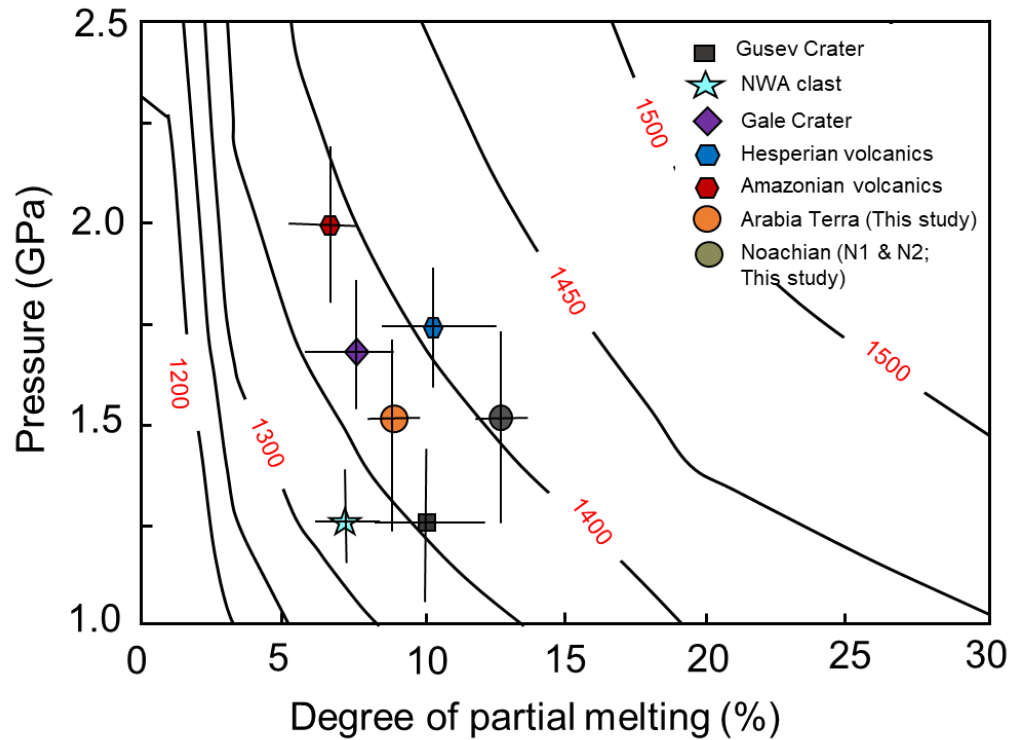


Figure 4.8: Pressure and degree of partial melting of basalts from *in situ* investigation, surface volcanics (Noachian to Amazonian) from GRS measurements. Contours represent mantle potential temperature in degree Celsius.

4.4.2 Implications of estimated formation P - T in volcanic provinces

Mars' surface is largely covered with igneous rocks like basalt. We consider SiO_2 , Al_2O_3 , FeO , MgO , and K_2O oxides, which are the major rock-forming element oxides to constrain the P - T conditions. These elements are present in high concentrations in the rock-forming minerals, and control crystallization–melting behavior in igneous systems. Earlier studies considered only SiO_2 , FeO , and Th to calculate the formation P - T conditions of the volcanic regions (Baratoux et al., 2011). We follow a simplified magmatic model that predicts a single-stage partial melting of the Martian mantle

without significant fractional crystallization contributions prior to its eruption on the surface (McSween et al., 2006; El Maarry et al., 2009; Baratoux et al., 2014), which implies that melt is in the equilibrium with the Martian mantle. The calculated pressure ranges from 1.3-1.7 GPa while temperature varies from 1310 to 1400 °C for the studied Noachian regions. We have observed that the nominally hydrous Martian mantle does not show much variation in the P - T conditions in comparison to the dry mantle, indicating pMELTS is least sensitive at a few 100 ppm H₂O contents of the Martian mantle. Volatiles normalized and without normalized Noachian volcanic provinces fall nearly within the uncertainty range of the pMELTS calculated compositions (Smith and

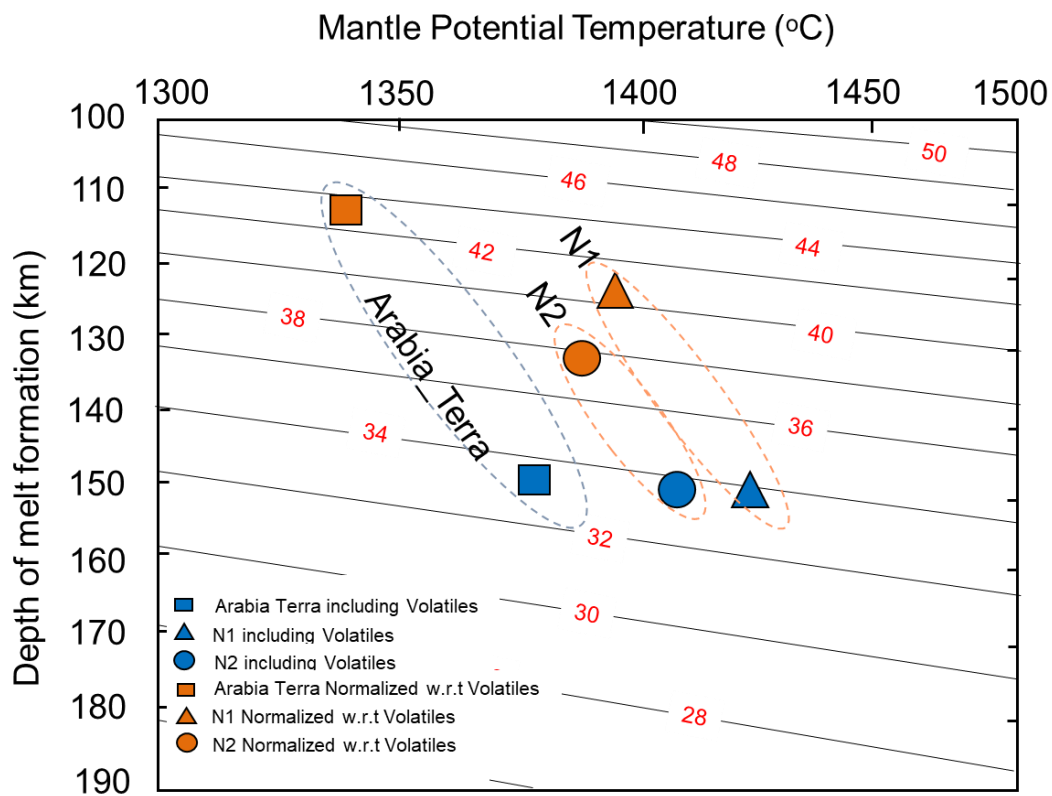


Figure 4.9: Depth of melt formation vs mantle potential temperature for Noachian magmatism. The depth of melt and mantle potential temperature are derived from pressure and degree of partial melting. Heat flow contours (milliwatts per square metre) are calculated from the depth of melt and melting temperature assuming a conductivity of the lithosphere as $3.0 \text{ Wm}^{-1} \text{ K}^{-1}$.

Asimow 2005). The study regions N1 & N2 yield relatively higher formation pressure (~1.4 -1.8 GPa), and a higher degree of partial melting (~10-12%), which further corresponds to a greater depth of melt formation compared to Arabia Terra (P~ 1.3-1.7 GPa and degree of melting ~ 8%). This could imply that the Arabia Terra region corresponds to a shallow melting regime (Figure 4.7, Tables 4.5a-c) which is consistent with the hypothesis proposed by previous studies by Michalski and Bleacher, (2013) and Rani et al (2021).

In addition, previous in situ studies of Noachian aged basalts of Gusev and Gale craters show diverse variability of P-T conditions, which may imply a more complex set of processes than those acting in the Hesperian and Amazonian (Figure 4.8, Tables 4.5a-c) (Baratoux et al., 2011; Baratoux et al., 2013), including varying degrees of partial melting and magmatic differentiation. However, compared to Hesperian and Amazonian average magma formation conditions, the Noachian volcanic regions have a relatively higher pressure, temperature, and degree of partial melting (Figure 4.8, Tables 4.5a–4.5c). Our investigation follows a decreasing trend of pressure from Noachian to Amazonian.

4.4.3 Depth of melting and mantle potential temperature (T_p)

Estimated formation P - T conditions of Noachian aged provinces derived from pMELTS simulations allow us to constrain the mantle potential temperature (T_p) with formation depth of melt and corresponding heat flow for all three provinces (Arabia Terra, N1, and N2). The derived equilibrium pressure, gravitational constant for Mars, and density of Martian lithosphere are used to compute the depth of melt formation for each province. Given that crustal thickness models of Mars suffer from the non-uniqueness problem that plague many other geophysical constraints (cf., Baratoux et al., 2014; Goossens et al., 2017; Wieczorek et al., 2022), the melting depth is nearly consistent in all three Noachian provinces when the volatiles are incorporated into the bulk composition, i.e., without volatiles normalization, that is approximately 150 km. However, a little variation has been observed among Arabia Terra, N1, and N2 in the case of normalization with respect to all volatiles, which is not very significant

concerning expected depth errors. The melting depth with volatiles of Arabia Terra ($d \sim 114 \pm 10$ km) is less compared to that of N1 ($d \sim 133 \pm 10$ km) and N2 ($d \sim 123 \pm 10$ km) regions (Figure 4.9, Tables 4.5a,b). The mantle potential temperature is calculated using latent heat of fusion, average equilibrium temperature corresponding to the degree of partial melt derived from pMELTS, and Martian adiabatic gradient. Mantle potential temperature for melt without normalized volatiles is high, ranging from 1380-1425 °C, with heat flow of ~ 33 -35 mWm⁻². On the other hand, the similar melt composition with normalized volatiles shows low $T_p \sim 1340$ -1396 °C, with high heat flow ~ 38 -44 mWm⁻² (Figure 4.8-4.9, Tables 4.5a, b). The formation depth of the melt with normalized volatiles is shallower than that of the without normalized volatiles (Figure 4.9, Tables 4.5a,b).

4.4.4 Implication to cooling of Martian mantle

The variation in mantle potential temperature resulting from compositional variability has been discussed above and they are suggestive of different magmatic processes including varying degrees of partial melting and magmatic differentiation. However, the observed diversity among the Martian basalts, notably that of different ages can help to explain the variations observed in mantle potential temperature and melting conditions. For example, in addition to earlier in situ investigations on the basalts from Gusev crater, Gale crater, and Meridiani Planum (Arvidson *et al.*, 2003; Greeley *et al.*, 2005; Farley *et al.*, 2014), which are Noachian or late Noachian/early Hesperian in age, we have estimated mantle potential for the Noachian aged volcanic provinces using GRS. Furthermore, we have compared the mantle potential temperature of our studied Noachian volcanic provinces with that of the Hesperian and Amazonian volcanic provinces (Baratoux *et al.*, 2011; Baratoux *et al.*, 2013). To establish any link present between the mantle potential temperature and crystallization age of the Martian surface rocks, we observe a trend of decreasing temperature over time, which is consistent with previous observations from in-situ analyses and Hesperian-Amazonian volcanics only (Baratoux *et al.*, 2011; Filiberto and Dasgupta, 2015; Filiberto, 2017).

We suggest a cooling of the Martian mantle through time, which includes the Noachian volcanic region for the first time (Figure 4.10). However, the basaltic shergottites cannot be correlated with the secular cooling trend, which perhaps implies different evolution related to the mantle plume, as was suggested by Kiefer and Li, (2016) and Filiberto (2017). We have carried out a regression calculation by incorporating the data of surface regional volcanics and in situ studies along with this study of Noachian-aged volcanic provinces and excluding shergottites. Martian cooling polynomial best fit with an R^2 of 0.70 is:

$$\text{Temperature } (T_p, \text{ }^\circ\text{C}) = 16.54 (\text{age, Ga})^2 - 63.19 (\text{age, Ga}) + 1427.21 \text{---- (4.5)}$$

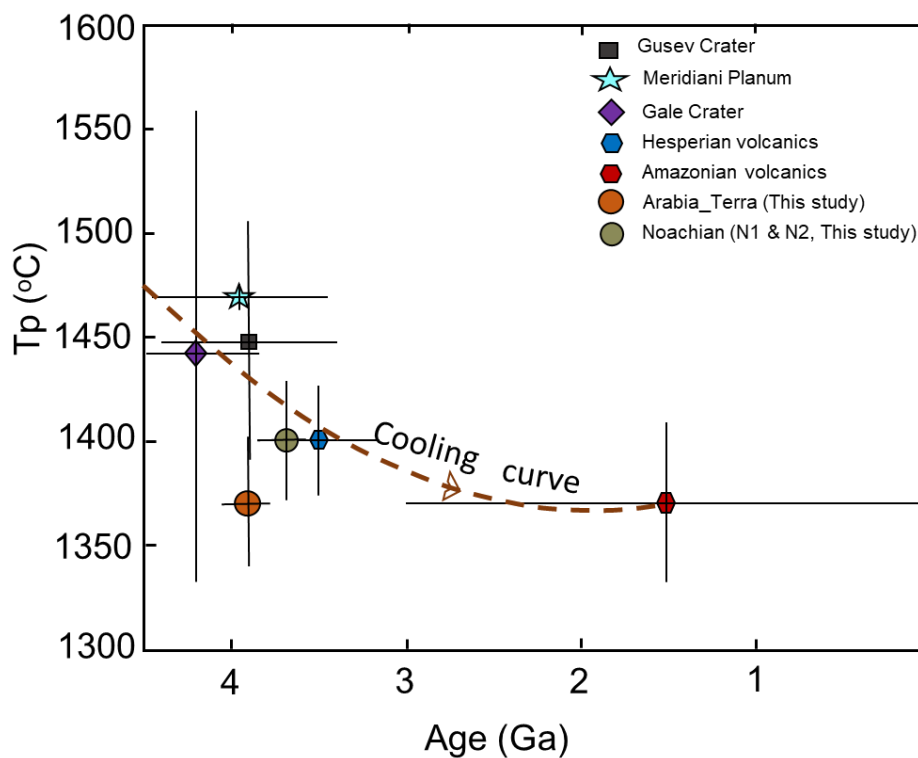


Figure 4.10: The average mantle potential temperature (T_p $^\circ\text{C}$) through time is estimated for basalts from Gusev, Gale, and Meridiani Planum, along with the studied Noachian volcanic provinces in this work. Hesperian and Amazonian surface volcanics are also plotted (from Baratoux et al., 2011). The best polynomial fit represents the cooling curve of the martian interior.

Due to a lack of samples, the given equation is a polynomial best fit with significant uncertainty. With the future returned samples and more surficial investigation of Mars, the precision of the polynomial best fit will improve.

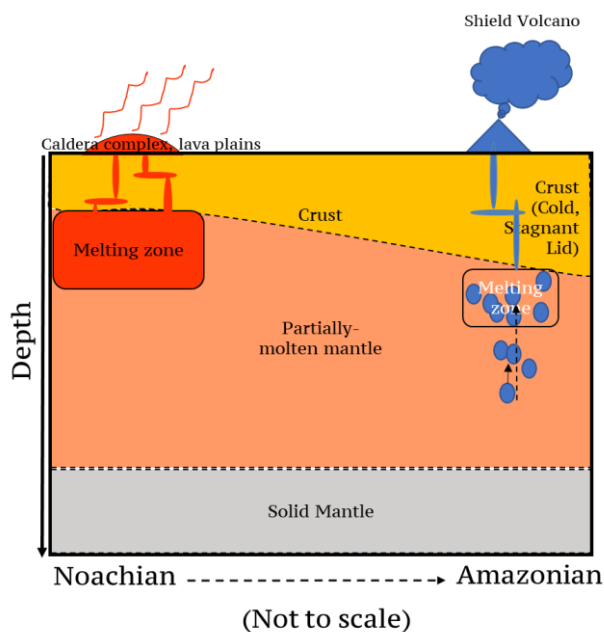


Figure 4.11: Schematic diagram for evolution of martian mantle over time.

4.5 Summary and conclusion

The major elemental chemistry of Noachian-aged provinces is consistent with primary rock composition at a GRS scale. The melt of compositions similar to Noachian-aged provinces could be produced by 8-12% partial melting of the mantle with a composition similar to DW85 at a pressure range from 1.3 to 1.8 GPa. The average composition of GRS over a broad scale lacks the contribution of a local chemical signature that could affect the composition on the surface. Noachian study regions (N1 & N2) reflect a condition with higher pressure, degree of melting, and mantle potential temperature in comparison to the lower pressure, degree of melting, and mantle potential temperature in Arabia Terra and in-situ study regions. Therefore, the petrological investigation infers a relatively shallower depth of formation or thin

lithosphere of Arabia Terra compared to N1 & N2, which could reflect the lithospheric thinning process in the near dichotomy Arabia Terra, which is consistent with the previous hypothesis (Michalski and Bleacher, 2013; Rani et al., 2021). Compared to Hesperian and Amazonian, diverse compositional variability among surface volcanics and in-situ analyzed basalts of the Noachian age depicts a more complex set of processes including varying degrees of partial melting and magmatic differentiation. The mantle potential temperature for surface volcanics and surface basalts gives a correlation of decreasing temperature trend through time, depicts cooling of the Martian interior and increase of lithospheric thickness during Martian geologic evolution (Figures 4.10 and 4.11).

Chapter 5 Summary and Future Work

5.1 Introduction

Since last four-decades planetary space missions to Mars starting from the Mariner 9 mission in 1972 till the present Mars Reconnaissance Orbiter mission show that Mars has been volcanically active throughout its history, starting from Noachian (>3.6 Ga) to Late Amazonian (<150 Ma). This depicts that volcanic activity or volcanism has played a significant role in the crustal and mantle evolution of Mars. Earlier studies probed the magmatic evolution of Mars in Hesperian (3.6 Ga-3.0 Ga) and Amazonian (<3.0 Ga) timescales. However, the earliest magmatic evolution of Noachian (>3.6 Ga) age, which is expected to record extensive volcanism, has not been explored yet. Thus, Noachian-aged volcanism is an important source of information for early Martian geologic studies that remain to be understood, even though extensive magmatism and volcanism are expected in the early stage of the Martian crust formation. The long-term resurfacing and degradation of geomorphological evidence of volcanism namely low shield highland and ridged plains might be one reason that complicated the detailed investigation of Noachian volcanism. Therefore, to understand the thermal evolution and formation of the Martian mantle and crust at its early stage, we carried out a detailed investigation of Noachian-aged volcanic regions.

5.2 Tectono-volcanism in north-central Arabia Terra, Mars: Insights from morphology and structural analysis

The morphological and structural investigation of linear tectonic features in North-Central (NC) Arabia Terra (geographic extent: -4°E to 60°E and 44°N to 8°N), and geomorphological and morphometric study of the distinct igneous landforms (cones and dikes) in an unnamed crater (now called **Ramanathan crater**) have been used to constrain the regional extent of volcanic province and unveil the evidence of tectono-volcanism in Arabia Terra.

Our regional investigation of pre-existing tectonic structures such as wrinkle ridges in Arabia Terra anticipated that orientation converges with magmatic cone-dike systems' of Ramanathan crater. Therefore, our finding of igneous dikes and cones within the Ramanathan crater may represent a broader extent of the thinned crust of Arabia Terra. The thin crust could have resulted as a function of regional tectono-magmatism, an inference based on the similar orientations of linear features in the Ramanathan crater and Arabia Terra. As a result, the late Noachian - early Hesperian Ramanathan crater in the North-Central Arabia Terra region, describes a new class of diminutive volcanic centres in Arabia Terra resulting from regional tectono-volcanism and provides pieces of evidence of volcanic resurfacing in Arabia Terra. Furthermore, the presence of dikes and cones predominantly at the centre of the study crater, suggests that the igneous structures formed during the syn-deformational stage of the impact, or that volcanism was later rejuvenated along linear weak zones (i.e., faults and fractures). This was likely facilitated by a thinner crust proximal to the dichotomy boundary. While the formation of the volcanic structures in the study crater cannot be explained by impact-induced magmatism, magmatism triggered by the impact that was further facilitated by a thin crust is plausible. Therefore, this study illustrates that the possible extent of volcanism is not only constrained in the NW part of Arabia Terra, as shown

by previous studies, but it has a regional significance most plausibly throughout the entire Arabia Terra.

5.3 Arabia Terra and other chemical provinces on Mars: Implications for geologic interpretations

Noachian-aged Arabia Terra represents many fundamental aspects of Martian geology, such as a thinner crust than the other parts of the southern highland, large-scale structural and tectonic deformation, preserved large, thick, and complex sedimentary records, and volcanic resurfacing with a volatile-rich surface. Although various studies provide several hypotheses for the volatiles' enrichment in Arabia Terra, the source of volatiles is still unknown. Further, the nature of volatiles (H₂O, Cl, and S) distributions in Arabia Terra, as well as the relative relevance of volatile origin (sedimentary or volcanic) processes, also remains unknown. Hence, to address whether volatile enrichment relates broadly to sedimentary processes or volcanic resurfacing, we need to demarcate the geochemical extent of Arabia Terra and deduce the bulk composition of the study region. Therefore, to estimate the bulk composition of Arabia Terra, we synthesize and advance prior multivariate methods to derive the first consolidated chemical provinces of Mars using GRS-derived chemical datasets.

The consolidated chemical provinces of Mars imply several geochemical signatures of broad geologic importance. Four consolidated chemical provinces (A-D) of Mars are derived from the integration of the three different multivariate cluster analysis techniques. Compared to prior works, the emergence of distinct regions as well as the exclusion of previously suggested provinces reflects our methodological advances with the incorporation of Al and S. Consolidated chemical provinces correspond to differences in mapped geology, unlike a decade ago geochemical studies. This convergence indicates that the chemical compositions represent both underlying geology and bulk regolith processes. Furthermore, our findings demonstrate chemical trends among the southern highland provinces A-C and mid-Noachian aged Arabia

Terra. Province A and C represent the mid-Noachian to early Hesperian period, while Province B represents Late Hesperian to Amazonian period. These chemical trends may indicate complex processes of an evolving degree of partial melting within a highly differentiated mantle source for the highlands. The distinct lithology of the late Hesperian lowland unit (Province-D), does not follow the chemical trends like highland provinces. This could provide a mechanism for sampling a high-pressure, garnet-rich source for the lowland regions. Summarily, chemical trends suggest complex processes of melting in the heterogeneous mantle for the highlands, which differs from a possibly garnet-rich lowland source. We also find that even older volatile-rich regions like Arabia Terra and Medusae Fossae Formation (MFF) preserve igneous composition, consistent with water-limited isochemical weathering throughout Mars's geologic history.

5.4 Noachian volcanism and its implication for thermo-chemical evolution of early Mars

This work constitutes an effort to constrain the understanding of magma genesis in Noachian-aged (>3.6 Ga) volcanic regions utilizing petrological, chemical analysis, and magmatic process modelling. We also worked to deduce the magmatic processes and pressure-temperature (P-T) conditions of their formation. We have constrained the melting depth using the thermal vigor of melting in the early Martian mantle of the Noachian age. A detailed geochemical investigation of Noachian-aged volcanic provinces, e.g., Solis (N1), Argyre (N2) in the southern part of Tharsis province, and the recently discovered volcanic province Arabia Terra, has been carried out. The main goal of this research is to have a better understanding of the spatiotemporal changes in the interior of Mars during Noachian. Understanding the internal thermal conditions and processes during the Noachian, such as magmatic differentiation and mantle melting, through orbital geochemical data analysis of Arabia Terra and other Noachian-aged volcanic regions, is crucial for inferring the geological evolution of Mars.

Our geochemical analysis of the Noachian-aged volcanic regions is consistent with primary rock composition at a broader scale of GRS. Melts were produced by 8-12% partial melting of the primitive Martian mantle composition proposed by DW85 (Dreibus & Wanke, 1985) at a pressure range from 1.3 to 1.8 GPa. The average composition of GRS over a broad scale lacks the contribution of a local chemical signature that could affect the composition on the surface. Furthermore, our study depicts that the study regions N1 & N2 yield high-pressure (1.7 ± 0.2 GPa) formation, whereas Arabia Terra yields a low formation P (1.3 ± 0.2 GPa). Therefore, the geochemical investigation infers a relatively shallower depth or thin lithosphere of Arabia Terra compared to N1 & N2. This could reflect the lithospheric thinning process of Arabia Terra. The lithospheric thinning process derived from the geochemical investigation is consistent with the previously proposed hypothesis of supervolcanic eruption based on a morphological investigation by Michalski and Bleacher (2013). Compared to Hesperian and Amazonian, diverse compositional variability among the Noachian-aged in-situ basalts implies various degrees of partial melting and magmatic differentiation. Furthermore, the mantle potential temperature for the in-situ basalts gives a good correlation of decreasing average temperature through time from Noachian (1470 ± 50 °C) to Amazonian (1370 ± 40 °C), implying cooling of the Martian interior with an increase of lithospheric thickness from Noachian (114 ± 30 km) to Amazonian (170 ± 30 km).

Overall, this thesis work used volcanic provinces as fingerprints to understand the spatiotemporal evolution of the Martian mantle. The evolution of Martian magmatism implies that volcanic activity has played a significant role in the crustal and mantle evolution of Mars. Therefore, we use the surface composition of various age to determine the P - T conditions, degrees, and depths of melting at the mantle source as functions of time.

5.5 Potential for future work

- Fundamental insight from the Arabia Terra will be realized only with detailed and more robust compositional characterization. This could be achieved by doing local mineralogic characterization with additional geomorphologic analyses. However, heavily mantled dust is one of the greatest challenges in mapping the mineralogy of Arabia Terra. Because optically thick fine-grained debris blankets (i.e., dust) obscure deeper mineralogical signatures of the Arabia Terra region from orbital remote sensing data such as Visible, Near, and Thermal-Infrared spectroscopy (VNTIR). However, fresh impact craters formed in recent years, which have disturbed the surface dust, can provide unique opportunities to investigate the comparatively dust-free mineralogic compositions of these locations. These fresh craters, plus other small exposures of less dusty materials, can be resolved spatially in high-resolution targeted observations of visible/short-wave infrared spectral reflectance by the Compact Reconnaissance Imaging Spectrometer for Mars (CRISM). Using this we can also derive stratigraphically coupled mineralogy to the extent unobscured by fine debris cover (i.e., dust) in the Arabia Terra region.
- Our new approach for the consolidated chemical provinces of Mars, which demonstrates the overall utility of the integrative multivariate methodology, is also motivational for the possible applications to other planetary bodies having no or thin atmosphere (e.g., Mercury, Moon, and Vesta) with comparable datasets.

Bibliography

Agee, C.B. *et al.* (2013) 'Unique meteorite from early Amazonian Mars: Water-rich basaltic breccia Northwest Africa 7034', *Science*, 339(6121), pp. 780–785.

Ahmad, A. and Nair, A.M. (2021) 'Landform evolution of Tharsis Montes and Olympus Mons of Mars: Insights from morphometric, hypsometric and chronologic evidences', *Journal of Earth System Science*, 130(3), pp. 1–20.

Allen, C.C. and Oehler, D.Z. (2008) 'A case for ancient springs in Arabia Terra, Mars', *Astrobiology*, 8(6), pp. 1093–1112.

Anderson, R. *et al.* (2008) 'Centers of tectonic activity in the eastern hemisphere of Mars', *Icarus*, 195(2), pp. 537–546.

Anderson, R.C. *et al.* (2001) 'Primary centers and secondary concentrations of tectonic activity through time in the western hemisphere of Mars', *Journal of Geophysical Research E: Planets*, 106(E9), pp. 20563–20585. Available at: <https://doi.org/10.1029/2000JE001278>.

Andrews-Hanna, J.C., Zuber, M.T. and Banerdt, W.B. (2008) 'The Borealis basin and the origin of the martian crustal dichotomy', *Nature*, 453(7199), pp. 1212–1215.

Anguita, F. *et al.* (1997) 'Arabia Terra, Mars: Tectonic and palaeoclimatic evolution of a remarkable sector of Martian lithosphere', *Earth, Moon, and Planets*, 77(1), pp. 55–72.

Ann Hodges, C. and Moore, H.J. (1979) 'The subglacial birth of Olympus Mons and its aureoles', *Journal of Geophysical Research: Solid Earth*, 84(B14), pp. 8061–8074.

Arvidson, R. *et al.* (2003) 'Mantled and exhumed terrains in Terra Meridiani, Mars', *Journal of Geophysical Research: Planets*, 108(E12).

Baer, G. (1991) 'Mechanisms of dike propagation in layered rocks and in massive, porous sedimentary rocks', *Journal of Geophysical Research: Solid Earth*, 96(B7), pp. 11911–11929.

Balme, M. and Gallagher, C. (2009) 'An equatorial periglacial landscape on Mars', *Earth and Planetary Science Letters*, 285(1–2), pp. 1–15.

Balta, J.B. and McSween Jr, H.Y. (2013) 'Water and the composition of Martian magmas', *Geology*, 41(10), pp. 1115–1118.

-
- Bamberg, M. *et al.* (2014) 'Floor-fractured craters on Mars - Observations and origin', *Planetary and Space Science*, 98, pp. 146–162. Available at: <https://doi.org/10.1016/j.pss.2013.09.017>.
- Bandfield, J.L., Amador, E.S. and Thomas, N.H. (2013) 'Extensive hydrated silica materials in western Hellas Basin, Mars', *Icarus*, 226(2), pp. 1489–1498.
- Bandfield, J.L., Hamilton, V.E. and Christensen, P.R. (2000) 'A global view of Martian surface compositions from MGS-TES', *Science*, 287(5458), pp. 1626–1630.
- Banerdt, W.B., Golombek, M.P. and Tanaka, K.L. (1992) 'Stress and tectonics on Mars.', *Mars*, pp. 249–297.
- Baratoux, D. *et al.* (2011) 'Thermal history of Mars inferred from orbital geochemistry of volcanic provinces', *Nature*, 472(7343), pp. 338–341.
- Baratoux, D. *et al.* (2013) 'The petrological expression of early Mars volcanism', *Journal of Geophysical Research: Planets*, 118(1), pp. 59–64.
- Baratoux, D. *et al.* (2014) 'Petrological constraints on the density of the Martian crust', *Journal of Geophysical Research: Planets*, 119(7), pp. 1707–1727.
- Barlow, N.G. and Perez, C.B. (2003) 'Martian impact crater ejecta morphologies as indicators of the distribution of subsurface volatiles', *Journal of Geophysical Research: Planets*, 108(E8).
- Barosio, A. and Galicia, J.V. (2002) 'Mars thermal history based on its tectonic and structural systems', *Geofísica Internacional*, 41(2), pp. 189–193.
- Basu Sarbadhikari, A.B. *et al.* (2009) 'Petrogenesis of olivine-phyric shergottite Larkman Nunatak 06319: Implications for enriched components in martian basalts', *Geochimica et Cosmochimica Acta*, 73(7), pp. 2190–2214.
- Basu Sarbadhikari, A.B. *et al.* (2011) 'Evidence for heterogeneous enriched shergottite mantle sources in Mars from olivine-hosted melt inclusions in Larkman Nunatak 06319', *Geochimica et Cosmochimica Acta*, 75(22), pp. 6803–6820.
- Basu Sarbadhikari, A. *et al.* (2016) 'Martian meteorite Tissint records unique petrogenesis among the depleted shergottites', *Meteoritics & Planetary Science*, 51(9), pp. 1588–1610.
- Basu Sarbadhikari, A., Babu, E. and Vijaya Kumar, T. (2017) 'Chemical layering in the upper mantle of Mars: Evidence from olivine-hosted melt inclusions in Tissint', *Meteoritics & Planetary Science*, 52(2), pp. 251–267.
- Bertka, C.M. and Holloway, J.R. (1994) 'Anhydrous partial melting of an iron-rich mantle II: primary melt compositions at 15 kbar', *Contributions to Mineralogy and Petrology*, 115(3), pp. 323–338.

Beuthe, M. (2010) 'East–west faults due to planetary contraction', *Icarus*, 209(2), pp. 795–817.

Bevington, P.R. and Robinson, D.K. (2003) 'Data reduction and error analysis', *McGraw-Hill, New York* [Preprint].

Bleacher, J.E. *et al.* (2009) 'Spatial and alignment analyses for a field of small volcanic vents south of Pavonis Mons and implications for the Tharsis province, Mars', *Journal of Volcanology and Geothermal Research*, 185(1–2), pp. 96–102. Available at: <https://doi.org/10.1016/j.jvolgeores.2009.04.008>.

Bourke, M. *et al.* (2006) 'A comparison of methods used to estimate the height of sand dunes on Mars', *Geomorphology*, 81(3–4), pp. 440–452.

Boynton, W. *et al.* (2007) 'Concentration of H, Si, Cl, K, Fe, and Th in the low-and mid-latitude regions of Mars', *Journal of Geophysical Research: Planets*, 112(E12).

Breuer, D. and Moore, W. (2007) 'Dynamics and thermal history of the terrestrial planets, the Moon, and Io', *Planets and moons. Treatise on geophysics*, 10, pp. 299–348.

Breuer, D. and Spohn, T. (2006) 'Viscosity of the Martian mantle and its initial temperature: Constraints from crust formation history and the evolution of the magnetic field', *Planetary and Space Science*, 54(2), pp. 153–169.

Brož, P. *et al.* (2015) 'Scoria cones on Mars: Detailed investigation of morphometry based on high-resolution digital elevation models', *Journal of Geophysical Research: Planets*, 120(9), pp. 1512–1527.

Brož, P. *et al.* (2017) 'Amazonian volcanism inside Valles Marineris on Mars', *Earth and Planetary Science Letters*, 473, pp. 122–130. Available at: <https://doi.org/10.1016/j.epsl.2017.06.003>.

Brož, P. *et al.* (2019) 'Subsurface sediment mobilization in the southern Chryse Planitia on Mars', *Journal of Geophysical Research: Planets*, 124(3), pp. 703–720.

Brož, P. and Hauber, E. (2012) 'A unique volcanic field in Tharsis, Mars: Pyroclastic cones as evidence for explosive eruptions', *Icarus*, 218(1), pp. 88–99. Available at: <https://doi.org/10.1016/j.icarus.2011.11.030>.

Burr, D.M., Tanaka, K.L. and Yoshikawa, K. (2009) 'Pingos on Earth and Mars', *Planetary and Space Science*, 57(5–6), pp. 541–555.

Carr, M.H. (1973) 'Volcanism on mars', *Journal of Geophysical Research*, 78(20), pp. 4049–4062.

Carr, M.H. (2007) *The surface of Mars*. Cambridge University Press.

-
- Carr, M.H. and Head, J.W. (2010) 'Geologic history of Mars', *Earth and Planetary Science Letters*, 294(3–4), pp. 185–203. Available at: <https://doi.org/10.1016/j.epsl.2009.06.042>.
- Carter, J. and Poulet, F. (2013) 'Ancient plutonic processes on Mars inferred from the detection of possible anorthositic terrains', *Nature Geoscience*, 6(12), pp. 1008–1012.
- Charrad, M. *et al.* (2014) 'NbClust: an R package for determining the relevant number of clusters in a data set', *Journal of statistical software*, 61, pp. 1–36.
- Chicarro, A.F., Schultz, P.H. and Masson, P. (1985) 'Global and regional ridge patterns on Mars', *Icarus*, 63(1), pp. 153–174.
- Christensen, P.R. *et al.* (2001) 'Mars Global Surveyor Thermal Emission Spectrometer experiment: investigation description and surface science results', *Journal of Geophysical Research: Planets*, 106(E10), pp. 23823–23871.
- Christensen, P.R. *et al.* (2002) 'THE THERMAL EMISSION IMAGING SYSTEM (THEMIS) FOR THE MARS 2001 ODYSSEY MISSION A major goal of the Mars Exploration Program is to obtain data that will help determine whether life ever existed on Mars . This goal will ultimately be addressed via detaile', *Space Science Reviews*, 110, pp. 85–130. Available at: <https://doi.org/10.1023/B:SPAC.0000021008.16305.94>.
- Christensen, P.R. *et al.* (2003) 'Morphology and composition of the surface of Mars: Mars Odyssey THEMIS results', *science*, 300(5628), pp. 2056–2061.
- Christensen, P.R. *et al.* (2005) 'Evidence for magmatic evolution and diversity on Mars from infrared observations', *Nature*, 436(7050), pp. 504–509. Available at: <https://doi.org/10.1038/nature03639>.
- Chu, Y.Y.Y. *et al.* (2021) 'Caldera Collapse and Volcanic Resurfacing in Arabia Terra Provide Hints of Vast Under-Recognized Early Martian Volcanism', *Geophysical Research Letters*, 48(15), p. e2021GL093118.
- Cormack, R.M. (1971) 'A review of classification', *Journal of the Royal Statistical Society: Series A (General)*, 134(3), pp. 321–353.
- Crow, R. *et al.* (2008) 'History of Quaternary volcanism and lava dams in western Grand Canyon based on lidar analysis, ⁴⁰Ar/³⁹Ar dating, and field studies: Implications for flow stratigraphy, timing of volcanic events, and lava dams', *Geosphere*, 4(1), pp. 183–206.
- Crumpler, L. *et al.* (2015) 'Context of ancient aqueous environments on Mars from in situ geologic mapping at Endeavour Crater', *Journal of Geophysical Research: Planets*, 120(3), pp. 538–569.

-
- Cushing, G. *et al.* (2009) 'THEMIS high-resolution digital terrain: Topographic and thermophysical mapping of Gusev Crater, Mars', *Journal of Geophysical Research: Planets*, 114(E7).
- Davis, J.M. *et al.* (2016) 'Extensive Noachian fluvial systems in Arabia Terra: Implications for early Martian climate', *Geology*, 44(10), pp. 847–850. Available at: <https://doi.org/10.1130/G38247.1>.
- Debaille, V. *et al.* (2009) 'Early martian mantle overturn inferred from isotopic composition of nakhlite meteorites', *Nature Geoscience*, 2(8), pp. 548–552.
- Diez, B. *et al.* (2008) 'H layering in the top meter of Mars', *Icarus*, 196(2), pp. 409–421.
- Diez, B. *et al.* (2009) 'Contribution of mars odyssey GRS at central Elysium planitia', *Icarus*, 200(1), pp. 19–29.
- Dohm, J.M. *et al.* (2007) 'Possible ancient giant basin and related water enrichment in the Arabia Terra province, Mars', *Icarus*, 190(1), pp. 74–92. Available at: <https://doi.org/10.1016/j.icarus.2007.03.006>.
- Dohm, J.M. and Tanaka, K.L. (1999) 'Geology of the Thaumasia region, Mars: Plateau development, valley origins, and magmatic evolution', *Planetary and Space Science*, 47(3–4), pp. 411–431.
- Dreibus, G. and Wa, H. (1987) 'Volatiles on Earth and Mars: A comparison', *Icarus*, 71(2), pp. 225–240.
- Ehlmann, B.L. *et al.* (2011) 'Subsurface water and clay mineral formation during the early history of Mars', *Nature*, 479(7371), pp. 53–60.
- El Maarry, M.R. *et al.* (2009) 'Gamma-ray constraints on the chemical composition of the martian surface in the Tharsis region: A signature of partial melting of the mantle?', *Journal of Volcanology and Geothermal Research*, 185(1–2), pp. 116–122. Available at: <https://doi.org/10.1016/j.jvolgeores.2008.11.027>.
- Elkins-Tanton, L.T. and Hager, B.H. (2005) 'Giant meteoroid impacts can cause volcanism', *Earth and Planetary Science Letters*, 239(3–4), pp. 219–232. Available at: <https://doi.org/10.1016/j.epsl.2005.07.029>.
- Fagents, S., Lanagan, P. and Greeley, R. (2002) 'Rootless cones on Mars: A consequence of lava-ground ice interaction', *Geological Society, London, Special Publications*, 202(1), pp. 295–317.
- Fagents, S.A. and Wilson, L. (1996) 'Numerical modeling of ejecta dispersal from transient volcanic explosions on Mars', *Icarus*, 123(2), pp. 284–295.

- Farley, K. *et al.* (2014) 'In situ radiometric and exposure age dating of the Martian surface', *science*, 343(6169), p. 1247166.
- Farrand, W.H., Gaddis, L.R. and Keszthelyi, L. (2005) 'Pitted cones and domes on Mars: Observations in Acidalia Planitia and Cydonia Mensae using MOC, THEMIS, and TES data', *Journal of Geophysical Research: Planets*, 110(E5).
- Fassett, C.I. and Head, J.W. (2007) 'Layered mantling deposits in northeast Arabia Terra, Mars: Noachian-Hesperian sedimentation, erosion, and terrain inversion', *Journal of Geophysical Research E: Planets*, 112(8), pp. 1–19. Available at: <https://doi.org/10.1029/2006JE002875>.
- Fassett, C.I. and Head, J.W. (2008) 'Valley network-fed, open-basin lakes on Mars: Distribution and implications for Noachian surface and subsurface hydrology', *Icarus*, 198(1), pp. 37–56. Available at: <https://doi.org/10.1016/j.icarus.2008.06.016>.
- Feldman, W.C. *et al.* (2011) 'Mars Odyssey neutron data: 2. Search for buried excess water ice deposits at nonpolar latitudes on Mars', *Journal of Geophysical Research: Planets*, 116(E11).
- Ferguson, R.L., Christensen, P.R. and Kieffer, H.H. (2006) 'High-resolution thermal inertia derived from the Thermal Emission Imaging System (THEMIS): Thermal model and applications', *Journal of Geophysical Research: Planets*, 111(E12).
- Ferguson, R. L., Hare, T. M., & Laura, J. (2018). HRSC and MOLA blended digital elevation Model at 200m v2Astrogeology PDS annex. U.S. Geological Survey. Retrieved from http://bit.ly/HRSC_MOLA_Blend_v0
- Filiberto, J. *et al.* (2012) 'Geochemistry of intermediate olivine-phyric shergottite Northwest Africa 6234, with similarities to basaltic shergottite Northwest Africa 480 and olivine-phyric shergottite Northwest Africa 2990', *Meteoritics & Planetary Science*, 47(8), pp. 1256–1273.
- Filiberto, J. (2017) 'Geochemistry of Martian basalts with constraints on magma genesis', *Chemical Geology*, 466, pp. 1–14.
- Filiberto, J. and Dasgupta, R. (2011) 'Fe²⁺-Mg partitioning between olivine and basaltic melts: Applications to genesis of olivine-phyric shergottites and conditions of melting in the Martian interior', *Earth and Planetary Science Letters*, 304(3–4), pp. 527–537.
- Filiberto, J. and Dasgupta, R. (2015) 'Constraints on the depth and thermal vigor of melting in the Martian mantle', *Journal of Geophysical Research: Planets*, 120(1), pp. 109–122.
- Filiberto, J., Gross, J. and McCubbin, F.M. (2016) 'Constraints on the water, chlorine, and fluorine content of the Martian mantle', *Meteoritics & Planetary Science*, 51(11), pp. 2023–2035.

-
- Flahaut, J. *et al.* (2012) 'Pristine Noachian crust and key geologic transitions in the lower walls of Valles Marineris: Insights into early igneous processes on Mars', *Icarus*, 221(1), pp. 420–435.
- Frey, H., Lowry, B.L. and Chase, S.A. (1979) 'Pseudocraters on Mars', *Journal of Geophysical Research: Solid Earth*, 84(B14), pp. 8075–8086.
- Frey, H. and Schultz, R.A. (1988) 'Large impact basins and the mega-impact origin for the crustal dichotomy on Mars', *Geophysical Research Letters*, 15(3), pp. 229–232.
- Friese, N. *et al.* (2013) 'From feeder dykes to scoria cones: the tectonically controlled plumbing system of the Rauðhólar volcanic chain, Northern Volcanic Zone, Iceland', *Bulletin of Volcanology*, 75(6), pp. 1–19.
- Gasnault, O. *et al.* (2010) 'Quantitative geochemical mapping of Martian elemental provinces', *Icarus*, 207(1), pp. 226–247.
- Geological Survey (US), Greeley, R. and Guest, J. (1987) 'Geologic map of the eastern equatorial region of Mars'.
- Ghiorso, M.S. *et al.* (2002) 'The pMELTS: A revision of MELTS for improved calculation of phase relations and major element partitioning related to partial melting of the mantle to 3 GPa', *Geochemistry, Geophysics, Geosystems*, 3(5), pp. 1–35.
- Ghosal, A., Randeria, M. and Trivedi, N. (1998) 'Role of spatial amplitude fluctuations in highly disordered s-wave superconductors', *Physical review letters*, 81(18), p. 3940.
- Goetz, W. *et al.* (2005) 'Indication of drier periods on Mars from the chemistry and mineralogy of atmospheric dust', *Nature*, 436(7047), pp. 62–65.
- Golombek, M., Anderson, F. and Zuber, M. (2001) 'Martian wrinkle ridge topography: Evidence for subsurface faults from MOLA', *Journal of Geophysical Research: Planets*, 106(E10), pp. 23811–23821.
- Golombek, M., Tanaka, K. and Franklin, B. (1996) 'Extension across Tempe Terra, Mars, from measurements of fault scarp widths and deformed craters', *Journal of Geophysical Research: Planets*, 101(E11), pp. 26119–26130.
- Golombek, M.P. and Phillips, R.J. (2010a) 'Mars tectonics', *Planetary tectonics*, 11, pp. 183–232.
- Golombek, M.P. and Phillips, R.J. (2010b) 'Mars tectonics', *Planetary tectonics*, 11, pp. 183–232.
- Goossens, S. *et al.* (2017) 'Evidence for a low bulk crustal density for Mars from gravity and topography', *Geophysical research letters*, 44(15), 7686–7694.

-
- Greeley, R. *et al.* (2005) 'Fluid lava flows in Gusev crater, Mars', *Journal of Geophysical Research: Planets*, 110(E5).
- Greeley, R. and Schneid, B.D. (1991) 'Magma generation on Mars: Amounts, rates, and comparisons with Earth, Moon, and Venus', *Science*, 254(5034), pp. 996–998.
- Greeley, R. and Spudis, P.D. (1981) 'Volcanism on mars', *Reviews of Geophysics*, 19(1), pp. 13–41.
- Grott, M. *et al.* (2007) 'Mechanical modeling of thrust faults in the Thaumasia region, Mars, and implications for the Noachian heat flux', *Icarus*, 186(2), pp. 517–526.
- Grott, M. *et al.* (2013) 'Long-term evolution of the Martian crust-mantle system', *Space Science Reviews*, 174(1), pp. 49–111.
- Halevy, I., Zuber, M.T. and Schrag, D.P. (2007) 'A sulfur dioxide climate feedback on early Mars', *Science*, 318(5858), pp. 1903–1907.
- Halliday, A. *et al.* (2001) 'The accretion, composition and early differentiation of Mars', *Space Science Reviews*, 96(1), pp. 197–230.
- Hartmann, W.K. and Neukum, G. (2001) 'Cratering chronology and the evolution of Mars', *Chronology and evolution of Mars*, pp. 165–194.
- Head, J.W. *et al.* (2006) 'The Huygens-Hellas giant dike system on Mars: Implications for Late Noachian-Early Hesperian volcanic resurfacing and climatic evolution', *Geology*, 34(4), pp. 285–288. Available at: <https://doi.org/10.1130/G22163.1>.
- Head, J.W. and Mustard, J.F. (2006) 'Breccia dikes and crater-related faults in impact craters on Mars: Erosion and exposure on the floor of a crater 75 km in diameter at the dichotomy boundary', *Meteoritics and Planetary Science*, 41(10), pp. 1675–1690. Available at: <https://doi.org/10.1111/j.1945-5100.2006.tb00444.x>.
- Head, J.W. and Solomon, S.C. (1981) 'Tectonic evolution of the terrestrial planets', *Science*, 213(4503), pp. 62–76.
- Hemmi, R. and Miyamoto, H. (2017) 'Distribution, morphology, and morphometry of circular mounds in the elongated basin of northern terra sirenum, mars', *Progress in Earth and Planetary Science*, 4(1). Available at: <https://doi.org/10.1186/s40645-017-0141-x>.
- Hemmi, R. and Miyamoto, H. (2018) 'High-resolution topographic analyses of mounds in southern acidalia planitia, mars: Implications for possible mud volcanism in submarine and subaerial environments', *Geosciences (Switzerland)*, 8(5). Available at: <https://doi.org/10.3390/geosciences8050152>.

-
- Hiesinger, H. and Head III, J. (2004) 'The Syrtis Major volcanic province, Mars: Synthesis from Mars global surveyor data', *Journal of Geophysical Research: Planets*, 109(E1).
- Hirschmann, M.M. *et al.* (1998) 'Calculation of peridotite partial melting from thermodynamic models of minerals and melts. I. Review of methods and comparison with experiments', *Journal of Petrology*, 39(6), pp. 1091–1115.
- Hood, D. *et al.* (2019) 'Contrasting regional soil alteration across the topographic dichotomy of Mars', *Geophysical Research Letters*, 46(23), pp. 13668–13677.
- Hood, D.R. *et al.* (2016) 'Assessing the geologic evolution of Greater Thaumasia, Mars', *Journal of Geophysical Research: Planets*, 121(9), pp. 1753–1769.
- Humayun, M. *et al.* (2013) 'Origin and age of the earliest Martian crust from meteorite NWA 7533', *Nature*, 503(7477), pp. 513–516.
- Hurowitz, J.A. and McLennan, S.M. (2007) 'A ~ 3.5 Ga record of water-limited, acidic weathering conditions on Mars', *Earth and Planetary Science Letters*, 260(3–4), pp. 432–443.
- Hynek, B.M. and Phillips, R.J. (2001) 'Evidence for extensive denudation of the Martian highlands', *Geology*, 29(5), pp. 407–410.
- Irwin III, R.P., Tanaka, K.L. and Robbins, S.J. (2013) 'Distribution of Early, Middle, and Late Noachian cratered surfaces in the Martian highlands: Implications for resurfacing events and processes', *Journal of Geophysical Research: Planets*, 118(2), pp. 278–291.
- Ivanov, B. and Melosh, H. (2003) 'Impacts do not initiate volcanic eruptions: Eruptions close to the crater', *Geology*, 31(10), pp. 869–872.
- Ivanov, B.A. (2001) 'Mars/Moon cratering rate ratio estimates', *Space Science Reviews*, 96(1), pp. 87–104.
- Ivanov, M.A. *et al.* (2014) 'Mud volcanism and morphology of impact craters in Utopia Planitia on Mars: Evidence for the ancient ocean', *Icarus*, 228, pp. 121–140. Available at: <https://doi.org/10.1016/j.icarus.2013.09.018>.
- Karunatillake, S. *et al.* (2006) 'Composition of northern low-albedo regions of Mars: Insights from the Mars Odyssey Gamma Ray Spectrometer', *Journal of Geophysical Research: Planets*, 111(E3).
- Karunatillake, S. *et al.* (2009) 'Chemically striking regions on Mars and Stealth revisited', *Journal of Geophysical Research: Planets*, 114(E12).
- Kaufman, L. and Rousseeuw, P.J. (2009) *Finding groups in data: an introduction to cluster analysis*. John Wiley & Sons.

- Keller, J.M. *et al.* (2006) 'Equatorial and midlatitude distribution of chlorine measured by Mars Odyssey GRS', *Journal of Geophysical Research: Planets*, 111(E3).
- Kerber, L. *et al.* (2017) 'Polygonal ridge networks on Mars: Diversity of morphologies and the special case of the Eastern Medusae Fossae Formation', *Icarus*, 281, pp. 200–219. Available at: <https://doi.org/10.1016/j.icarus.2016.08.020>.
- Kerber, L. and Head, J.W. (2010) 'The age of the Medusae Fossae Formation: Evidence of Hesperian emplacement from crater morphology, stratigraphy, and ancient lava contacts', *Icarus*, 206(2), pp. 669–684.
- Keszthelyi, L. *et al.* (2010) 'Hydrovolcanic features on Mars: Preliminary observations from the first Mars year of HiRISE imaging', *Icarus*, 205(1), pp. 211–229.
- Kiefer, W. (2013) 'Mantle Plumes and Geologically Recent Volcanism on Mars', in *AGU Fall Meeting Abstracts*, pp. DI21A-2263.
- Kiefer, W.S. (2003) 'Melting in the Martian mantle: Shergottite formation and implications for present-day mantle convection on Mars', *Meteoritics & Planetary Science*, 38(12), pp. 1815–1832.
- Kiefer, W.S. *et al.* (2016) 'Constraints on Mantle Plume Melting Conditions in the Martian Mantle Based on Improved Melting Phase Relationships of Olivine-Phyric Shergottite Yamato 980459', in *Lunar and Planetary Science Conference*.
- Kiefer, W.S. and Li, Q. (2016) 'Water undersaturated mantle plume volcanism on present-day Mars', *Meteoritics & Planetary Science*, 51(11), pp. 1993–2010.
- King, P.L. and McLennan, S.M. (2010) 'Sulfur on mars', *Elements*, 6(2), pp. 107–112.
- Kneissl, T., van Gasselt, S. and Neukum, G. (2011) 'Map-projection-independent crater size-frequency determination in GIS environments—New software tool for ArcGIS', *Planetary and Space Science*, 59(11–12), pp. 1243–1254.
- Komatsu, G. *et al.* (2011) 'Roles of methane and carbon dioxide in geological processes on Mars', *Planetary and Space Science*, 59(2–3), pp. 169–181.
- Komatsu, G. *et al.* (2016) 'Small edifice features in Chryse Planitia, Mars: assessment of a mud volcano hypothesis', *Icarus*, 268, pp. 56–75.
- Kronberg, P. *et al.* (2007) 'Acheron Fossae, Mars: Tectonic rifting, volcanism, and implications for lithospheric thickness', *Journal of Geophysical Research: Planets*, 112(E4).
- Lanz, J.K. *et al.* (2010) 'Rift zone volcanism and associated cinder cone field in Utopia Planitia, Mars', *Journal of Geophysical Research E: Planets*, 115(12). Available at: <https://doi.org/10.1029/2010JE003578>.

-
- Le Corvec, N. *et al.* (2013) 'Spatial distribution and alignments of volcanic centers: clues to the formation of monogenetic volcanic fields', *Earth-Science Reviews*, 124, pp. 96–114.
- Lodders, K. (1998) 'A survey of shergottite, nakhlite and chassigny meteorites whole-rock compositions', *Meteoritics & Planetary Science*, 33(S4), pp. A183–A190.
- Lucchitta, B.K. (1981) 'Mars and Earth: Comparison of cold-climate features', *Icarus*, 45(2), pp. 264–303.
- Lucchitta, B.K. *et al.* (1992) 'The canyon system on Mars.', *Mars*, pp. 453–492.
- Lutz, T.M. (1986) 'An analysis of the orientations of large-scale crustal structures: A statistical approach based on areal distributions of pointlike features', *Journal of Geophysical Research: Solid Earth*, 91(B1), pp. 421–434.
- Malin, M.C. *et al.* (2007) 'Context camera investigation on board the Mars Reconnaissance Orbiter', *Journal of Geophysical Research: Planets*, 112(E5).
- Malin, M.C. and Edgett, K.S. (2000) 'Sedimentary rocks of early Mars', *Science*, 290(5498), pp. 1927–1937. Available at: <https://doi.org/10.1126/science.290.5498.1927>.
- Mandt, K.E. *et al.* (2008) 'Origin of the Medusae Fossae Formation, Mars: Insights from a synoptic approach', *Journal of Geophysical Research: Planets*, 113(E12).
- Mangold, N. *et al.* (2000) 'Chronology of compressional deformation on Mars: Evidence for a single and global origin', *Planetary and Space Science*, 48(12–14), pp. 1201–1211.
- Mangold, N., Allemand, P. and Thomas, P. (1998) 'Wrinkle ridges of Mars: Structural analysis and evidence for shallow deformation controlled by ice-rich décollements', *Planetary and Space Science*, 46(4), pp. 345–356.
- Martí, J. *et al.* (2016) 'Stress controls of monogenetic volcanism: a review', *Frontiers in Earth Science*, 4, p. 106.
- Maurice, S. *et al.* (2011) 'Mars Odyssey neutron data: 1. Data processing and models of water-equivalent-hydrogen distribution', *Journal of Geophysical Research: Planets*, 116(E11).
- McEwen, A.S. *et al.* (2007) 'Mars reconnaissance orbiter's high resolution imaging science experiment (HiRISE)', *Journal of Geophysical Research: Planets*, 112(E5).
- McGill, G.E. (2000) 'Crustal history of north central Arabia Terra, Mars', *Journal of Geophysical Research E: Planets*, 105(E3), pp. 6945–6959. Available at: <https://doi.org/10.1029/1999JE001175>.

- McGowan, E. (2009) 'Spatial distribution of putative water related features in Southern Acidalia/Cydonia Mensae, Mars', *Icarus*, 202(1), pp. 78–89.
- McLennan, S.M. (2012) 'Geochemistry of sedimentary processes on Mars'.
- McNeil, J.D. *et al.* (2021) 'Morphology, morphometry and distribution of isolated landforms in southern Chryse Planitia, Mars', *Journal of Geophysical Research: Planets*, 126(5), p. e2020JE006775.
- McSween, H.Y. *et al.* (2006) 'Characterization and petrologic interpretation of olivine-rich basalts at Gusev Crater, Mars', *Journal of Geophysical Research: Planets*, 111(E2).
- McSween Jr, H.Y., Taylor, G.J. and Wyatt, M.B. (2009) 'Elemental composition of the Martian crust', *science*, 324(5928), pp. 736–739.
- Médard, E. and Grove, T.L. (2006) 'Early hydrous melting and degassing of the Martian interior', *Journal of Geophysical Research: Planets*, 111(E11).
- Meresse, S. *et al.* (2008) 'Formation and evolution of the chaotic terrains by subsidence and magmatism: Hydrates Chaos, Mars', *Icarus*, 194(2), pp. 487–500.
- Mezger, K., Debaille, V. and Kleine, T. (2013) 'Core formation and mantle differentiation on Mars', *Space science reviews*, 174(1), pp. 27–48.
- Michael, G. (2013) 'Planetary surface dating from crater size–frequency distribution measurements: Multiple resurfacing episodes and differential isochron fitting', *Icarus*, 226(1), pp. 885–890.
- Michael, G. and Neukum, G. (2010) 'Planetary surface dating from crater size–frequency distribution measurements: Partial resurfacing events and statistical age uncertainty', *Earth and Planetary Science Letters*, 294(3–4), pp. 223–229.
- Michalski, J.R. and Bleacher, J.E. (2013) 'Supervolcanoes within an ancient volcanic province in Arabia Terra, Mars', *Nature*, 502(7469), pp. 47–52. Available at: <https://doi.org/10.1038/nature12482>.
- Ming, D.W. *et al.* (2008) 'Geochemical properties of rocks and soils in Gusev crater, Mars: Results of the Alpha Particle X-ray Spectrometer from Cumberland Ridge to Home Plate', *Journal of Geophysical Research: Planets*, 113(E12).
- Moore, J.M. (1990) 'Nature of the mantling deposit in the heavily cratered terrain of northeastern Arabia, Mars', *Journal of Geophysical Research*, 95(B9). Available at: <https://doi.org/10.1029/jb095ib09p14279>.
- Morschhauser, A., Grott, M. and Breuer, D. (2011) 'Crustal recycling, mantle dehydration, and the thermal evolution of Mars', *Icarus*, 212(2), pp. 541–558.

-
- Nachon, M. *et al.* (2014) 'Calcium sulfate veins characterized by ChemCam/Curiosity at Gale crater, Mars', *Journal of Geophysical Research: Planets*, 119(9), pp. 1991–2016.
- Nagle-McNaughton, T. and Scuderi, L. (2021) 'A geomorphological case for multistage evolution of transverse aeolian ridges', *Planetary and Space Science*, 200, p. 105192.
- Nahm, A.L. and Schultz, R.A. (2010) 'Evaluation of the orogenic belt hypothesis for the formation of the Thaumasia Highlands, Mars', *Journal of Geophysical Research: Planets*, 115(E4).
- Nesbitt, H. and Wilson, R. (1992) 'Recent chemical weathering of basalts', *American Journal of science*, 292(10), pp. 740–777.
- Nesbitt, Hw. and Young, G. (1982) 'Early Proterozoic climates and plate motions inferred from major element chemistry of lutites', *nature*, 299(5885), pp. 715–717.
- Neukum, G. *et al.* (2010) 'The geologic evolution of Mars: Episodicity of resurfacing events and ages from cratering analysis of image data and correlation with radiometric ages of Martian meteorites', *Earth and Planetary Science Letters*, 294(3–4), pp. 204–222.
- Neumann, G. *et al.* (2004) 'Crustal structure of Mars from gravity and topography', *Journal of Geophysical Research: Planets*, 109(E8).
- Newsom, H.E. and Hagerty, J.J. (1997) 'Chemical components of the Martian soil: Melt degassing, hydrothermal alteration, and chondritic debris', *Journal of Geophysical Research: Planets*, 102(E8), pp. 19345–19355.
- Nimmo, F. and Tanaka, K. (2005) 'Early crustal evolution of Mars', *Annual Review of Earth and Planetary Sciences*, 33(1), pp. 133–161.
- Noe Dobrea, E. *et al.* (2010) 'Mineralogy and stratigraphy of phyllosilicate-bearing and dark mantling units in the greater Mawrth Vallis/west Arabia Terra area: Constraints on geological origin', *Journal of Geophysical Research: Planets*, 115(E7).
- Ody, A. *et al.* (2013) 'Global investigation of olivine on Mars: Insights into crust and mantle compositions', *Journal of Geophysical Research: Planets*, 118(2), pp. 234–262.
- Oehler, D.Z. and Allen, C.C. (2010) 'Evidence for pervasive mud volcanism in Acidalia Planitia, Mars', *Icarus*, 208(2), pp. 636–657. Available at: <https://doi.org/10.1016/j.icarus.2010.03.031>.
- Ojha, L. *et al.* (2018) 'The Medusae Fossae Formation as the single largest source of dust on Mars', *Nature communications*, 9(1), pp. 1–7.

Ojha, L. *et al.* (2021) ‘Amagmatic hydrothermal systems on Mars from radiogenic heat’, *Nature communications*, 12(1), pp. 1–11.

Pain, C., Clarke, J. and Thomas, M. (2007) ‘Inversion of relief on Mars’, *Icarus*, 190(2), pp. 478–491.

Pan, C., Rogers, A. and Michalski, J. (2015) ‘Thermal and near-infrared analyses of central peaks of Martian impact craters: Evidence for a heterogeneous Martian crust’, *Journal of Geophysical Research: Planets*, 120(4), pp. 662–688.

Pan, L. *et al.* (2017) ‘The stratigraphy and history of Mars’ northern lowlands through mineralogy of impact craters: A comprehensive survey’, *Journal of Geophysical Research: Planets*, 122(9), pp. 1824–1854.

Parfitt, L. and Wilson, L. (2009) *Fundamentals of physical volcanology*. John Wiley & Sons.

Parro, L.M. *et al.* (2017) ‘Present-day heat flow model of Mars’, *Scientific reports*, 7(1), pp. 1–9.

Pascuzzo, A.C. *et al.* (2019) ‘The formation of irregular polygonal ridge networks, Nili Fossae, Mars: Implications for extensive subsurface channelized fluid flow in the Noachian’, *Icarus*, 319(May 2018), pp. 852–868. Available at: <https://doi.org/10.1016/j.icarus.2018.10.020>.

Pedersen, G.B.M., Head, J.W. and Wilson, L. (2010) ‘Formation, erosion and exposure of Early Amazonian dikes, dike swarms and possible subglacial eruptions in the Elysium Rise/Utopia Basin Region, Mars’, *Earth and Planetary Science Letters*, 294(3–4), pp. 424–439. Available at: <https://doi.org/10.1016/j.epsl.2009.08.010>.

Phillips, R.J. *et al.* (2001) ‘Ancient geodynamics and global-scale hydrology on Mars’, *Science*, 291(5513), pp. 2587–2591. Available at: <https://doi.org/10.1126/science.1058701>.

Platz, T. *et al.* (2015) ‘Volcanism and tectonism across the inner solar system: An overview’, *Geological Society Special Publication*, 401, pp. 1–56. Available at: <https://doi.org/10.1144/SP401.22>.

Plesa, A. *et al.* (2018) ‘The thermal state and interior structure of Mars’, *Geophysical Research Letters*, 45(22), pp. 12–198.

Plescia, J. (2004) ‘Morphometric properties of Martian volcanoes’, *Journal of Geophysical Research: Planets*, 109(E3).

Pondrelli, M. *et al.* (2011) ‘Mud volcanoes in the geologic record of Mars: The case of Firsoff crater’, *Earth and Planetary Science Letters*, 304(3–4), pp. 511–519. Available at: <https://doi.org/10.1016/j.epsl.2011.02.027>.

-
- Pondrelli, M. *et al.* (2015) 'Equatorial layered deposits in Arabia Terra, Mars: Facies and process variability', *Bulletin of the Geological Society of America*, 127(7–8), pp. 1064–1089. Available at: <https://doi.org/10.1130/B31225.1>.
- Pozzobon, R. *et al.* (2021) 'Volcano dynamics vs tectonics on Mars: evidence from Pavonis Mons', *Journal of Volcanology and Geothermal Research*, 410, p. 107148.
- Quantin-Nataf, C. *et al.* (2018) 'MarsSI: Martian surface data processing information system', *Planetary and Space Science*, 150, pp. 157–170.
- Rani, A., et al., (2020) 'Mounds and ridges inside a floor-fractured crater in central eastern Arabia Terra' *51st Lunar and Planetary Institute Science Conference*, Abstracts # 1955.
- Rani, A. *et al.* (2021) 'Evidence of Regionally Distributed Tectono-Volcanism in a Floor Fractured Crater of North-Central Arabia Terra, Mars', *Journal of Geophysical Research: Planets*, 126(11), p. e2020JE006748.
- Rani, A., *et al.* (2021) 'Synthesis of chemical provinces on mars and their geologic interpretations' *52nd Lunar and Planetary Institute Science Conference*, #Abstract No. 2353.
- Rani, A., and Basu Sarbadhikari, A., 'Noachian Volcanism and its Implication to the Thermal Evolution of Mars' *AGU Fall Meeting 2021*, #Abstract No. P54A-03.
- Rani, A. et al. (2022) 'Consolidated Chemical Provinces on Mars: Implications for Geologic Interpretations', *Geophysical Research Letters*, (Accepted, DOI: 10.1029/2022GL099235).
- Robbins, S.J., Di Achille, G. and Hynek, B.M. (2011) 'The volcanic history of Mars: High-resolution crater-based studies of the calderas of 20 volcanoes', *Icarus*, 211(2), pp. 1179–1203. Available at: <https://doi.org/10.1016/j.icarus.2010.11.012>.
- Roberts, J.H. and Zhong, S. (2006) 'Degree-1 convection in the Martian mantle and the origin of the hemispheric dichotomy', *Journal of Geophysical Research: Planets*, 111(E6).
- Roberts, K.S. *et al.* (2011) 'Structural controls on mud volcano vent distributions: examples from Azerbaijan and Lusi, east Java', *Journal of the Geological Society*, 168(4), pp. 1013–1030.
- Rodriguez, J.A.P. *et al.* (2010) 'The sedimentology and dynamics of crater-affiliated wind streaks in western Arabia Terra, Mars and Patagonia, Argentina', *Geomorphology*, 121(1–2), pp. 30–54.
- Rogers, A.D., Bandfield, J.L. and Christensen, P.R. (2007) 'Global spectral classification of Martian low-albedo regions with Mars Global Surveyor Thermal

- Emission Spectrometer (MGS-TES) data', *Journal of Geophysical Research: Planets*, 112(E2).
- Rogers, A.D. and Fergason, R.L. (2011) 'Regional-scale stratigraphy of surface units in Tyrrhena and Iapygia Terrae, Mars: Insights into highland crustal evolution and alteration history', *Journal of Geophysical Research: Planets*, 116(E8).
- Rogers, A.D. and Hamilton, V.E. (2015) 'Compositional provinces of Mars from statistical analyses of TES, GRS, OMEGA and CRISM data', *Journal of Geophysical Research: Planets*, 120(1), pp. 62–91.
- Rousseeuw, P.J. (1987) 'Silhouettes: a graphical aid to the interpretation and validation of cluster analysis', *Journal of computational and applied mathematics*, 20, pp. 53–65.
- Ruiz, J. *et al.* (2011) 'The thermal evolution of Mars as constrained by paleo-heat flows', *Icarus*, 215(2), pp. 508–517.
- Ruiz, J. (2014) 'The early heat loss evolution of Mars and their implications for internal and environmental history', *Scientific reports*, 4(1), pp. 1–7.
- Salvatore, M.R. *et al.* (2010) 'Definitive evidence of Hesperian basalt in Acidalia and Chryse planitiae', *Journal of Geophysical Research: Planets*, 115(E7).
- Santos, A.R. *et al.* (2015) 'Petrology of igneous clasts in Northwest Africa 7034: Implications for the petrologic diversity of the Martian crust', *Geochimica et Cosmochimica Acta*, 157, pp. 56–85.
- Saper, L. and Mustard, J.F. (2013) 'Extensive linear ridge networks in Nili Fossae and Nilosyrtis, Mars: Implications for fluid flow in the ancient crust', *Geophysical Research Letters*, 40(2), pp. 245–249. Available at: <https://doi.org/10.1002/grl.50106>.
- Sautter, V. *et al.* (2014) 'Igneous mineralogy at Bradbury Rise: The first ChemCam campaign at Gale crater', *Journal of Geophysical Research: Planets*, 119(1), pp. 30–46.
- Sautter, V. *et al.* (2015a) 'In situ evidence for continental crust on early Mars', *Nature Geoscience*, 8(8), pp. 605–609.
- Sautter, V. *et al.* (2015b) 'In situ evidence for continental crust on early Mars', *Nature Geoscience*, 8(8), pp. 605–609.
- Schultz, P.H. and Glicken, H. (1979) 'on Mars', 84(9), pp. 8033–8047.
- Schultz, R.A. (1998) 'Multiple-process origin of Valles Marineris basins and troughs, Mars', *Planetary and space science*, 46(6–7), pp. 827–834.

-
- Schultz, R.A. (2000) 'Fault-population statistics at the Valles Marineris Extensional Province, Mars: implications for segment linkage, crustal strains, and its geodynamical development', *Tectonophysics*, 316(1–2), pp. 169–193.
- Schumacher, S. and Breuer, D. (2007) 'An alternative mechanism for recent volcanism on Mars', *Geophysical research letters*, 34(14).
- Scott, D.H. and Tanaka, K.L. (1981) 'Mars: Paleostratigraphic restoration of buried surfaces in Tharsis Montes', *Icarus*, 45(2), pp. 304–319.
- Shean, D. E., *et al.*, (2011) 'MRO CTX stereo image processing and preliminary DEM quality assessment' *46th Lunar and Planetary Institute Science Conference*, Abstracts # 2646
- Silvestro, S. *et al.* (2011) 'Active aeolian processes on Mars: A regional study in Arabia and Meridiani Terrae', *Geophysical Research Letters*, 38(20).
- Smith, D.E. *et al.* (2001) 'Mars Orbiter Laser Altimeter: Experiment summary after the first year of global mapping of Mars', *Journal of Geophysical Research: Planets*, 106(E10), pp. 23689–23722.
- Smith, P.M. and Asimow, P.D. (2005) 'Adiabat_1ph: A new public front-end to the MELTS, pMELTS, and pHMELTS models', *Geochemistry, Geophysics, Geosystems*, 6(2).
- Stephens, T.L. *et al.* (2017) 'Igneous sills record far-field and near-field stress interactions during volcano construction: Isle of Mull, Scotland', *Earth and Planetary Science Letters*, 478, pp. 159–174.
- Stephens, T.L. *et al.* (2018) 'Mechanical models to estimate the paleostress state from igneous intrusions', *Solid earth*, 9(4), pp. 847–858.
- Tanaka, K.L. (1997) 'Sedimentary history and mass flow structures of Chryse and Acidalia Planitiae, Mars', *Journal of Geophysical Research: Planets*, 102(E2), pp. 4131–4149.
- Tanaka, K.L. *et al.* (2003) 'Resurfacing history of the northern plains of Mars based on geologic mapping of Mars Global Surveyor data', *Journal of Geophysical Research: Planets*, 108(E4).
- Tanaka, K.L. *et al.* (2014) 'Geologic Map of Mars (Scientific Investigations Map 3292)', *U.S. Geological Survey Geologic Investigations* [Preprint]. Available at: <https://doi.org/10.3133/sim3292>.
- Tanaka, K.L., Golombek, M.P. and Banerdt, W.B. (1991) 'Reconciliation of stress and structural histories of the Tharsis region of Mars', *Journal of Geophysical Research: Planets*, 96(E1), pp. 15617–15633.

-
- Taylor, G.J., Boynton, W., *et al.* (2006) 'Bulk composition and early differentiation of Mars', *Journal of Geophysical Research: Planets*, 111(E3).
- Taylor, G.J., Stopar, J., *et al.* (2006) 'Variations in K/Th on Mars', *Journal of Geophysical Research: Planets*, 111(E3).
- Taylor, G.J. *et al.* (2010) 'Mapping Mars geochemically', *Geology*, 38(2), pp. 183–186.
- Taylor, G.J. (2013) 'The bulk composition of Mars', *Geochemistry*, 73(4), pp. 401–420.
- Thomson, B.J. and Head III, J.W. (2001) 'Utopia Basin, Mars: Characterization of topography and morphology and assessment of the origin and evolution of basin internal structure', *Journal of Geophysical Research: Planets*, 106(E10), pp. 23209–23230.
- Toksöz, M.N. and Hsui, A.T. (1978) 'Thermal history and evolution of Mars', *Icarus*, 34(3), pp. 537–547.
- Tosca, N.J. *et al.* (2008) 'Fe oxidation processes at Meridiani Planum and implications for secondary Fe mineralogy on Mars', *Journal of Geophysical Research: Planets*, 113(E5).
- Treiman, A.H. *et al.* (1986) 'Core formation in the Earth and shergottite parent body (SPB): Chemical evidence from basalts', *Geochimica et Cosmochimica Acta*, 50(6), pp. 1071–1091.
- Treiman, A.H. (2003) 'Chemical compositions of martian basalts (shergottites): Some inferences on b; formation, mantle metasomatism, and differentiation in Mars', *Meteoritics & Planetary Science*, 38(12), pp. 1849–1864.
- Treiman, A.H. *et al.* (2016) 'Mineralogy, provenance, and diagenesis of a potassic basaltic sandstone on Mars: CheMin X-ray diffraction of the Windjana sample (Kimberley area, Gale Crater)', *Journal of Geophysical Research: Planets*, 121(1), pp. 75–106.
- Treiman, A.H. and Filiberto, J. (2015) 'Geochemical diversity of shergottite basalts: Mixing and fractionation, and their relation to Mars surface basalts', *Meteoritics & Planetary Science*, 50(4), pp. 632–648.
- Tuff, J., Wade, J. and Wood, B. (2013) 'Volcanism on Mars controlled by early oxidation of the upper mantle', *Nature*, 498(7454), pp. 342–345.
- Udry, A. *et al.* (2014) 'Petrogenesis of a vitrophyre in the martian meteorite breccia NWA 7034', *Geochimica et Cosmochimica Acta*, 141, pp. 281–293.
- Udry, A. *et al.* (2020) 'What martian meteorites reveal about the interior and surface of Mars'.

Ulrich, G. (1987) 'SP Mountain cinder cone and lava flow, northern Arizona', *Centennial Field Guide*, 2, pp. 385–388.

Virgo, S., Abe, S. and Urai, J.L. (2014) 'The evolution of crack seal vein and fracture networks in an evolving stress field: Insights from Discrete Element Models of fracture sealing', *Journal of Geophysical Research: Solid Earth*, 119(12), pp. 8708–8727.

Wadge, G. and Cross, A. (1988) 'Quantitative methods for detecting aligned points: an application to the volcanic vents of the Michoacan-Guanajuato volcanic field, Mexico', *Geology*, 16(9), pp. 815–818.

Watters, T.R. (1993) 'Compressional tectonism on Mars', *Journal of Geophysical Research: Planets*, 98(E9), pp. 17049–17060.

Watters, T.R. (2003) 'Lithospheric flexure and the origin of the dichotomy boundary on Mars', *Geology*, 31(3), pp. 271–274.

Werner, S.C. (2009) 'The global martian volcanic evolutionary history', *Icarus*, 201(1), pp. 44–68. Available at: <https://doi.org/10.1016/j.icarus.2008.12.019>.

Whelley, P. *et al.* (2021) 'Stratigraphic evidence for early martian explosive volcanism in Arabia Terra', *Geophysical Research Letters*, 48(15), p. e2021GL094109.

Wieczorek, M. A., Broquet, A., McLennan, S. M., Rivoldini, A., Golombek, M., Antonangeli, D., ... & Banerdt, W. B. (2022) 'InSight constraints on the global character of the Martian crust', *Journal of Geophysical Research: Planets*, e2022JE007298.

Wiens, R.C. *et al.* (2012) 'The ChemCam instrument suite on the Mars Science Laboratory (MSL) rover: Body unit and combined system tests', *Space science reviews*, 170(1), pp. 167–227.

Wilhelms, D. and Squyres, S. (1984) 'The Borealis basin of Mars.', *NASA Tech. Memo., NASA TM-86246*, pp. 110–112.

Williams, D.A. *et al.* (2010) 'The circum-Hellas volcanic province, Mars: Assessment of wrinkle-ridged plains', *Earth and Planetary Science Letters*, 294(3–4), pp. 492–505.

Williams, J. *et al.* (2008) 'The formation of Tharsis on Mars: What the line-of-sight gravity is telling us', *Journal of Geophysical Research: Planets*, 113(E10).

Williams, R.M., Moersch, J.E. and Ferguson, R.L. (2018) 'Thermophysical properties of Martian fluvial sinuous ridges: Inferences on "inverted channel" induration agent', *Earth and Space Science*, 5(9), pp. 516–528.

Wilson, J.T. *et al.* (2018) 'Equatorial locations of water on Mars: Improved resolution maps based on Mars Odyssey Neutron Spectrometer data', *Icarus*, 299, pp. 148–160.

Wilson, L. (2009) 'Volcanism in the solar system', *Nature Geoscience*, 2(6), pp. 389–397.

Wilson, L. and Head III, J.W. (1981) 'Ascent and eruption of basaltic magma on the Earth and Moon', *Journal of Geophysical Research: Solid Earth*, 86(B4), pp. 2971–3001.

Wilson, L. and Head III, J.W. (2002) 'Tharsis-radial graben systems as the surface manifestation of plume-related dike intrusion complexes: Models and implications', *Journal of Geophysical Research: Planets*, 107(E8), pp. 1–1.

Wilson, L. and Head, J.W. (1983) 'A comparison of volcanic eruption processes on Earth, Moon, Mars, Io and Venus', *Nature*, 302(5910), pp. 663–669.

Wilson, L. and Head, J.W. (1994) 'Review and Analysis and of Volcanic Eruption To Theory Relationships Landforms', *Reviews of Geophysics*, 32(3), pp. 221–263. Available at: <https://doi.org/10.1029/94RG01113>.

Wittmann, A. *et al.* (2015) 'Petrography and composition of Martian regolith breccia meteorite Northwest Africa 7475', *Meteoritics & Planetary Science*, 50(2), pp. 326–352.

Wood, C. (1979) 'Cindercones on Earth, Moon and Mars', in: *Lunar and Planetary Science Conference*, pp. 1370–1372.

Wordsworth, R. (2016) 'The climate of early Mars', *arXiv preprint arXiv:1606.02813* [Preprint].

Wray, J.J. *et al.* (2013) 'Prolonged magmatic activity on Mars inferred from the detection of felsic rocks', *Nature Geoscience*, 6(12), pp. 1013–1017.

Xiao, L. *et al.* (2012) 'Ancient volcanism and its implication for thermal evolution of Mars', *Earth and Planetary Science Letters*, 323–324, pp. 9–18. Available at: <https://doi.org/10.1016/j.epsl.2012.01.027>.

Yin, A. (2012) 'Structural analysis of the Valles Marineris fault zone: Possible evidence for large-scale strike-slip faulting on Mars', *Lithosphere*, 4(4), pp. 286–330.

Zabusky, K., Andrews-Hanna, J.C. and Wiseman, S.M. (2012) 'Reconstructing the distribution and depositional history of the sedimentary deposits of Arabia Terra, Mars', *Icarus*, 220(2), pp. 311–330. Available at: <https://doi.org/10.1016/j.icarus.2012.05.007>.

Zeilhofer, M.F., Chandler, C.O. and Barlow, N.G. (2018) 'Evidence of low-latitude fluvial and glacial activity during the martian Amazonian era', *arXiv preprint arXiv:1807.09716* [Preprint].

Zhong, S. and Zuber, M.T. (2001) 'Degree-1 mantle convection and the crustal dichotomy on Mars', *Earth and Planetary Science Letters*, 189(1–2), pp. 75–84.

Zimbelman, J.R., Gregg, Tracey KP and Gregg, Tracy KP (2000) *Environmental effects on volcanic eruptions: From deep oceans to deep space*. Springer Science & Business Media.

Zimbelman, J.R. and Scheidt, S.P. (2012) 'Hesperian age for western medusae fossae formation, Mars', *Science*, 336(6089), pp. 1683–1683.

Zipfel, J. *et al.* (2011) 'Bounce Rock—A shergottite-like basalt encountered at Meridiani Planum, Mars', *Meteoritics & Planetary Science*, 46(1), pp. 1–20.

Zuber, M.T. *et al.* (2000) 'Internal structure and early thermal evolution of Mars from Mars Global Surveyor topography and gravity', *science*, 287(5459), pp. 1788–1793.

List of Publications

1. **Rani, A.**, Basu Sarbadhikari, A., Sinha, R. K., Karunatillake, S., Komatsu, G., and Bates, A., (2021). "Evidence of regionally distributed tectono-volcanism in a floor fractured crater of North-Central Arabia Terra, Mars" *Journal of Geophysical Research: Planets*, 126(11). <https://doi.org/10.1029/2020JE006748>.
2. **Rani, A.**, Basu Sarbadhikari, A., Hood, D., Gasnault, O., Nambiar, S., and Karunatillake, S. (2022). "Consolidated Chemical Provinces on Mars: Implications for Geologic Interpretations". *Geophysical Research Letters*, 49(14), <https://doi.org/10.1029/2022GL099235>
3. Sinha, R. K., **Rani, A.**, Conway, S. J., Vijayan, S., Basu Sarbadhikari, A., Massé, M., Mangold N., and Anil Bhardwaj (2020). "Boulder fall activity in the Jezero crater, Mars", *Geophysical Research Letters*, 47 (23). <https://doi.org/10.1029/2020GL090362>.
4. Srivastava, Y., Kumar, A., Basu Sarbadhikari, A., Ray, D., Nair, V. M., Das, A., Shukla, A. D., Sathiyaseelan, S., Ramachandran, R., Sivaraman, B., Vijayan, S., Panwar, N., Verma, A. J., Srivastava, N., **Rani, A.**, Arora, G., Mahajan, R. R. and Anil Bhardwaj. "The Diyodar meteorite: A new fall in India". (*Accepted in Current Science*).

Under Review

1. Sinha, Rishitosh K., **Rani, A.**, Ruj, T., and Anil Bhardwaj. "Formation age and seismicity of the lobate scarp in the vicinity of Chandrayaan-3 landing site in the southern high latitudes of the Moon", (*Submitted in Icarus*)

Under Preparation

1. **Rani, A.**, Basu Sarbadhikari, A. and Karunatillake, S. "Noachian Volcanism: Implication to the thermal evolution of early Mars."

2. Sinha, Rishitosh K., Panwar, N., **Rani, A.**, Srivastava, N., and Anil Bhardwaj. "Geological investigation of boulder-fall activity in the Vitello crater region of the Moon"

Recognition and Awards

1. Cover page of JGR-Planets based on '*Evidence of regionally distributed tectono-volcanism in a floor fractured crater of North-Central Arabia Terra, Mars*'. <https://agupubs.onlinelibrary.wiley.com/doi/epdf/10.1002/jgre.21394>.
Research/Science News

Research/Science News

1. A crater at Arabia Terra of Mars is named after Prof. K. R. Ramanathan, the First Director of PRL. <https://planetarynames.wr.usgs.gov/Feature/16039>
2. "Evidence of Tectono-Volcanism in Arabia Terra, Mars" hosted on Planetary Geomorphology Image of the Month. <https://planetarygeomorphology.wordpress.com/2022/02/01/evidence-of-tectono-volcanism-in-arabia-terra-mars/>

Presentations at Conference/Symposium

1. **Rani, A.**, Basu Sarbadhikari, A., and Sinha, R. K., Geological characterization of an FFC in North-Central Arabia Terra, Mars: Implications for possible igneous processes in the earlier epochs, In *National Space Science Symposium 2022, India*.
2. **Rani, A.**, and Basu Sarbadhikari, A., Noachian Volcanism and its Implication to the Thermal Evolution of Mars. In *AGU Fall Meeting 2021* (#Abstract No. P54A-03).

3. **Rani, A.**, and Basu Sarbadhikari, A., Phosphorus in Martian magmas: Implications for potential mantle sources. In *AGU Fall Meeting 2021* (#Abstract No. P55B-1927).
4. Basu Sarbadhikari, A., Srivastava, Y., and **Rani, A.**, Silicic Highlands vs Basaltic Plains of Venus: Geochemical Significance. In *Venus Science Conference (Venus-SC-2021)*, India.
5. **Rani, A.**, Basu Sarbadhikari, A., Hood, D. R., Karunatillake, S. and Nambiar S., 2021. Chemical Provinces of Mars Complementing Mapped Geology. In *Annual meeting of Planetary Geologic Mappers 2021* (#Abstract No. 7041).
6. **Rani, A.**, Basu Sarbadhikari, A., Hood, D. R., Karunatillake, S. and Nambiar S., Synthesis of chemical provinces on mars and their geologic interpretations. In *Lunar and Planetary Science Conference 2021* (#Abstract No. 2353).
7. **Rani, A.**, Srivastava, Y., and Basu Sarbadhikari, A., Synthesis of chemical provinces on Mars with the latest geochemical maps and implications for geologic interpretations. In *Indian Planetary Science Conference 2021*.
8. Srivastava, Y., **Rani, A.**, and Basu Sarbadhikari, A., Highly Siderophile Element conundrum of the Moon. In *Indian Planetary Science Conference 2021*.
9. Basu Sarbadhikari, A.; **Rani, A.**, Hood, D. R., Karunatillake, S., Synthesis of chemical provinces on Mars with the latest geochemical maps and implications for geologic interpretations. In *AGU Abstract Fall Meeting 2020*. (#Abstract No. 768038)
10. Fuqua Haviland, H., Karunatillake, S., Moitra, P., **Rani, A.**, Ojha, L., Baratoux, D. and Susko, D., Characterizing Martian Volcanic Provinces' Magmatic Evolution and Chemistry through Equations of State Modeling Initial Study. In *AGU Abstract Fall Meeting 2020*.
11. **Rani, A.**, Basu Sarbadhikari, A., and Sinha, R. K., Study of a Floor-Fractured Crater in Central Eastern Arabia Terra of Mars. In *Indian Planetary Science Conference 2020*.
12. **Rani, A.**, Basu Sarbadhikari, A., Sinha, R. K., Karunatillake, S., Komatsu, G., and Bates, A., Mounds and ridges inside a Floor-Fractured Crater in Central

Eastern Arabia. In *Lunar and Planetary Science Conference 2020* (#Abstract No. 1955).

13. **Rani, A.**, Sinha, R. K., and Basu Sarbadhikari, A., Karunatillake, S., Komatsu, G., and Bates, A., Geological Study of a FFC in the SE Arabia Terra, Mars: Possible evidences for early igneous processes on Mars. In *National Space Science Symposium 2019, India*.